The measurement and simulation of indoor air flow

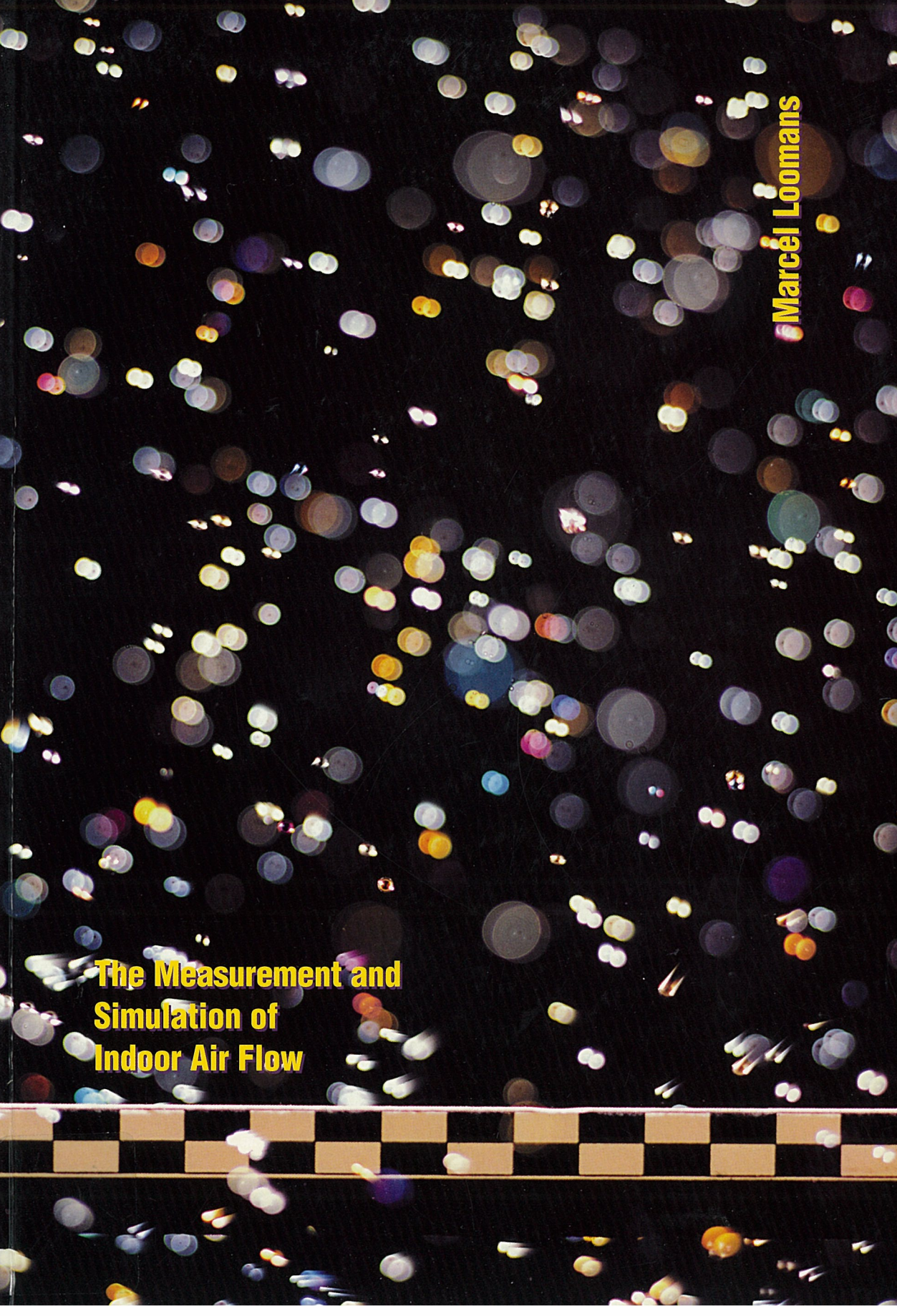
Marcel Loomans
The Measurement and Simulation of Indoor Air Flow

The Measurement and Simulation of Indoor Air Flow

The Measurement and Simulation of Indoor Air Flow

PROEFSCHRIFT

ter verkrijging van de graad van doctor aan de
Technische Universiteit Eindhoven, op gezag van de
Rector Magnificus, prof.dr. M. Rem, voor een
commissie aangewezen door het College voor
Promoties in het openbaar te verdedigen op
maandag 14 december 1998 om 16.00 uur

door

Marcel Gerardus Louis Cornelius Loomans
geboren te Dongen

Dit proefschrift is goedgekeurd door de promotoren:

prof.ir. P.G.S. Rutten

en

prof.ir. J.A. Wisse

Copromotor:

dr.ir. Q. Chen

ISBN 90 6814 085 X

This research was partially funded by a grant from the Dutch Organisation for Scientific Research (NWO - STIMULANS).

Contents

Summary

As the majority of people spend most of their time indoors and often share the same space, knowledge and prediction of the indoor climate conditions is important to optimise the indoor climate for the occupants at the design phase. A gamut of parameters determine the indoor climate and are important for the well-being of the occupant of a room in terms of thermal comfort and (perceived) indoor air quality. This research has focussed on two parameters, namely velocity and temperature.

In recent years in literature an overall consensus is found on the fact that thermal comfort is above all a personal experience. This point of departure differs from the established professional attitude to design an uniform climate for a building instead of creating comfort for people. It has lead to a renewed interest for personal control within a building and especially for task conditioning systems. Such systems intend to condition a small space around the occupant, controlled by the occupant.

Given the focus on the occupant level, more detailed information is required on the climate within a small space around the person: the micro-climate. The air change rate and the supply and exhaust conditions at the room level (or the macro-climate) do not present sufficient information to evaluate the micro-climate. The flow pattern determines the effectiveness with which a room is ventilated and has a large influence on the local thermal conditions.

For the determination and prediction of the indoor air flow pattern two important tools are available: *measurement* and *simulation* (Computational Fluid Dynamics - CFD). Both tools currently however have limitations in accuracy and reliability with which the flow pattern can be determined. In this thesis the measurement and simulation tool are investigated extensively in order to give a contribution to the reliability with which the indoor climate can be predicted and optimised.

With regard to *measurement*; Focus has been set on velocity measurement techniques. From an evaluation of the measurement principles, the currently most practical and mostly applied technique, the hot sphere anemometer, and the most promising technique for indoor air velocity registration, Particle Tracking Velocimetry (PTV), have been investigated on various aspects, experimentally as well as numerically.

- Summary -

The accuracy that can be obtained with the hot sphere anemometer is very restricted. This anemometer derives the velocity from the heat transfer between the probe and the surrounding air. Such a measurement technique requires an accurate conformity between calibration and application conditions to attain the expected measurement accuracy. Instead of a low velocity wind tunnel, a relative simple calibration set-up and procedure have been developed for the calibration. Despite its restrictions it was concluded that the hot sphere anemometer currently is the most readily applicable measuring device for indoor air velocities. However, a lot of effort is required to obtain quantitative information over the total room.

The application of PTV is very much hampered by the sufficient and homogeneous production of the applied tracer particle, a helium-filled soap bubble, that is used to visualise the flow pattern. Apart from this restriction, theoretical analysis concludes that the technique is pre-eminently suited for the measurement of the indoor air velocity. An example of a PTV-experiment is shown to illustrate its potential.

With regard to *simulation*; Prediction of the indoor air flow using the CFD tool is very attractive given the restrictions and effort to measure the flow. Nevertheless, despite numerous encouraging results described in literature, a case study for an office room with a displacement ventilation system brings some of the restrictions on discretisation and wall heat transfer to the fore. Experimental validation of a CFD-model remains necessary for a quantitative credibility of the results. The number of accurately described full-scale three dimensional validation studies for indoor air flow however is very limited. This applies for all types of air conditioning systems and especially for newly designed task ventilation concepts. The above described restrictions in the measurement tool have contributed to this situation.

Therefore, an important part of this thesis is aimed at obtaining accurate full-scale indoor air flow measurement data for the air flow in an office room equipped with an air conditioning system that combines the task conditioning and displacement ventilation principle. The applicability of this so called desk displacement ventilation (DDV-) concept for standard office environments forms an additional part of the experimental research that is described.

Temperature and velocity measurement data have been obtained for a configuration in which the supply temperature, the supply flow rate and the room heat load were varied. The obtained measurement results have been discussed in relation to results described in literature and were found to be realistic and suitable for comparison with similar numerical simulations. The data and the configuration can be downloaded from the internet (http://www.tue.nl/bwk/bfa/research/aio_research.html).

In the experimental configuration, for some investigated cases, the wall heat transfer accounts for a significant part of the total heat balance. This has a non-negligible effect on the air flow characteristics. For example, free convection flows along the wall may influence the contaminant concentration gradient as found in a displacement ventilation flow pattern and heat transfer at floor and ceiling may have a large influence on the vertical temperature gradient for such flow patterns.

Given the indicated restrictions for the correct simulation of the wall heat transfer, the importance of the wall heat transfer in the experiments was interesting for numerical simulation purposes. CFD-simulations of the experimental configuration, using the available turbulence models and wall functions, confirmed the earlier findings. Only by prescription of the wall heat transfer coefficient, which was estimated from the measurements and tuned by comparison to the measured vertical temperature profile, an agreement between measurement and simulation was obtained. This fact limits the applicability of CFD for indoor air flow simulation severely as the (local) heat transfer coefficient is difficult to determine. Given the series of measurements that have been performed and the importance of the wall heat transfer in these experiments, the data obtained in this research are interesting and suitable to validate newly derived wall functions or empirical relations.

The measurement data were also used to compare simulation results for different turbulence models (standard k-ε model and the high- and low-Reynolds number variant of the *RNG*-k-ε model). The low-Reynolds number variant of the *RNG*-k-ε model was preferred for the simulation of the investigated displacement ventilation flow pattern. The low-Reynolds number relation for the turbulent viscosity better predicts the turbulent characteristics of the air flow in the room. This is important in the determination of the ventilation effectiveness.

Finally, the obtained steady-state measurement and simulation results were used to evaluate the DDV-concept. In addition, the transient behaviour of the system was investigated to determine the micro-climate response to a change in the supply settings. The steady state as well as the transient results indicate that the application of the displacement ventilation principle for task conditioning purposes on its own is not feasible, unless the room configuration is paid attention to. An improved version of the DDV-concept has been investigated with the validated CFD-model. The applicability of CFD for this type of qualitative study was confirmed.

The reliability of quantitative information from a simulated indoor air flow pattern currently remains difficult to determine. This certainly is the case when heat transfer to the enclosure forms an important part of the total heat balance. A discussion is presented for this and other configurations. A CFD-result nevertheless presents information on the flow pattern

which is very hard to obtain otherwise, e.g., three dimensional flow pattern, ventilation effectiveness (Roos 1998[a]). Because of this fact and the experimental restrictions and because of the ever increasing computer capacity, CFD most probably will develop into the most important tool for the design of indoor climate. The results in this thesis nevertheless summarise some of the important reservations with regard to the use of CFD for indoor air flow and present data that may be used for improving its reliability.

Chapter 1

INTRODUCTION

1.1 PROBLEM STATEMENT

The main objective of buildings has always been to provide shelter for sun, wind, cold and rain. In the past designs were relatively simple and took into consideration the local environmental conditions. With respect to the indoor climate, passive cooling was provided through natural ventilation and/or thermal mass and additional heating was possible. Often "builder" and "occupant" were one and the same. This meant that issues such as personal comfort were given a high priority.

At the end of the 19th century new building construction technology was introduced. This new technology and materials such as steel made it possible to design higher and deeper buildings. Artificial lighting and ventilation created an indoor climate largely independent of outdoor climate conditions. The increased technological complexity and size of modern buildings lead to specialisation in the building industry. As a result buildings very often are not being built around the needs of individual occupants, but for broader functions.

Importance of indoor air flow - To date, most people spend the majority of their time indoors, often in shared spaces. With the introduction of mechanical environmental control systems, and the resulting increased control of the indoor climate, the expectations of the occupant for a thermally comfortable indoor climate have risen. The fulfilment to these expectations however is impeded by the fact that thermal comfort conditions within a building enclosure, for a typical person, are limited to a narrow range (Fanger 1970) and that this range differs per individual (Ong 1995). Despite the existence of extensive environmental control systems in buildings, complaints about the indoor climate still are commonplace (Jaakkola 1994; Brightman et al. 1997).

In addition to thermal comfort, indoor air quality (IAQ) has become a topic of concern. This problem originated in the early 1970's energy crisis, when saving energy became a priority above all other requirements. From this time on building facades were gradually better insulated and sealed to prevent air leakage. Natural or local mechanical ventilation was replaced with central mechanical ventilation. As a further measure, the air flow rate was also reduced. A centrally controlled ventilation system with a low room ventilation rate makes maintaining acceptable conditions at occupant level more difficult. Fresh air cannot be provided directly to the occupant. Furthermore, correction of the conditions via natural ventilation (i.e. opening a window) is no longer possible because of a sealed facade.

The result of tightly sealing and reducing fresh air in buildings was aggravated by the build up of outgases from modern building materials, furniture and cleaning products. The consequence of which manifested itself in an increased occurrence of mild to serious building related health problems for occupants. Despite efforts in recent years to improve the indoor climate, a 1995 European study on indoor air quality, carried out in 56 office buildings in nine countries, reported that 30% of the occupants indicated dissatisfaction with the indoor environment (Bluyssen et al. 1995).

The negative effect of poor indoor climate conditions on the performance of the occupant is described in several earlier investigations (Jaakkola et al. 1989; Wyon 1993). The significance of maintaining good indoor climate is self-evident when one considers that in every modern economy a significant part of the Gross National Product (GNP) is earned by people working in office buildings.

In view of the importance of thermal comfort and indoor air quality, the design challenge is to achieve acceptable indoor environmental conditions for each individual occupant of a building. Such an approach to design is in stark contrast with the current prevailing attitude which is directed towards designing an uniform *climate* for buildings rather than *comfort* for people.

In order to focus on the occupant instead of the room or the building requires knowledge about the indoor air flow pattern. The rate of air changes and descriptions of the supply and exhaust conditions do not provide enough information about the thermal comfort and air quality conditions for individual occupants. A room or building cannot be regarded anymore as a single zone. W.H. Carrier, one of the founders of air conditioning systems, already recognised this with his statement: 'No air conditioning is better than its air distribution.'.

Given this awareness of the importance of the indoor air flow pattern, tools are required to determine and predict the flow characteristics in the early design phase. This topic is introduced below.

Tools to determine indoor air flow - The options currently available to determine and predict indoor air flow are limited. The air flow in a room is characterised as being non-isothermal, turbulent, three-dimensional and non-steady. As a result, the indoor air flow research has mainly remained an area of experimental and empirical research (e.g., Katz 1989 and Mundt 1996) and for the most part has been limited to simplified models of the physical indoor environment.

With the introduction of Computational Fluid Dynamics (CFD), Nielsen (1974) presented an attractive alternative for the empirical research of indoor air flow. CFD opened a route to numerically predict the indoor climate on a detailed level with high flexibility in terms of configurations and boundary conditions. Information on thermal comfort and the effectiveness of the proposed ventilation system can be derived from the calculated indoor air flow pattern, temperature and contaminant distributions.

Encouraging results have been obtained from simulations of simplified (scaled) models of the indoor environment. Developments in turbulence modelling and solver techniques for calculating the flow problem have improved the simulation process considerably. The ever increasing processing speed and memory now available on today's PCs make it easier to use CFD for tackling engineering flow problems. Despite these encouraging results there are still many uncertainties in the applied flow modelling and in the available solver algorithms (Chen 1997, Baker et al. 1997). Validation of CFD-simulations and the quality of the model remain an intrinsic part of the process but are often skipped because of experimental or computational restrictions.

The limited availability of validation data currently restricts the reliability of indoor air flow simulations by CFD. Full-scale validation studies of realistic indoor configurations have not been reported on extensively in literature (Lemaire 1992). This is likely due to the high costs related to undertaking full-scale experimental research and the limitations of currently available measurement techniques (Loomans and van Mook 1995). The characteristics of indoor air flow (low velocity and high turbulence intensity) and the level of accuracy required for validation place high demands on measurement techniques.

In recent years a number of new ventilation systems and strategies have been introduced to improve air quality, thermal comfort, and energy efficiency. This has changed the nature of

current air flow problems. However, most CFD-results that have been presented so far are for relatively simple and stylistic configurations.

Approach - Given the status of indoor climate research described above and the obvious importance of good indoor environmental conditions, new research is needed to bring the current shortcomings in the prediction of the indoor air flow to the fore. Currently the available information, both experimental and numerical, is limited and often fragmented (Loomans and van Mook 1995). This study should therefore consider the two most important methodologies to acquire data that are applied in indoor climate research:

1. *Measurements*;
   - measurement techniques,
   - available and new indoor climate data.
2. *Simulations*;
   - simulation techniques,
   - validity and sensitivity.

Furthermore, this study should focus on: *Contemporary ventilation strategies*.

So far, a study that combines all of these aspects has, to the best of our knowledge, not been undertaken.

1.2 STATUS OF RESEARCH

This section provides a further elaboration of the subjects to be investigated in this study. This includes a discussion of the status of indoor environmental research and ventilation strategies.

1.2.1 Measurements

Data - Data on air velocity and temperature describe the flow field characteristics and are required for numerical validation purposes. Some experimental benchmark studies are available. For example: a two-dimensional isothermal ceiling jet in an enclosure (Nielsen 1974) and a differentially heated cavity with a hot and a cold wall (Cheesewright et al. 1986). These studies have been used extensively to validate CFD-programs and simulations, but the configurations generally differ from practical indoor air flow problems. Therefore, the measurement of a realistic indoor air flow pattern is necessary to judge the validity of a corresponding CFD-simulation. In order to make a comparison, the data, obtained by measurement or simulation, should be accompanied by the prevailing boundary conditions.

Extensive in-situ measurement series by Thorsauge (1982), Hanzawa et al. (1987) and Melikov et al. (1988 and 1990) provided a better understanding of the actual indoor air flow characteristics. These results however are not suitable for validation purposes as boundary conditions are not known and there are not enough measurements for a single flow pattern.

Other than the Annex 20 'Air flow patterns within buildings' by the International Energy Agency [IEA] (Lemaire 1992) there are very few sources of well documented full-scale indoor air flow measurement results. Given the additional consideration for variation in indoor air flow patterns, the number of full-scale indoor air flow measurements for comparison with, and validation of CFD-simulations is very limited.

Technique - Nearly all of the studies to date applied a hot sphere anemometer to measure the air velocity (Dantec 1985, Crommelin and Dubbeld 1976). Although this type of anemometer has been especially developed for indoor air flow registration, the signal tends to drift over time and its accuracy depends highly on the application conditions and on regular calibration. In addition, the sensitivity to the calibration conditions and the dynamic characteristics of the sensor are not well-known.

Given the shortcomings of the hot sphere anemometer, there is a great interest to use new measurement techniques. However, the indoor flow characteristics restrict the number of applicable techniques considerably. In order to select the right technique to use, a good overview of the available measurement principles is necessary. However, such an overview does not yet exist.

1.2.2 Simulations

Over the last years CFD has taken a prominent position for simulation of indoor air flow problems. One of its main advantages over other tools is its ability to simulate a wide range of configurations. The development of commercial versions of the CFD-program with extensive data handling possibilities, combined with the rapid increase in computer power, over recent years have further enhanced its practical application. Since its introduction CFD has been applied for a wide range of indoor air flow problems (see proceedings of Roomvent 1992; 1994; 1996; 1998).

CFD was first deployed for the simulation of fundamental indoor air flow patterns shortly after the development of the first code (Nielsen 1974). It took approximately ten years before CFD was used for more practical indoor air flow problems. This was largely due to limitations of computer processing power. The validity of the applied turbulence models was confirmed for typical benchmark studies. However, for practical indoor air flow

problems differences between measurement and simulation were always found (Chen 1988). In most cases, the qualitative solution is in agreement with experimental data, but for a quantitative agreement the model often had to be adjusted with empirical data. This is because discretisation and turbulence modelling have oversimplified the flow problem. To date there still are prevailing uncertainties with the turbulence modelling and the solver techniques. Yet a lot of simulation results are presented without comparison to measurement results. Therefore, the reliability of these simulation results is not known.

Efforts to improve the reliability of the CFD-technique is only possible through comparison with accurate full-scale measurement results. The empty room has been the most commonly used subject of investigation and relatively good results have been reported (Lemaire 1992). A more realistic flow problem is one that takes into account the effect of multiple heat sources and obstacles in a room. This puts much higher demands on the simulation process. There are only few examples of this type of flow problem (e.g. Lemaire et al. 1995). This is particularly true for cases where contemporary ventilation techniques are being used.

1.2.3 Ventilation techniques

The number of indoor air flow configurations is very large. Selecting the right strategy to ventilate a room is dependent on many factors including the function of the building. This work focuses on mechanical ventilation in office buildings.

Two main principles are available for mechanical ventilation of an office room: (1) mixing ventilation and (2) displacement ventilation. Mixing ventilation means that the air is supplied to the room at relatively high velocity. The entrainment of room air in the supply jet causes a high degree of mixing to take place. As a result the temperature and contaminant concentration tends to remain uniform. Mixing ventilation has been the most important ventilation principle since the introduction of mechanical ventilation (Carrier 1965).

With displacement ventilation relatively cool and clean air is supplied at floor level at a low velocity. Air from the lower part of the room is induced upward by rising convection flows from heat sources in the room and then is removed at ceiling level. The air velocities in the room are very low. A distinct characteristic of displacement ventilation is the vertical temperature and contaminant concentration gradient, with a sharp horizontal interface between the lower relatively clean and fresh air layer and the upper air layer which is relatively warm and contaminated. Displacement ventilation is only applicable in cooling situations. It was introduced for office environments in the early 80’s (Mundt 1996).

Figure 1.1 describes the characteristic differences between the two ventilation principles. The left part of the figure shows the flow pattern and to the right is the averaged velocity magnitude, temperature and contaminant concentration as function of the height.

Although the vertical temperature gradient may negatively impact on the thermal comfort requirements, displacement ventilation increases the ventilation effectiveness due to the contaminant concentration gradient. The ventilation effectiveness gives an indication on the effectiveness with which fresh air is supplied to the inhabited zone. Given the improved ventilation effectiveness and the better air quality levels that can be obtained near the occupant in comparison to mixing ventilation at the same amount of supplied air (Brohus 1997), displacement ventilation is increasingly being applied.

It is also possible to ventilate a room naturally. This is achieved by refreshing indoor air with outside air through openings in the facade. For office rooms, natural ventilation alone is, also in a moderate climate as in the Netherlands, unable to maintain the high level of indoor air quality required throughout the year. Therefore, especially for larger office buildings, mostly (central) mechanical ventilation is used.

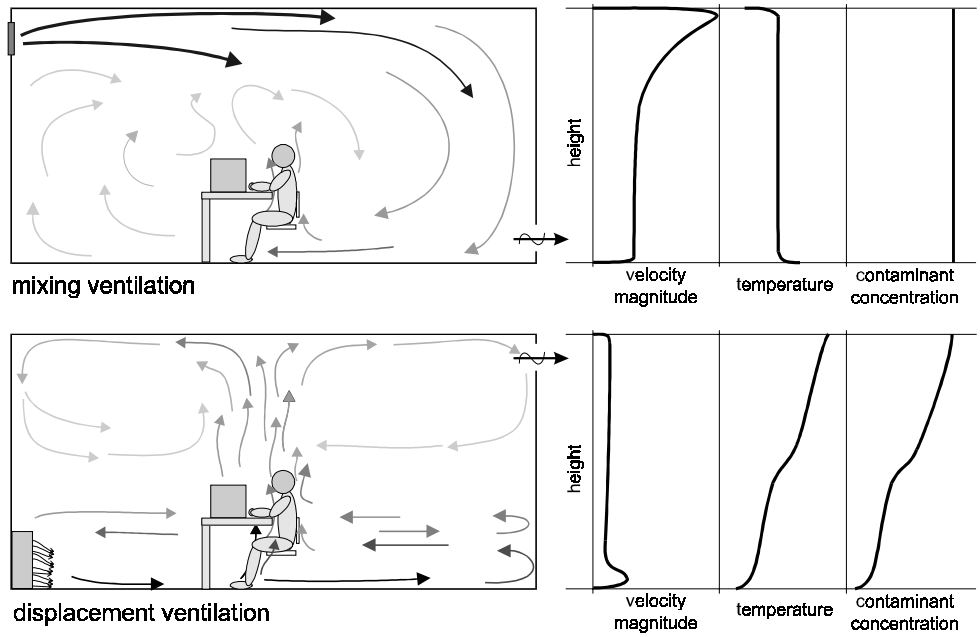

Figure 1.1. Schematised representation of the mixing and displacement ventilation principle; flow pattern (left) and variable gradients of the height (right). At a given height the variable has been averaged over the total horizontal plane in the room.

Centrally controlled air conditioning systems ignore the apparent differences in thermal comfort requirements between persons (Benzinger 1979). The lack of occupant influence on indoor thermal conditions has increased building related complaints (WHO 1983). These complaints, along with an increasing environmental awareness, has lead to a search for alternatives that allow a more natural way of climatising the indoor environment that also provide more individual control (Hawkes 1996). This is known as '*bioclimatic design*'. In these designs the outdoor climate supports the indoor climate and individual control becomes possible through control of well-thought out facade openings.

Despite this trend to use more natural ventilation, mechanical air conditioning may still be necessary under extreme outdoor climate conditions. In order to achieve thermal comfort, air quality and low energy use, increasing attention is being given to systems which intend to influence only the immediate surrounding of the person operating the system: *task conditioning systems* (Bauman et al. 1994). These systems create a micro-climate within a macro-climate (see Figure 1.2). As a result of having local zones, strict comfort-related requirements for the air conditioning of the macro-climate may be mitigated, thereby improving for example, energy efficiency (Bauman and Arens 1996). Providing individual control of thermal conditions within the micro-zone is seen as the major factor in improving user satisfaction. Therefore, task conditioning systems are considered to be an integral part of the new so-called '*high tech buildings*'.

In contrast to mixing and displacement ventilation, the effectiveness of natural ventilation and task conditioning systems is extremely difficult to predict; particularly with today's tools. As a result very little is currently known about the performance of these new innovative systems. Given the strict requirements put in standards (ASHRAE 1992) and the potentially high life cycle costs involved in climatising a building, a reliable prediction of indoor air conditions nevertheless is needed.

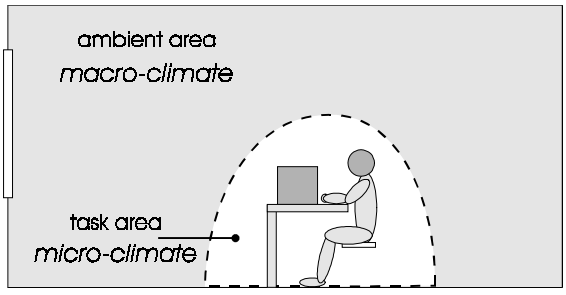

Figure 1.2. Objective of the task conditioning principle: micro- versus macro-climate.

1.3 RESEARCH OBJECTIVE

As discussed in the previous section, current tools and methods being used for the prediction of the indoor climate still have information gaps which reduce their reliability and accuracy. The increasing complexity of the flow problem created by new and innovative ventilation systems only underscores the need for more reliable tools.

The main aim of this research therefore is to improve the knowledge on the techniques used to predict the indoor climate. If the indoor climate can be predicted more reliably by better verified techniques, then it will be possible to optimise indoor air quality, thermal comfort and energy use during the design phase.

The objectives of this thesis are:

- To explore and summarise the options for measurement of indoor air flow patterns, with respect to accuracy, sensitivity and applicability.
- To reveal current limitations in the numerical simulation of indoor air flow and its sensitivity to input parameters. (Attention is put on the numerical result rather than to improve the turbulence modelling.)
- To obtain well documented full-scale measurements in a climate chamber that can be used for comparison with CFD-simulations.
- To investigate a type of flow problem that subscribes to the current view in ventilation; i.e. task conditioning.

1.4 OUTLINE OF THE THESIS

In this thesis the above mentioned objectives are elaborated on. First however, in *Chapter 2*, an introduction will be given to thermal comfort and ventilation. This chapter provides the framework for this thesis. Especially the current attitude towards predicting thermal comfort will be discussed by comparing the two main approaches to mathematically model thermal comfort: the climate chamber and the adaptive approach. The description of the ventilation of a room is focussed on task conditioning. Here also the desk displacement ventilation (DDV-) concept is introduced. This concept will be applied in the full-scale experiments that are discussed later on.

Before the experiments are discussed, *Chapter 3* and *Chapter 4* focus on the tools under investigation: measurement and simulation techniques. With respect to the measurement technique an overview is given of velocity measurement principles and an evaluation is

made on the applicable techniques for measurement at indoor air flows. From this evaluation the hot sphere anemometer and particle tracking velocimetry are explored further, experimentally as well as numerically. *Chapter 4* presents a short introduction into turbulence modelling and numerical simulation of air flow. A case study of a displacement ventilated office room is used to indicate some of the restrictions of CFD. Also a comparison of different available grid techniques is presented.

Extensive full-scale climate chamber experiments of an office room ventilated with the DDV-concept are discussed in the next two chapters. *Chapter 5* presents an accurate description of the experimental set-up and the measurement tools and procedure. In *Chapter 6* the results of the full-scale experiments are discussed for eight cases in which the supply air - wall temperature difference, the flow rate and the heat load have been varied. In this discussion comparison is made with results found in literature. The importance of the wall heat transfer on the total heat balance is a typical aspect of the described experiments. The applicability of the measurement results for comparison with CFD-simulations is confirmed.

In *Chapter 7* the experimental results are compared with similar CFD-simulations. Focus has been put on the influence of wall heat transfer and turbulence modelling on the simulated indoor air flow. This chapter is concluded with a discussion of the simulation results for all investigated cases.

Finally, in *Chapter 8*, the DDV-concept is evaluated from the experimental and numerical steady state results as described in the previous two chapters. Furthermore, the transient behaviour is investigated experimentally and numerically to determine the applicability of the DDV-concept, as task conditioning system, for normal office configurations. Results of an improved version, investigated with the in Chapter 7 validated CFD-model, end this chapter.

The most important discussions and conclusions are summarised in *Chapter 9*. Furthermore, possible future developments are indicated.

Chapter 2

THERMAL COMFORT AND VENTILATION

2.1 INTRODUCTION

The occupant appreciates the indoor climate mainly by its air quality and thermal conditions. The air quality in a room, as perceived by the occupant, is a function of the indoor air pollution. If the thermal conditions satisfy the requirements of the occupant thermal comfort is obtained.

Indoor air pollution may consist of compounds from different sources. Examples are, inorganic (CO_2, CO, etc.), organic (volatile organic compounds) and environmental (tobacco smoke, radon) pollutants and biological agents (fungi, mites, etc.). It originates from outdoor air, building materials, furniture and from man and his activities (Brohus 1997). To obtain minimum acceptable indoor air quality levels, a room must be ventilated with fresh air. Minimum acceptable air quality levels are described in the standards in the form of maximum concentration levels of chemical compounds and biological substances and minimum air flow rates (NEN 1087, DIN 1946). Minimum air flow rates already were prescribed in the previous century with respect to health as a result of growing cities and increased governmental responsibility on public welfare (Donaldson and Nagengast 1994).

The perceived air quality cannot be determined objectively. It is defined as the immediate impression of the indoor air quality experienced by people entering a space (Fanger 1988). In this methodology, developed by Fanger, the perceived air quality is determined by a sensory panel. The air quality is assessed in decipol or in the percentage of dissatisfied, the air pollution load is given in olf (Fanger 1988). Though the assessment of the perceived air quality as proposed by Fanger is shown to be successful (Fitzner 1998), it cannot be used yet to predict the perceived air quality of a typical configuration.

Thermal comfort/discomfort, conveys the general state of the human thermoregulatory system. It is a function of amongst others the thermal conditions, the clothing, the activity level and the physical condition of the occupant. Thermal comfort already was a topic of concern in the previous century. In 1883 Hermans developed a theory on discomfort which connected poor ventilation with the body heat loss mechanisms (Donaldson and Nagengast 1994). This theory has been elaborated on in the 20th century and forms the basis for the present comfort requirements in relation to thermal conditions and ventilation, i.e. thermal comfort. In the standards thermal comfort is defined as "the condition of mind that expresses satisfaction with the thermal environment" (ASHRAE 1992, ISO 1984). The prediction of thermal comfort has been standardised with models that have been derived by Fanger (1970) and Fanger et al. (1988). However, the predicted comfort as is obtained from these models are not in good agreement with the actually sensed thermal comfort. This will be discussed further in Chapter 2.2.2.

The requirements for indoor air quality and thermal comfort are counteracting. High air flow rates, as preferred for indoor air quality, may cause draught problems in the inhabited zone. An optimal indoor climate, i.e. good indoor air quality and thermal comfort for each individual occupant of a room is aimed at nevertheless. Preferably this already should be confirmed in the design phase. Given these demands, present research is focussing on:

- the emission and absorption characteristics of materials,
- thermal comfort, and
- ventilation effectiveness.

Knowledge of the indoor emission of contaminants and the diffusion of the air flow are necessary to predict the indoor air quality. As the indoor emission is not considered within the scope of this thesis, the indoor air quality will not be discussed further.

The prediction of thermal comfort with the models of Fanger has shown to be unfeasible in a large number of cases and therefore thermal comfort has remained a topic of concern since. Currently new insights and new techniques are used to improve the creation of thermally comfortable conditions to the occupant.

The effectiveness of a ventilation system is mainly determined by (a) the removal of internally produced contaminants from the room and (b) the supply of fresh air of acceptable quality in the room, in particular to the inhabited zone. The ventilation effectiveness depends on the entire air flow pattern in a room. The availability of Computational Fluid Dynamics significantly enlarged the possibilities to further investigate this topic. In Roos (1998[a]) the effectiveness of ventilation is discussed extensively. The basis of the work of Roos is defined by the age-of-air concept as has been introduced by Sandberg and Sjöberg (1983).

The present chapter on thermal comfort and ventilation describes the framework of this thesis. Thermal comfort is discussed with respect to contemporary insights and thermal requirements. Different ventilation principles are available to ventilate a room. After a short overview, recently introduced design principles and techniques are discussed.

2.2 THERMAL COMFORT

2.2.1 Introduction

The human temperature regulation determines the physiological thermal comfort of the occupant of a room, as the human body exchanges heat with the environment. Heat is exchanged by radiation, convection and evaporation. The heat is primarily produced by metabolism, which results from digestion. During normal rest and exercise this results in an average temperature of the vital organs near 37^{o}C. The body's temperature control system tries to maintain this temperature when internal or environmental thermal disturbances occur.

Figure 2.1 shows the human thermoregulatory system as presented by Hensel (1981). The controlled variable in the system is a weighted mean body temperature. It represents a combined value of the internal body temperature and the average skin temperature, in which the internal body temperature has an approximately ten times higher weight. Thermal disturbances are either internal, e.g. heat generation due to exercise, or external, e.g. hot or cold environments. Thermoreceptors in the skin register external thermal disturbances so that the thermoregulatory system can react before the disturbance has reached the body core. This thermoreceptive system also responds to the rate of change of temperature.

The human thermoregulation system can be subdivided in an autonomic and a behavioural regulation (Hensel 1981). The *autonomic* regulation is controlled by the hypothalamus, governing the heat production (e.g. by shivering); the internal thermal resistance (e.g. by control of the skin blood flow); the external thermal resistance (e.g. by respiratory dry heat loss) and water secretion and evaporation (e.g. by sweating and respiratory evaporative heat loss). The set-temperatures for these various autonomic control actions can be different for each person and they may vary separately and independently. The *behavioural* thermoregulation is associated with conscious temperature sensation and feelings of thermal comfort/discomfort (Hensel 1981). The temperature sensation results from the thermoreceptor activity. Thermal comfort/discomfort conveys the general state of the thermoregulatory system, i.e. the resultant of the thermoreceptor signals, internally and at the skin. Examples of the behavioural regulation are active movement and adjustment of

clothing. The *technical* regulation, indicated in Figure 2.1, relates to artificial control systems, e.g. an air conditioning system.

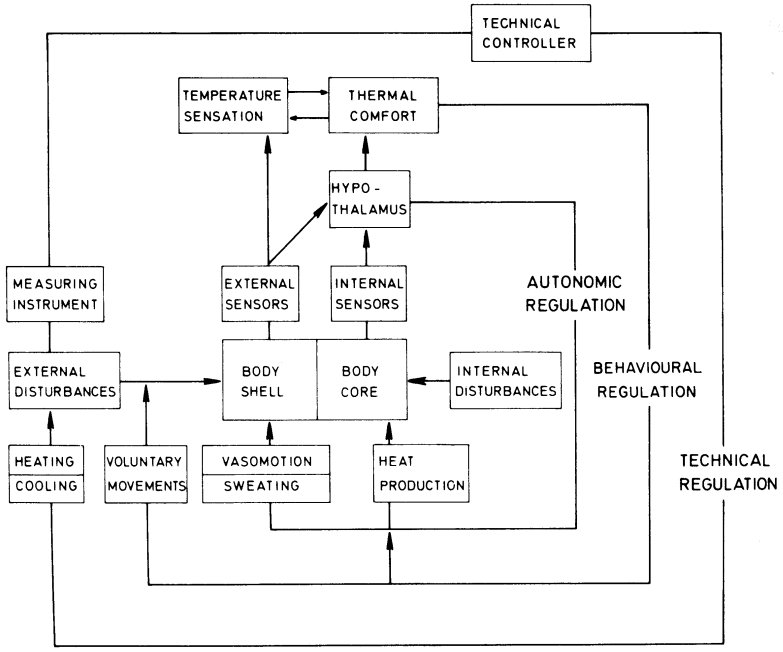

Figure 2.1. Schematic diagram of the human thermoregulatory system (from Hensel (1981)).

The human response to the thermal environment can be found to depend on seven factors (Rohles et al. 1993): (a) air temperature, (b) relative humidity, (c) mean radiant temperature, (d) air velocity, (e) physical activity of the human occupant, (f) thermal resistance of the clothing and (g) the temporal nature of the exposure. Given the thermal parameters (a) to (d), thermal comfort can be attained by tuning the behavioural parameters (e) to (g) or reverse. The perception of thermal stimuli is innate (Cabanac 1981). Whether thermal comfort is attained is determined by the condition of the human body, which is monitored by the sensory organs (Hensel 1979, Benzinger 1979).

In Hensel (1981) a summary is given of the physiological conditions for steady state general thermal comfort. General thermal comfort results from the integrated signals from various internal and external thermoreceptors. Warm discomfort is closely related to the rate of sweating, which in itself is initiated by a warmth-sensation receptor in the hypothalamus (Benzinger 1979). Cold discomfort is a response to the temperature of the skin, as monitored by cold-receptors in the skin. Ideal thermal comfort, according to Benzinger, therefore can be defined objectively as “the absence of punitive impulses from both receptor

fields" or "a state in which there are no driving impulses to correct the environment by behaviour". Ideal thermal comfort is defined by the absence of cold-reception at the skin and central warmth-reception, without overlapping. In most cases however, e.g. when performing exercises, a mixed comfort situation is obtained with cold discomfort at the skin and warm discomfort due to a too high central temperature.

When designing the indoor climate, thermal comfort should be attainable for the occupants. Given the complexity, due to the variation in parameters (a) to (g) as mentioned above and the differences between people, mathematical models have been derived that predict the average acceptability of an indoor climate. Two types of approaches are found to predict steady state thermal comfort. One approach is based on the heat balance of the human body. The second approach assumes an adaptation to the thermal environment to a certain degree. Furthermore, besides the physiological and behavioural adaptation also psychological adaptation may be distinguished. The two types of approaches will be discussed next.

2.2.2 Models for thermal comfort

Different concepts have been applied to derive a practical relation between the thermal environment and the physiological and psychological well-being of the person that is or will be exposed to this environment. These concepts can be categorised into two clearly distinguishable approaches:
(1) *the heat balance approach*; a method for the calculation of steady state thermal comfort obtained from climate chamber research.
(2) *the adaptive approach*; a relation for steady state thermal comfort derived from studies in the field. Assuming people will have adapted to the indoor thermal conditions, incorporating known and unknown psychological influences, the indoor and outdoor temperatures are the dependent variables.

In this section the two approaches will be discussed and evaluated with respect to the practical application.

The heat balance approach - Fanger (1970) is a well-known representative of the heat balance approach. Fanger assumed homogeneous climatological conditions around the human body and formulated a steady state heat balance equation for the human body to arrive at a thermal comfort relation. This heat balance equation is given by:

$$\begin{aligned} &H - E_d - E_{sw} - E_{re} - L = K \\ &K = R + C, \end{aligned} \qquad (2.1)$$

where, H is the internal heat production in the human body, E_d the heat loss by water vapour diffusion through the skin, E_{sw} the heat loss by evaporation of sweat from the surface of the skin, E_{re} the latent respiration heat loss, L the dry respiration heat loss, K the heat transfer from the skin to the outer surface of the clothed body (conduction through the clothing), R the heat loss by radiation from the outer surface of the clothed body and C the heat loss by convection from the outer surface of the clothed body.

Fanger defined satisfaction of Equation 2.1 to be a necessary but certainly not sufficient condition for steady state thermal comfort. The human thermoregulatory system is very effective and therefore will be able to create heat balance within wide limits of the environmental variables, even if thermal comfort does not exist. In Equation 2.1, the skin temperature (T_{sk}), as appears in E_d and K, and the sweat secretion (E_{sw}) are the only physiological variables that can influence the heat balance at a certain activity level. However, the range over which T_{sk} and E_{sw} may vary is limited for thermal comfort conditions and only applicable to an individual person at a specific activity level (Hensel 1979, Benzinger 1979). Climate chamber results were applied to develop empirical relations for the mean skin temperature and sweat secretion as a function of activity level, clothing insulation and environmental conditions (Fanger 1970).

Predicted Mean Vote - Practical application of the heat balance equation was proposed by Fanger, by formulating a thermal comfort equation which allows the prediction of the thermal sensation of a group of persons in an arbitrary, but stationary, climate, the Predicted Mean Vote (*PMV*). The basis of this equation was obtained from the above mentioned experiments, in which the thermal sensation vote indicated the personally experienced deviation to the heat balance (-3 [cold] to +3 [hot]; seven point scale, 0 = neutral (optimum)). Applying this *PMV*-equation, the thermal sensation for a large group of persons can be determined as a function of the activity, clothing, air temperature, mean radiant temperature, relative air velocity and air humidity.

In Figure 2.2 the sensitivity of *PMV* to velocity, humidity, clothing insulation and metabolism is presented as a function of the temperature. For each variable the range that can be found in a normal office environment is indicated (ASHRAE 1992, Loomans and van Mook 1995). Given the boundary conditions and the applied ranges, in Figure 2.2 *PMV* generally varies between cool (-2) and warm (+2). The sensitivity of *PMV* to the temperature is largest. Of the other variables, the sensitivity to the metabolism is most pronounced. The standards require $|PMV| \leq 0.5$ for an office environment (ASHRAE 1992, ISO 1984).

Fanger assumed that the vapour permeability of the clothing was not important in the prediction of *PMV*. The heat loss from sweat secretion is defined at the surface of the skin

and assumed to evaporate completely at the skin at moderate sweat secretion and air temperatures. An improvement of the *PMV*-model was proposed by Gagge et al. (1986) by including the physiological heat strain caused by the relative humidity and vapour permeability properties of clothing.

Predicted Percentage of Dissatisfied - Fanger derived a second equation, the Predicted Percentage of Dissatisfied (*PPD*), which indicated the variance in the thermal sensation of the group of persons exposed to the same conditions. This equation was derived from the earlier described experiments. Dissatisfaction with the thermal environment, discomfort, was defined for those who voted cool (-2), cold (-3), warm (+2) or hot (+3). Under optimal thermal conditions (*PMV* = 0) a minimum of 5% dissatisfied is found, assuming identical activity levels, clothing and environmental conditions. In Figure 2.2 the *PPD*-value is given at the outermost right axis (non-linear scale).

Fanger (1970) furthermore assumed that a room-averaged *PPD*-value can be derived for thermally non-uniform rooms. From the measured thermal variables at equally distributed positions in the occupied zone of a room the *PMV* and the corresponding *PPD*-value can be calculated. The room-*PPD*-value then can be determined as the average from the *PPD*-

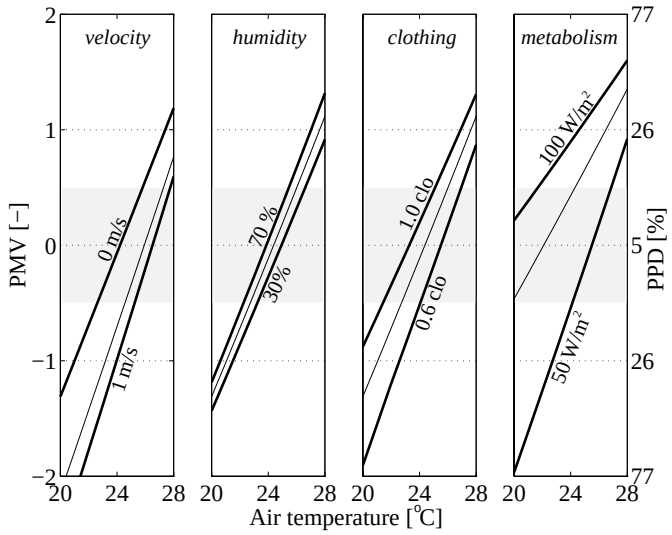

Figure 2.2. Sensitivity of PMV to variation in velocity, humidity, clothing insulation and metabolism as function of the homogeneous air temperature ($T_{mrt} = T_{air}$). For each variable three lines are given. The thick lines present the result for the indicated range of the investigated variable and the thin line the result for the median value. When the variable is not changed constant values are used: u = 0.1 m/s, φ = 50%, I_{clo} = 0.8 clo, M = 58.2 W/m^2. The corresponding PPD-value is indicated at the outermost right axis (non-linear scale).

values at the points. As Fanger derived the thermal comfort equation from experiments in a thermally uniform environment, the validity of a *PPD*-value in a point in a non-uniform environment however is questionable. It supposes thermal comfort in a point, whereas the mathematical model has been based on the judgement by people (at a larger scale).

Asymmetric Thermal Conditions - It is possible to balance Equation 2.1 under asymmetrical thermal conditions, but there are restrictions with respect to the degree of asymmetry for thermal comfort. Fanger (1970) indicated three causes for non-uniform heating of the body: asymmetric radiant fields, warm or cold floors and draught. The vertical air temperature gradient can be an additional cause for discomfort due to asymmetric conditions.

In Fanger (1970) and Krühne (1995) experimental results are described which indicate that more than 95% of the people are satisfied when the differences in radiant temperatures within the enclosure as function of the direction remain below 10^{o}C. For warm ceilings the radiant asymmetry should not exceed 3.5^{o}C (Krühne 1995). The influence of warm or cold floors on thermal comfort is highly dependent on the foot wear. High floor temperatures of 29^{o}C did not show discomfort for persons wearing light shoes. The lower temperatures at which comfort can be attained is 17-18^{o}C (Nevins and Feyerherm 1967).

The sensation of draught, defined as an unwanted local convective cooling of a person, is dependent of the thermal comfort state of the person. Persons already feeling cool will complain of the sensation of draught, whereas the same condition may have a positive effect on a person feeling warm. Fanger et al. (1988) derived a relation for the risk of draught, the predicted percentage of dissatisfied due to draught (*PD*), as a function of the temperature, the mean air velocity and the turbulence intensity (*TI*; see Chapter 3.2 for the definition). This relation was obtained from similar climate chamber research as for the *PMV*-model. The velocity and turbulence intensity were registered at three points in a vertical line at 0.15 m behind the neck of a seated person. The registered values at head level (1.1 m) were used for the *PD*-model.

The draught risk model has been introduced to compensate for the heat transfer effect of turbulence which is not accounted for in the *PMV*-model. Under normal office indoor air conditions, the draught risk model typically leads to the requirement to keep the velocities very low (u < 15 m/s). In Figure 2.3 the sensitivity of *PD* to the turbulence intensity and the temperature as a function of the velocity is shown. The standards (ASHRAE 1992) require that *PD* < 15% (grey area in Figure 2.3)

Warm discomfort at the head and/or cold discomfort at the feet can be expected in thermally stratified flow patterns as for example present in a displacement ventilated room (see Figure 1.1). Olesen et al. (1979) reported that more than 5% of the people feel locally

uncomfortable when the air temperature difference between head (1.1 m) and ankle (0.1 m) is larger than 2.8°C. The test were made for 3 hours occupancy.

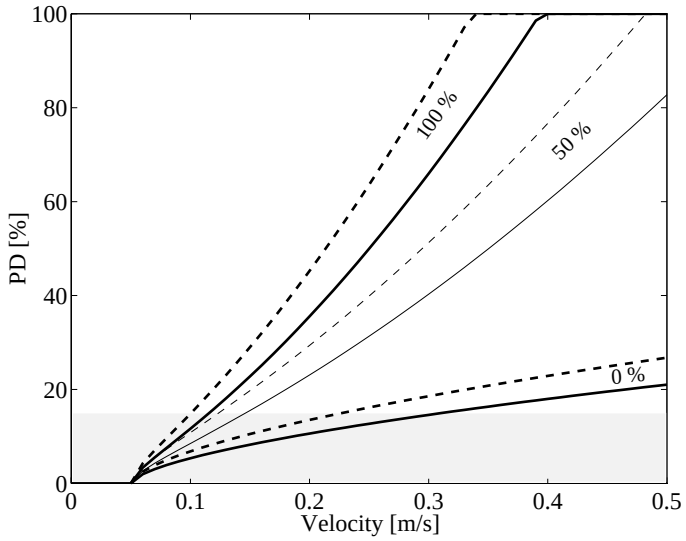

Figure 2.3. Sensitivity of PD to turbulence intensity (TI = 0..100 %) and temperature [| | | | : T = 23°C; | | | : T = 20°C] as function of the velocity. For each temperature three lines are indicated. The thick lines present the range (0 and 100%) and the thin line the result for the median value (50%).

Non-Steady Thermal Conditions - According to Fanger (1970) the *PMV*-equation can also be applied under quasi-steady-state conditions. Fanger concludes that sudden changes in the temperature are anticipated promptly by the regulatory mechanism. From a comfort point of view, harmonic temperature fluctuations were found to be acceptable if $\Delta T^2 \cdot cph < 4.6^oC^2/h$, where ΔT is the peak-to-peak amplitude of the air temperature and *cph* the cycling frequency per hour (Sprague and McNall 1970). The peak-to-peak temperature amplitude decreases with increasing fluctuation frequency as the cold-receptors at the skin also sense the rate of change of the temperature. Therefore it is an additional critical parameter for thermal comfort. Radiant temperature fluctuations were not included in the temperature fluctuation experiments of Sprague and McNall. Hensen (1991) derived a peak-to-peak amplitude and cycle rate of the operative temperature at $\Delta T^2 \cdot cph < 1.2^oC^2/h$, if the operative temperature is defined as the arithmetic mean of the dry bulb temperature and the mean radiant temperature.

Besides cyclic temperature changes, thermal comfort can also be influenced by non-cyclic temperature changes (passive or actively controlled). Berglund and Gonzalez (1978[a,b]) found that, for sedentary persons, a 0.5°C/h temperature change up to 2°C from the neutral

point reduces the thermal acceptability to about 80%. Benzinger (1979) found that there is a steady daily rhythmic change of the set point of the human thermostat with an amplitude of ±0.5°C. The minimum set point occurs in the early morning and the maximum late in the afternoon and early evening. When cooling, an energy conserving slow rise during day-time therefore may be preferable, as the tolerance for heat increases during the day (Benzinger 1979).

The adaptive approach - Instead of the use of climate chamber experiments to determine the heat balance as found in the work of Fanger, Humphreys (1976, 1994) supports the so called adaptive approach. From a global field-study on the relation between thermal comfort and temperatures, Humpreys found the existence of large temperature differences between different groups of people feeling thermally comfortable. These differences could not be explained solely from differences in clothing, the range was about twice that large. As a result comfortable temperatures as derived from the heat balance approach could not be brought into agreement with the comfort conditions found in daily life (Humphreys 1976).

Humphreys, unlike Fanger (1970), found a relation between the mean temperature (T_m), defined as the mean air temperature experienced by the population under investigation during their waking hours over a period of a month, and the neutral room temperature (T_n), defined as the air temperature found to be "neither warm nor cool" (or "comfortable"). So people will adapt to certain outdoor climatic conditions. E.g., in a hot climate people will acclimatise to higher temperatures indoors than in temperate climates, even though other environmental thermal comfort parameters suggest a too high *PMV*. Given this fact Humphreys (1976) derived a relation for the prediction of thermal comfort as a function of the prevailing room temperature and the above defined T_m.

Discussion thermal comfort concepts - Comparison of the thermal comfort votes obtained from questionnaires and the estimated *PMV*-value applying the heat balance approach shows large discrepancies (Humphreys 1994). An average error of ±3°C was found between the mean vote on thermal comfort and the *PMV*. Gan and Croome (1994) found that the neutral temperature for occupants of five naturally ventilated offices, situated in the United Kingdom, was 1 to 2°C lower than the temperature that would be determined from Fanger (1970). A thermal comfort study in naturally ventilated and air conditioned offices in Thailand indicated acceptable temperatures respectively 5°C and 2°C higher than the comfort standard's value (Busch 1992). Increasing deviations in the estimated comfort value are found when clothing and activity level differ from the sedentary subject in light clothing. As activity levels frequently vary and often differ from the sedentary activity, the thermal comfort prediction as found via *PMV* therefore is questionable.

An invariable neutral temperature for thermal comfort at standard metabolic rate and standard clothing, though expected to exist, seems to vary more profoundly than presumed. Humphreys (1978) indicates that (personal) comfort temperatures seem to be correlated with climatological conditions. Despite the lighter clothing and higher velocities, evidence of acclimatisation was also proposed by Busch (1992) to describe the contrasts in thermal neutrality between Thai office workers in naturally ventilated and air conditioned offices. Hensel (1981) summarises some results which discuss the accommodation to extreme thermal conditions. However, in Brager and de Dear (1998) results are summarised which do not subscribe to the effect of accommodation of building occupants to the outdoor conditions. The work of Humphreys in this respect can be criticised, as non-temperature related changes in the thermal comfort parameters have not been addressed in the field studies. Therefore, the influence of these other parameters on the thermal comfort cannot be judged.

The sensitivity of the thermal comfort equations to the different variables is shown in Figures 2.2 and 2.3. The grey areas in both figures indicate the combined value for the different variables which satisfy the standards criteria (ASHRAE 1992, ISO 1984). Besides the requirement of uniform thermal conditions, the accurate prediction of thermal comfort by the *PMV*- and *PD*-equation is hampered by,

- uncertainties in the estimated clothing insulation,
- uncertainties in the estimated metabolic rate,
- uncertainties in the posture in relation to the effective surface area,
- uncertainties regarding the generalisation of the results obtained for a particular group under particular conditions.

Several authors discuss results which indicate the above mentioned restrictions of the use of *PMV* and other comfort equations for the determination of thermal comfort (Wyon 1994, Brager et al. 1995, Ong 1995, Parsons 1994, Brager and de Dear 1998). E.g. the metabolism is sensitive to the weight, the health and the gender of a person. Even for sitting quietly the difference can mount up to 40% (Ong 1995). A broad consensus can be found on the fact that thermal comfort or neutral thermal sensation is not necessarily equal for a significant number of people. Brager et al. (1995) conclude that “people’s preferences for non-neutral (warm or cool) thermal sensations are common, vary asymmetrically around neutrality, and in several cases are influenced by season”. Wyon (1994) shows that the average neutral temperature is of little interest because the 95% range of the individual neutral temperature falls within a wide range of 10^{o}C.

Further remarks can be made on the steady state of thermal comfort. Though most comfort indices, such as *PMV*, were determined for steady state conditions, everyday live is far from

being steady state. For example, time lags appear between the start of an activity and the thermal equilibrium of the body. Typically this time lag is small, in the order of several minutes. However the recovery of thermal comfort after ending the activity normally takes longer.

Finally, a psychological point of departure for the concept of thermal comfort is given by Cabanac (1996). When comfort is defined as the "subjective indifference to the thermal environment", indicating a stable situation, sensory pleasure is aroused if a troubled situation is corrected. Sensory pleasure, which is more pleasant than the indifferent comfort, is temporary, as from the troubled situation a comfortable situation is wanted. Therefore, if the human being is given the freedom to change a situation, it will strive for maximising the pleasure. From this concept one may conclude that variations in the thermal comfort conditions (in time and place) shouldn't be avoided at all costs, as long as one is able to correct the situation to a comfortable one. In this context McIntyre (1981) stated that "a person's reaction to a temperature which is less than perfect will depend very much on his expectations, personality and what else he is doing at the time". Brager and de Dear (1998) describe that people's expectations in naturally ventilated offices were much more relaxed than those for closely controlled air conditioned buildings. They conclude that not only behavioural adjustment but also expectation has a great influence on thermal comfort.

2.2.3 Current attitude to thermal comfort

After the discussion on thermal comfort concepts in the previous section, the question remains which concept can be applied best for assessing thermal comfort. Despite the indicated reservations, the standards (ASHRAE 1992, ISO 1984) prescribe the results as obtained from the climate chamber approach. Humphreys (1994) adheres to an inclusive approach instead of clinging on to one of the two concepts. Feedback will always take place, people are not passive in the acceptance of the provided environment, they will modify the environment or change places in order to arrive at a desired thermally comfortable situation. But when adaption is not possible due to requirements in posture, activity level, clothing ensemble and thermal environment, the heat balance approach will perform better (Humphreys 1994).

Fanger (1994) already indicated that some people, due to inter-individual differences, will still be feeling thermally uncomfortable though the fixed group optimal temperature level, i.e. the optimum solution, is obtained. The work of Humphreys and others underline the restrictions of the *PMV*-model on this point, but they don't provide a direct solution on how to deal with the personal thermal comfort that is to be predicted for newly designed buildings.

A direct result of the apparently unbridgeable differences between individuals regarding thermal comfort levels, physiological activity and the psychological state of mind, is that thermal comfort only can be achieved when each individual is able to set thermal comfort parameters themselves. This has recently also been recognised by Fanger (1997). When the influence on the thermal conditions is restricted to a small area around the personal, thermal comfort in principle can be obtained for every person occupying a room. Different studies show that a reduction in sick leave and in sick building syndrome (SBS) related symptoms (WHO 1983) can be obtained when individuals can control their own thermal environment (Preller et al. 1990, Raw et al. 1990; in Wyon 1994).

The range over which individual control should be possible has not been described extensively in literature. Wyon (1996) presents results of the performance improvement of a task when individual control is possible in the temperature range of $\pm 3^{o}$C. In that case 99% of the occupants are able to achieve thermal comfort when the room temperature is set to the group average neutral temperature. At $\pm 2^{o}$C, this would be 90%.

A first indication on the flow velocities necessary within the controlling range of the occupant has been investigated by Fountain et al. (1994). From climate chamber experiments Fountain et al. obtained air velocity preferences of people who have control over local air movement sources, aimed at the head, under varying ambient air temperatures within a range of 25.5 - 28.5^{o}C. The results were obtained from three different air movement sources. From these results Fountain et al. derived a relation for the predicted percentage of satisfied (*PS*), as a function of the operative temperature and the preferred velocity. In these results no effect of turbulence was evident. The operative temperature is the average of the air temperature and the mean radiant temperature weighted by their respective heat transfer coefficients (ASHRAE 1992).

The *PS*-model predicts the percentage of satisfied in contrast with the model of Fanger et al. (1988) which predicts the percentage of dissatisfied due to draught (*PD*). Figure 2.4 presents the preferred velocity as function of the operative temperature for *PS* = 85% and for *PD* = 15% at different constant turbulence intensities. Because people are not assumed to have control over the thermal environment in the *PD*-model, differences between velocities as predicted by the *PS*- and the *PD*-model already are rather large at low turbulence intensity levels. Remark that the *PD*-model as derived by Fanger et al. was fitted from experimental results for a maximum air temperature of 26^{o}C.

The applicability of the *PS*-model of Fountain et al. is restricted, as it is only valid for relatively high air temperatures. Under normal temperature conditions the preferred velocities will remain low, even when the thermal conditions are controlled individually.

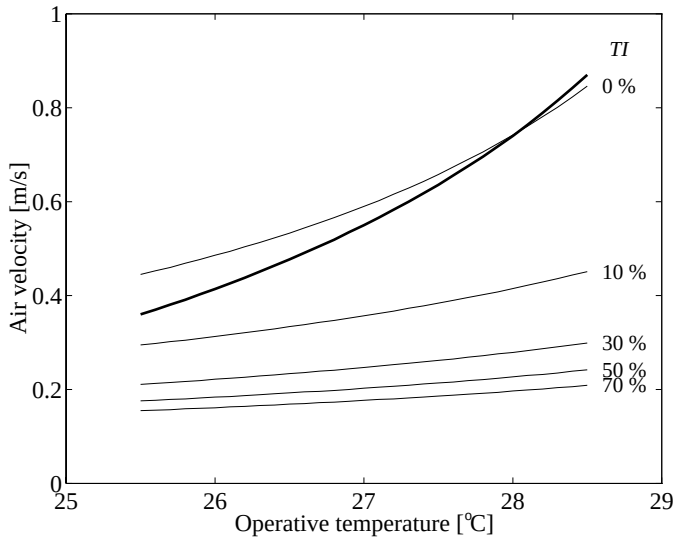

Figure 2.4. Preferred velocity as function of the temperature for PS = 85% [▏▏▏▏]*, the predicted percentage of satisfied according to Fountain et al. (1994), and for PD = 15%* [———] *at different turbulence intensities (TI), the predicted percentage of dissatisfied according to Fanger et al. (1988).*

The work of Wyon and Fountain et al., nevertheless, provides a point of departure for the thermal conditions that should be attainable. However apparent issues remain open. How to avoid interference between work places ? What to do when persons move around ? Can the individual user effectively control the environment ? Is the user able to select optimum conditions ? (Parsons, 1994) These questions need to be answered before individual control can be accepted and preferred beyond any doubt above other solutions.

2.3 VENTILATION

An important part in the search for optimal indoor air quality and thermal comfort is reserved for ventilation systems and the resulting characteristics of the air flow pattern. A short overview of established and recently introduced ventilation principles is presented.

2.3.1 Overview

A subdivision in natural and mechanical ventilation is made. Mechanical ventilation is applied most often as it allows a close control of air quality. Furthermore, the supply air may be conditioned with respect to temperature and humidity and, to a certain level, may be cleaned of outdoor contaminants and dust. In the past few years natural ventilation however

has regained interest, mainly because of consciousness of energy reduction and complaints of SBS. For natural ventilation the flow pattern that is obtained is a function of the outdoor conditions and the position and type of the apertures. Therefore, control of the air flow rate is low and sometimes the minimum required air flow rate for an acceptable air quality level cannot be obtained. Zeidler and Fitzner (1998) furthermore indicate restrictions in the maximum cooling capacity (in the order of 20 W/m^2) when using natural ventilation.

With mechanical ventilation the air mostly is introduced at relatively high velocity ($u > 1$ m/s). Therefore mixing of the supplied air with the room air, through entrainment, should take place before the air enters the inhabited zone. As a result, the mixing ventilation principle is characterised by the absence of significant room temperature and contaminant gradients. Displacement ventilation is different from mixing ventilation: the air is introduced near floor level at a lower temperature and at relatively low velocity ($u < 1$ m/s) and turbulence intensity. The exhaust is located at ceiling level. The characteristic differences in the flow pattern between these two ventilation principles have been described in Chapter 1.2.3.

A more recent air distribution principle for office environments, which like displacement ventilation also originates from industrial application, is the task conditioning principle (Bauman and Arens 1996). Here the supply air is introduced near the workplace close to the occupant, so fresh air is supplied close to the occupant. The main objective of task conditioning is to create a comfortable micro-climate within a macro-climate (see Figure 1.2). For office buildings the individual control of the thermal conditions within the micro-zone is seen as a major design aspect for improving the user satisfaction. This characteristic of task conditioning systems meets the current attitude with regard to thermal comfort as described in Chapter 2.2.

Ventilation techniques for the entire room volume as mixing and displacement ventilation cannot provide the required specifications for individual control and the conditioning of a micro-climate, when more than one person occupies the room. These specifications only can be obtained by task conditioning systems. Task conditioning is possible via natural ventilation (*bioclimatic design*; see Chapter 1.2.3). The application then however is restricted due to the variation in the outdoor conditions and the subsequent possible mismatch with the required ventilation flow rates and thermal conditions. Though individual control is possible given a conscious design, the creation of a micro-zone around the occupant is difficult to obtain and often limited to the perimeter (Zeidler and Fitzner 1998). As a result, mechanical ventilation systems will remain most interesting when the application of task conditioning is concerned (*high tech buildings*; see Chapter 1.2.3). This topic is discussed in the next sections.

A hybrid ventilation system presents an integrated approach. It combines the positive aspects of both natural and mechanical ventilation. The research into hybrid systems has only started recently. Though the hybrid approach may be focussed on whole room ventilation, it can also be applied for task conditioning. Then the mechanical part of the hybrid ventilation system seems to be pre-eminently suited for air conditioning the micro-climate near the occupant, whereas natural ventilation may be deployed for the conditioning of the macro-climate.

2.3.2 Task conditioning systems

For the creation of a micro-climate by mechanical ventilation, the supply diffuser must be situated close to the occupant. Task conditioning systems for office environments already were identified in the 70's to correct the thermal conditions near the occupant. Different furniture-based and floor mounted supply diffusers for office environments and assembly rooms can be found in Krantz (1984). Investment costs and the practicality of the technical implementation however hampered its wide-spread introduction. These types of personalised air supplies still form the basis of design for new task conditioning systems.

An overview of the currently available task conditioning systems is found in Bauman and Arens (1996). These systems normally introduce the air from relatively small diffusers at relatively high velocity and turbulence intensity to allow a high entrainment flow rate. In Figure 2.5 five possible locations for task conditioning based supply diffuser are indicated. Nearly all positions around the occupant may be used to create a micro-climate.

The in Figure 2.5 identified locations for task conditioning based supply diffusers can be arranged to floor-based, desktop-based, partition-based and ceiling-based systems. The exhaust normally is situated near ceiling level. The separate supply locations will be discussed shortly using the information described in Bauman and Arens (1996). *Floor-based* systems currently are the most commonly applied type of task conditioning system. They are incorporated in raised floor systems and therefore, due to its modularity, have a high flexibility. The control options heavily depend on the type of system. As relative high supply velocities are required, draught discomfort may occur more often when the system is not properly controlled. *Desktop-based* systems are available in a wide variety. For example: free standing supply nozzles and desktop level grills at the back of the desk surface or a linear grill at the front edge of the desk, facing the occupant. Mostly a floor plenum is required to deliver the air to the desk. The main advantage of these systems is the close and efficient control of the thermal conditions near the occupant. However, the air velocity can be high and, because these systems mostly have a limited flexibility, the supply diffuser may be covered or may be standing in the way. *Partition-based* systems can be

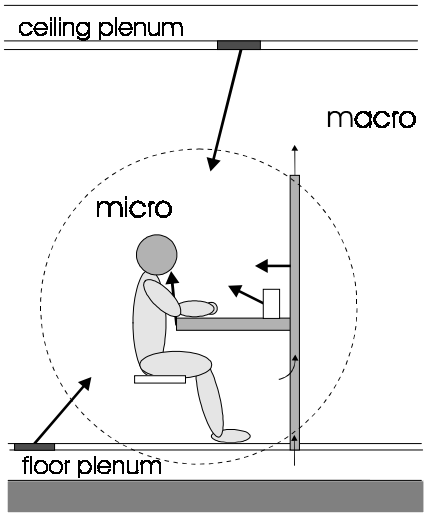

Figure 2.5. Overview of the identified locations for task conditioning based supply diffusers.

used in open-plan office buildings with partitioned work-stations. The air is supplied above desktop level and is delivered from the plenum through the partition. These systems therefore have similar supply characteristics as desktop-based systems. An additional advantage of partition-based systems is the option to condition the macro-climate through openings on the top of the partition. *Ceiling-based* systems, generally adjustable jet nozzles, have been designed in response to retrofit demands for conventional ceiling-based air distribution systems. The control of these systems is possible through a remote control, but the effectivity of the ceiling-based task conditioning systems is largely hampered by the large distance between supply and occupant.

2.3.3. Desk displacement ventilation concept

In contrast to the characteristics of the above described task conditioning systems, the Desk Displacement Ventilation (DDV-) concept is introduced. With the DDV-concept it is intended to create a micro-climate by introducing the supply air below the desk, close to the occupant (see Figure 2.6), applying the rules set by the displacement ventilation principle; introduction of air over a relative large area at low velocity (0.1…0.2 m/s). In this concept a displacement ventilation unit is situated below the desk top, against the back of it. A fan may be incorporated in the unit to extract fresh air from a floor plenum. The fan-setting then determines the flow rate. The temperature may be controlled via an electrical heater or by adjusting the amount of recirculated room air with a mixing valve. Other air distribution and air supply systems are possible to control the supply flow rate and temperature, e.g. a twin duct system (Rutten 1996).

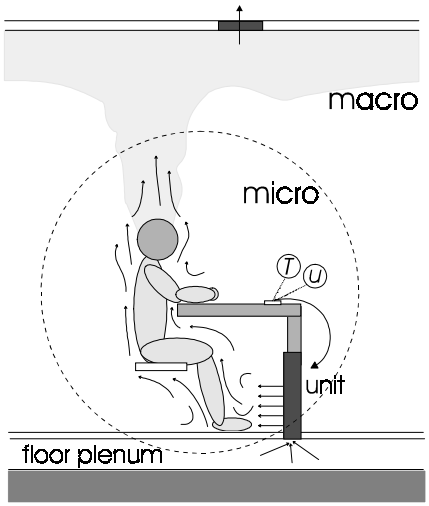

Figure 2.6. Schematic drawing of the desk displacement ventilation concept.

The DDV-concept intends to combine the positive features of displacement ventilation, e.g. the ventilation effectiveness, with those for task conditioning, e.g. control on thermal comfort requirements. This concept has been applied successfully in a high cooling load project at a dealers room in Sydney, Australia[1]. The performance of the DDV-concept for normal office configurations however is not clear. When the supply temperature is below room temperature relative cool air is provided directly at a critical position of the body, i.e. the ankles. Though thermal comfort is in direct control of the occupant, it is not evident:

- whether a micro-/macro-climate is created,
- what the performance of the DDV-system is in terms of cooling load and pollutant removal capacities, under a wide range of occupant settings,
- what the macro-climate conditions are (given a micro-climate) and under which circumstances additional cooling and fresh air is required.

The investigation into the applicability of the desk displacement ventilation concept for normal office configurations is used for the full-scale experimental and numerical research as indicated as the final objective in Chapter 1.3. The experimental and numerical set-up and the results for an office room ventilated according to the DDV-concept will be described in the Chapters 5 to 8. First however the applied tools for this investigation will be discussed: measurement and simulation techniques.

[1] The DDV-concept was first applied by P.G.S.Rutten when he was with Lincolne Scott Australia Pty Ltd.

Chapter 3

THE MEASUREMENT OF INDOOR AIR FLOW

3.1 INTRODUCTION

The impression of an occupant on a certain indoor environment is based on personal experience and the physiological and psychological state of this occupant, i.e. the 'sensor'. Objective information is obtained when the indoor environment is measured by a technique that is able to register a specific quantity unbiased and with a given accuracy. The data then can be used to describe the indoor environment. The result also may be used to compare with numerical simulations.

In Chapter 2 a number of important parameters, such as temperature, velocity, contaminant concentration and ventilation effectiveness, have been given to describe the indoor environment. This research is limited to the parameters flow velocity and air temperature. The measurement of the ventilation effectiveness is described extensively in a related work by Roos (1998[a]).

For temperature measurements well established techniques are available, e.g., the thermocouple (ASTM 1981), the positive temperature coefficient resistor and infrared thermography (Tanis et al. 1976).

The measurement of the room air velocity is more difficult than that of temperature. This is especially true as the velocity is low (0…1.0 m/s) and the turbulence intensity is high (> 10%), as is the case in the indoor environment. Because measurement of the velocity is not straightforward, this chapter concentrates on velocity measurement techniques for the measurement of indoor air flow.

First, the flow quantities and statistics that relate to indoor air flow are described. Next a summary is given of indoor air flow measurement data found in literature. This overview allows an estimation of the flow characteristics indoors. The available data is also assessed on its applicability for validation of numerical simulations. The chapter is continued with a summary of the principles to measure the air velocity. They are discussed with respect to the requirements for usage in indoor air flow. From the latter discussion two techniques are evaluated in depth, the hot sphere anemometer and particle tracking velocimetry. The actual measurement at a full-scale configuration of an indoor air flow pattern will be discussed in Chapter 5 and 6.

3.2 AIR FLOW PARAMETERS

The turbulent indoor air flow can be characterised by the instantaneous velocity $u(x,t)$ of the flow at position x and time t. The instantaneous velocity in the i-direction can be thought of being composed of a mean velocity component, $\overline{u}_i$, and a fluctuating component, u_i', superpositioned on it,

$$u_i = \overline{u}_i + u_i', \tag{3.1}$$

where i refers to the velocity component in the i-direction. Equation (3.1) is known as the Reynolds decomposition. The averaged value of the instantaneous velocity can be determined over a specific time period at a fixed point x, $\overline{u}_i^T$, in which T is the averaging time; the Eulerian velocity. Or u_i can be averaged spatially over a line segment at a fixed time-point t, $\overline{u}_i^L$, in which L is the averaging length; the Lagrangian velocity. For both expressions the averaged value of the fluctuating component, u_i', is defined zero.

From the fluctuating velocity at one point the turbulent kinetic energy per unit mass (k) is defined as

$$k = \frac{1}{2}\overline{u_i'^2}\,. \tag{3.2}$$

The Einstein-summation convention is used. The relation of the turbulent kinetic energy to the mean velocity, the turbulence intensity (TI), is defined as

$$TI = \frac{\sqrt{\overline{u_i'^2}}}{\overline{u}_i} = \frac{\sigma_u}{\overline{u}_i}, \tag{3.3}$$

where σ_u is the standard deviation. the turbulence intensity (TI) often is multiplied by 100 to give a percentage expression.

Via auto-correlation information on the length scales of the flow can be determined if, for point measurements, the Taylor hypothesis of 'frozen' turbulence ($\partial/\partial t \approx -\overline{u}_i \, \partial/\partial x_i$) is assumed. When the flow is simultaneously measured in more than one point, spatial, space-time and time cross-correlations can be deduced (Hinze 1975).

Figure 3.1a presents the result of velocity measurements as registered in two separate points in a room equipped with a displacement ventilation system (see Chapter 5 and further). The measurements are obtained by a hot sphere anemometer with a 10 Hz sampling frequency.

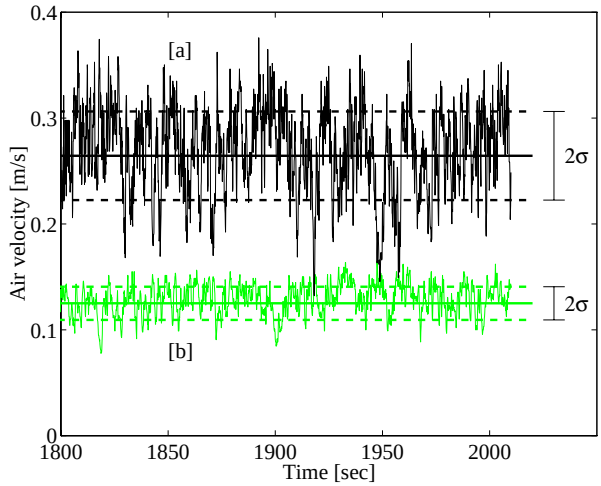

Figure 3.1a. Velocity registration at two positions in an indoor air flow pattern with a hot sphere anemometer with a sampling rate of 10 Hz.

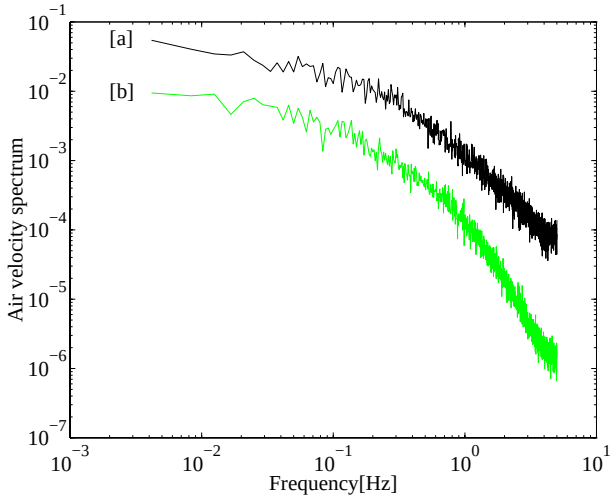

Figure 3.1b. Power density spectrum of the velocity registration as shown in Figure 3.1a.

The sampling time is in the order of the Kolmogorov time scale (Nieuwstadt 1994) for indoor air flow. The mean velocity derived for each measurement is indicated by the full line. The standard deviation to the mean value is indicated by the dashed line.

Figure 3.1b presents the spectral distribution of the signal applying Fourier transformation. From the air velocity spectrum the spectral distribution of the turbulent kinetic energy can be derived. The large eddies in the mean flow cause fluctuations in the low frequency range. They are the main source for the production of turbulent kinetic energy due to shear in the mean flow. The high frequency fluctuations are caused by the smaller eddies (Hinze 1975). The turbulent kinetic energy as produced in the large eddies is transported to the smaller eddies and eventually transformed to heat via viscous dissipation in the smallest eddies. However, the transfer of energy to larger scales, the so called backscatter, is possible (Piomelli et al. 1991).

3.3 TURBULENCE AND STATISTICS

If $\overline{u}_i$ is continuously determined over a time-period or a line segment, the Reynolds decomposition condition $\overline{\bar{f} \cdot g} = \bar{f} \cdot \overline{g}$, where *f* and *g* are fluctuating quantities, theoretically is not complied with. This is due to the chaotic nature of turbulence, which says $\overline{\overline{u}_i} \neq \overline{u}_i$ in case the integration interval increases (Nieuwstadt 1992). The *ensemble average* should be used instead, by repeating an experiment *N* times (same initial and boundary conditions). Every realisation will have a different result and the ensemble average then is defined as

$$\overline{u}_i = \lim_{N \to \infty} \frac{1}{N} \sum_{n=1}^{N} u_i^{(n)} \; ; \tag{3.4}$$

in which *n* describes the realisation of the experiment.

Applying the 'Ergodic theorem', which states that stationary processes exhibit the property of ergodicity[1], for a stationary process the time averaged velocity can be derived from

$$\lim_{T_{avg} \to \infty} \overline{u}_i^{T_{avg}} = \overline{u}_i \, . \tag{3.5}$$

In a stationary process the probability density function is independent in time, the statistical averages are constant or only dependent on the time span. Fluctuations in a stationary process therefore by definition have a limited time scale, the integral time scale T_s^{int}. The integral time scale is a measure of the interval for which u_i is correlated with respect to

[1]Ergodicity: the statistical parameters of a process, obtained by averaging over an ensemble of realisations, are identical to the parameters obtained for a single experiment by averaging over time.

time. When the averaging time T_{avg} comprises a large number of statistically independent time intervals (= T_s^{int}), the hypothesis supposes the time averaged value $\overline{u}_i^{T_{avg}}$ to be equivalent with the ensemble averaged value $\overline{u}_i$. The same theorem holds for a homogeneous process (Nieuwstadt 1992).

Given the above, the uncertainty in the measurement of the mean velocity $\overline{u}_i$ and the fluctuating component u_i' on the one hand is a function of the mean velocity, the integral length scale ($L_s^{int} = \overline{u}_i \cdot T_s^{int}$) and the turbulence intensity of the flow and on the other hand of the sampling interval (Δt) and the total sampling time (T_s^{tot}) (Bruun 1995). As a result, the level of accuracy that can be obtained is related to the flow pattern that is under investigation and the number of independent samples (N) taken. In Appendix A a summary is given of the derivation of the statistical uncertainty in a measurement. An example of the statistical uncertainty is given below.

Consider a typical indoor air flow with an average velocity $\overline{u}$ = 0.1 m/s and a turbulence intensity TI = 0.3. If the mean measured velocity, $\hat{\overline{u}}$, should be determined with an inaccuracy of ±1% with a 98% confidence level, N can be determined at 4886 samples. The optimum sampling interval is calculated from the integral time scale (T_s^{int}), that can be estimated from the integral length scale and the mean velocity of the flow. When L_s^{int} is estimated at 0.2 m (Melikov et al. 1988), then $T_s^{int} \cong L_s^{int} / \overline{u}$ = 2 sec. The optimum sampling interval is calculated at $\Delta t = 2 T_s^{int}$ = 4 sec and the total sampling time at $T_s^{tot} = N \cdot \Delta t$ = $19.5 \cdot 10^3$ sec. If the turbulence intensity is to be determined at the same accuracy and confidence level, the total sampling time should be $T_s^{tot} = 22 \cdot 10^4$ sec.

Table 3.1. Number of samples necessary for required accuracy of $\overline{u}$ at TI = 0.3.

	Inaccuracy		
Probability	±1%	±5%	±10%
90 %	2450	98	25
95 %	3458	139	35
98 %	4886	196	49
99 %	5945	238	60

When the total sampling time is 180 sec, as prescribed in ASHRAE (1992), the accuracy that can be obtained depends on the flow that is under investigation. When the same conditions are assumed as above, the maximum available number of independent samples is N = 45. Table 3.1 presents a summary of the number of samples necessary for the required accuracy and probability. A ±10% inaccuracy at a 95% confidence level can be obtained for the given conditions and sampling time. If the turbulence intensity would be TI = 0.1, a ±5%

inaccuracy at 99%-confidence level is possible. The required accuracy for a measurement, therefore, either can be obtained by measuring over a very long time period at a large sampling interval or by adopting an iterative measurement procedure.

3.4 INDOOR AIR FLOW MEASUREMENTS

The most extensive experimental studies into in-situ indoor air flows have been described by Thorsauge (1982), Hanzawa et al. (1987) and Melikov et al. (1988 and 1990). The measurements comprised a wide range of typical mechanical and natural ventilated spaces (test rooms, living rooms, office rooms, theatres, etc.) and were performed in the occupied zone at four different heights. The main conclusion from these studies is that mean velocities and turbulence characteristics varied widely over the investigated spaces. Typically, mechanically ventilated rooms revealed higher velocities, whereas the turbulence intensities are of the same order of magnitude (0.05 - 0.40 m/s; 10 - 70% versus 0 - 0.20 m/s; 10 - 60%). Despite the extent of the measurements, they are not useful as a starting point for numerical validation due to the limited information on boundary conditions and experimental data. The measurements were meant for analysis of potential draught problems (Fanger et al. 1988).

Results of climate chamber studies on offices are available more widely. Most of these studies are performed for comparison with numerical results by techniques as Computational Fluid Dynamics (CFD). Often scaled models of the physical indoor environment have been used. Nielsen (1974) was one of the first to present indoor air flow data for validation purposes. The flow was steady two-dimensional isothermal forced convection, later extended to non-isothermal (Nielsen et al. 1979) and to three dimensional flow patterns (Gosman et al. 1980). Another indoor air flow benchmark is the free convection flow in a differentially heated cavity (Cheesewright et al. 1986, Cheesewright and Ziai 1986, Nansteel and Greif 1981). For both benchmark studies good agreement was found between measurements and CFD-simulations (Nielsen 1974 and Henkes and Hoogendoorn 1992). For the differential heated cavity however special attention is required for the discretisation and the turbulence modelling (Henkes and Hoogendoorn 1992).

Climate chamber data for more realistic indoor air flow configurations are presented in among others Chen (1988) and the IEA Annex 20 research (Lemaire 1992). Both references describe results for different types of ventilation configurations, experimentally as well as numerically. Examples of more recent full-scale experimental results found in literature are Jouini et al. (1994), Hawkins et al. (1995), Hu et al. (1996) and Yuan et al. (1997). Given

the diversity in indoor air flow configurations, the number of available measurement results nevertheless is restricted.

Characterisation - From full-scale measurement results as discussed above, an estimation of the room flow characteristics can be derived to define the specifications for a measurement technique. Table 3.2 presents an overview of this estimation. In Chapter 3.2 the flow parameters have been introduced. For the estimation the room is subdivided in three zones, according to the flow regimes that can be recognised (see also Figure 3.2):

- The region or a part of the room volume, referred to as *zone*, in which the air flow is directly influenced by a source is indicated as the *source-zone*. Examples are terminals of heating, ventilation and air conditioning (HVAC-) systems such as a radiator, an induction unit or a cold ceiling. The flow in this zone considerably influences the thermal comfort and the ventilation effectiveness. The source-zone definition may be refined when the energy supply to the flow is considered: forced and free convection.
- Besides the well recognisable sources for an air flow, other objects also influence the flow, e.g., walls and furniture. This zone is indicated as the *boundary-zone*.
- Finally, if the flow is the resultant of a combination of source and boundary influences, this zone is indicated as the *free-zone*, defined as the room minus source-zone minus boundary-zone.

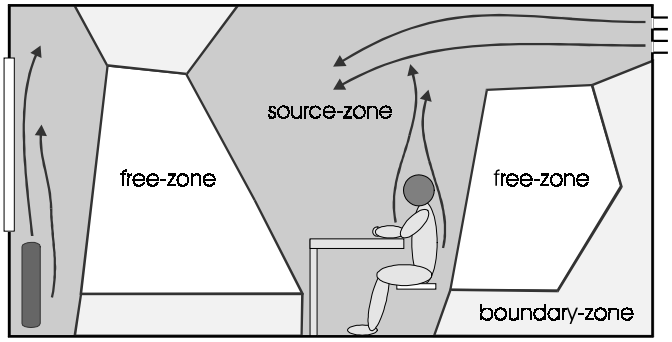

Figure 3.2. Graphical representation of the subdivision of a room into zones, according to the prevailing flow regimes.

Table 3.2. Estimation of the zonal air flow characteristics measured in rooms [scale 1:1] as summarised from literature (Loomans and van Mook 1995).

Parameters		*source zone*	*boundary zone*	*free zone*
mean velocity ($\overline{u}$)	[m/s]	0.1…2.0	0.05…0.3	0.0…0.15
turbulence intensity (*TI*)	[%]	5…25	10…30	10…50 to 100
frequency domain (*f*)	[Hz]	~0…15	~0…10	~0…5
integral length scale (L_s^{int})	[m]	--	--	0.05…0.20

Discussion - The values as presented in Table 3.2 are coarse but allow an indication on the bandwidth of the prevailing conditions within each zone. A further narrowing of this bandwidth is not practical given the wide variety in indoor air flow patterns. Highest velocities naturally are found in the source zone. Given the type of diffuser or heat source and its dimensions, the velocity can reach high values (1.0…2.0 m/s). These high velocities are not found in the free-zone, which often corresponds with the inhabited zone, as draught-discomfort must be avoided. In the boundary zone an estimation of the velocity is more difficult. Higher velocities are only expected at a position where the flow impinges the wall or where the flow hugs to the wall.

The turbulence intensity in most situations is high (>10%). This is due to the low velocities that prevail and to the applied definition of turbulence intensity (see Equation 3.3). The frequency domain which contains 80 % of the energy is restricted to the lower frequencies. From the frequency distribution Hanzawa et al. (1987) and Melikov et al. (1988) also derived information on the length scales of the flow pattern. The integral length scale presents information on the largest eddies that appear in the flow. Given the low velocities and the measurement technique that was used, the latter result however only presents an order of magnitude value.

Most measurement results described above were obtained with hot sphere anemometers. This type of anemometer has been specially designed for indoor air flow application, but is known to have a restricted accuracy due to, e.g., the omni-directional registration, the self-heating of the sensor and the calibration requirements. Moreover, this anemometer is sensitive to the way it is being applied, on which only little information is available. Despite these known drawbacks and the increasing interest in the indoor air flow, the applicability of new techniques for the measurement at indoor air flows has not been discussed widely. The next sections present a contribution to this discussion.

3.5 PRINCIPLES OF VELOCIMETRY

From the above summarised results, it is obvious that velocities are measured under a wide range of flow and boundary conditions. The specifications of the velocity measurement technique determine the feasibility to utilise it under given conditions. A first categorisation of the available techniques is possible by distinguishing the operating principle;

- *Visualisation techniques* - These techniques make the whole flow pattern visible (for the human eye). From recorded images of the visualised flow pattern it is eventually possible to retrieve quantitative information; Examples: smoke and helium-filled soap bubbles.

- *Heat-transfer techniques* - These techniques are based on the transfer of thermal energy from a heat source to the fluid flow. The quantity of transferred energy is a measure for the flow velocity; Example: hot wire anemometry.
- *Time-of-flight techniques* - In these techniques (1) the time interval between the upstream injection of the tracer and its downstream detection is measured, or (2) the displacement of a tracer during a time interval is measured. Sonic pulses, heat pulses, ions or particles can act as tracer; Examples: sonic anemometry and particle tracking velocimetry (PTV).
- *Kinetic energy techniques* - The kinetic energy is transformed into a pressure difference, which is a measure for the velocity of the fluid; Examples: Pitot tube and cup anemometer.
- *Doppler effect techniques* - Velocities are determined from changes in the propagation of (light) waves through the fluid. The waves are scattered by particles in the fluid, causing a frequency shift (Doppler shift) of the emitted wave; Example: laser-Doppler anemometry (LDA).

Given the dimensions of the sensor, the physical boundary conditions, the flow range and the accuracy, an applicable measurement technique can be determined by matching its specifications to the requirements. The indoor air flow presents a challenge to most available techniques, as low velocities are accompanied by relative high turbulence intensities, albeit in the low frequency range (see Table 3.2).

Following an extensive literature study into available and new measurement techniques and the principles on which they are based conclusions were drawn with respect to the applicability of these techniques for measurement at indoor air flow (Loomans and van Mook 1995). The results of this study are summarised in Table 3.3. For each principle a specific technique is evaluated. Besides a subdivision in zones (see Figure 3.2), also the application area is distinguished: laboratory or in-situ. A differentiation is made via +'s and -'s, ranging from well suited (++) to unsuited (--).

The evaluation is based on the estimated flow characteristics for the different zones, as given in Table 3.2, and the specifications of the technique. In Fingerson and Freymuth (1983) and Tavoularis (1986) a set of requirements is given that may be used to perform an evaluation. Spatial, temporal, dynamic, distortion and use requirements were taken into account. Some examples of requirements are:

- frequency response; range and sensitivity (also to temperature and humidity);
- mechanical or thermal disturbance of the flow;
- calibration necessity and user-friendliness.

Table 3.3. Applicability of techniques for the measurement at indoor air flow (laboratory [lab.]; in-situ [i.-s.]) .

principle	zone / measuring location / technique	source		boundary		free	
		lab.	i.-s.	lab.	i.-s.	lab.	i.-s.
Visualisation	*smoke*	+	+	+	+	+	+
Heat-transfer	*hot sphere anemometer*	+/-	+/-	-	-	+/-	+/-
Time-of-flight	*PTV*	+	+/-	+/-	+/-	++	+/-
Kinetic energy	*pitot tube*	+	+	-	-	--	--
Doppler effect	*LDA*	++	-	++	-	++	-

From the in Table 3.3 summarised evaluation, the interesting measurement techniques are discussed point by point:

- The (constant temperature difference) hot sphere anemometer applies the heat-transfer technique and is used most often for quantitative measurement of indoor air flows. The principle shows an increasing sensitivity with a decreasing velocity (u = 0.05…0.5 m/s) and the technique is well-developed and readily applicable. The probe, however, is omni-directional, the inaccuracy is in the order of 10 - 20% at 0.05 - 0.5 m/s and there is a need for regular calibration.
- The Laser-Doppler Anemometer (LDA) currently gives the most accurate and reliable information on the velocity magnitude and the turbulent characteristics of the flow in one or more directions. Whereas LDA is a reliable measuring technique, it is less suited for extensive measurements at indoor air flows, because it is a point measuring device and a single LDA already requires considerable investments.
- The time-of-flight technique as used for the Sonic Anemometer (SA; not indicated in Table 3.3) is a direct measuring technique that in principle allows the measurement of very low air velocities. However, the velocity is spatially averaged and dynamic restrictions may be found in the frequency response (van Mook 1995). These restrictions do not apply to the PTV-technique which is discussed below.
- Visualisation of the flow using smoke can afford extensive information on the flow pattern in almost every situation without much effort. Visualisation often is also used to support measurement results obtained from other techniques. Quantitative information can be derived from the visualised flow if the time-of-flight and the helium bubble visualisation method are combined. This technique is used in Particle Tracking Velocimetry (PTV) or Particle Streak Velocimetry (PSV) (Scholzen 1997). The velocity vector can be determined by imaging small tracer particles that are carried by the flow. This technique, in principle, is capable of measuring very low (Lagrangian) velocities in two components in a plane or in the three dimensions of the flow pattern.

From the literature review summarised above (Loomans and van Mook 1995) currently only two techniques are indicated as being feasible for application in full-scale laboratory or in-situ indoor air flow; the low-velocity hot sphere anemometer and the particle tracking/particle streak velocimetry technique. In the next two sections both techniques are discussed. Visualisation of the flow field using smoke most certainly forms an important part in the study of indoor air flow. However, given its ease of use, this technique will not be discussed more in depth.

3.6 HOT SPHERE ANEMOMETER

The hot sphere anemometer has been specially designed for indoor air flow application. It is derived from the hot wire anemometer, which history goes back to the end of the 19th century. The hot wire sensor, a thin metal wire, is heated by an electrical current. The passing fluid cools the sensor, predominantly by convection, and changes the electrical resistance of the wire. This is an indirect technique as the relation between the convective heat loss and the velocity of the flow must be determined. The relation is often expressed according to King (1914):

$$Nu_d = Y + Z \cdot Re_d^{0.5}, \qquad (3.6)$$

where the Nusselt (Nu_d) and Reynolds (Re_d) number are based on the diameter (d) of the hot wire and Y and Z, which are a function of the air temperature, are obtained by calibration.

After a short description of the hot sphere anemometer, the next sections discuss the specifications of the anemometer under stationary and transient conditions.

3.6.1 Description of the anemometer

The investigated hot sphere anemometer consists of two almost identical spherical sensors (d = 0.003 m) which are located at 0.025 m distance from each other (see Figure 3.3 and Dantec, 1985). The sensors are made out of glass and are finished off with a thin film of nickel. They are connected to the opposite arms of a Wheatstone bridge which is integrated in an electrical circuit. The bridge is balanced if one sensor is heated to a temperature of about 30^{o}C above the temperature as measured at the second 'cold' sensor. The bridge voltage is correlated with the velocity of the passing flow due to the temperature dependency of the electrical resistance of the nickel film. This correlation is not fixed in time, ageing and contamination of the sensor require a regular calibration.

A numerical model which has been developed by in 't Zandt (1995; in Loomans and van Schijndel 1998) describes the electrical circuit of the anemometer and its heat transfer

characteristics. It is elucidated further in Appendix B. The model has been used, together with two experimental calibration set-ups, to perform a parameter study at the hot sphere anemometer, under stationary and transient conditions.

Different types of anemometers are available that have a set-up that is similar to the system under investigation (e.g. Crommelin and Dubbeld 1976). Differences generally are found in the construction of the sensor and therefore the transient characteristics. Nevertheless, the described qualitative results in principle also apply to these - similar - anemometers.

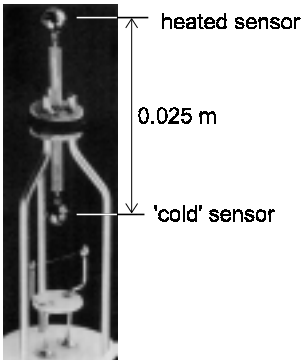

Figure 3.3. Close-up of the velocity (heated) sensor and the reference ('cold') sensor of the hot sphere anemometer (modified from Awbi (1991)).

3.6.2 Stationary conditions

Calibration set-up - For low-speed steady state calibration the laminar pipe flow method has been used (Lee and Budwig 1991). Pressurised air is introduced into a glass tube (l = 1.31 m; d = 0.031 m) that is positioned at the end of a small contraction (see Figure 3.4). The heated sensor of the anemometer is positioned in the centre of the exit plane of the tube. A mass flow meter measures the flow rate through the tube. For a Poisseuille flow the centre-line velocity is determined from $2 \cdot \overline{u}_p$, where $\overline{u}_p$ is the average velocity over a cross-section of the pipe. In order to ensure a fully developed Poisseuille flow at the exit plane, the length of the entrance region should exceed $l_{99} = 0.056\, d \cdot Re_d$, for Re_d > 500 (Ward-Smith 1980). In this relation l_{99} is the distance over which the centre-line velocity has developed to 99% of the fully-developed value, d is the tube diameter and Re_d the flow Reynolds number based on the tube diameter. Given the set-up a fully developed Poisseuille flow is obtained for Re_d < 750. Higher Re_d-values require a correction for the entrance influence. For Re_d < 500 the entrance length is smaller than the tube length (Ward-Smith 1980).

A second, smaller, tube is positioned below the large tube to enable a similar air velocity at the 'cold' sensor as will be described later on. Furthermore, the anemometer is sheltered from the environment so the outflow from both tubes is not disturbed. Measurements take place in an air conditioned laboratory.

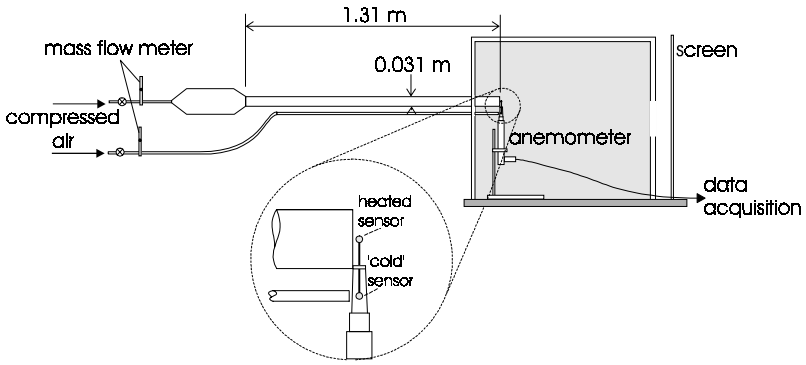

Figure 3.4. Laminar pipe-flow calibration set-up.

Calibration and measurement accuracy - Systematic errors arise in the calibration set-up due to the measuring of the dimensions and due to the size and the positioning of the sensor relative to the Poisseuille profile. These errors, which would have caused a systematic error of about 1%, have been corrected as much as possible (Loomans and van Schijndel 1998). Furthermore, for accurate measurement, one should pay attention to the following:

- The description of the hot sphere anemometer design indicates the importance of the 'cold' sensor which acts as the reference point for the heated sensor. Deviations in the conditions close to the 'cold' sensor compared to the prevailing conditions at the heated sensor will directly influence the measurement result;
- If experimental conditions differ from the thermal conditions (not the air temperature) under which the calibration has been performed, deviations can be expected;
- The sensor is not fully omni-directional;
- At low velocities a small free convection flow is induced due to self-heating; and
- The anemometer measures absolute values.

The anemometer has been tested on seven parameters, through experiments applying the described experimental set-up, by numerical simulations or by statistics. The parameters are listed in Table 3.4.

Table 3.4. Investigated parameters for the hot sphere anemometer.

	Parameter	Description
1.	Velocity gradient over heated and 'cold' sensor	$u_{cs} \neq u_{hs}$
2.	Air temperature gradient over heated and 'cold' sensor	$T_{air,hs} \neq T_{air,cs}$
3.	Directional sensitivity (perpendicular; parallel)	$\rightarrow \vert \; ; \rightarrow —$
4.	Radiation	$T_{mrt,calibration} \neq T_{mrt,measurement}$
5.	Relative humidity	$\varphi_{calibration} \neq \varphi_{measurement}$
6.	Buoyancy	$\uparrow \vert$
7.	Turbulence intensity	$\int \vert \vec{u} \vert dt$

(1) *Velocity gradient over heated and 'cold' sensor* - The 'cold' sensor represents the air temperature, i.e., the reference point, for the heated sensor. The principle to measure the temperature at the 'cold' sensor requires the temperature to be slightly higher than the ambient temperature. In the numerical model of the anemometer, the temperature at the 'cold' sensor was simulated to be 1.4°C higher than the air temperature. A velocity difference between the two sensors will result in different convective heat transfer characteristics and therefore in a deviation of the registered velocity. The resulting effect has been investigated experimentally in the calibration set-up. Figure 3.5 schematically describes the applied procedure in three steps. Each step is explained further in the figure caption.

In Figure 3.6a the measured velocity deviation as a result of a varying velocity at the 'cold' sensor is shown (*Step 3*, Figure 3.5). The deviation is obtained for different base velocities at the heated sensor, starting from no flow condition at the 'cold' sensor (u_{cs} = 0 m/s). A curve has been fitted through the measurement results at equal flow conditions for the heated and the 'cold' sensor ($u_{hs} = u_{cs}$). The results show that at u_{hs} = 0.5 m/s and u_{cs} = 0 m/s, the velocity is overestimated up to ~26%. To avoid this deviation both sensors should be positioned in the same streamline. Figure 3.6b presents a contour diagram of the (measured) correction velocity for a velocity difference over the two sensors. At zero difference no correction is required.

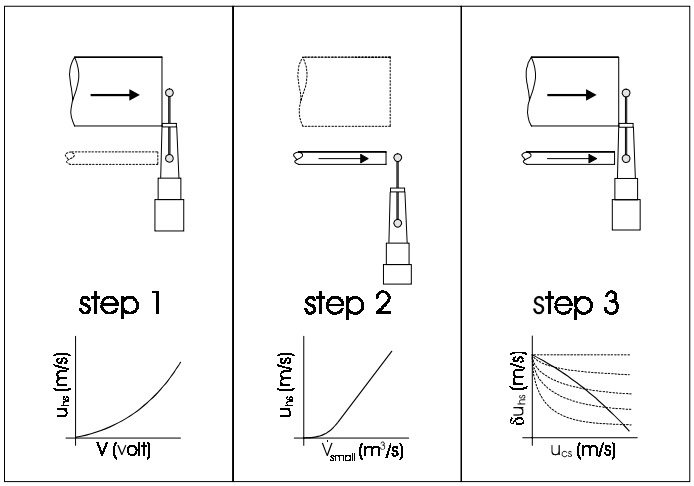

Figure 3.5. Measurement procedure for the hot sphere anemometer when using the laminar pipe-flow method. Procedure: Step 1: determination of the voltage-velocity relation with no flow conditions at the 'cold' sensor (u_{cs} = 0 m/s); Step 2: determination of the velocity-flow rate relation for the small tube applying the calibration result obtained from Step 1 (u_{cs} = 0 m/s); Step 3: determination of the velocity correction (δu_{hs}) for the result of Step 1 by varying the velocity at the 'cold' sensor at constant velocity at the heated sensor.

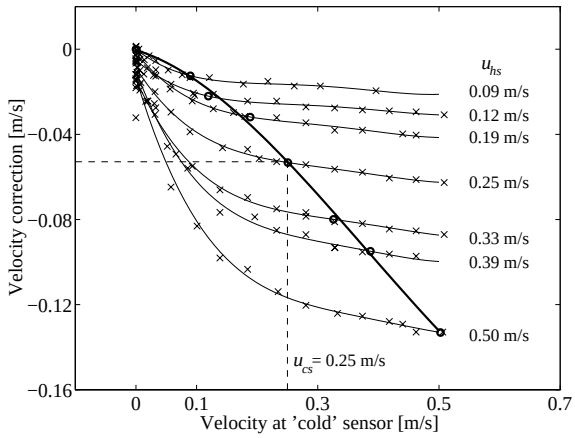

*Figure 3.6a. Measured velocity correction for a varying velocity at the 'cold' sensor (Step 3, Figure 3.5), starting from u_{cs} = 0 m/s ([×] measurements, [**o**] $u_{hs} = u_{cs}$, [▏▏▏▏] curve fit $u_{hs} = u_{cs}$). **Example**: For u_{hs} = 0.25 m/s and u_{cs} = 0.25 m/s a correction of 0.05 m/s should be subtracted from the original calibration result with u_{cs} = 0 m/s (Step 1, Figure 3.5).*

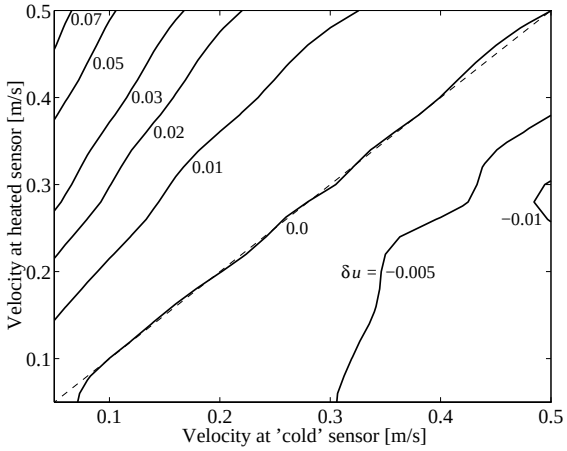

Figure 3.6b. Correction diagram for velocity gradient over heated and 'cold' sensor ([▏▏▏▏] measurement results, [– – –] $u_{hs} = u_{cs}$; correction in m/s, zero correction for $u_{hs} = u_{cs}$).

The measured velocity deviation (Figure 3.6a) implies that the calibration procedure using the laminar pipe flow method must be extended with the above described procedure (Figure 3.5). The calibration results corrected accordingly have been compared with measurement results obtained in a low velocity wind tunnel calibration set-up (Crommelin, 1992). The comparison indicated the applicability of the corrected laminar pipe flow method (Loomans

and van Schijndel 1998). The repeatability was within 2% for the 0.1 - 0.5 m/s velocity range. Comparison with another anemometer indicated a maximum deviation of 3%.

The numerical model of the anemometer has been compared with the measurement results as obtained in *Step 3* (Figure 3.6a). Figure 3.7 shows the numerical results. The calculated deviation is a factor 2.5 smaller than in the experiments, however the course of the velocity correction curve is similar. The difference is explained from uncertainties in the applied model resistors and from deviations in the actual heat transfer characteristics at the sensor (e.g., contamination). The model however is regarded suitable for a general qualitative parameter study. Moreover, each anemometer has unique characteristics which require individual and regular calibration. Substitution of the calibration relation by a numerically determined relation therefore is not possible.

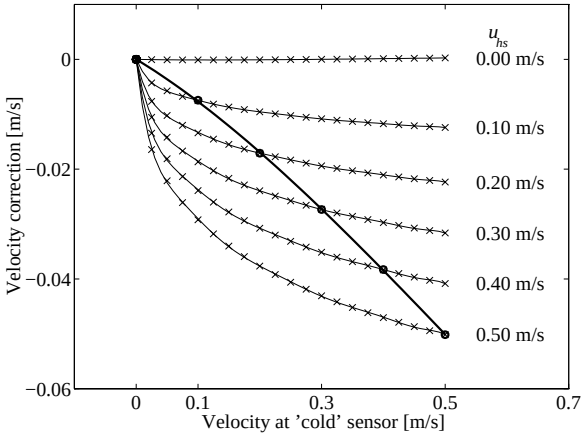

Figure 3.7. Simulated velocity correction for a varying velocity at the 'cold' sensor (Step 3, Figure 3.5), starting from u_{cs} = 0 m/s ([×] *simulations,* [**o**] $u_{hs} = u_{cs}$, [| | | |] *curve fit* $u_{hs} = u_{cs}$*).*

(2) *Air temperature gradient over heated and 'cold' sensor* - The hot sphere anemometer is temperature independent as the 'cold' sensor represents the ambient temperature. An error is introduced when the air temperature at the separate sensors differs. The calibration set-up is not able to reliably introduce an air temperature difference over the sensors. The influence of the temperature gradient therefore has been investigated numerically instead.

Figure 3.8 indicates the simulated velocity correction that should be introduced when the temperature at the 'cold' sensor deviates from the constant ambient temperature of 22°C at the 'heated' sensor. A 1°C higher air temperature at the 'cold' sensor overestimates the actual velocity by nearly 10%. Therefore, if possible the temperature gradient over the sensors should be limited.

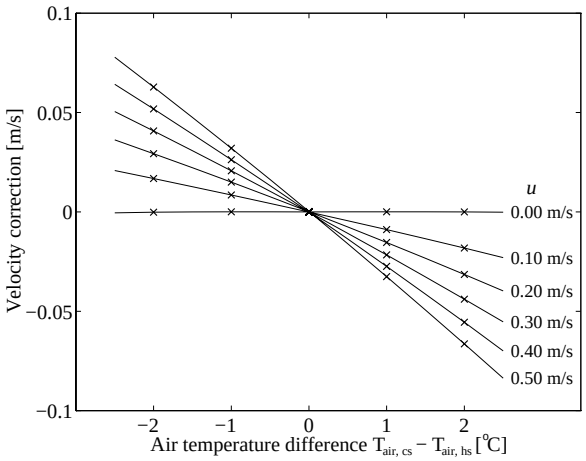

Figure 3.8. Velocity correction for an air temperature gradient over the heated and the 'cold' sensor at different velocities, u, ([×] simulations; $T_{air} = T_{mrt} = 295$ K).

Melikov et al. (1997) present results which indicate that the maximum air temperature gradient over 0.02 m can be as high as 0.3°C due to turbulent fluctuations. As the time constant of the 'cold' sensor is in the order of 8 to 10 seconds (Dantec 1985), rapid temperature fluctuations may result in a similar error.

(3) *Directional sensitivity* - The sensor is omni-directional. Directional sensitivity exists however due to the probe support. Measurement data have been obtained with the described calibration set-up for a parallel (→ —) and perpendicular (→ | ; corrected) approach. Figure 3.9 indicates that the relative deviation can vary up to 14% at ~0.22 m/s. If the zero-point reading is not taken as the bridge voltage reference, the deviation can increase to 20%. The bridge voltage reference is the bridge voltage at zero velocity.

The directional sensitivity is partly explained from the fact that in the parallel approach the 'cold' sensor is in the wake of the heated sensor and, therefore, less exposed to the flow and located in a higher air temperature (with reference to the velocity and temperature gradient results). The deviation indicates that the calibration position preferably should correspond with the flow direction at which the anemometer is approached.

(4) *Radiation* - The influence of radiant heat transfer normally is neglected as it is incorporated implicitly in the calibration procedure. The sensor is finished off with a film of nickel that is assumed to have a radiant emissivity factor ε = 0.2. Measurements at a 5°C higher mean radiant temperature (T_{mrt}) and subsequent simulations indicate that the influence is negligible (< 0.1%/K).

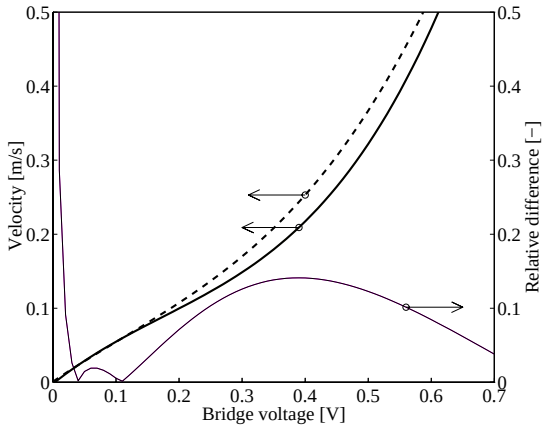

Figure 3.9. Directional sensitivity to the flow approach [left axis] + relative measurement difference between a perpendicular and a parallel approach [right axis] ([▏▏▏▏] *perpendicular flow* (→ ▏), [▏ ▏ ▏] *parallel flow* (→ —), [————] *relative difference).*

(5) *Relative humidity* - Schubauer (1935) measured velocity errors up to 6% when varying the relative humidity (φ) between 25% and 70%. In the described calibration set-up a low relative humidity prevails (φ ≈ 1%), whereas the sensor will be applied under normal conditions (φ ≈ 30…70%). Comparison of calibration results for a varying flow rate at the sensor, at low relative humidity (φ ≈ 1%) and at higher relative humidity (φ ≈ 30% (high velocities) to φ ≈ 80% (low velocities)) gave negligible differences. The influence of humidity on the measurement results therefore can be disregarded (<< 0.1 % per % relative humidity).

(6) *Buoyancy* - The sensor of a hot wire anemometer generally is heated well over 100°C above the mean flow temperature. At very low velocities therefore a mixed-flow regime exists due to self-heating. Results of Stengele (1993) indicate that free convection is noticeable up to 0.017 m/s and almost independent of the wire temperature. In Bruun (1995) results are summarised that indicate that the influence of free convection is negligible above 0.015 m/s.

The hot sphere anemometer is designed such that the over-temperature of the heated sensor is approximately 30°C above the air temperature. Despite a lower over-temperature, due to the dimensions of the sensor a larger heat dissipation results than for the hot wire anemometer. Therefore, at velocities below 0.05 m/s multivalent readings are found as a result of the present mixed-flow regime. At no flow conditions the sensor creates velocities of ~0.03 - 0.05 m/s when placed vertically (Dantec 1985).

Measurements at the exit plane of a larger pipe (d = 0.06 m; $u_{hs} = u_{cs}$) with an upward directed flow resulted in an amplification of the signal obtained under horizontal conditions. At 0.05 m/s the velocity was measured to be approximately 0.01 m/s too high. This overestimation reduced to 0.007 m/s at a velocity of 0.1 m/s and remained relatively constant up to 0.2 m/s. Higher velocities than 0.2 m/s have not been measured due to the limitations of the calibration set-up. The influence of buoyancy on the measurement signal will reduce further at higher flow velocities. For well observable upward directed flows in the 0.05-0.25 m/s flow range a correction of the measured velocity may be appropriate. Calibration of the anemometer in the position and flow direction as expected in the measurement presents a more solid alternative.

(7) *Turbulence intensity* - The hot sphere anemometer is designed to measure absolute values. This leads to an overestimation of the mean velocity and an underestimation of the turbulence intensity if the fluctuating velocity vector has positive and negative values, as

$$\frac{1}{T_s^{tot}} \int_0^{T_s^{tot}} |\vec{u}| dt > \left| \frac{1}{T_s^{tot}} \int_0^{T_s^{tot}} \vec{u} dt \right|, \tag{3.7}$$

where T_s^{tot} is the total sampling time and $\vec{u}$ the fluctuating velocity vector. Assuming that the measurements correspond to a Gaussian probability distribution, the results are affected at a turbulence intensity higher than 30% (see Figure 3.10).

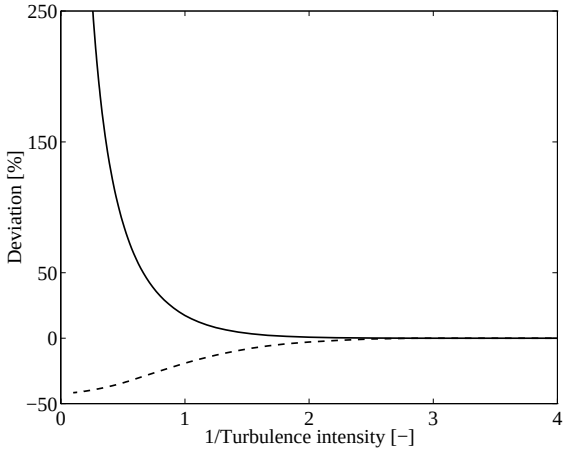

Figure 3.10. Deviation in the measured mean velocity and turbulence intensity as a function of the reciprocal of the turbulence intensity, due to the omni-directional velocity registration ([| | | |] mean velocity, [| | |] turbulence intensity).

3.6.3 Transient conditions

The indoor air flow normally is characterised by large fluctuations in the average flow velocity (see Figure 3.1a). The frequency distribution of the turbulent indoor air flow has not been measured extensively. Melikov et al. (1990) concluded that the fluctuations appear in the low frequency range (0.01 - 20 Hz) and that the spectrum is a function of the measurement position in the room and the type of ventilation and/or heating system that is used.

Due to thermal inertia of the sensor and the characteristics of the electrical circuit, fluctuations cannot be measured at high frequencies. The amplitude of the velocity fluctuation is attenuated and, as a result, the measured turbulence intensity will underestimate the actual value. If this amplitude damping however is taken into consideration the actual turbulence intensity can be determined from the measurement results via the amplitude transfer function (H(*f*)) of the system. The amplitude damping, *r* [dB], is defined as:

$$r[\mathrm{dB}] = 10^{10}\log\left(r[-]\right), \tag{3.8}$$

where *r*[-] is determined from the ratio,

$$r[-] = \overline{\left(\frac{\left(u_{\max} - u_{\min}\right)_{\text{measured/simulated}}}{\left(u_{\max} - u_{\min}\right)_{\text{actual}}}\right)}. \tag{3.9}$$

The numerical model, introduced in Chapter 3.6.1, has been applied to determine the (non-linear) response of the anemometer, ergo the amplitude damping. The measurement of the dynamic response has been performed in a specially designed wind tunnel configuration (Loomans and van Schijndel 1998). Figure 3.11 presents the input signal and the measured response of the anemometer for two transient situations; one for a 13.1 sec periodical movement and one for a 3.4 sec periodical movement of the sensor, at a given base wind tunnel velocity. In Figure 3.11 the simulated response of the numerical model to the input signal is also shown. The difference to the input signal for simulation and measurement is of the same order, given the measurement accuracy at low velocities. For the 3.4 sec periodical movement, the model somewhat overestimates the measured amplitude damping of the anemometer. Given the restrictions and the accuracy of this type of measurements, the validity of the numerical model is indicated. The results show that the damping is very significant at frequencies in the order of 1 Hz and higher. This is in the range of fluctuations that can be found indoors.

In Figure 3.12 simulated amplitude transfer functions for different harmonic input signals, with the indicated amplitude and mean velocity, are presented for the 0.03 - 10 Hz

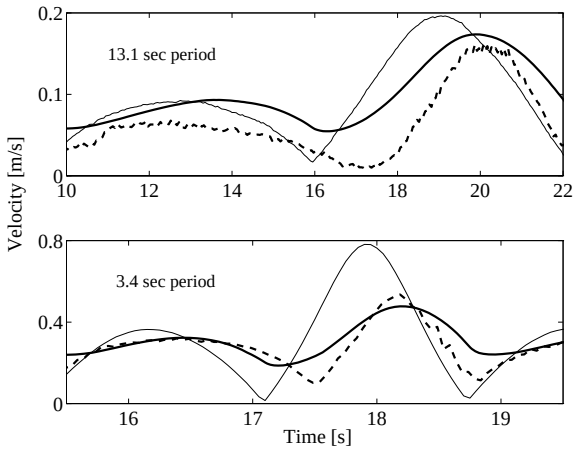

Figure 3.11. Measured and simulated response to an input signal with a 13.1 sec periodical movement and a 3.4 sec periodical movement of the sensor at a given mean velocity ([———] input, [\| \| \|] measurement, [\|\|\|\|] simulation).

frequency range. Typical response curves for a system with two time constants can be found if 5% of the total heat capacity of the sensor is allotted to the surface shell and 95% to the kernel (see Appendix B). These results are in agreement with Dantec (1985).

The amplitude transfer function is a function of the mean velocity and indicates the non-linear behaviour of the system. The sensitivity of the transfer function to the amplitude (not shown in Figure 3.12) is about an order of magnitude smaller. The non-linearity is caused by the heat transfer coefficient, the omni-directional design (not modelled) and the electrical

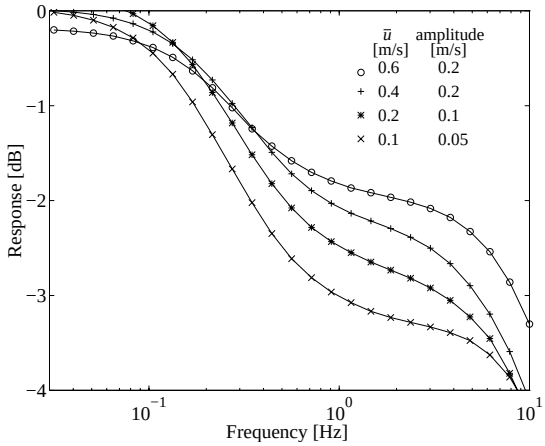

Figure 3.12. Simulated amplitude transfer functions for different harmonic input signals with the indicated mean velocity and amplitude.

circuit. Results described by Popiolek et al. (1996) confirm the non-linear response of this type of anemometer.

For stationary turbulent flows a correction for the dynamic response of the anemometer is possible. For a given mean velocity and a well chosen characteristic amplitude (e.g. σ_u) a single amplitude transfer function can be determined from which compensation then is calculated by performing Fourier analysis. A more accurate compensation is possible when also the sensitivity to the amplitude is taken into account. For unsteady state turbulent flows a single transfer function cannot be obtained.

3.6.4 Conclusions with regard to the hot sphere anemometer

From the investigation of the hot sphere anemometer the following conclusions are drawn:

1. The described laminar pipe flow calibration set-up can replace a low velocity wind tunnel calibration facility when the effect of the no flow condition at the 'cold' sensor is corrected for.
2. The described corrections and systematic errors indicate the restrictions of the anemometer. The inaccuracy of the system therefore remains high (~30% [0.05 m/s] to ~10% [0.25 m/s]) and is highly dependent on the utilisation.
3. Damping already arises in the low-frequency range (0.1 - 1 Hz) leading to an underestimation of the actual turbulence intensity. In this frequency range the average damping is simulated to be about 20%. The hot sphere anemometer that has been under investigation is known to have a relative fast response. The same type of anemometer also has been used in the research that lead to the definition of the percentage of dissatisfied due to draught (*PD*; Fanger et al. 1988, see Chapter 2.2.2). The sensitivity of the *PD*-value to the turbulence intensity becomes significant at higher velocities. An underestimation of the turbulence intensity by 20% at $\overline{u}$ = 0.20 m/s and *TI* = 40% results in an underestimation of the *PD*-value by 10%. Therefore, a system that is able to measure (e.g. LDA) or simulate (CFD) the actual turbulence intensity will overestimate the actual *PD*-value. Furthermore, other hot sphere anemometers are available that operate in a similar way as the described anemometer. The time constants of those systems, e.g. Crommelin and Dubbeld (1976), typically are larger due to the design and construction, the response therefore is slower. The damping then will result in an underestimation of the turbulence intensity and therefore of the *PD*-value.

3.7 PARTICLE TRACKING VELOCIMETRY (PTV)

Extensive information on the (instantaneous) spatial structure of the flow cannot be obtained by point measuring devices as the hot sphere anemometer or LDA. Two- or three-dimensional quantitative information on the flow pattern is only possible when the flow is visualised and the changes in the visualised flow pattern are monitored. Different techniques are available which utilise this type of monitoring. They can be subdivided with respect to the concentration of tracer particles used (Westerweel 1993).

With Particle Tracking Velocimetry (PTV) individual particles are tracked on their path through the flow. These individual particles should be small and preferably be neutrally buoyant, i.e., the particle has the same density as the fluid. Two-dimensional images of the particles in the fluid are obtained by a light sheet. The motion of the particles in the constant intensity light sheet, for PTV, usually is recorded with a video camera. The separate particles are located in each successive video image and related to the previous image in order to determine the displacement. A small displacement can be determined with more certainty and the accuracy therefore increases at lower velocities. The velocity is determined from the displacement of the particles over a certain time interval. As the number of seeded particles is low, the velocity only can be determined at positions where the particles are present.

Quantitative visualisation techniques for the measurement of indoor air flow have been introduced by, among others, Besse (1992), Scholzen (1997) and Linden et al. (1998). These researchers used stereo-photography which allows the velocity to be determined in the three dimensions of the flow field. Given the shutter time and assuming a constant velocity vector the instantaneous velocity can be calculated. Müller and Renz (1998[b]) introduced a different technique to determine three dimensional information on the velocity vector. Instead of a single light sheet, Müller and Renz included depth information via overlapping colour coded light sheets. Both techniques are referred to as Particle Streak Velocimetry (PSV). Recently results obtained with a variant of the Particle Image Velocimetry (PIV-) and the PTV technique have been presented by Kaga et al. (1996). Smoke was applied as tracer and smoke patterns were identified in sequential images.

The PSV-technique is less interesting for the determination of the mean and turbulent indoor air flow characteristics as only instantaneous results can be obtained. When the image frequency is increased to frequencies used with PTV, the differences between the two techniques more or less vanish. The PSV-technique then approaches the PTV-technique. Currently the maximum frequency with which a picture can be processed is one minute

(Müller 1998). The application of pattern tracking is attractive but may find its restrictions in the resolution of the flow pattern. Therefore, in addition to the above mentioned tracking techniques, the actual PTV-technique is investigated for the determination of the average and transient characteristics of the indoor air flow pattern.

3.7.1 Measurement set-up

The set-up for a PTV-measurement is shown in Figure 3.13. In air, helium filled soap bubbles are used as tracer particle. In order to attain neutral buoyancy in air, the diameter of the soap bubbles approximately should be 0.003 m (film thickness ≈ 0.5 μm (Hale et al. 1971); d_p = 0.0029 m), when it is filled with 100% helium. These bubbles are produced by a special bubble generator and have an average life span of several minutes. A small light sheet with constant intensity is projected through the flow, thereby showing a two-dimensional image of the particle movement in a specific slice of the flow. The displacement of the particles in the light sheet is recorded by a S-VHS video camera (512 × 512 pixels). The recorded video images are analysed using a video tape recorder, frame grabber, computer and software.

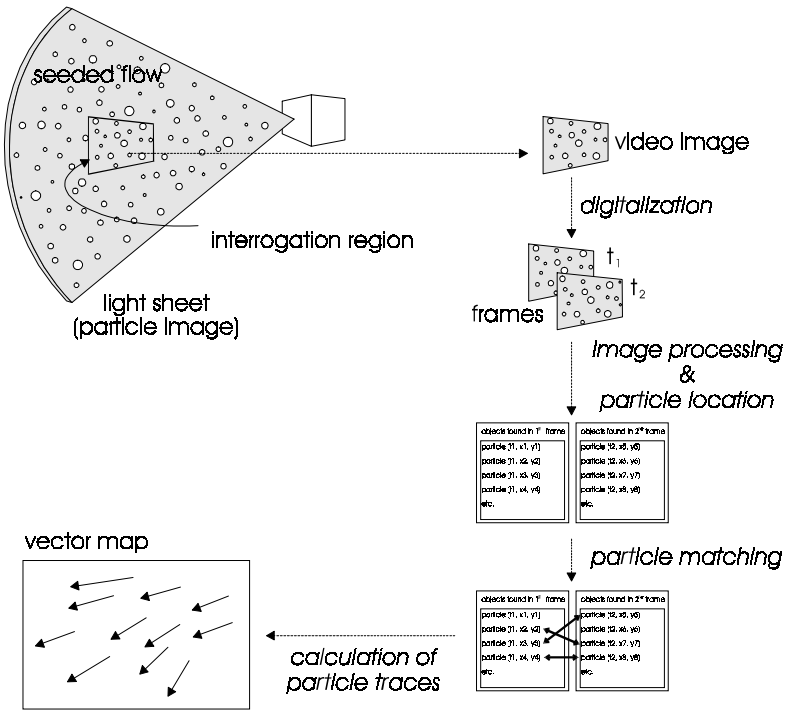

Figure 3.13. Principle of a PTV-system and measurement set-up.

At equally spaced time intervals (25 Hz or 50 Hz) images are grabbed. Individual images of tracer particles are identified and located via intensity differences between pixels representing a particle or the background. A matching algorithm is used to determine the most likely combination between particles in image n and n+1. The software (Dalziel 1995) uses a so-called *cost function* which indicates the probability that two particles in two consecutive frames are one and the same. The basic cost function of an association (B_{ij}) between particle image p_i at time $t = t_n$ and particle image q_j at time $t = t_{n+1}$ is calculated from

$$B_{ij} = \left| x_i + \gamma u_i \left(t_{n+1} - t_n \right) - x_j \right|^m , \tag{3.10}$$

where x_i is the position of particle p_i at t_n, x_j the position of particle q_j at t_{n+1}, u_i the velocity of particle p_i at t_n, γ is a weighting function (typically unity) and m a positive value. For m = 1, the minimum acceleration criterion is applied. Then, B_{ij} is the distance between the position of particle p_i at t_{n+1}, based on its velocity at t_n, and the position of particle q_j at t_{n+1}. The cost value of B_{ij} is low when particle q_j is close to the estimated place of p_i. Additional cost parameters comprise criteria which set a limit to, e.g., the ellipticity, size and average intensity. Not complying with the criteria set will result in a more difficult matching process for that specific particle. Finally, the velocity can be extracted from the Lagrangian path via

$$u_p = \frac{x_{q_J} - x_{p_I}}{\Delta t} + \mathrm{O}(\Delta t), \tag{3.11}$$

where u_p is the particle velocity, Δt the time step and O(Δt) higher order terms.

The accuracy of a PTV-experiment is influenced by the criteria that are set for the cost function. In case these criteria are set too broadly, non-related particles may be matched, resulting in an incorrect particle path and particle velocity. Furthermore, accurate tracking requires that the tracer particle is represented by 3×3 to 4×4 pixels. Theoretically one pixel may be sufficient, but the location of the particle then becomes more ambiguous (Loomans et al. 1996). Given the particle size and the camera resolution, the interrogation region therefore is restricted to 0.5×0.5 m^2.

3.7.2 Measurement accuracy

The quality of the tracking is primarily determined by the degree in which the particle follows the fluid. Under the assumptions that the size of the particle is small compared to the smallest wave length present in the turbulence, that the particles do not interact with each other and that the bubble remains spherical, the motion of a particle in an accelerating fluid is calculated from (Hinze 1975; Auton et al. 1988)

$$\frac{\pi d_p^3}{6}\rho_p \frac{du_p}{dt} = \frac{1}{2}\rho_p c_w \frac{\pi d_p^2}{4}\left|u_f - u_p\right|\left(u_f - u_p\right) + \frac{\pi d_p^3}{6}\rho_f \frac{Du_f}{Dt}$$
$$+\frac{1}{2}\frac{\pi d_p^3}{6}\rho_f\left(\frac{Du_f}{Dt} - \frac{du_p}{dt}\right) + \frac{3}{2}d_p^2\sqrt{\pi\rho_f\mu}\int_{t_0}^{t}\frac{\frac{du_f}{dt'} - \frac{du_p}{dt'}}{\sqrt{t-t'}}dt' + F_e, \qquad (3.12)$$

where the left-hand side term represents the force to accelerate the particle. The first term on the right-hand side is the viscous resistance force and the second term is due to the pressure gradient in the fluid surrounding the particle, caused by the acceleration of the fluid. The third term is the force to accelerate the 'added' mass of the fluid surrounding the particle. The fourth term is the Basset-history integral and the fifth term is the external force (e.g. buoyancy). In Equation 3.12, Du_f/Dt denotes the total derivative.

Few results are available on the tracking characteristics of a helium filled soap bubble in air. Kerho (1989) analysed the tracking characteristics of a helium filled soap bubble for a high velocity flow around an air foil. For an air velocity of ~16 m/s and $\rho_p/\rho_f \approx 0.6$ the time constant (τ) of the soap bubble for the described experiments could be estimated at $\tau <$ 0.001s.

For a fluid at rest, without external forces, Equation 3.12 changes to the Basset-Boussinesq-Oseen-equation when gradients in the flow are neglected. This equation has been solved numerically to estimate the time constant for a helium filled soap bubble with an initial velocity that is released in stagnant air (see Figure 3.14; the velocity is normalised to the

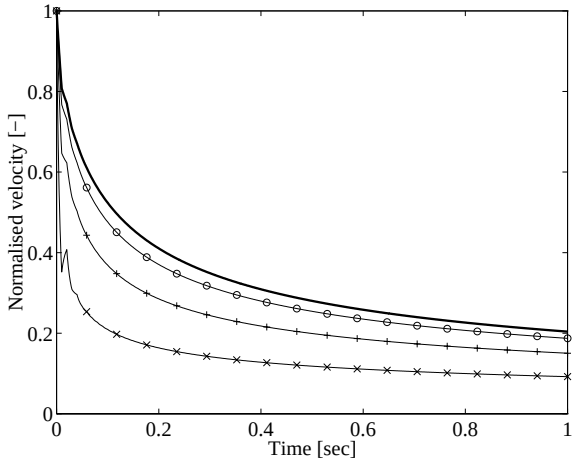

Figure 3.14. Deceleration of a neutrally buoyant particle (d_p = 0.0029 m) with an initial velocity ($u_{p,0}$) in a stagnant fluid ([ ] Stokes, [———] Klyachko, [o] $u_{p,0}$ = 0.01 m/s, [+] $u_{p,0}$ = 0.10 m/s, [x] $u_{p,0}$ = 1.00 m/s; velocity normalised to $u_{p,0}$).

initial velocity). The model was validated with results as described in Clift et al. (1978). Using Stokes' law for the determination of the drag coefficient ($Re_d < 1$), a density ratio $\rho_p/\rho_f = 1$ and $d_p = 0.0029$ m this results in $\tau = 0.26$ s. At higher initial velocities the empirical relation as proposed by Klyachko (in Fuchs 1964) is applied: $c_w = (24 + 4Re_d^{2/3})/Re_d$, $3 < Re_d < 400$, where Re_d is based on the fluid-particle velocity difference. The time constant is seen to reduce further. However, due to the Basset term the deceleration of the particle does not follow an exponential path.

The calculated time constant applying Stokes' law can be regarded as the longest time constant for the investigated neutrally buoyant soap bubble in an air flow. When $u_f - u_p = 0$ m/s, the neutrally buoyant particle will follow the fluid flow exactly as Equation 3.12 reduces to $du_p/dt = du_f/dt$. The calculated time constants indicate that most fluctuations in the indoor air flow will be tracked when (nearly) neutrally buoyant tracer particles are applied. The diameter of the above applied particle is in the order of the Kolmogorov length scale for indoor air flow, which however can be smaller than 0.1 mm (Murakami and Kato 1989). A smaller particle will reduce the interrogation region further. A larger neutrally buoyant particle will have a longer time constant (at $d_p = 0.01$ m, $\tau = 3.2$ sec when Stokes' law is applied). Furthermore, a larger particle will not be able to follow the movement of the smallest eddies.

External forces that change the particle path of the soap bubble from the streamline of an air flow are, besides buoyancy forces, lift forces and radiometric forces due to thermophoresis or photophoresis. The settling velocity ($u_{p,y}$) due to buoyancy forces, in the direction of the gravity (g), is calculated from

$$u_{p,y} = \sqrt{\frac{4}{3}\frac{d_p g}{c_w}\frac{\rho_p - \rho_f}{\rho_f}}\,. \qquad (3.13)$$

At small particle-fluid density differences the settling velocity already may obscure the air flow velocity component in the direction of the gravity; given $d_p = 0.0029$ m and $\rho_p - \rho_f = 0.1 \cdot \rho_f$ this results in $u_{p,y} = 1.8 \cdot 10^{-2}$ m/s. When the particle-fluid density difference is constant for all tracer particles this may be corrected within the matching algorithm. Lift forces appear perpendicularly to the velocity vector at a velocity gradient over the particle, as a result of a present slip velocity (Saffman 1965). Indoor air flow velocity gradients generally remain relatively small and the lift force normally can be neglected compared to the buoyancy force. Thermophoresis and photophoresis (Fuchs 1964) are a result of temperature gradients in the flow or of one-sided heating up of the tracer particle because of radiant heat transfer. Due to the relative small temperature gradients and low heat rates for normal indoor air flows, radiometric forces are negligible when compared to the buoyancy force.

From the theoretical analysis the PTV-technique thus is found suitable for velocity measurement at indoor air flow when a (nearly) neutrally buoyant tracer particle is applied.

3.7.3 Results

In Loomans et al. (1996) examples are given of PTV-results as obtained for forced and free convection flows. These results have been obtained applying the set-up as shown in Figure 3.13. A further example is given of a combined convection flow pattern. In Figure 3.15 the experimental set-up is schematised. In a large climate chamber a heat source (vessel; h = 0.58 m, d = 0.38 m, Q = 200 W) is placed symmetrically at 0.6 m distance from a rectangular displacement ventilation unit (h = 0.35 m, w = 0.95 m, $\dot{V}$ = 0.036 m^3/s; Fransen 1997) with an isothermal supply flow. A light sheet is projected between the heat source and the unit via a mirror positioned in the plenum. About 1000 lux is required for optimum contrast. The tracer particles (helium filled soap bubbles) are introduced in the displacement ventilation unit. The size of the perforations at the supply grille (0.0075 × 0.015 m^2) allow the tracer particles to pass the supply grille. As within the unit guiding paddles are placed, the soap bubbles are filtered. Only the (nearly) neutrally buoyant particles will leave the displacement ventilation unit due to this filtering.

In Figure 3.16a and b the results are shown for a PTV-experiment where the heat source was turned off (a) and an experiment where the heat source was on (b). In both cases the flow has been analysed for 30 seconds. On average 31,000 tracks were found. The results were filtered on spurious vectors and averaged over a grid (20×14). For each grid cell a minimum of 40 tracked values have been used to obtain the mean velocity component.

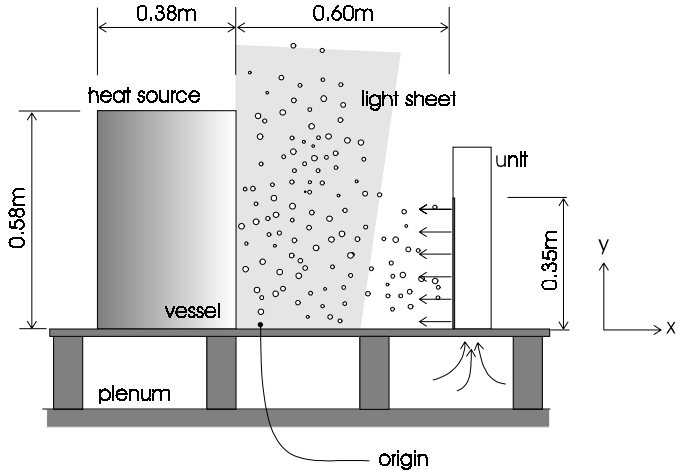

Figure 3.15. Schematised set-up PTV experiment of combined forced and free convection flow.

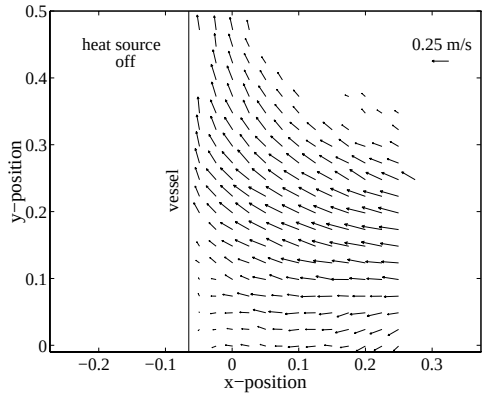

Figure 3.16a. Velocity vector pattern from PTV-experiment, heat source off.

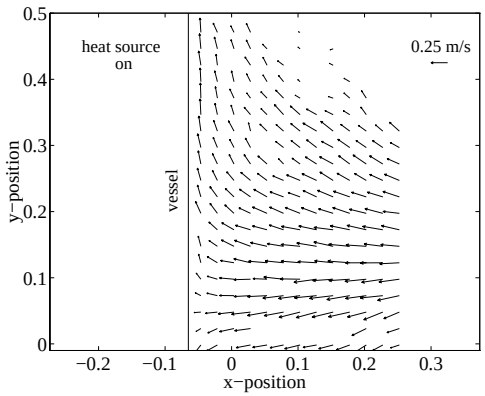

Figure 3.16b. Velocity vector pattern from PTV-experiment, heat source on.

Subtle differences are found when the two results are compared. Due to the size of the heat source and the width of the supply, the flow is forced over the vessel also when the heat source is turned off. The flow near the floor is decelerated due to the stagnation point at the cylindrical obstruction. When the heat source is turned on, the flow direction towards the vessel indicates the stagnation point less clearly. Due to the free convection flow at the heat source (estimated at 0.008 m^3/h at 0.5 m height; Skistad 1994) the flow close to the floor presumes a more horizontal direction. Near the vessel the flow has a more profound vertical direction then in case the heat source is turned off.

The indicated subtle differences would be very difficult to find using a point measuring device. From this type of PTV-results it is also possible to obtain an indication on the turbulence characteristics, taking into account the restricted duration of the measurements and the limited number of tracks that have been used.

3.7.4 Conclusions with regard to Particle Tracking Velocimetry

From the investigation into the PTV-technique the following conclusions have been drawn.

1. The theoretical analysis indicates the applicability of the helium filled soap bubble as tracer particle for particle tracking at an indoor air flow. The principle as used for PTV is suitable for the measurement of indoor air flow patterns.
2. The influence of the buoyancy force on the particle path requires that the particle-fluid density difference is limited and constant for all tracer particles. The homogeneous production of sufficient, (nearly) neutrally buoyant helium filled soap bubbles however is difficult (Loomans et al. 1996). This fact and the surface contamination require the replacement of the helium filled soap bubble by an equally sized non-staining tracer

particle that can be produced with a constant density. A usable substitute tracer particle for the helium-filled soap bubble is not yet available.

3. The described PTV set-up allows the two dimensional registration of the three dimensional flow pattern and the derivation of the accompanying statistical characteristics. Due to the camera resolution and the image-requirements for accurate particle tracking, the interrogation region remains restricted to maximum 0.5×0.5 m^2, when helium filled soap bubbles are used. For smaller particles this region will reduce further. The interrogation area is too small, a higher camera resolution should be applied to allow enlargement of the region.
4. Despite the described merits of the PTV-technique, the demerits summarised above currently restrict the practical application considerably. Improvements especially are required in the applied tracer particle and tracer particle production. Therefore, in this research the hot sphere anemometer has been preferred over the PTV-technique.

3.8 SUMMARY

1. A comprehensive literature review on the measurement of indoor air flow indicates a number of in-situ and full-scale climate chamber experiments. Most described measurements have been performed with the hot sphere anemometer. For comparison with numerical simulation techniques the indoor air flow problem has been mainly represented by simplified models of the physical indoor environment. The number of full-scale measurements with realistic occupation of the room is very restricted. Furthermore, there is a need for additional full-scale experimental results in which contemporary ventilation techniques are applied.
2. The accurate measurement of the mean and turbulent characteristics of the indoor air flow is very difficult. Given the required accuracy, the sample and measuring time are a function of the flow and may vary considerably throughout the flow.
3. Of the available measurement principles and techniques most techniques are not applicable for the determination of the indoor air flow characteristics (velocity: 0…1.0 m/s; turbulence intensity: >10 %). The omni-directional hot sphere anemometer and the Particle Tracking Velocimetry (PTV)-technique presently are, respectively, the most practical and in principle the most promising technique for the measurement at indoor air flow.
4. The accuracy of the described hot sphere anemometer is highly dependent on the similarity between measurement situation and calibration conditions. The measurement error can mount up to 10% or higher in the 0…0.5 m/s velocity range, not taking into account the specifications of the anemometer and the calibration accuracy. The amplitude damping in the measurement of a fluctuating velocity already is significant in

the lower frequency range (0.1…1 Hz). Simulations show that the amplitude in that range is damped up to 20%. Hence, the high frequency turbulent characteristics of a flow cannot be measured reliably with the hot sphere anemometer. Fanger et al. (1988) used a similar anemometer to the one under investigation for the derivation of the draught discomfort sensitivity to the turbulence intensity. This means that sensors with different dynamic characteristics will measure a different *PD*-value.

5. Theoretical analysis supports the applicability of the (nearly) neutrally buoyant helium filled soap bubble ($d_p \approx 0.003$ m) for application as tracer particle in the Particle Tracking Velocimetry (PTV-) technique. The applied PTV-set-up can determine the averaged two-dimensional velocity vector field in a plane of the flow, taking into account the necessary tracking time. The practical application of the PTV-technique however is very much restricted through the requirement of a constant and sufficient production of (nearly) neutrally buoyant particles at constant density. Preferably the helium filled soap bubble should be replaced by a better verifiable tracer particle. Furthermore, the camera resolution should be increased to allow a larger interrogation area to be monitored.

Chapter 4

THE SIMULATION OF INDOOR AIR FLOW

4.1 INTRODUCTION

Calculating the flow field is attractive in terms of time and costs given the difficulty to determine the flow field experimentally (see Chapter 3). Numerical models have been developed to allow the study of the stationary and transient characteristics of an air flow pattern with regard to energy use, indoor air quality and thermal comfort. In this introduction a short summary of model concepts is given.

A wide range of models is available. Semi-empirical models for the (non-) isothermal jet as presented by Regenscheit (1959) and Grimitlin (1970) allow the calculation of a jet extending into a room. These models are based on the boundary layer and turbulence hypotheses. Mass, momentum and energy conservation also forms the basis for semi-empirical models that have been derived to calculate the characteristics of a displacement ventilation flow pattern, especially the convection flow from heat sources (Morton 1956; Mundt 1996) and the vertical temperature and contaminant distribution (Krühne 1995). These models present relative simple steady state solutions of the flow field characteristics in order to determine thermal comfort conditions and contaminant distribution.

The applicability of the semi-empirical relations often is restricted. For more detailed information on the flow field the full Navier-Stokes equations and the equation for conservation of heat must be solved. This technique is applied in Computational Fluid Dynamics (CFD). In CFD the equations have been discretised in order to solve the flow field numerically. Nielsen (1974) was one of the first to apply CFD for the numerical prediction of the indoor air flow. Since then the technique has evolved and numerous results have indicated the wide-spread applicability of CFD for the simulation of an indoor air flow pattern. The developments in computer capacity have further enhanced the application of this type of simulations. CFD has become an increasing important tool in the prediction of

the stationary indoor air flow pattern. Experience however also indicates the limitations of the current available CFD-methods, with respect to, e.g., the reliability and the sensitivity, and the necessity to validate CFD-results of typical indoor air flow patterns (Chen and Jiang 1992; Chen 1997; Baker et al. 1997).

The above discussed flow modelling is focussed on stationary characteristics with a view to assess indoor air quality and thermal comfort. Analysis of the energy use of a room or a building however requires information on the transient characteristics of the indoor climate. In building simulation programs (e.g. ESP-r (Clarke 1985)) the room air flow normally is modelled as a single node in an air flow network, assuming a fully mixed room. As a result the effect of thermal stratification within the room on the energy use or the thermal comfort is not taken into account. A more accurate representation is possible when the room is divided into a limited number of fully-mixed sub-zones (Hensen et al. 1996). Though incorporation in a whole building air flow network is straightforward, the inter zonal flow characteristics must be pre-defined. A more rigorous analysis is possible when a CFD-program is integrated in the network model. Given the geometry and grid distribution, the flow problem then is solved from the boundary conditions presented by the nodal network.

Due to the complexity and high computing demands CFD is applied in various ways in building simulation and cooling load programs. For specific air supply systems Chen (1988) and Niu (1994) determined relations for the temperature distribution in the room, as a function of the internal heat load and the ventilation rate, from a range of simulated air flow patterns using CFD. Such a relation then was incorporated in a cooling load program for further calculations. A similar approach was adopted by Peng (1996). A fully integrated CFD-program in a building simulation program has been described by Negrão (1995, 1998). Negrão indicated the potential of the combined approach of CFD and whole building simulation. The main restrictions lie in the difficult convergence of the combined flow network and CFD-domain and the high computational effort required.

From the above it can be concluded that CFD in principle is applicable for unsteady state indoor air flow problems. Nevertheless, up to now only the CFD-based investigation of steady state flow and heat transfer problems in the indoor environment has proven useful and an important extension to the available options. The validity of CFD-results however remains an issue of concern given the necessary discretisation and the numerical input parameters (Whittle 1991; Chen 1997). Chen (1997) indicates the necessity of an experimental validation of a flow model. The literature review described in Chapter 3 concludes that the number of full scale measurements of realistic indoor air flow patterns however is restricted.

This chapter briefly describes the main mathematical and numerical characteristics of a CFD fluid flow simulation. Furthermore, recent developments in relation to the simulation of indoor air flow will be pointed out. The second part of this chapter indicates the important restrictions of CFD by means of a case study for an office equipped with a displacement ventilation system. Finally, a comparison is made between different type of grid topologies that can be applied within the CFD-environment.

4.2 THE MATHEMATICAL MODEL

4.2.1 Governing equations and turbulence modelling

A flow field can be described by the conservation of mass, momentum and energy. Given the boundary conditions, the resulting flow pattern is determined by solving the combined Navier-Stokes and energy or any other scalar equations (Equation 4.1 to 4.3).

$$\frac{\partial \rho}{\partial t} + \frac{\partial}{\partial x_i}(\rho u_i) = 0 \,, \tag{4.1}$$

$$\frac{\partial}{\partial t}(\rho u_i) + \frac{\partial}{\partial x_j}(\rho u_i u_j) = -\frac{\partial p}{\partial x_i} + \frac{\partial}{\partial x_j}\left[\mu\left(\frac{\partial u_i}{\partial x_j} + \frac{\partial u_j}{\partial x_i}\right)\right] + \rho g_i \,, \tag{4.2}$$

$$\frac{\partial}{\partial t}(\rho H) + \frac{\partial}{\partial x_i}(\rho u_i H) = \frac{\partial}{\partial x_i}\left[\frac{k}{c_p}\frac{\partial H}{\partial x_i}\right] + S_H \,, \tag{4.3}$$

where, u_i is the velocity component (u,v,w), p is the pressure, H the enthalpy and S a source term. The diffusion term is indicated by the kinematic viscosity μ, the thermal conductivity k and the specific heat c_p. The time is indicated with t, x_i is the coordinate axis (x,y,z), ρ is the density and g_i is the gravitational acceleration.

For the prediction of the turbulent flow characteristics different options are available. *Direct Numerical Simulation* (DNS) calculates the turbulent motion by solving the Navier-Stokes equations. A fine grid and a small time step are required to determine the flow field up to the smallest length scale (in indoor air flow fields the scale can be less than 0.1 mm (Murakami and Kato 1989)). The number of required grid cells (in the order of $Re^{9/4}$ (Nieuwstadt 1992)) and the limitations in computer capacity currently restrict the application of DNS to flows with a moderate Reynolds number. *Large Eddy Simulation* (LES) has been developed in order to reduce the computer capacity. In LES the small-scale eddies (see Chapter 3.2) are removed from the turbulent flow via filtering. As a result only the large-scale eddies are fully resolved. The effect of the small-scale eddies on the

turbulent flow field is modelled. This approach arises from the knowledge that the large eddies of the macro-structure are mostly anisotropic and depend on the geometry of the flow field (Eggels 1994). The small eddies of the micro-structure on the other hand are considered to be close to isotropical and less dependent on the flow geometry, given the energy cascade and 'the return to isotropy'. Some LES-results for a simple indoor air flow geometry have been presented by Davidson and Nielsen (1996) and Bennetsen et al. (1996). A good agreement with experimental results has been obtained. The need to simulate the flow field three dimensionally, at a sufficient fine mesh and time step to capture all the essential spatial and time scales, however still requires a relative large amount of computing time. Therefore, *turbulence models for the mean turbulent flow* have been developed that calculate the statistical characteristics of the turbulent motion by averaging the flow equations over a time scale much larger than that of the turbulent motion. This approach assumes that for many engineering flow problems knowledge of the high frequency fluctuating motion of the turbulent flow often is superfluous. The calculation of the average turbulent flow pattern is possible on a relative coarse mesh and, for steady state flow problems, at steady state. As a result computing time is brief compared to DNS and LES. Hence, these turbulence models were used at the beginning of the numerical simulation of turbulent flows and today still find wide-spread application.

For the above mentioned turbulence models, mean conservation equations are derived by introducing the Reynolds decomposition (Equation 3.1) for the instantaneous variables in Equations 4.1 to 4.3 and time averaging the equations (Nieuwstadt 1992). The averaging process results in new unknown terms, $-\rho\overline{u_i'u_j'}$ and $-\rho\overline{u_i'H'}$, the so called Reynolds terms. The first term is the eddy shear stress which is called the Reynolds stress (τ_{ij}). The latter can be considered as a diffusion term for the enthalpy or any other scalar quantity under consideration.

The determination of the Reynolds terms requires extra equations to solve the problem. This represents the *closure problem.* The correlation of the Reynolds terms to the mean flow field is resolved by turbulence models. Most turbulence models are based on the concept proposed by Boussinesq (1877) which assumes that the turbulent stresses are proportional to the mean velocity gradients, analogous to the viscous stresses in laminar flows:

$$\tau_{ij} = -\rho\overline{u_i'u_j'} = \mu_t\left(\frac{\partial\overline{u}_i}{\partial x_j} + \frac{\partial\overline{u}_j}{\partial x_i}\right) - \frac{2}{3}\delta_{ij}\rho k\,, \tag{4.4}$$

$$-\rho\overline{u_i'H'} = \Gamma_t\frac{\partial\overline{H}}{\partial x_i}\,, \tag{4.5}$$

where μ_t is the turbulent or eddy viscosity, a property of the flow, Γ_t the turbulent scalar diffusivity (also given as μ_t/σ_H, where σ_H is the turbulent Prandtl-number), δ_{ij} the Kronecker delta and k the turbulent kinetic energy ($1/2 \cdot u_i'^2$). The second term on the right hand side of Equation 4.4, which can be considered as a dynamic pressure, will be ignored because it is small (Chen 1988).

Different models are available to determine the unknown variable μ_t. One of the earlier and at present most widely used turbulence model is the standard k-ε model (Launder and Spalding 1974, Chen 1995). This model will be discussed in the next section.

4.2.2 Standard k-ε model

The standard k-ε model calculates the turbulent viscosity (μ_t) isotropically from

$$\mu_t = c_\mu \rho \frac{k^2}{\varepsilon}, \tag{4.6}$$

where ε is the rate of dissipation of turbulent kinetic energy and c_μ an empirically determined constant (c_μ = 0.09; Launder and Spalding 1974). The calculation of the turbulent viscosity thus requires the derivation of two additional equations to determine k and ε. The standard k-ε model therefore is called a two-equation model. The derivation of these equations can be found in for example Nieuwstadt (1992).

A general equation for the mass, momentum and scalar conservation equations can be formulated for the standard k-ε model, when Equation 4.4 and 4.5 are substituted into Equation 4.2 and 4.3 and the superscript '-', indicating the mean value, is omitted,

$$\frac{\partial}{\partial t}(\rho\phi) = \frac{\partial}{\partial x_i}\left(\Gamma_\phi \frac{\partial \phi}{\partial x_i} - \rho u_i \phi\right) + S_\phi, \tag{4.7}$$

where ϕ represents a mean velocity component (u_i) or any mean scalar variable (k, ε, H, C). The description of the diffusion coefficient (Γ_ϕ) and the source terms (S_ϕ) are given in Table 4.1. Furthermore, the k-ε model comprises several constants which have been determined from experiments as, e.g., the decay of turbulence behind a grid and the turbulent flow near a wall (Launder and Spalding 1974). The value of these constants is also given in Table 4.1.

Due to the no-slip condition at the wall and the resulting damping, close to the wall a laminar flow is found. The standard k-ε model (Equation 4.6 and 4.7) however is only valid for flow regions where the turbulent transport is dominating. Instead the flow near by walls is solved with wall functions, the so-called *law of the wall* (Tennekes and Lumley 1972):

$$u^+ = \frac{1}{\kappa}\ln\left(Ey^+\right); \qquad 30< y^+ <130, \tag{4.8}$$

$$u^+ = y^+; \qquad 0< y^+ <5, \tag{4.9}$$

where y^+ is the normal-distance Reynolds number ($y^+ = \rho y u_\tau/\mu$, where the friction velocity $u_\tau = (\tau_w/\rho)^{0.5}$) and y is the normal-distance to the wall), u^+ the dimensionless velocity ($u^+ = u/u_\tau$), κ the von Karman's constant ($\kappa = 0.42$) and E a constant that is a function of the wall roughness (smooth wall: $E = 9.81$ (Fluent 1996[a])).

The constants in the logarithmic wall function (Equation 4.8) have been fitted from typical forced convection boundary layer flows. This function is valid in the inertial sublayer and links the fully turbulent outer layer flow with the near wall flow profile by asymptotic matching (Tennekes and Lumley 1972). Close to the wall the turbulence cannot sustain itself as the integral length scale becomes smaller than the Kolmogorov micro-scale. Experimental results show that the Reynolds stresses remain small up to about $y^+ = 5$. This region is called the viscous sublayer. In this layer the velocity profile is linear when the Reynolds stresses are neglected (Equation 4.9). The intermediate region is called the buffer layer. In this layer viscous stresses as well as Reynolds stresses are effective. In the inertial sublayer the Reynolds stresses dominate (Tennekes and Lumley 1972).

Given the Reynolds' analogy between momentum and energy transfer, as found in the Stanton number ($St = Nu/RePr = h_c/\rho c_p u$), the temperature profile at the wall can be described with similar functions:

Table 4.1 description of diffusion coefficient (Γ_ϕ) and the source terms (S_ϕ) for variable ϕ.

ϕ	Γ_ϕ	S_ϕ	equation
1	0	0	continuity
u_i	$\mu + \mu_t$	$-\partial p/\partial x_i - \rho g_i$	momentum
k	$\mu + \mu_t/\sigma_k$	$P_k - \rho\varepsilon + G_b$	turb.kin.energy (k)
ε	$\mu + \mu_t/\sigma_\varepsilon$	$(c_{\varepsilon 1}P_k + c_{\varepsilon 1}c_{\varepsilon 3}G_b - c_{\varepsilon 2}\varepsilon)\varepsilon/k$	dissipation rate of k
H	$\mu/Pr + \mu_t/\sigma_H$	S_H	enthalpy
C	$\mu/Sc + \mu_t/\sigma_C$	S_C	concentration

$$P_k = \mu_t\left(\frac{\partial u_i}{\partial x_j} + \frac{\partial u_j}{\partial x_i}\right)\frac{\partial u_i}{\partial x_j}; G_b = \frac{g_i\beta}{c_p}\frac{\mu_t}{\sigma_H}\frac{\partial\theta}{\partial x_i}; \theta = H - H_0.$$

$c_{\varepsilon 1} = 1.44$; $c_{\varepsilon 2} = 1.92$; $c_{\varepsilon 3} = 1.0$ (Henkes 1990); $\sigma_k = 1.0$; $\sigma_\varepsilon = 1.3$; $\sigma_H = 0.85$; $\sigma_C = 1.0$.

$$T^+ = \sigma_H \left(u^+ + P\left(Pr/\sigma_H\right)\right), \tag{4.10}$$

$$T^+ = \mathrm{Pr} \cdot y^+, \tag{4.11}$$

where,

$$T^+ = \frac{T_s - T}{T_\tau} = \frac{\left(H_s - H\right)\rho u_\tau}{\dot{q}_s} \tag{4.12}$$

and $P(Pr/\sigma_H)$ a constant value which is a function of the laminar and turbulent Prandtl number. For air, P is determined at approximately -1.4. In Equation (4.12), $\dot{q}_s$ is the surface heat flux. In Fluent (1996[a]), the linear wall function (Equation 4.9) is used when $y^+ <$ 11.225. For the linear temperature profile (Equation 4.11) this value is $y^+ < 11.225/Pr$.

The conservation equation for the turbulent kinetic energy (k) is solved up to the wall-adjacent cells. At the wall the boundary condition is $\partial k/\partial x_i = 0$ (Fluent 1996[a]). Assuming local equilibrium between the production of k and its dissipation rate, the dissipation rate in the wall-adjacent cell is calculated from $\varepsilon = u_\tau^3 / (\kappa y)$ (Prasad 1994).

The validity of the law of the wall is queried for the flow field as appears indoors (Chen 1988; Baker and Kelso 1990; Niu 1994). In Chapter 4.4.3 the validity of the wall functions is discussed more in depth.

The standard k-ε model has shown to be broadly applicable for fully turbulent flows where the turbulence based Reynolds number ($Re_t = k^2\rho/\mu\varepsilon$) is large. For low Reynolds number flows, the standard k-ε model however overestimates the turbulent diffusivity. The standard k-ε model therefore has been subject to modifications to improve the validity at low-Reynolds number flows. In these so-called low-Reynolds number turbulence models, functions are introduced in the calculation of μ_t and in the k and ε equation that are a function of, amongst others, Re_t. Henkes (1990) gives a summary of several available models.

In Chen (1995) some of the modified k-ε models are compared for four typical two-dimensional validation cases. From this comparison the Renormalisation Group (RNG-) k-ε model was recommended for the simulation of indoor air flows. The RNG-k-ε model performed better than the standard k-ε model for a mixed convection flow case and an impinging jet. The results for the free and forced convection flow cases agreed with the results from the standard k-ε model (Chen 1995). The RNG-k-ε model will be explained in more detail in the next section.

4.2.3 Renormalisation Group (RNG-) *k*-ε model

The RNG-*k*-ε model is a two-equation turbulence model, similar to the standard *k*-ε model, that is derived by using renormalisation group methods (Yakhot and Orszag 1986). From the RNG technique a theory for large scale turbulence has been derived in which the effects of small scales are represented by modified transport coefficients. The derivation is based on the *correspondence principle* (Yakhot and Orszag 1986); the Navier-Stokes equations are solved with a random force that describes the inertial range.

For the turbulence modelling, the small scale eddies are eliminated via the RNG-method and introduced into modified Navier-Stokes equations which comprise a modified (turbulent) viscosity, a modified force and a modified non-linear coupling (Fluent 1993). The RNG-method is used to determine the values of similar coefficients as arise in the standard *k*-ε model. Furthermore, the turbulent Prandtl numbers for *k*, ε and *H* are obtained from an analytical relation which accounts for the molecular Prandtl number and for low-Reynolds number effects. An additional source term *R* is included in the equation for the dissipation rate of turbulent energy (Fluent 1993). These deviations from the standard *k*-ε model are summarised below.

- The constant model coefficients are obtained from the RNG theory,

$$c_\mu = 0.0845;\ c_{\varepsilon 1} = 1.42;\ c_{\varepsilon 2} = 1.68. \tag{4.13}$$

- The RNG method results in a low Reynolds number interpolation formula for the turbulent viscosity which is valid for low to high Reynolds number flows,

$$\mu_{eff} = \mu + \mu_t = \mu\left(1 + \sqrt{\frac{c_\mu}{\mu}}\frac{k}{\sqrt{\varepsilon}}\right)^2, \tag{4.14}$$

where μ_{eff} is the effective viscosity. As the RNG-*k*-ε model accounts for low-Reynolds number effects, wall functions can be abandoned. For high Reynolds number flows Equation (4.14) approaches the expression as applied in the standard *k*-ε model.

- The turbulent diffusion coefficient ($\Gamma_{eff} = \zeta_{eff} \cdot \mu_{eff}$) results from an expression in terms of the effective viscosity and the effective inverse Prandtl number (ζ_{eff}), where ζ_{eff} is determined from:

$$\left|\frac{\zeta_{eff} - 1.3929}{\zeta - 1.3929}\right|^{0.6321}\left|\frac{\zeta_{eff} + 2.3929}{\zeta + 2.3929}\right|^{0.3679} = \frac{\mu}{\mu_{eff}}, \tag{4.15}$$

where $\zeta = 1.0$ for the *k* and ε-transport equations and $\zeta \equiv 1/Pr$ for the heat transfer equation.

- The additional source term *R* in the dissipation-rate transport equation is calculated from

$$R = \frac{c_\mu \eta^3 (1-\eta/\eta_0)}{1+\chi\eta^3}\frac{\varepsilon^2}{k};\ \eta = S\frac{k}{\varepsilon};\ S = \left(2S_{ij}S_{ij}\right)^{1/2};\ S_{ij} = \frac{1}{2}\left(\frac{\partial \overline{u}_i}{\partial x_j} + \frac{\partial \overline{u}_j}{\partial x_i}\right), \qquad (4.16)$$

where S_{ij} is the mean rate-of-strain, $\eta_0 = 4.8$ and $\chi = 0.012$.

In regions of large strain rates the production of turbulent kinetic energy is overestimated in the standard *k*-ε model. As a result flow field features as separation and vortex shedding are obscured at downstream positions (Launder 1991). The lower value for $c_{\varepsilon 2}$ in the RNG-theory compared to its value in the standard *k*-ε model (see Table 4.1) decreases the rate of production of *k* and the rate of dissipation of ε. Similarly, for $\eta > \eta_0$, the *R* term reduces the effect of the destruction term ($c_{\varepsilon 2}\varepsilon^2/k$) in the dissipation rate equation and therewith of the production of turbulent kinetic energy. It ultimately results in a suppression of the turbulent viscosity. When $R > 0$, the increase in μ_{eff} typically is smaller than the value obtained with the standard *k*-ε theory (Fluent 1993).

The above properties of the RNG-*k*-ε model and the resulting extension of the model to low-Reynolds number flow problems favour it for indoor air flow applications. Despite the mathematical derivation of the model coefficients Yakhot and Orszag (1986) indicate that the RNG-based *k*-ε model must be validated by means of experiments. This is due to non-linear terms generated by the RNG-method that may take on a finite non-zero value. The effect of turbulence modelling on a simulated realistic three dimensional flow pattern will be discussed in Chapter 7, using measurement results that have been obtained in this research. These measurements are described in Chapter 5 and 6.

4.3 NUMERICAL METHODS

An analytic solution of the coupled, non-linear, partial differential equations for a three-dimensional, turbulent flow field is not possible. The use of numerical methods is inevitable and therefore the calculation of a flow problem requires the discretisation of that flow field into space and time. Finite volume and finite element methods are used to obtain a numerical solution. In both methods the discretised equations represent the flow problem in each control volume or element. The first method will be discussed more closely as it is applied in the software (Fluent 1995, 1996[a], 1998) for solving the flow problems described in this thesis. In Baker et al. (1994) and Williams et al. (1994) more information is available on the application of the finite element method for the simulation of indoor air flow.

Discretisation - Discretisation in space requires the flow field to be divided in small control volumes. Different type of control volumes and grid topologies are possible; hexahedral and tetrahedral control volumes and structured or unstructured grids. In Chapter 4.5 the different

available grid techniques are discussed. The solution process for both grid topologies is nearly similar (Fluent 1996[a]).

Integration over the control volume in order to balance the conservation equations requires the calculation of the cell face values of the scalar variable ϕ so that the convective and diffusive fluxes can be determined. This requires an interpolation from the ϕ-value at the cell centre to the cell face. Different interpolation schemes are available (Ferziger and Peric 1996). The application of a specific scheme for a variable (among others) depends on the grid alignment to the flow field. Higher order schemes present a better accuracy as a first order scheme introduces numerical diffusion when the flow field is oblique to the grid alignment. Higher order schemes however show a less stable solution procedure.

Solver - Solving the equations on a structured grid allows the application of line-iterative methods as the line Gauss-Seidel (LGS) method. The equations for a variable are solved directly along one line of control volumes applying the tridiagonal matrix algorithm (Patankar 1980). The calculation is proceeded with the next line applying the latest available boundary values. The solution process can be improved via block correction along a line of control volumes. The added correction satisfies the balance over the control volume block (Patankar 1981). A further improvement can be obtained by applying a multigrid solver. Corrections are determined from a successively coarser grid which is constructed from a block of control volumes. These corrections are added to the fine grid solution during the iteration process (Hutchinson and Raithby 1986). For unstructured grids a line-iterative method cannot be applied. The Gauss-Seidel solution process is combined with the multigrid technique. An algebraic scheme then is used to determine the coarse level mesh (Fluent 1996[a], Ferziger and Peric 1996).

An iterative approach is required to obtain the separate but coupled flow field variables, described by Equation 4.7, from an initial guessed flow field. The solution of the flow field is complicated by the pressure source term in the momentum equation. The pressure field cannot be determined from a separate equation. Patankar (1980) describes a procedure in which the pressure field is obtained via the continuity equation, the Semi-Implicit Method for Pressure-Linked Equations (SIMPLE). Given an initial pressure field, the momentum equations are solved. A pressure correction is obtained from the revised continuity equation and the velocity component values are corrected subsequently. After calculation of the coupled flow field variables, as temperature and turbulent quantities, the corrected pressure is taken as the new pressure field and the operation is repeated until a converged solution is obtained.

All flow field variables are stored in the cell centre of the control volume. A linear interpolation procedure is applied to obtain the pressure value at the face of the control volume, as is necessary for solving the momentum equation (Rhie and Chow 1983). In this way an oscillatory pressure field is prevented without the application of a staggered grid (Patankar 1980). This approach is useful when boundary fitted coordinates are used for non-orthogonal boundaries of a flow problem. For large local gradients of the pressure, as with large buoyant forces, the discretisation should be refined. Also a staggered grid approach may be re-introduced for the calculation of the face pressure (Fluent 1996[a]). To prevent a similar oscillatory solution for the flow field when solving the continuity equation, a momentum-weighted averaging is applied for the velocity that is based on the convection and diffusion effects (Majumdar 1988).

When the buoyancy force is of the same order of magnitude as the pressure gradient the convergence is poor because of the relative small contribution of the convective and viscous terms. This results from the sequential solving process of the SIMPLE-algorithm. A correction term can be incorporated in the revised continuity equation that accounts for the buoyancy force (Fluent 1995 and 1996[a]).

Convergence - Because of the non-linearity of the problem the solution process is controlled via relaxation factors. A relaxation factor controls the change of a variable as calculated at each iteration. The convergence is checked by several criteria: the mass and heat conservation should be balanced; the residuals of the discretised conservation equations must steadily decrease; and the change in field values between two iterations should be very small.

4.4 CFD CASE STUDY

4.4.1 Introduction

Following the above described mathematical and numerical modelling, the continuous improvements and the developments in computer capacity, CFD has become an increasingly interesting tool for the simulation of the indoor air flow. Literature presents numerous results of CFD-simulations of an indoor air flow field. However, a validation of the simulated results mostly is not possible due to a lack of measurement results. Furthermore, the sensitivity of the solution, as e.g. to boundary conditions and parameter settings, mostly is not indicated. This especially applies to realistic indoor air flow patterns.

In the next sections results of a three dimensional simulation of a displacement ventilated office room are discussed. From this simulation some of the typical restrictions in the CFD-simulation of indoor air flow patterns are indicated. Besides a model verification, including grid dependency check and discretisation scheme variation, the sensitivity to supply boundary conditions has been investigated.

4.4.2 Problem set-up and modelling

The flow under investigation results from a displacement ventilation system that is situated in an office in which several heat sources are present. This flow pattern has been investigated experimentally by Cox and Elkhuizen (1995). The case considered is a standard office module ($4.5 \times 3.6 \times 2.7$ m^3) with a West facing facade (see Figure 4.1a). The air enters the room in the corner of the side wall and the facade at an angle of 45^o. The exhaust is placed at the ceiling in the middle of the room at 1 m from the East wall. The heat sources in the room are represented by orthorhombic obstructions at which a constant heat flux is prescribed. The walls are represented isothermally at a constant temperature. A full description of the flow problem and the applied boundary conditions can be found in Appendix C. A summary of the boundary conditions is presented in Figure 4.1b.

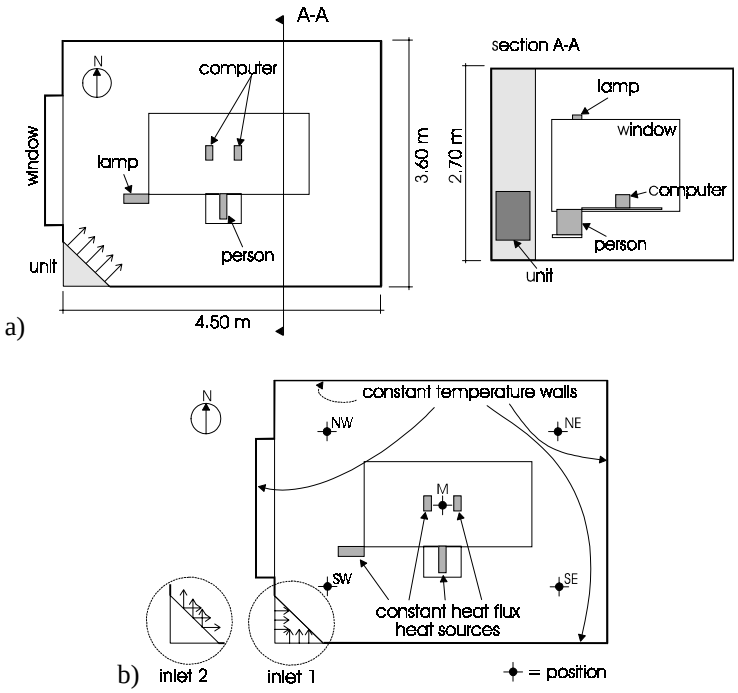

Figure 4.1. Simulated office configuration (a) and boundary condition representation (b).

The modelling of the air supply is important but paradoxical. The supply obviously influences the flow pattern but the detailed supply characteristics cannot be modelled given the restrictions in computer capacity and the requirements for the spatial discretisation of the complete room. Heikkinen (1991) describes four methods which can be applied to replace a complex diffuser:

- The *basic model* replaces the diffuser by a simple opening with the same effective area of the diffuser.
- The *momentum model* applies the actual dimensions of the diffuser, but separates the boundary conditions for the continuity and momentum equations. The flow rate is controlled from the continuity equation. The momentum and turbulent quantities agree to the actual values.
- In the *box model* measured boundary conditions are set at an imaginary box around the supply opening.
- In the *prescribed velocity model* the basic model is applied to describe the supply opening. Measured velocities are imposed onto the flow field at the most important locations.

Emvin and Davidson (1996) reject the basic and the momentum model. In the basic model the penetration length will be overestimated due to an underestimation of the turbulent mixing area. This will be most evident for diffusers with a small aperture percentage. Their analysis of the momentum model is not correct and resulted in the wrong conclusion (Chen 1998).

For the present study none of the mentioned methods has been used as no specific experimental results for the supply were available. Instead the full diffuser area has been modelled. As the flow rate is prescribed and the opening percentage could not be modelled the momentum therefore is underestimated. The effect of the supply momentum deficit on the total flow pattern in the room normally is less decisive for a displacement ventilation flow pattern. In such a pattern the supplied air generally is distributed over the total floor area first, without influencing the other parts of the room. The total flow pattern is mainly determined from the heat sources in the room. Also near the floor the supply momentum normally is less important as, in contrast with a jet characteristic, the supply velocity is relatively low.

The simulations have been performed with Fluent V.4.32 (Fluent 1995). Due to the rectangular geometry of the room and the positions of the objects a cartesian grid (33×31×48) has been preferred over a boundary fitted grid. As a result the flow enters the room at an angle of 45^{o} to the grid lines. This case is indicated as the reference case. Grid dependency was checked by increasing the number of grid points to a nearly doubled grid (64×60×94). This case is indicated as double grid case.

The standard *k*-ε model has been used to model the turbulence and standard wall functions have been applied to represent the near wall flow field. The RNG-*k*-ε model was not considered for these simulations because of the limited number of available measurement results and the limited experience with the RNG model at the time of investigation. As mentioned earlier, the turbulence modelling will be discussed in Chapter 7. The simulation results described in this chapter do not concern the turbulence model, but merely the characteristics of a CFD-simulation. The power-law interpolation scheme was used as the discretisation scheme (Patankar 1980). Furthermore, the LGS method and the SIMPLE algorithm were part of the solution process. Though the flow problem is stationary the problem has been solved time dependent. The time-step serves as an additional relaxation factor. The application of the time in the solving procedure results from experience in the simulation of similar flow problems.

The simulation was regarded converged when the mass and heat balance are accurate within 1% of the mass flow rate and the total heat input respectively. Furthermore, the variation of flow variables (*u*, *v*, *w*, *T*) at specified positions in the flow field must be less than 1% over the last 100 time steps for absolute values larger than 0.01.

4.4.3 Model verification

Measurements from Cox and Elkhuizen (1995) were used for comparison with the CFD-results. A qualitative comparison of the flow in the room indicates a good agreement between the predicted and the visualised flow field. Buoyant plumes are simulated above the heat sources and a pronounced vertical temperature gradient is calculated. Table 4.2 presents a quantitative comparison between measured and simulated velocities (reference and double grid case) at five positions in the room. The measurements were performed with a hot sphere measurement device (inaccuracy approximately 20 - 30%). In Figure 4.2 the simulated profiles of the velocity magnitude for the reference and double grid case are shown for the positions indicated in the room (see Figure 4.1b).

Table 4.2. Measured and simulated air velocity at five different positions in the room as indicated in Figure 4.1b.

position		height	measurement	simulation	
				reference	double grid
		[m]	[m/s]	[m/s]	[m/s]
South West	(SW)	0.1	0.08	0.17	0.21
South West	(SW)	0.6	0.28	0.10	0.13
Middle	(M)	1.1	0.05	0.06	0.07
Middle	(M)	1.7	0.05	0.02	0.02
North East	(NE)	0.1	0.10	0.07	0.08

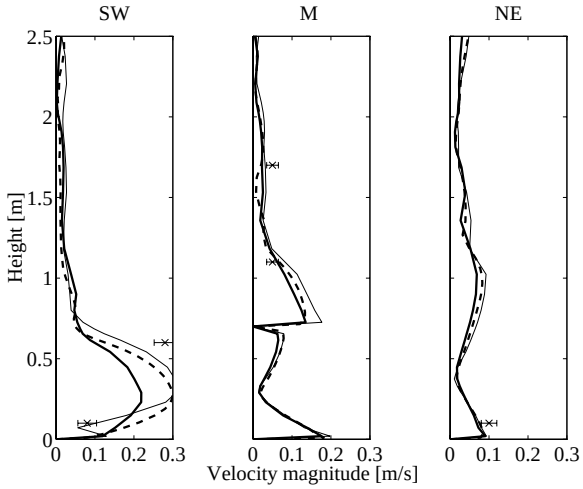

Figure 4.2. Simulated profile of the velocity magnitude at three positions in the room (see Figure 4.1b) ([×] *measurements,* [| | | |] *reference case,* [| | |] *double grid case ;* [———] *results for reference case when a higher order interpolation scheme is applied).*

When the measurement results are compared with the simulations (Table 4.2), the influence of the supply modelling in the CFD-simulations is apparent. A significant difference is found for the South West position. The actual supply dimensions were modelled so that the momentum was underestimated (estimated effective area of the supply ~30%). The penetration length is reduced by the underestimation of the modelled momentum. The penetration length is defined as the length over which the air flow is directly influenced by the supply flow.

Table 4.2 and Figure 4.2 show that the simulated velocity flow field near the supply is grid dependent and do not agree with the measurement results. This deviation is mainly caused by numerical diffusion (Patanker 1980) as a result of the oblique direction of the supply velocity vector to the grid. At positions further downstream comparison with the measurement results is more difficult as the registered velocities are low. Apart from the supply region the (coarse) grid of the reference case however results in grid independent solutions. Therefore, at about 50,000 cells, a grid independent solution is possible for the flow in an office room equipped with a displacement ventilation system. This however requires a careful grid refinement near walls and heat sources.

The simulations were performed with the power-law interpolation scheme. In case of the use of a higher order interpolation scheme for the reference case, the numerical diffusion close to the supply as discussed above is reduced (see Figure 4.2). The stability of the solving process is however weak. Unrealistic flow field features appear for the higher order

solution. For example the buoyant plume above the heat sources is reduced significantly. As a result, the problem is simulated most reliably by aligning the grid to the streamlines at the supply.

For the comparison of the temperature distribution in the room Cox and Elkhuizen (1995) defined the temperature effectivity as

$$E_T = \left(T_{exhaust} - T_{supply}\right) / \left(T_x - T_{supply}\right), \qquad (4.17)$$

where T is the temperature at the exhaust, at the supply or at a specific location in the room (x). In Table 4.3 a quantitative comparison is given of the measured and simulated temperature effectivity. In Figure 4.3 simulated temperature profiles (in ^{o}C) are shown for three positions in the room for the reference as well as for the double grid case. As no information is available on $T_{exhaust}$, measurement results cannot be indicated in Figure 4.3. Given the unrealistic flow field features obtained with the higher order interpolation scheme, as discussed above, these results are not shown.

Contrary to the velocity, for the temperature effectivity distinct differences are found between measurement and simulation, and also between the two simulation variants. These differences mainly result from differences in the simulated heat transfer rate at the constant temperature walls. For the double grid case the increased overall wall heat transfer to the room results in a higher room and exhaust temperature. These higher values result in a better agreement with the measured temperature effectivity than obtained from the reference case. Only close to the supply the reduced numerical diffusion influences the temperature profile differently.

For the reference case the averaged y^+-value is determined at 20 viscous units (see Equation 4.8). For the double grid case this value is smaller than 11 viscous units. The applied wall functions for the temperature profile (Equation 4.10 and 4.11) underestimate the heat transfer for the given grid set-up. Chen (1995) indicates that reliable heat transfer characteristics are obtained when the y^+-value is controlled at 10. This value however is arbitrarily and results from experience. Niu (1994) determined $y^+ = 9.2$ as the optimum value

Table 4.3. Measured and simulated temperature effectivity E_t [-] at twelve different positions in the room.

height	South West (SW)			Middle (M)			North East (NE)		
[m]	meas.	ref.	double	meas.	ref.	double	meas.	ref.	double
0.1	4.28	13.87	28.59	2.35	3.30	2.90	1.79	2.32	2.03
0.6	2.93	2.52	2.43	1.57	2.28	1.99	1.50	2.16	1.92
1.1	1.24	1.52	1.17	1.28	1.56	1.37	1.26	1.63	1.39
1.7	0.95	1.22	1.10	0.98	1.18	1.10	1.01	1.18	1.10

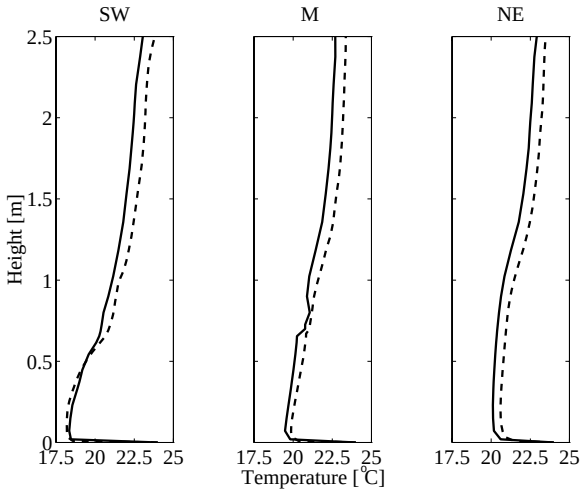

Figure 4.3. Simulated temperature profile at three positions in the room (see Figure 4.1b) ([▏▏▏▏] *reference case,* [▏ ▏ ▏] *double grid case).*

for the numerical prediction of the heat transfer coefficient for a free convection flow problem.

The restricted validity of the wall functions follows from the assumptions that have been made to solve boundary layer flows (Tennekes and Lumley 1972). These assumptions are not valid for boundary layer flows that arise indoors. E.g., the wall function as given in Equation 4.8 is not valid for developing boundary layers, is derived for two-dimensional flows parallel to the wall (Prasad 1994) and is not valid when pressure gradients are present (separation and impinging flows).

An improvement in the simulation of the heat transfer characteristics is possible when the near wall flow field is solved more accurately. This is possible with low-Reynolds-number modified turbulence models. They allow to model the flow up to the wall, without the use of wall functions. This requires however a fine grid distribution in the near wall layer. Given the grid considerations for whole room flows and the required computing costs, possibilities for near wall grid refinement are nevertheless restricted. As a result a valid simulation of the heat transfer characteristics for indoor air flow fields is very difficult to obtain (Niu 1994).

To overcome the modelling and grid restrictions when simulating the heat transfer, CFD-results often are obtained by imposing a heat transfer coefficient in the definition of the wall boundary condition. The coefficient is determined from measurements or is calculated from an empirical relation. The application of a convective heat transfer coefficient (h_c) requires

information on its definition. Unless mentioned otherwise, in this thesis the convective heat transfer coefficient is defined according to Chen (1988),

$$h_c = \dot{q}_c / (T_s - T_{0.1m}), \tag{4.18}$$

where $\dot{q}_c$ is the convective heat flux, T_s the surface temperature and $T_{0.1\mathrm{m}}$ the air temperature at 0.1 m from the surface.

It is clear from the simulation results for the office configuration with displacement ventilation, given in Table 4.3, that there are considerable deviations with the measurement results. The temperature differences between the simulation variants however are within 1°C (Figure 4.3). Because the heat sources in the office room are modelled by their known (convective) heat input, grid variation does not influence the total heat input into the room by the heat sources. The convective heat transfer coefficient at the heat source however is underestimated. This results in an overestimation of the surface temperature and consequently of the radiant heat transfer. Therefore, the simulation of combined convective and radiant heat transfer is not feasible for the given simulation model. The applied version of the CFD-program does not allow the introduction of a convective heat transfer coefficient as part of the boundary condition of a wall, nor the control of the y^+-value at a predefined value. Furthermore, the number of available measurement results is too restricted for a more in depth evaluation of the effect of the underestimation of the heat transfer. As for the turbulence modelling, this effect is discussed further in Chapter 7 using more extensive measurement results that have been obtained within this research. These measurements are dealt with in Chapter 5 and 6.

4.4.4 Supply definition sensitivity

Despite the incomplete validation of the office model discussed above, the numerical office model is used to investigate the sensitivity of the simulation of air supply into the room in case of displacement ventilation. Table 4.4 summarises the four cases that have been compared with the reference case. The investigated parameters deal with the flow direction and the modelling of the supply. In Figure 4.4 a graphical comparison is presented for the velocity magnitude and the temperature at the indicated positions in the room. The result for case 4 is not shown in Figure 4.4 as the difference with the result for case 1 is negligible.

Table 4.4. Simulation variants

Case	based on	changed parameter
1	reference case	modelling of the supply (supply 2 instead of supply 1; see Figure 4.1b.)
2	case 1	vertical supply angle: 45° upward
3	case 1	horizontal supply angle: 0°, parallel to the facade
4	case 1	supply turbulence intensity: 10% instead of 35%

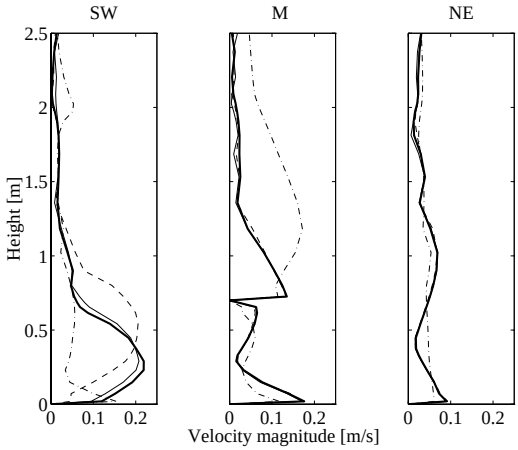

Figure 4.4a. Simulated velocity profiles ([┃┃┃┃] reference case; variants: [———] case 1/case 4, [– – –] case 2, [– · – · –] case 3 (positions are indicated in Figure 4.1b, the cases are defined in Table 4.4)).

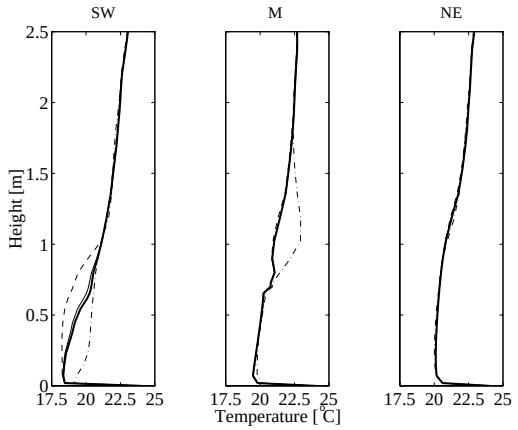

Figure 4.4b. Simulated temperature profiles ([┃┃┃┃] reference case; variants: [———] case 1/case 4, [– – –] case 2, [– · – · –] case 3 (positions are indicated in Figure 4.1b, the cases are defined in Table 4.4)).

Changing the supply model (case 1) causes differences in the velocity profile near the supply, but the flow field in the rest of the room remains nearly unchanged. Similar conclusions follow when the vertical supply angle is altered from 0^o to 45^o upward (case 2; note that the numerical diffusion in this case is even more pronounced). However, the differences close to the supply are more distinct and result in an area near the desk with decreased thermal comfort. The flow field just above floor level is totally altered when the supply flow direction is set parallel to the facade (case 3).

A change in the supply turbulence intensity (case 4) has no influence on the flow field. The influence of the earlier discussed numerical diffusion however must be taken into account. Joubert et al. (1996) found the same conclusions for a numerical study of a jet in a two dimensional cavity in which the turbulence intensity was varied between 4% and 37.4%. Joubert et al. also found that the geometry of the supply velocity profile (flat or parabolic profile) does not influence the mean velocity within the cavity. The difference in the simulated turbulent kinetic energy in the cavity however was significant. Due to the parabolic supply profile additional shear by the jet results in a higher production of turbulent kinetic energy. This effect will be less apparent for displacement ventilation.

4.5 GRID TECHNIQUE

4.5.1 Introduction

The simulation of the indoor air flow requires a simplification of the flow problem by discretisation in time and space. Structured cartesian grids are used most often to represent the flow problem configuration. A structured grid is characterised by continuous grid lines between the opposite boundaries of the discretised flow problem. To reduce the number of grid cells a non-uniform grid is preferred over an equidistant grid. For indoor air flow problems, heat sources placed in the room require grid refinement close to these sources. As a result for a non-uniform grid small grid cells may appear at locations in the flow field where the gradients of the calculated variables are small. Furthermore, the increased aspect ratio (height-to-width ratio) of a grid cell may introduce numerical errors when the velocity vector is perpendicular to the cell direction.

Optimisation of the grid set-up therefore is directed towards a more efficient use of grid elements with a view to obtain an improved representation of the non-rectangular flow problem at the lowest computing time. As a result different type of volume cells and grid topologies have become available. Table 4.5 summarises some of these grid topologies.

Table 4.5. Grid topologies under consideration.

	grid	volume element	location index	grid line requirement
a.	structured (single block)	hexahedral	i,j,k index to locate neighbouring cell	continuous between opposite boundaries
b.	pseudo-unstructured (multi-block)	hexahedral	i,j,k index to locate neighbouring cell within each block.	continuous between opposite boundaries of a block
c.	unstructured	tetrahedral	no location index, grid structure part of total data structure	no requirements
d.	unstructured (adapted)	hexahedral	grid structure is part of the total data structure.	no requirements

The structured grid already was discussed above. The pseudo-unstructured grid combines blocks of structured grids, which as a whole may result in an unstructured grid. Truly unstructured grids are obtained when tetrahedral volume cells are applied for the flow field discretisation. Finally, a separate grid topology may appear as a result of grid adaption. In this case the grid is refined or coarsened applying user-defined adaption parameters that can be solution dependent.

4.5.2 Configuration and meshing considerations

In this section a comparison of the mentioned grid topologies is described, to determine the applicability for the simulation of an indoor air flow field. First the configuration and meshing considerations will be discussed, then the results are described.

For the investigation of the grid topology a new room configuration has been used. It is presented in Figure 4.5 and consists of a displacement ventilation unit that is placed underneath a desk, facing the person seated at the desk. The desk is positioned in the middle of the room. The slot exhaust is placed in a side wall just underneath the ceiling. An extensive description of this configuration is given in Chapter 5.

The room boundaries are represented as constant temperature boundaries. A constant heat flux is prescribed for the person seated at the desk. The supply velocity profile is flat and the supply temperature is below the average room temperature. Consequently a stratified flow field should develop. Identical boundary conditions are prescribed for the different grid topologies.

Figure 4.6 presents a graphical summary of the different grid topologies that have been applied for the simulation of the flow configuration. Note that there are small differences in the definition of the person seated at the desk for the different meshing configurations. The

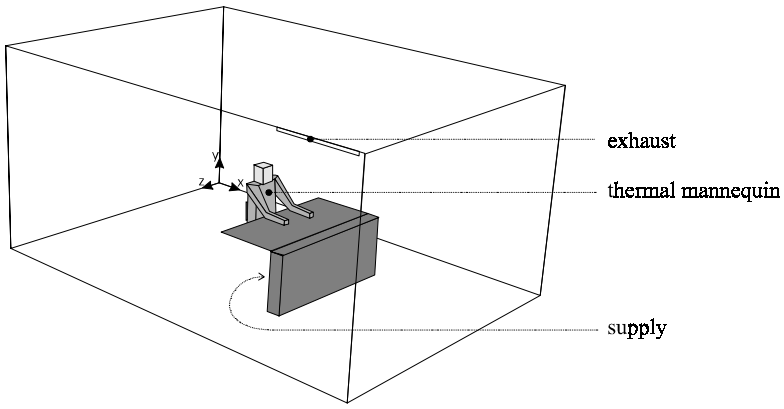

Figure 4.5. Configuration flow problem.

adapted grid is not shown. The structured grid has been set up with Fluent V.4.3 (Fluent 1995). The pseudo-unstructured and unstructured meshes have been constructed with the mesh generator GeoMesh (Fluent 1996[c]) and Tgrid (Fluent 1996[b]). The main characteristics of each grid are summarised in Table 4.6 and will be discussed below.

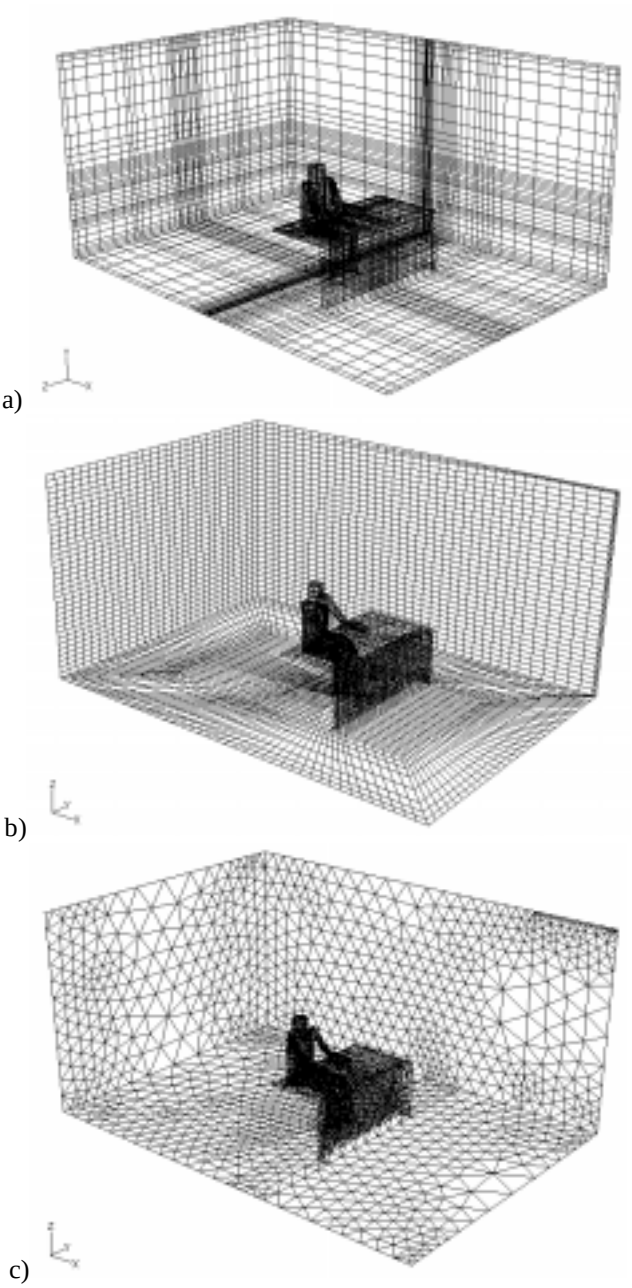

Figure 4.6. Graphical summary of the applied grid topologies; (a) structured grid; (b) pseudo-unstructured grid; (c) unstructured grid.

Table 4.6. Summary of the mesh characteristics.

a. stuctured (single block)	b. pseudo-unstructured (multi-block)	c. unstructured	d. unstructured* (adapted)
49×35×38 cells	48 structured blocks	125 face parts	4 different adaption variants
53,750 internal cells	82,784 internal cells	51,757 internal cells	67,036 - 125,997 internal cells
		maximum skewness: 0.91	(reference: structured)

* not shown in Figure 4.6

In Figure 4.6a a typical structured grid is shown as applied most often for the simulation of indoor air flow. The continuation of the volume cell distribution outside the area of interest causes the reduced effectiveness of this grid topology. The problem set-up is straightforward and highly controllable and the solution process normally is found to be very stable in combination with the standard k-ε turbulence model (Niu 1994). A structured grid can also be used for non-rectangular flow problems through a boundary fitted grid. In that case the grid is fitted to the configuration shape. The set-up for a boundary fitted grid however is rather laborious, because of the strict grid requirements. Outside the region of interest the grid distribution will still lead to superfluous grid refinements.

With the pseudo-unstructured grid set-up (Figure 4.6b) the fine grid distribution remains concentrated at the region(s) of interest. However, as the separate structured blocks must connect properly, the total number of grid cells cannot be reduced significantly. A better distribution outside the region of interest is evident. Due to the grid requirements and the fact that the grid is boundary fitted the set-up for this flow problem is complicated. The influence on the discretisation process nevertheless is high.

The unstructured mesh is shown in Figure 4.6c. Given a predefined triangular boundary mesh a three dimensional tetrahedral grid is created applying a constrained version of the Delauny method (Fluent 1996[b]). In a Delauny mesh there are no nodes that lie inside the circumscribed sphere of any cell. Though the meshing process is relatively straightforward, this type of grid generation restricts the user influence on the final grid distribution considerably. The applicability of the calculated grid is determined by the skewness of the control volumes. The skewness is defined as:

$$\text{skewness} = \frac{\text{optimal cell size} - \text{cell size}}{\text{optimal cell size}}, \tag{4.19}$$

where the optimal cell size is the size of an equilateral cell with the same radius for the circumscribed sphere (Fluent 1996[b]). Zero skewness represents an optimal cell. Given the calculated grid, a limited local grid improvement is possible to reduce the skewness of separate control volumes.

The adapted grid can be derived from any of the meshes as described above. As a test different grid refinement adaption cases were determined from simulation results for the structured grid. Several adaption types were recognised and combined: gradient adaption (velocity magnitude), iso-value adaption (maximum velocity), volume adaption (volume change) and region adaption. The grid refinement concentrates on the supply and the plume above the heat source. The boundary cells were excluded from the grid refinement with reference to the results as described in Chapter 4.4.3. In total four variants have been calculated. In all cases the hanging node adaption procedure is applied. This procedure performs an isotropical grid refinement for the hexahedral cells that have been marked for refinement (Fluent 1996[a]).

The simulations have been performed with Fluent/UNS v.4 (Fluent 1996[a]), an unstructured CFD-program. In all cases this time the RNG-k-ε model has been used. Low-Reynolds-number modifications to the turbulent viscosity, as provided by the RNG-theory, were included. As for Chapter 4.4 in these simulations the turbulence model is not evaluated further. Standard wall functions have been applied as grid refinement up to the wall was not considered due to restricted computing capacity. The momentum and energy equations have been solved applying a second order interpolation scheme. For the unstructured case all equations have been solved applying a second order scheme. In all simulations a multigrid solver and the SIMPLE algorithm have been applied. For the structured and pseudo-unstructured grid pressure interpolation was performed by a staggered grid approach (Fluent 1996[a]). For the unstructured grid the standard linear interpolation was applied. Furthermore, in all simulations a correction term was incorporated in the revised continuity equation to account for the buoyancy force (Fluent 1996[a]).

The problem was regarded as being converged in case the mass and heat balance is accurate within 1% of the mass flow rate and the total heat input respectively. Furthermore, the variation of flow variables (u, v, w, T) at specified positions in the flow field must approach a constant value or a constant sinusoidal variation with a restricted amplitude. Grid dependency has not been checked due to computer capacity restrictions. The unstructured grid approach requires higher memory and CPU overhead for referencing the grid. The computing expenses for the unstructured solver procedure is a factor two higher than for the common structured solver procedure.

4.5.3 Results

In Figure 4.7 the calculated vector field in a vertical cross-section in the middle of the room is presented. The vector scales for the different graphs are equal. Figure 4.8 presents the calculated temperature contours for the same plane. Similar contour values are applied.

a)

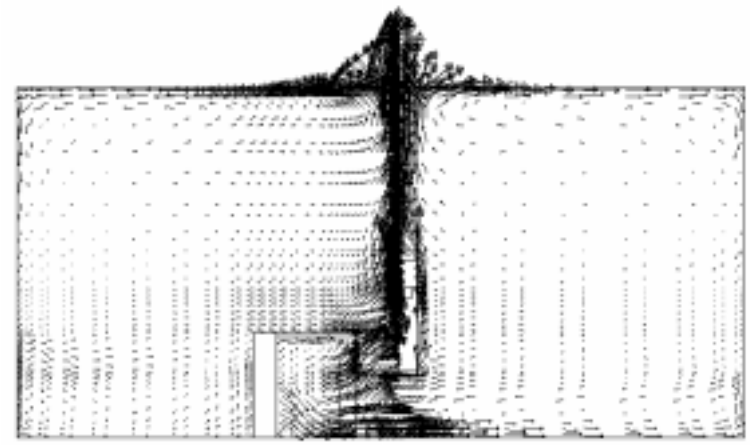

b)

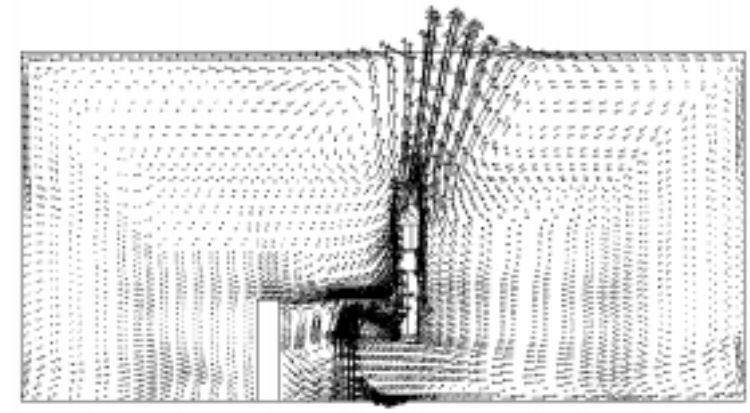

c)

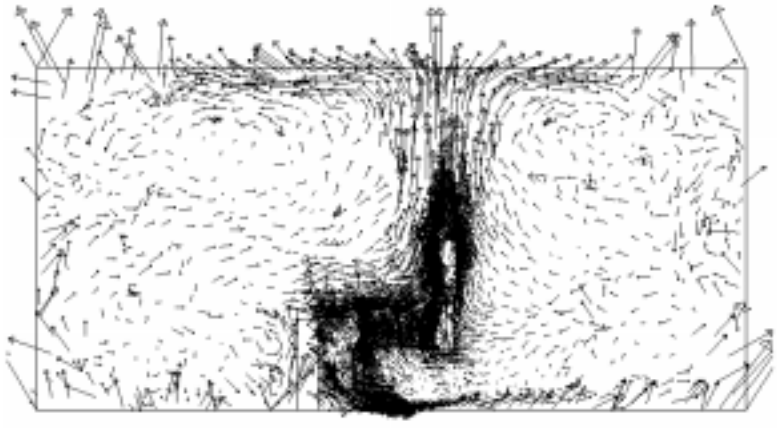

Figure 4.7. Calculated velocity vector field at the centre plane of the room for the different grid topologies, velocity range: 0…0.4 m/s; (a) structured grid; (b) pseudo-unstructured grid; (c) unstructured grid.

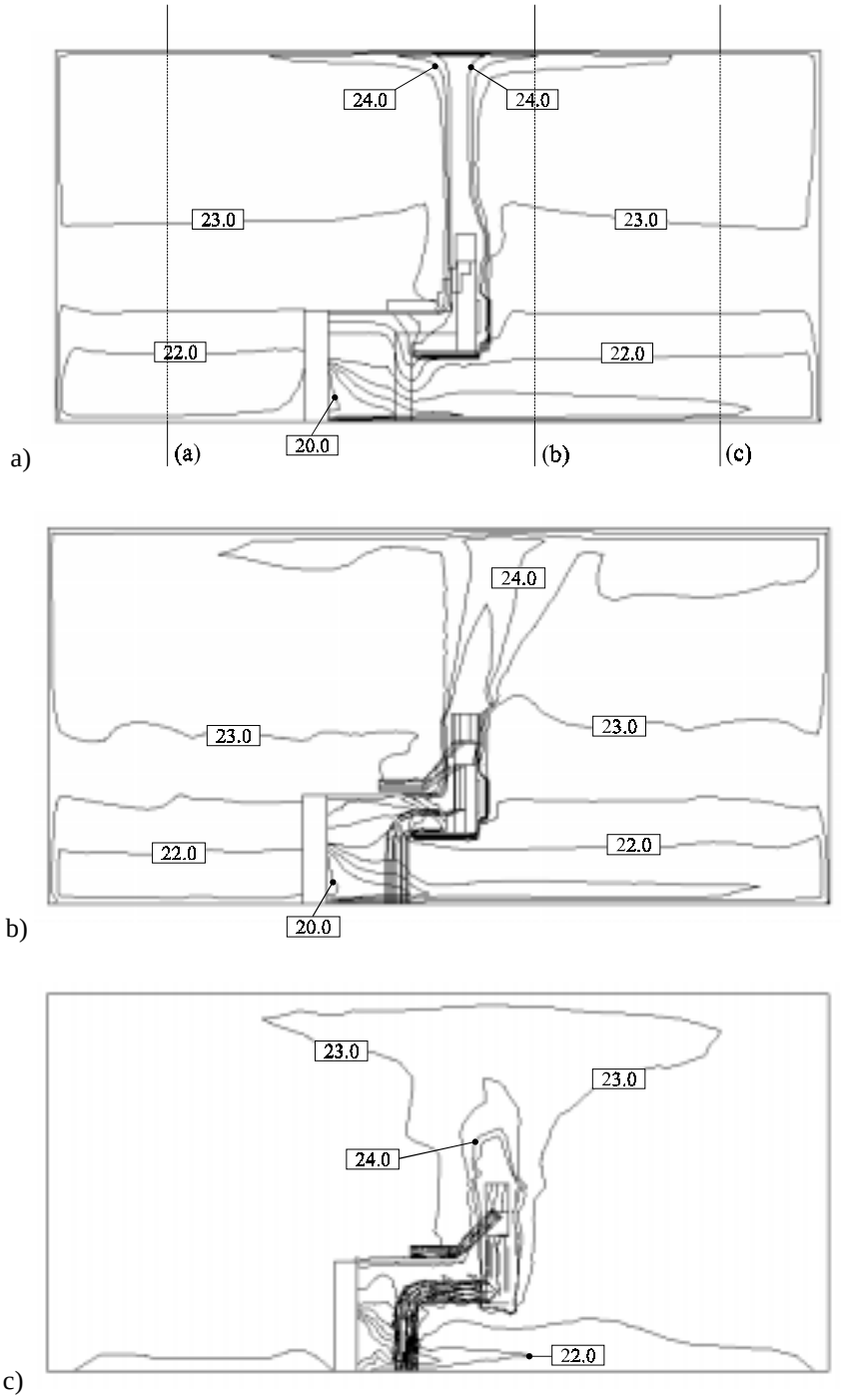

Figure 4.8. Calculated temperature contour field at the centre plane of the room for the different grid topologies; (a) structured grid; (b) pseudo-unstructured grid; (c) unstructured grid.

A typical displacement ventilation flow pattern is calculated for the structured and pseudo-unstructured grid. The introduction of colder air at the supply results in a horizontal velocity vectors just above floor level. Above the heat source a plume has developed and a positive vertical temperature gradient is present in the room. A more extensive description of this typical flow pattern is found in Chapter 6 and 7. The actual validation of the simulation will be discussed in Chapter 7.

For the unstructured grid, the horizontal velocity vectors as well as the plume are less well developed. Erroneous velocity vectors appear at the boundary cells. These results indicate that tetrahedral cells are less well suited for the generally rectangular shape of the room. This effect is amplified due to the significant impact of the buoyant force on the total flow pattern. For a tetrahedral grid an improved treatment for the calculation of the cell face pressure, i.e. a staggered grid construction, is not possible. The application of a segregated solver algorithm (SIMPLE) furthermore may have contributed to the result. In this procedure the connection between buoyancy force and pressure is weak. Given the available model, improvement is only obtained by a further grid refinement. From these results and due to the limitation of computing resources, the application of an unstructured tetrahedral grid for the simulation of a displacement ventilation flow pattern is rejected for the available version of the CFD-program.

A comparison of the structured and pseudo-unstructured grid indicates small differences in the velocity vector field and temperature distribution. The velocity vector field above the heat source is inclined slightly for the pseudo-unstructured grid. This inclination agrees with the grid course above the heat source but would typically not occur in a free convection flow field. Near the ceiling, at one side of the plume, the entrainment region is smaller than calculated for the structured variant. The difference in entrainment conditions between the two sides of the plume for the pseudo-unstructured grid does not occur in reality for this case. This difference furthermore results in a wider plume and lower plume velocities (up to 0.1 m/s) than calculated for the structured grid.

The temperature contours for the buoyant plume relate to the vector field findings. In Figure 4.9 the vertical temperature profiles for the structured and the pseudo-unstructured grid are compared for three positions in the plane as indicated in Figure 4.8a. The absolute differences in the temperature profiles are small (Figure 4.9). This difference is mainly explained from the difference in the wall heat transfer, in particular at the ceiling.

The simulation results for the adapted grid were found to be unstable. When the simulations are continued, despite apparent convergence, the flow field variables show increasing deviations. The instability is independent of the adaption conditions. The unstable solution process is explained from the increased volume change between two neighbouring cells as a

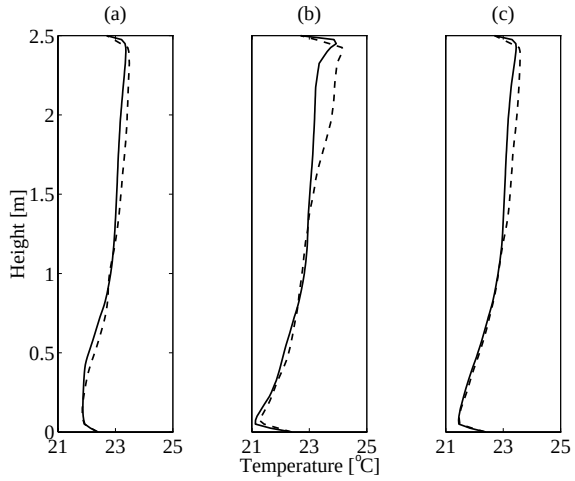

Figure 4.9. Vertical temperature profiles for three positions at the centre plane of the room as indicated in Figure 4.8a ([▏▏▏▏] structured grid, [▏ ▏ ▏] pseudo-unstructured; (a): x = 0.75 m, (b): x = 2.0 m, (c): x = 4.5 m).

result of the grid refinement and from the relative large influence of the buoyancy force on the total flow field and the segregated solver algorithm that is applied. The buoyancy force nevertheless is a typical element in indoor air flows. Given the applied solver and the available version of the CFD-program, grid adaption appears less suited for the simulation of a displacement ventilation flow pattern.

4.6 SUMMARY

1. Recent developments in the mathematical and numerical modelling of turbulent flows in theory allow an improved simulation of the indoor air flow problem. However, only a limited number of validation studies for realistic indoor air flow fields are available to allow a proper evaluation of these improved numerical models.
2. When a room with displacement ventilation is simulated, the correct calculation of the wall heat transfer forms an important problem in the simulation. The application of wall functions results in grid dependent solutions for the heat transfer and therewith for the room temperature. The improved treatment of the near wall flow field via low-Reynolds number turbulence models and grid refinement currently is restricted due to the available computer capacity. As a result the incorporation of a radiant heat transfer model is not feasible when heat sources in the flow problem are defined by their heat flux.
3. The sensitivity of the simulation of the room air flow characteristics to the modelling of the air supply conditions is small for a displacement ventilated flow pattern. The supply

was modelled with a 100% aperture. Close to the supply the differences are more pronounced and may require a more accurate definition when information should be obtained from that region. In such case the use of experimental data then mostly cannot be avoided.

4. The apparently improved grid use in pseudo-unstructured and unstructured grids has drawbacks in terms of the effort to build up the grid and the reliability of the final solution, for a particular problem and solver. A structured grid set-up therefore will remain the point of departure for the simulation of a displacement ventilation indoor air flow pattern.
5. A grid dependency check or a grid improvement in principle is possible via grid adaption. For the investigated flow problem, characterised by large buoyancy forces, the flow field variables adopted unrealistic values after initial apparent convergence. Different adaption strategies resulted in similar findings. For the applied solver, the advantage of grid adaption in the solution process for a displacement ventilation flow pattern therefore seems restricted. Other options to perform a grid dependency test are limited. From the double grid results described in Chapter 4.4.3 it is concluded that for an office room with a displacement ventilation system a grid independent solution is possible at about 50,000 cells. This however requires grid refinement at the heat sources and near the wall and minimisation of numerical diffusion.

Chapter 5

EXPERIMENTAL SET-UP AND PROCEDURE

5.1 INTRODUCTION

The Desk Displacement Ventilation (DDV-) concept was introduced in Chapter 2.3.3 as a concept for ventilation of a standard office configuration according to the task conditioning principle. The concept has been drawn schematically in Figure 2.6 and has been taken as a starting point for the configuration of a full-scale climate chamber set-up. The measurement results obtained from the climate chamber experiments are used to compare with the results from numerical simulations and for the evaluation of the DDV-concept.

In this chapter the design of the configuration and the measurement equipment are described. A thermal mannequin was designed and built to represent the occupant. Furthermore, a specific procedure was followed to perform the whole room measurements. This measurement procedure is described and supported by a set of additional experiments.

5.2 CLIMATE CHAMBER SET-UP

5.2.1 Configuration

In Chapter 2.3.3 the basic configuration requirements for the DDV-concept have been indicated. They are summarised in Table 5.1. These requirements have been used to design a full scale experimental model of an office room ventilated according to the DDV-concept.

Table 5.1. Basic requirements DDV-concept.

supply	below desk top, against back of the desk; large supply area, low supply velocity
exhaust	at ceiling height.
heat sources	person seated at desk; eventually other heat sources in room.

Climate chamber configuration - The model office room, $l \times w \times h = 5.16 \times 3.6 \times 2.7$ m^3 (0.2 m plenum height included), has been built in a larger climate chamber, $l \times w \times h = 5.16 \times 9.7 \times 2.7$ m^3 (at the Eindhoven University of Technology). Figure 5.1 shows the climate chamber configuration with the modelled office room centred in the climate chamber.

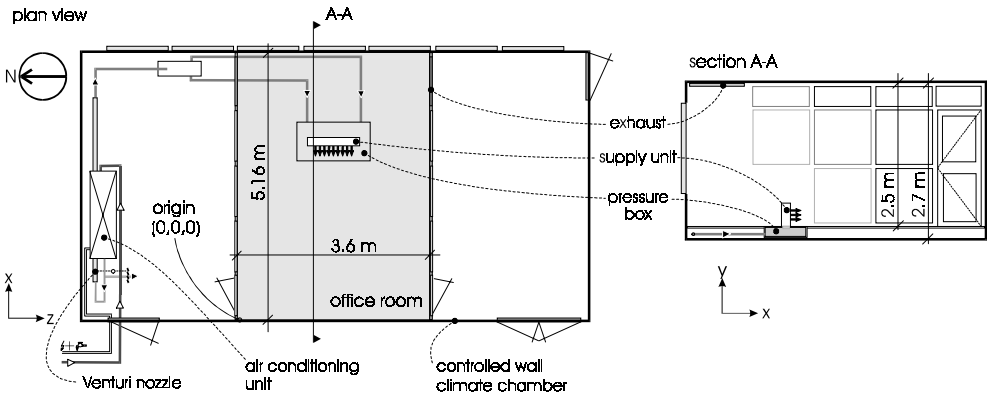

Figure 5.1. Climate chamber configuration.

All walls of the climate chamber are temperature controlled by the climate chamber control system. As a result four walls of the office model can be temperature controlled directly. The standard deviation of the controlled wall temperature is typically in the order of 0.1^{o}C over a period of ~10 hours. This value has been derived from the actual measurement of the wall temperature during the experiments. The temperature for the two remaining walls of the office model, which are transparent to allow visualisation of the flow pattern, results from the conditions in the climate chamber. These conditions, also in the office model, were kept as constant as possible by using dummy heat sources ('lighting') to simulate the heat when measurement equipment was switched off or no person was in the climate chamber. Direct radiant heat transfer from the measurement equipment and the dummy heat sources to the transparent wall was blocked out.

The walls of the model office room are flat planes, with the exception of the East wall in which three windows are situated. These windows also are temperature controlled. The control is linked with the remaining East wall and this wall is assumed flat.

In the model office room a floor plenum is incorporated to allow introduction of the air via the floor. Instead of pressurising the whole plenum, a pressure box was used to allow a homogeneous air supply to the displacement ventilation supply unit (see Figure 5.1). The air flow was introduced symmetrically into the pressure box. For that purpose the single air duct was split into two ducts.

An air conditioning unit is used to condition the air that is introduced into the model office room. The flow rate is determined via a Venturi nozzle and the supply set-point temperature is controlled by the climate chamber control system.

Model office room - A schematic drawing of the model office room is shown in Figure 5.2. The room dimensions and the applied coordinate system are shown in the figure. The boundaries of the room will be mentioned according to their orientation as indicated in Figure 5.2. The important room features are also shown. The supply is placed under the desk table and the exhaust is located in the South-East upper corner of the room. Different heat sources are placed in the room. A full description of the location of the different objects is given in Appendix D.

The thermal mannequin is seated in a chair. The upper part has a slight backward inclination (about 7^{o}). For the simulations described in Chapter 7, the upper part is assumed straight up. These values are indicated in Table D.2 in Appendix D. The design of the thermal mannequin is discussed in Chapter 5.2.3.

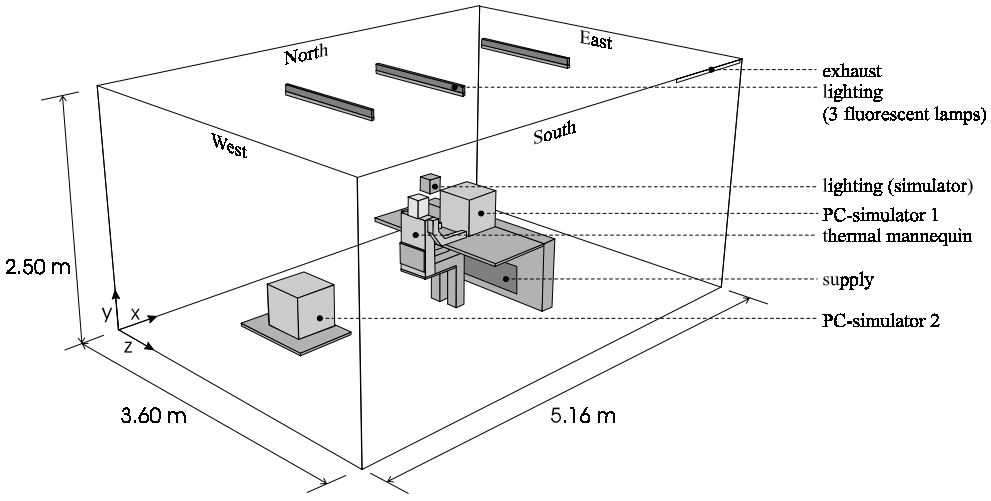

Figure 5.2. Model office room.

5.2.2 Supply system

Two different type of supply units have been investigated on velocity distribution and flow rate for application in the DDV-concept. Important demands for the supply system are:

- low velocity close to the supply area [0.05 … 0.2 m/s at 0.3 m from the supply],
- a symmetrical flow pattern over the width of the unit,
- control on the flow rate (velocity) [0.01…0.03 m^3/s] and temperature [± 3°C].

Supply units - The Desk Displacement Unit (indicated as 'unit 1') was specially designed for the DDV-concept (Loomans et al. 1996) and was obtained from the original manufacturer (Directflo Air Distribution Pty. LTD). This unit extracts air from a non-pressurised floor plenum by means of a fan which is incorporated in the unit. Three fan positions allow variation in the flow rate. The temperature is controlled through a mixing valve which allows mixing of the room air. Guiding paddles within the unit intend to improve the distribution of the air within the unit. The air is introduced into the room through a grille with a 60% aperture.

The second supply unit (indicated as 'unit 2') originally is designed as a standard displacement ventilation unit (displacement ventilation unit series QLE-U 1000×300, TROX GmbH). The air is introduced into the unit as described in Chapter 5.2.1. The supply grille has a 15% aperture. Direct adjustment of the flow parameters at this unit is not possible, but the configuration in principle allows control of the temperature and the flow rate.

Flow rate - Measurement of the flow rate for the different fan settings of unit 1 indicate that the variation in the flow rate is only 0.005 m^3/s between the lowest and the highest setting, at an average flow rate of 0.033 m^3/s at a measurement accuracy of ± 0.002 m^3/s. In the experiments the flow rate and the supply temperature of unit 2 were controlled by the air conditioning unit.

Velocity (distribution) - For both units the velocity and the velocity distribution have been measured at different planes in front of the supply grille, parallel to it. Measurements have been performed with the hot sphere anemometer (Dantec 1984). The accuracy of the measurements is estimated at 15% for velocities higher than 0.1 m/s (see Chapter 3.6). For unit 2 different flow rates have been investigated, whereas for unit 1 only the highest fan setting was used. For unit 2 the supply temperature was 3°C below the average wall temperature. Unit 1 was tested under isothermal conditions.

In Table 5.2 measured velocity characteristics are summarised for unit 1 and unit 2. In Table 5.2, $\bar{u}$ is the mean velocity over the total supply area, at a parallel plane to the supply

Table 5.2. Measured velocity characteristics for unit 1 ($\dot{V}$ = 0.036 m^3/s) and unit 2 ($\dot{V}$ = 0.029 m^3/s) at different distances to the unit.

		unit 1	$\dot{V}$ = 0.036 m^3/s	*unit 2*	$\dot{V}$ = 0.029 m^3/s
	distance =	0.1 m	0.5 m	0.08 m	0.15 m
$\bar{u}$	[m/s]	0.21	0.13	0.16	0.14
σ	[m/s]	0.10	0.05	0.07	0.06
u_{max}	[m/s]	0.61	0.26	0.39	0.31

unit at the indicated distance, σ is the standard deviation of the measured mean velocities at the plane and u_{max} is the maximum measured mean velocity at the plane. Figure 5.3 shows a typical distribution of the flow pattern for unit 2 as has been measured in three parallel planes for a flow rate of 0.019 m^3/s.

The measurement results for unit 1 (see Table 5.2) indicate very high velocities close to the supply. At 0.5 m distance the maximum velocity is still well above the draught discomfort limits (see Chapter 2.2.2). From the measured velocity distribution for unit 1 it is not possible to find a symmetry plane over the unit.

The measured velocities at unit 2 show that the velocities near the supply, especially the maximum velocity, are significantly lower than for unit 1. The velocity distribution for unit 2 shows a clear symmetry plane over the width of the supply. Highest velocities are found at the top as the air is introduced into the unit at the bottom. The supply temperature is lower than the room temperature, therefore the supplied flow is seen to drop as a result of buoyancy at larger distance from the supply (see Figure 5.3).

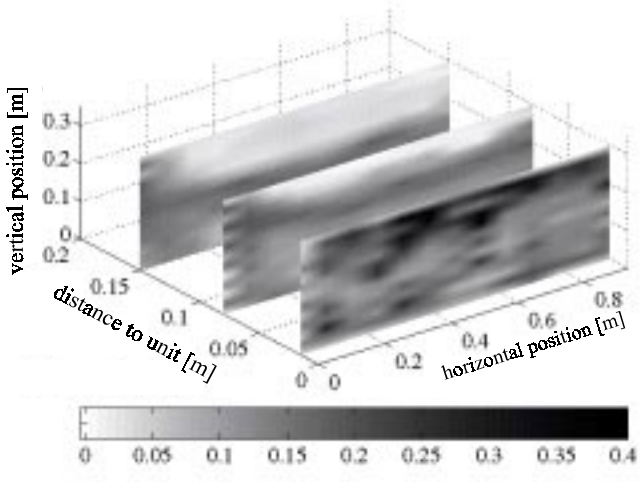

Figure 5.3. Velocity distribution at three parallel planes at different distance from the supply of unit 2 for an air flow rate of 0.019 m^3/s.

Unit selection - From the postulated demands and the above described measurement results unit 2 has been preferred for application in the experimental configuration. A vertical symmetry plane is identified in the middle of the unit, lower maximum velocities are found at a short distance to the unit and, furthermore, there are no mechanical parts in the unit. Direct control at the unit may be possible by combining the system with e.g. a Twin Duct system (Rutten 1996).

5.2.3 Heat Sources

Heat sources are used in the experimental configuration to simulate the heat load in the model office room. First the person seated at the desk is described and then the other heat sources in the room.

Person - In the DDV-concept the person that is seated at the desk forms an essential part of the total concept (see Figure 2.6). The upward convective flow around the person should deflect the horizontal impulse into a vertical flow. As this upward flow establishes itself because of the over-temperature of the body, it is important that the heat transfer and the temperature distribution of the heat source replacing a person in the experimental configuration should be realistic. Furthermore, as the person is sitting at a relative short distance from the supply, it is important that posture and dimensions of the heat source correspond with that of a human being.

A thermal mannequin has been designed that represents the proportions of the human body, both on the geometrical and on the heat transfer part. The shape and the heat distribution of the mannequin are simplified as much as possible in order to arrive at an acceptable balance between the close modelling of the mannequin and the complexity of the thermal aspects and the posture of the human body. Therefore, this mannequin *cannot* be used for thermal comfort predictions. In Appendix E the design and the dimensions of the thermal mannequin are summarised.

During normal exercise and rest the body produces heat. The metabolic rate for miscellaneous office work is set at 57.9 - 69.5 W/m^2 (Fanger 1970). The heat production per section is not evenly distributed as the distribution of e.g. the muscles mass is not proportional with the surface area of the sections. Furthermore, a basal metabolic rate and a basal evaporative heat loss is present at all time.

In Stolwijk (1971) the muscle distribution and an estimation of the heat distribution per section when cycling is given. From these data a first estimation has been derived of the heat load distribution for the thermal mannequin. Then a thermographical system was used

to compare the surface temperature distribution of the thermal mannequin and that of a real person. Following the thermographical results, the heat transfer coefficient has been increased for all but the head section by dressing the mannequin with a black cotton cloth. In this way the surface temperature was increased without additional heat input. Finally, the heat load distribution was fitted to the surface temperature of the real person (Loomans 1997). The heat input per section is provided by fans and lighting. The lighting and so the heat output can be tuned by a dimmer.

The comparison of the final result of the surface temperature distribution for the thermal mannequin is shown in Figure 5.4. In Appendix D the distribution of the total heat input per section ($Q_{section}$) is given. When the estimated latent heat loss (~21 W; Stolwijk 1971) is added to the total heat input, the metabolic rate for the thermal mannequin can be calculated at 76 W/m^2. This metabolic rate can be compared to that of miscellaneous office work (57.9 - 69.5 W/m^2) and laboratory work (81.4 - 93.0 W/m^2; Fanger 1970). The metabolism of the person (the experimenter) shown in Figure 5.4 was more close to that of laboratory work. With reference to the inter-individual differences in the metabolic rate (see Chapter 2.2.2), the total heat input in the thermal mannequin is assumed representative for performing experimental and numerical simulations with.

Based on the temperature distribution and the heat input, the convective part of the heat input has been estimated. The experiments were performed in a climatised room with an ambient temperature of 22^{o}C. Assuming that the mean radiant temperature (T_{mrt}) equals the ambient temperature, in Appendix D, Table D.2, the convective part of the heat input ($Q_{section\_c}$), in relation to the total heat input per section, is summarised.

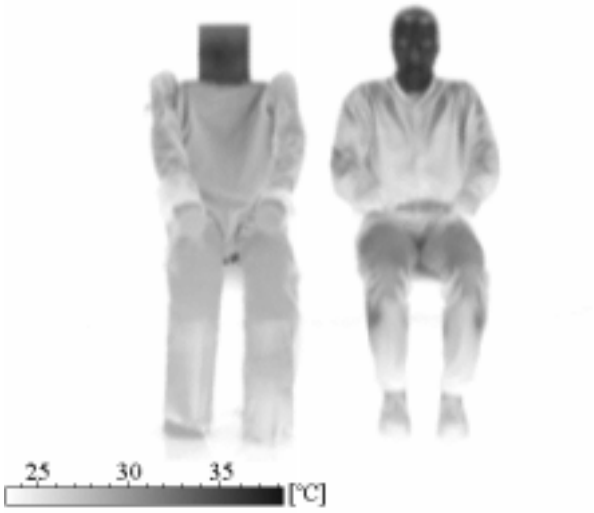

Figure 5.4. Surface temperature distribution for the thermal mannequin and a person measured from the front side.

In this procedure no correction was made for the fact that part of the leg- and chest-section was covered by the chair. This chair however was also used in the experiments. Furthermore, T_{mrt} was not corrected for the influence of radiant heat transfer from the different sections. The derived convective part of the heat transfer therefore will be underestimated. However, the actual experimental set-up will also have an effect on the heat transfer characteristics. This effect is difficult to determine. Therefore, the inaccuracy with which the convective part of the heat input has been determined is estimated at 10%. As the plume flow rate ($\dot{V}$) scales with $Q^{1/3}$ (Kofoed and Nielsen 1988), the plume flow rate may vary by 3%.

Other heat sources - To allow an increased heat load in the model office room different heat sources have been added. They represent typical features of an office room. Their shapes however have been simplified as much as possible.

PC-simulator - The PC-simulator is represented by a $0.4 \times 0.4 \times 0.4$ m^3 black painted plywood box with aluminium foil at the inside. The bottom part was open and the box was lifted 0.002 m from the table creating a slot along its circumference. The top consisted of a perforated aluminium plate (perforation ratio: 0.05), painted black on the outside. In the box a 100 W heat source (bowl reflector lamp) was placed at the floor in the middle of the box. In total two PC-simulators were placed in the model office room.

Lighting simulator - A desk lighting simulator was represented by a $0.15 \times 0.15 \times 0.15$ m^3 black painted closed plywood box with a wooden inner surface. In the middle of the box a 25 W heat source was placed.

Fluorescent lighting - Three 36 W TL-D fluorescent lamps without reflector have been mounted against the ceiling of the model office room. The ballast for each fluorescent lamp consumed approximately 14 W.

For each heat source the radiant part of the total heat input has been determined via infrared thermography, similar to the procedure for the thermal mannequin. The convective part then was calculated from these data. For the fluorescent lamps manufacturer data have been used to determine the convective heat input. The convective part of the heat input of the ballast was estimated at 50%. The convective part of the total heat load is summarised in Appendix D, Table D.1.

In Figure 5.5 a photograph is shown of the model office room in the climate chamber configuration, with the thermal mannequin sitting at the desk. The other heat sources are not shown in Figure 5.5. The traversing system will be discussed in Chapter 5.4.1.

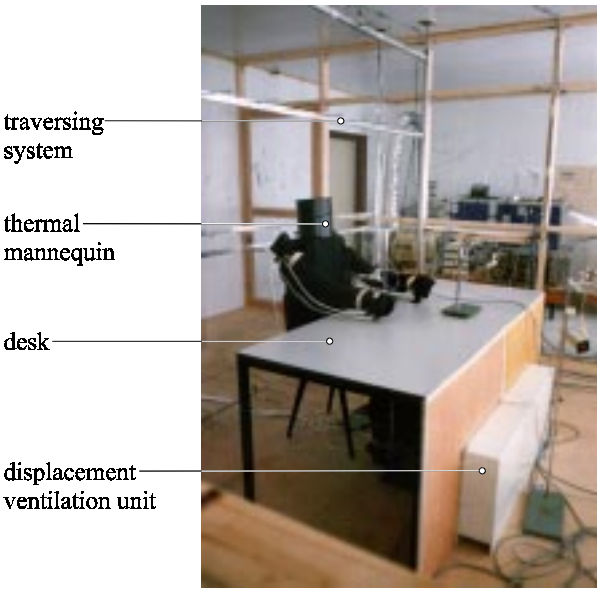

Figure 5.5. Overview of the climate chamber configuration.

5.3 MEASUREMENT EQUIPMENT

5.3.1 Velocity measurement system

In total twelve hot sphere anemometers (Low Velocity Transducer 54R10; Dantec 1984) have been used. A special configuration was made in combination with the 54N21 3-channel Input Module (Dantec) and an A/D converter (DATAshuttle DS-12-8-GP; Strawberry Tree 1995) to allow a simultaneous 10 Hz sampling frequency and storage of the bridge voltage output for all anemometers with an accuracy of 0.3% of the reading.

Calibration of the anemometers was performed according to the procedure described in Chapter 3.6. The anemometers have been calibrated in vertical and horizontal position. The calibration data were summarised in a calibration table. The accuracy of the measurements is determined at ±0.025 m/s at velocities between 0.05 - 0.50 m/s.

5.3.2 Temperature measurement system

In the experiments 40 type T thermocouples (copper-constantan) have been used for the measurement of the air temperature. An HP-3825A data acquisition/control unit has been applied to register the thermocouple output.

The wall temperatures have been measured with positive temperature coefficient resistors (PTC's). Squirrel meter/loggers have been applied to register the PTC output. In total 12 PTC's have been used to measure the wall temperatures, and two to measure the supply respectively the exhaust temperature. The wall temperature distribution has been determined with infrared thermography. For the walls that are directly controlled by the climate chamber control unit, the variation in temperature is less than 0.5^{o}C. For the indirectly controlled side walls a temperature gradient will result from the prevailing thermal conditions. The wall temperature was measured at two heights (1.0 m and 2.0 m). The averaged value was assumed as the average wall temperature. The floor temperature distribution will be influenced by the supplied colder air. The floor temperature has been measured at a position 2.0 m in front of the supply and at a position at the other side of the desk. The averaged value is assumed to represent the average floor temperature. The air temperature at seven positions close to the thermal mannequin also has been measured with PTC's, in order to determine the local air temperature distribution.

Calibration of the thermocouples and PTC's is performed applying the reference principle. A small climate chamber (Weiss SB22 160/40) was used to calibrate the sensors under different climatic conditions. All applied thermocouples and PTC's were calibrated under the same conditions. Only the temperature measurements obtained from these calibrated sensors have been used in the description of the experimental conditions and the measurement results. The accuracy of the temperature measurements with the thermocouples is determined at ±0.1^{o}C and with the PTC's at registration accuracy (±0.125^{o}C).

5.3.3 Supplementary measurement systems

Besides velocity and temperature, the flow rate and the heat input have been registered. The flow rate has been determined with a Validyne DP103-10 differential pressure transducer with 0.5% accuracy. The readings are corrected for the registered air temperature at the Venturi nozzle.

The heat input has been measured with a watt meter (erichMarek, type 55.21, accuracy 0.5% of full scale). Two watt-meters were applied, one for registering the heat input at the thermal mannequin and one for the remaining heat sources.

5.3.4 Data handling

A data handling procedure has been designed within the Matlab environment (The Mathworks 1993) to allow a fast transfer of all measurement readings into an uniform

output: a file with the boundary conditions and files with the velocity and the temperature readings at their respective *x*-*y*-*z* positions in the room. Calibration tables for the velocity, temperature and flow rate readings were used to transfer the measurement results. For the total heat input a further subdivision was made into the convective heat load of the different sections of the thermal mannequin and the other heat sources. Within the Matlab environment several graphical routines are available to view the results.

For the velocity readings the measured bridge voltage at zero velocity can be entered as the reference point. The indicated position of the anemometer and the direction at which the flow approaches the anemometer determine which calibration data from the calibration table are being used. Finally, the velocity is filtered for measurement readings below the anemometer specification level of 0.05 m/s. If more than 90% of the velocity readings during one measurement are below 0.05 m/s, the measurement could be rejected.

The thermocouples were not shielded from radiant heat transfer. On the one hand shielding may negate the influence of radiation effects, but on the other hand such shields impede the normal air flow at the measurement point. Instead, the temperature measurement obtained form a thermocouple has been corrected for radiant heat transfer from the walls by applying the measured wall temperatures and the location of the sensor in the room (Peng 1996). No correction is made for the influence of the heat sources on the measured temperature.

5.4 MEASUREMENT PROCEDURE

5.4.1 Traversing system

A manually operated traversing system was designed and built to allow measurement at different positions in the room. The system consists of two vertical posts that can be clamped between the floor and the ceiling. Between the two posts horizontal aluminium supports can be positioned at different heights. At these supports anemometers or thermocouples can be fixed at the required *x*-*y*-*z* position. The total construction can be moved through the test room and the horizontal support can be changed over the height. Two of these constructions are placed in the room. Both the volume and the cross section of the traversing system are negligible (<< 0.1% of the total volume/cross section).

5.4.2 Measurement time

A full scale measurement consists of 520 thermocouple measurements at different positions, sampled at a frequency of 0.1 Hz over 180 seconds, and 132 velocity measurements at different positions, sampled at 10 Hz over 180 seconds. Furthermore, the wall temperature, the heat input and the flow rate were registered during all measurements.

All registration values were used to determine the mean velocity and the standard deviation. The statistical independence of the samples was ignored (see Chapter 3.3). Measurement results (measurement period of 1 hour) for some typical positions in the flow pattern of the model office room indicated that the standard deviation in the mean velocity between sampling at 10 Hz and at 0.2 Hz is in the order of 0.5% and smaller.

For each measurement 40 thermocouples and 10 velocity transducers are put into their specific *x-y-z* position using the traversing system. For one full scale measurement the traversing system is moved in total 13 times into a new position (horizontally and/or vertically). Between the movement of the traversing system and the new measurement a waiting time is required to allow the flow pattern to recover to its original steady state situation.

Measurements have been performed to determine the recovery time of the flow pattern after a disturbance. For these measurements a fan was used which allowed thorough mixing of the air flow in the room. Before, during and after mixing, the air velocity and temperature were registered at different *x-y-z* positions in the configuration. Figure 5.6 and 5.7 show the measured velocity and temperature variation for a situation with an air change rate (*ACH*) of 0.75 h^{-1} ($\dot{V}$ = 0.010 m^3/s) and a displacement ventilation type of flow pattern (T_{wall} - T_{supply} = 3.0^{o}C, heat input from the thermal mannequin only).

In Figure 5.6 and 5.7 the bold dashed lines indicate the start and the end point of the flow disturbance. Velocities up to 1 m/s have been measured when the fan was mixing the air. The velocity however is seen to recover within five minutes after the disturbance has stopped. The longest recovery time is found for the buoyant plume (velocity > 0.1 m/s) as it has to re-establish itself.

As a result of the mixing the vertical temperature gradient in the room almost vanishes. The temperature distribution is seen to follow an exponential course after the disturbance stopped and the extra heat input was removed from the room. Steady state conditions are obtained within 15 minutes. The deviation from the steady state conditions before the disturbance is less than 0.1^{o}C. This effect partly results from a small increase in the floor temperature (~0.1^{o}C) during the measurements, which is within the control accuracy.

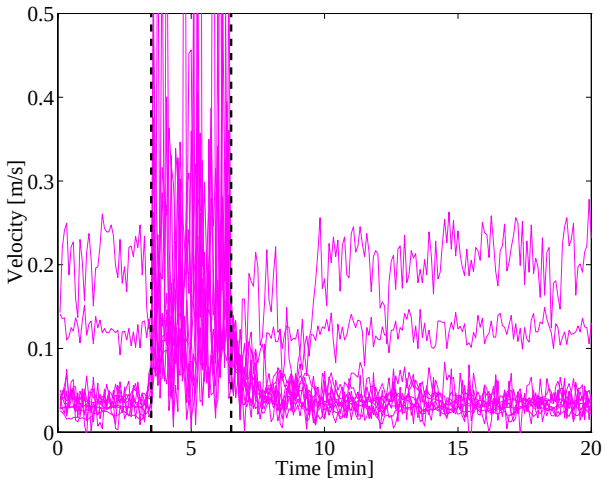

Figure 5.6. Velocity as function of time at twelve positions in the model office room before, during and after a disturbance; [| | |] *: start- and end-point of the flow disturbance.*

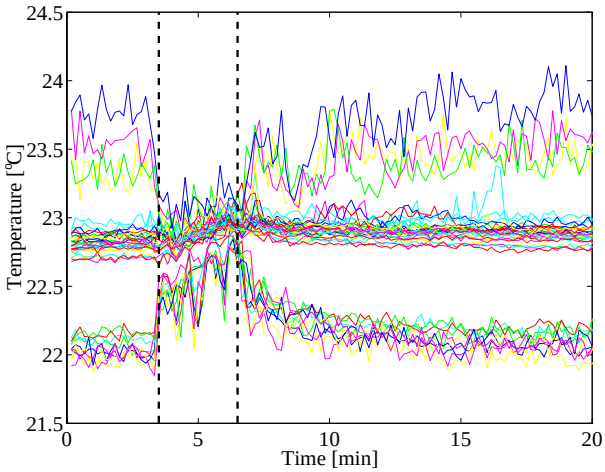

Figure 5.7. Temperature as function of time at 40 positions in the model office room before, during and after a disturbance; [| | |] *: start- and end-point of the flow disturbance.*

From these results the waiting time after a disturbance due to the repositioning of the traversing system was determined at 30 minutes minimum for ACH = 0.75 h^{-1}. The actual flow disturbance during the measurements due to the repositioning is smaller than for the above described experiments, as only one person walks quietly through the room.

5.4.3 Boundary conditions

Wall temperatures - The steady state boundary conditions for the flow pattern under investigation must be controlled rigidly during the measurements. For the full-scale measurements the wall temperature variation typically could be controlled within a standard deviation of 0.15^{o}C. For the floor and ceiling the deviation typically was smaller than 0.1^{o}C.

Heat input - An A.C. voltage stabiliser (Philips PE 1404/11) was used to control the variation in the heat input to within 1% of the total heat input. A ratio of distribution was applied to determine the heat input to the separate sources (see Appendix F). The heat load per heat source was checked regularly.

Flow rate - The flow rate was determined from the Venturi nozzle and the pressure transducer. The actual flow rate however deviated from the imposed flow rate as leakages were present in the duct system between the flow rate measurement point and the displacement ventilation unit. This difference was only revealed after an improvement of the numerical algorithm to determine the local mean age of the air from accurate tracer gas measurements (Roos 1998[a]).

In the search for leakages smoke visualisation has been used. From these visualisations it was confirmed that no significant leakages were present in the model office room itself. Therefore the flow rate introduced at the supply can be expected to leave the room via the exhaust. As a result the measurements of the local mean age of the air as presented by Roos (1998[a] and 1998[b]) can be used to determine a correction for the flow rate as measured with the Venturi nozzle. This correction is applied in the full-scale measurements. Due to this indirect procedure, the accuracy with which the flow rate can be determined is estimated at 5%.

Chapter 6

RESULTS OF FULL-SCALE EXPERIMENTS

6.1 INTRODUCTION

Full-scale measurements have been performed for different boundary conditions applying the experimental configuration described in the previous chapter. In this chapter focus is on the measurement data rather than the evaluation of the Desk Displacement Ventilation (DDV-) concept. The concept will be evaluated in Chapter 8.

First the investigated cases are summarised, then the results are described. The description of the results is subdivided by the type of flow pattern: displacement ventilation or mixing ventilation. The flow pattern is described qualitatively and quantitatively. Finally the results are discussed in relation to results from comparable research found in literature.

6.2 CASE DESCRIPTION

The temperature difference between supply and exhaust air and the supply flow rate ($\dot{V}$) determine the convective cooling capacity of the DDV-system. In this configuration the walls are controlled at a fixed temperature T_{wall}. As a result the wall heat transfer will also have a contribution to the room heat balance. The vertical temperature gradient is determined by the heat load in the room, the air change rate and the diffusion of the flow. This gradient influences the plume above a heat source.

Therefore, the most important variables that determine the room air flow pattern and the thermal conditions are:

- Temperature difference between supply air and wall temperature ($\Delta T = T_{supply} - T_{wall}$);
- Air change rate (ACH) [$= 3600 \cdot \dot{V} / V$ [h^{-1}])];
- Heat load in the room (Q).

Given the described configuration (see Figure 5.2), a displacement ventilation flow pattern is expected when $\Delta T < 0^{o}$C and a mixing ventilation flow pattern when $\Delta T > 0^{o}$C (see Figure 1.1). A further necessary requirement for a displacement type of flow pattern is that, above a certain relevant height, the interface height, the flow rate in the plume(s) is larger than the supply flow rate.

The maximum temperature difference between the wall and the supply air has been restricted to approximately $|\Delta T| = 3^{o}$C. This value is derived from the maximum vertical air temperature difference that is allowed to occur within the occupied zone (0.1 m - 1.7 m) for prevention of local discomfort (ASHRAE 1992; see Chapter 2.2.2). This criterion may be critical in the application of the desk displacement ventilation concept and will limit the cooling load capacity of this system. It will be discussed further in Chapter 8. Though the mean room temperature is of less importance, it has been kept in the order of 20 - 23^{o}C. ASHRAE (1992) defines a minimum operative temperature of 18^{o}C for sedentary occupancy.

The air change rate has been varied between a minimum of $ACH \approx 0.75$ h^{-1} ($\dot{V} \approx 0.010$ m^3/s) and a maximum of $ACH \approx 3.7$ h^{-1} ($\dot{V} \approx 0.047$ m^3/s). $\dot{V} \approx 0.010$ m^3/s presents the lower limit of the flow rate for one person in an office room, with regard to the steady state CO_2 concentration and the perceived indoor air quality (Liddament 1996). Due to draught discomfort requirements, the maximum flow rate has been limited to $\dot{V} \approx 0.047$ m^3/s. At $\dot{V} = 0.029$ m^3/s velocities up to 0.25 m/s were registered at 0.15 m from the supply unit. This already may be critical for draught sensation especially as the supply temperature is below room temperature. The highest investigated air change rate was investigated especially for comparison with numerical simulations.

The flow rate in the plume above a person is about 0.03 m^3/s at 0.75 m above the person (Mundt 1996, Mierzwinski 1981). The highest supply flow rate of 0.047 m^3/s is considerably higher than the flow rate above a person. This means that additional sources are necessary to keep the interface height at a relevant level. The extra heat input in the room results from the sources described in Chapter 5. Two heat load variants have been investigated. In the low heat load case ($Q \approx 125$ W) only the thermal mannequin is activated as heat source in the room. For the high heat load case ($Q \approx 500$ W) all available heat sources have been activated. The latter case presents a more realistic heat load situation for an office room in the interior zone of a building ($\dot{q} = 27$ W/m^2).

Table 6.1 summarises the different cases that have been investigated. This research has been focussed on displacement ventilation flow patterns because the DDV-concept is assumed to operate under these conditions in the micro-climate. For the lowest air change rates ΔT has

Table 6.1. Case description full-scale measurements.

case	ΔT [°C]	Q [W]	ACH [h^{-1}]	$\dot{V}$ [m^3/s]	abbreviation
1	-2.5	125	0.75	0.010	T-Q-V-
2	-3	125	2.3	0.029	T-Q-V+
3	-2.5	500	0.75	0.010	T-Q+V-
4	-3	500	1.5	0.019	T-Q+V×
5	-3	500	2.3	0.029	T-Q+V+
6	-3	500	3.7	0.047	T-Q+V*
7	-1	500	2.3	0.029	T×Q+V+
8	+3	500	1.5	0.019	T+Q+V×

been set at -2.5°C due to restrictions in the cooling capacity of the air conditioning unit and heat pick up over the distance over which the air was distributed to the supply unit.

The wall temperatures are controlled, therefore a reduced air change rate at constant supply and wall temperatures will result in an increased wall heat transfer in the total heat balance. The convective cooling capacity of the DDV-system then will be reduced. This capacity is defined as $\rho c_p \dot{V} (T_{exhaust} - T_{supply})$. Case 7 has been investigated to determine whether an increased supply temperature at a constant flow rate will present similar results as case 3. Case 8 presents a mixing ventilation case where the supplied flow heats up the room.

To indicate a case description in the text, each case is given an abbreviation. This is indicated in the last column of Table 6.1. In the abbreviated form T, Q and V stand for ΔT, Q and ACH respectively. The interpretation of the symbols can be taken from their respective values in Table 6.1. Besides the investigated parameters, the system performance is influenced by numerous other parameters, e.g., the disturbance of the flow by additional ventilation systems or the location of the unit in the room. These variables have not been investigated further.

6.3 RESULTS

6.3.1 Displacement ventilation conditions (cooling)

Qualitative description - A displacement ventilation flow pattern is established if $\Delta T < 0$°C. In Figure 6.1 the characteristic features of the displacement ventilation flow pattern in the central plane of the room and at a horizontal plane at approximately 0.1 m above floor level are sketched. The flow pattern was sketched from video recordings of the diffusion of smoke. In Figure 6.2 some details of the visualisations are shown. These visualisations are obtained for case 3 [T-Q+V-] and are typical for cases with a displacement ventilation flow pattern.

The incoming flow is colder than the room air temperature. As a result the air cascades down after the supply (Figure 6.2a) and spreads over the total floor area, similar to water in a bath tub (see Figure 6.1). The supply air will remain near floor level and is only carried along to ceiling level by induction into the buoyant plumes caused by the individual heat sources in the room (Figure 6.2b and 6.2c). For the visualisation of the buoyant plume of the thermal mannequin the smoke was introduced at the lap of the mannequin.

The free convection boundary layer at the person cannot entrain fully the total amount of fresh air. It entrains a part of the supplied air at once, the remaining moves in the circulation as shown in Figure 6.1. With a decreasing buoyancy, the air might circulate several times before being entrained. Assuming that otherwise no air can entrain the flow near the floor, an interface is found at the height where the supply flow rate equals the convection flow rate in the plume(s),

$$\dot{V}_{supply} = \dot{V}_{plume(s)} \,. \tag{6.1}$$

Due to the strong vertical temperature gradient a clear distinction between the different layers can be found (Figure 6.2d). The distinctive stratification at the interface is described by Krühne (1996) by measurement of the vertical contaminant gradient of particles released in the plume. For higher supply flow rates the interface height increases when the heat load and source types are not changed.

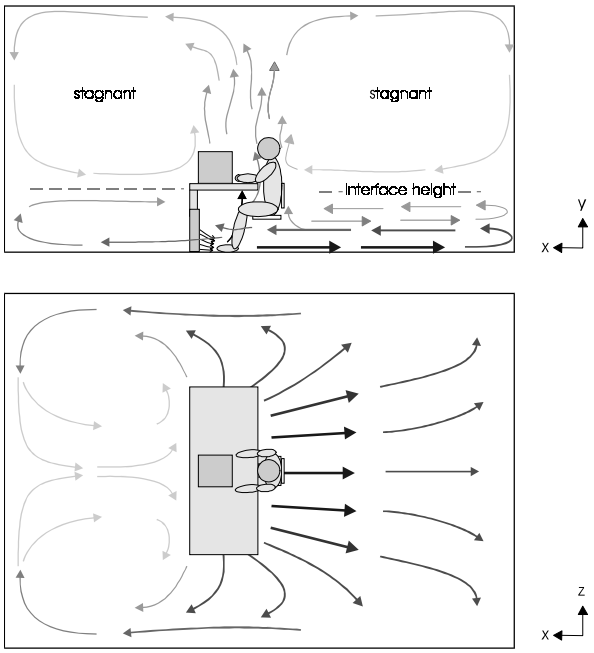

Figure 6.1. Flow features of the displacement ventilation flow pattern in the central plane of the room and at a horizontal plane at ~0.1 m above floor level.

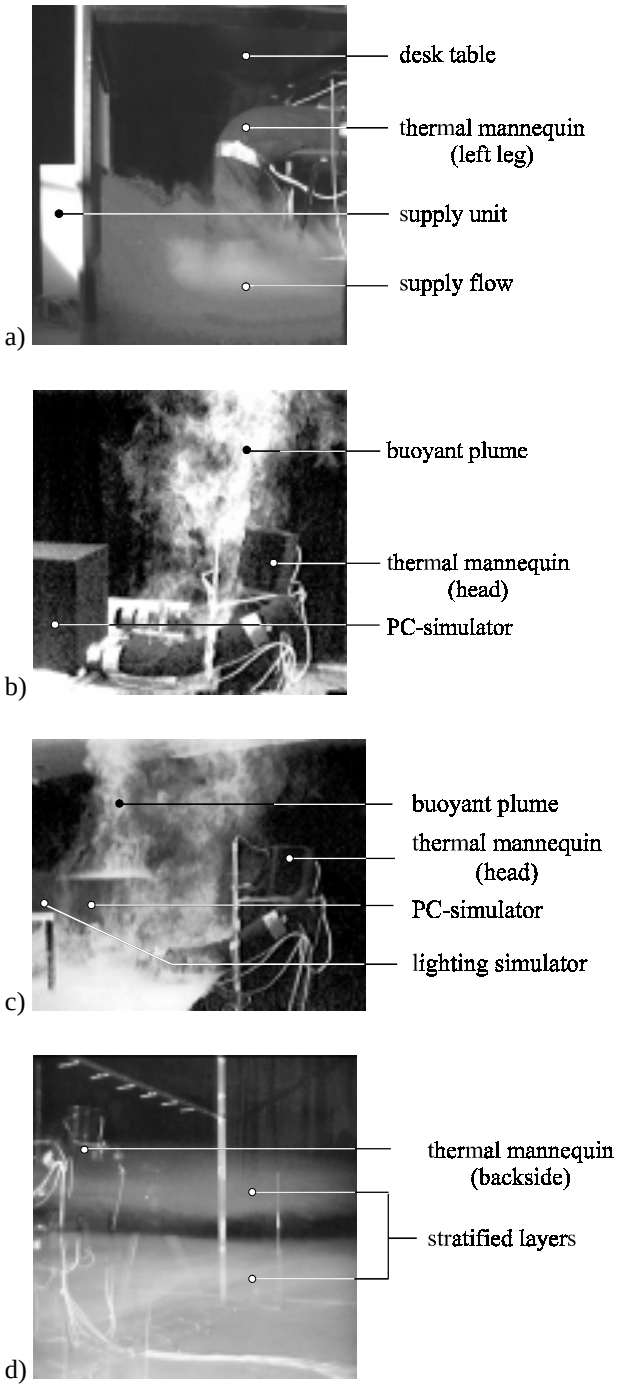

Figure 6.2. Visualisations of the displacement ventilation flow pattern (for case 3 [T-Q+V-]).

Quantitative description- The measurement results have been obtained according to the procedure as described in Chapter 5. All cases (except case 7 [T×Q+V+]) have been repeated in order to check the reproducibility of the measurements. The reproducibility was determined to be within measurement accuracy (Loomans 1998). In most of these measurements the *x*-*y*-*z* positions have been monitored in opposite order to determine any possible influence due to the measurement procedure. Measured temperatures and velocities are available in *x*-*y*-*z* format for all cases and can be downloaded from the internet (http:// www.tue.nl/bwk/bfa/research/aio_research.html). The prevailing boundary conditions for each case are summarised in Appendix F.

An example of the measured temperature distribution at different planes in the room is shown in Figure 6.3. The applied traversing system (see Chapter 5) confined the measurement area to y = 0.1 to 2.3 m, for x = 0.75 to 2.0 m and x = 3.5 to 4.5 m, and y = 1.5 to 2.3 m, for x = 2.25 to 3.0 m. In the z-direction measurements were taken between z = 0.675 m and z = 2.925 m. Figure 6.4a to d present the contour lines for the planes shown in Figure 6.3 and for plane x = 2.25 m. From these results it can be concluded that the horizontal temperature differences are small compared to the vertical ones, except for the buoyant plumes. The temperature gradient at y = 0.1 m is clearly larger at the supply side of the desk (x = 0.75 m) than at the opposite side (x = 4.50 m). These results are typical for all investigated displacement ventilated cases.

The velocity in a large part of the room is below the specified level of 0.05 m/s and therefore cannot be measured reliably. Only in the buoyant plumes velocities higher than 0.05 m/s are measured. The velocity measurements therefore have been limited to the

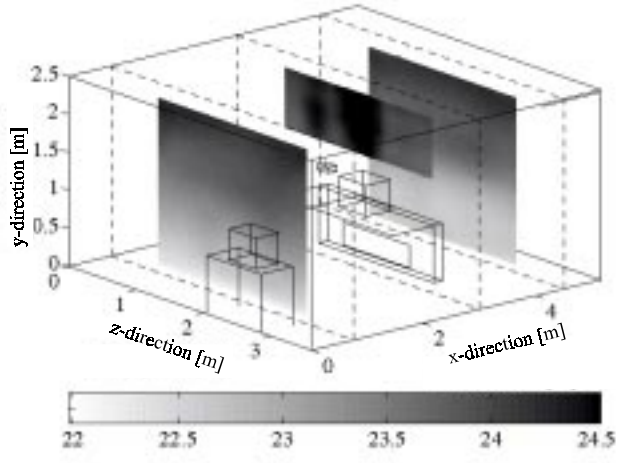

Figure 6.3. Measured temperature distribution for case 4 [T-Q+V×] (x = 0.75 / 3.0 [PC-simulator] / 4.5 m) in [°C].

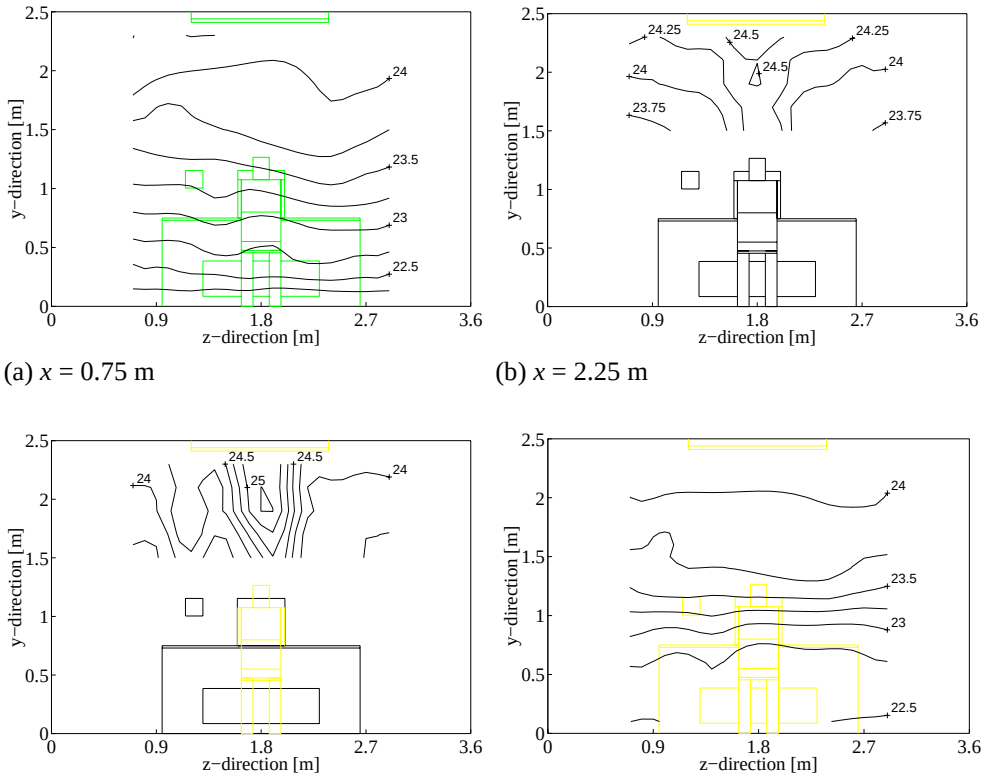

(a) x = 0.75 m (b) x = 2.25 m

(c) x = 3.00 m (b) x = 4.50 m

Figure 6.4. Measured temperature distribution for case 4 [T-Q+V×] in four different planes (x = 0.75 / 2.25 [thermal mannequin] / 3.0 [PC-simulator] / 4.5 m) in [°C].

plume, in particular above the thermal mannequin. Figure 6.5 presents measurement results for two planes above the thermal mannequin and one plane above the PC-simulator. From these results it can be concluded that the plumes remain confined to a small area above the heat source. The impinging plume will spread along the ceiling. This, however, could not be measured as the measurement points closest to the ceiling fall, for practical reasons, well beyond the area of interest.

The velocity in the plume above the PC-simulator is clearly higher than above the thermal mannequin. The influence of the lighting simulator on the flow pattern can be seen clearly at x = 3.0 m. Though the measurement plane does not cut the lighting simulator and its buoyant plume, at ceiling level the measured velocities are significantly higher. From the results it is clear that two separate plumes exist above the heat sources that are placed on the desk. This also applies to the plume above the thermal mannequin and the PC-simulator.

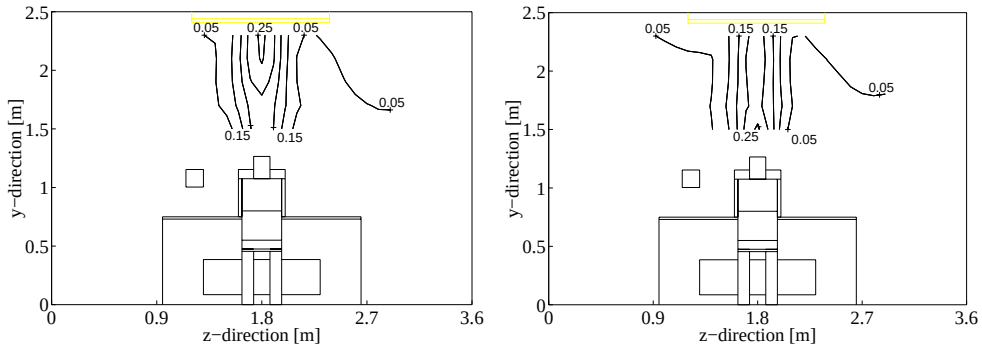

(a) x = 2.25 m (b) x = 2.40 m

(c) x = 3.00 m

Figure 6.5. Measured velocity distribution for case 4 [T-Q+V×] in three planes (x = 2.25/ 2.4 m: thermal mannequin, x = 3.0 m: PC-simulator) in [m/s].

6.3.2 Mixing ventilation conditions (heating)

Qualitative description - A mixing ventilation flow pattern is established when $\Delta T > 0^{o}$C. In Figure 6.6 the characteristic features of this flow pattern in the central plane of the room are sketched. In Figure 6.7 some visualisations are shown.

Because of the positive buoyancy effect, the air flow close to the supply unit is directed upwards (Figure 6.7a). The desk table however obstructs the flow and the supply flow is distributed underneath the desk table before it can enter the upper part of the room (Figure 6.7b). As a result the buoyant plume of the thermal mannequin is less confined than in the displacement ventilation case (Figure 6.7c). The air is thoroughly mixed with the exception of the air layer immediately above the floor, where the air is cooled by the cold floor. Near the walls a downward flow transports air into the lower room level. The air near floor level is predominantly transported into higher room levels through entrainment into the convection plume of the thermal mannequin.

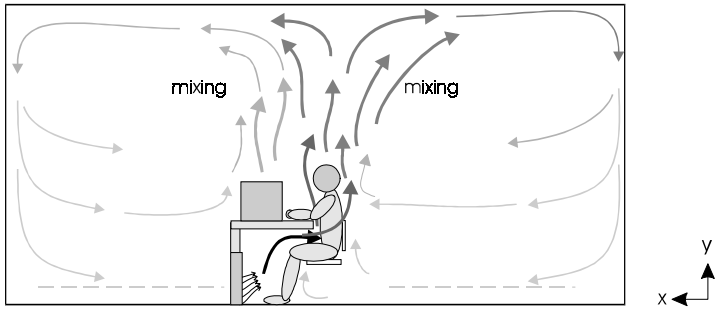

Figure 6.6. Flow features of the mixing ventilation flow pattern in the central plane of the room.

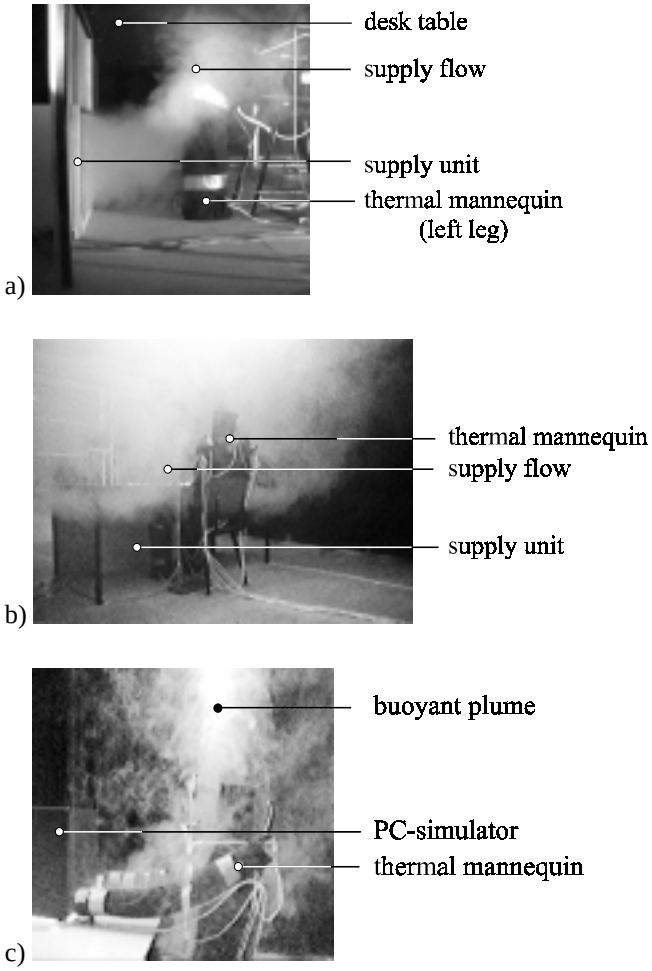

Figure 6.7. Visualisations of the mixing ventilation flow pattern (for case 8 [T+Q+V×]).

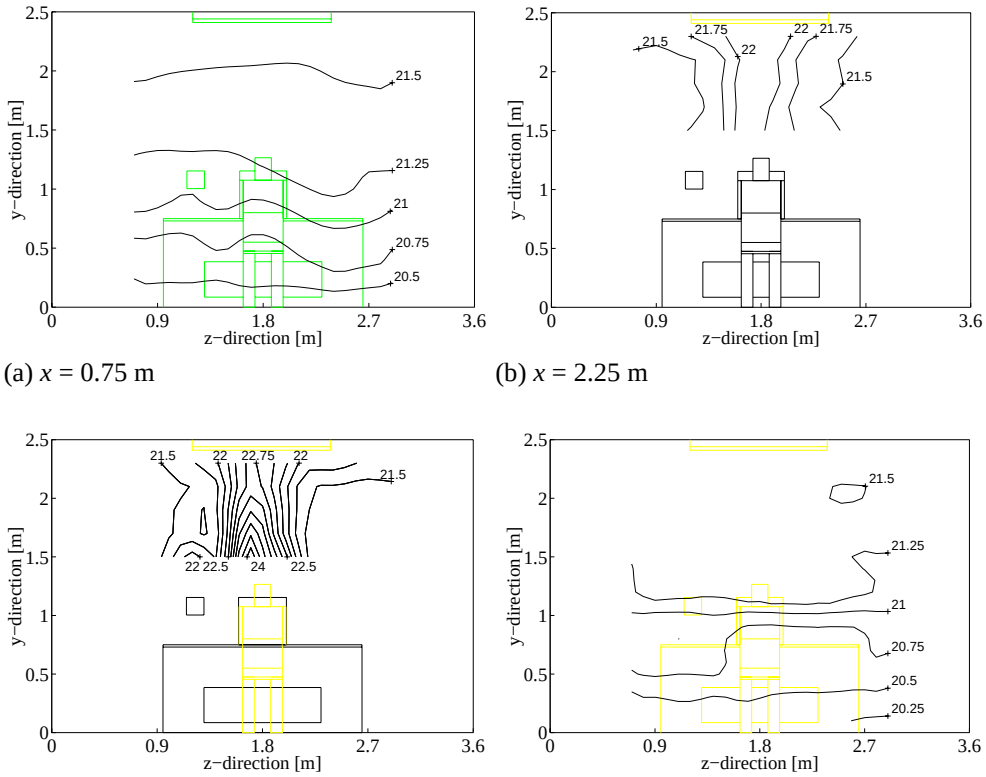

(a) x = 0.75 m (b) x = 2.25 m

(c) x = 3.00 m (d) x = 4.50 m

Figure 6.8. Measured temperature distribution for case 8 [T+Q+V×] in four different planes (x = 0.75 / 2.25 [thermal mannequin] / 3.0 [PC-simulator] / 4.5 m) in [°C].

Quantitative description - The temperature distribution at different planes in the room measured for case 8 [T+Q+V×] are presented in Figure 6.8a to d. As for the displacement ventilation case, the horizontal temperature distribution is small compared to the vertical one. The vertical temperature gradient for the upper part of the room is relatively small compared to the one obtained for the displacement ventilation flow pattern. There is no obvious temperature difference between the two sides of the desk, as found for the case with displacement ventilation.

The velocity measurements also indicate the thermal plumes above the heat sources (Figure 6.9a to c). Outside the plumes, near the table edge, higher velocities are measured due to the rising flow as is visualised in Figure 6.7b. The measured plume velocities above the PC-simulator are lower than for the case with displacement ventilation at slightly higher turbulence intensities. This is caused by the increased entrainment of air into the rising flow near the table edge. This entrainment suppresses the plume development above the PC-simulator.

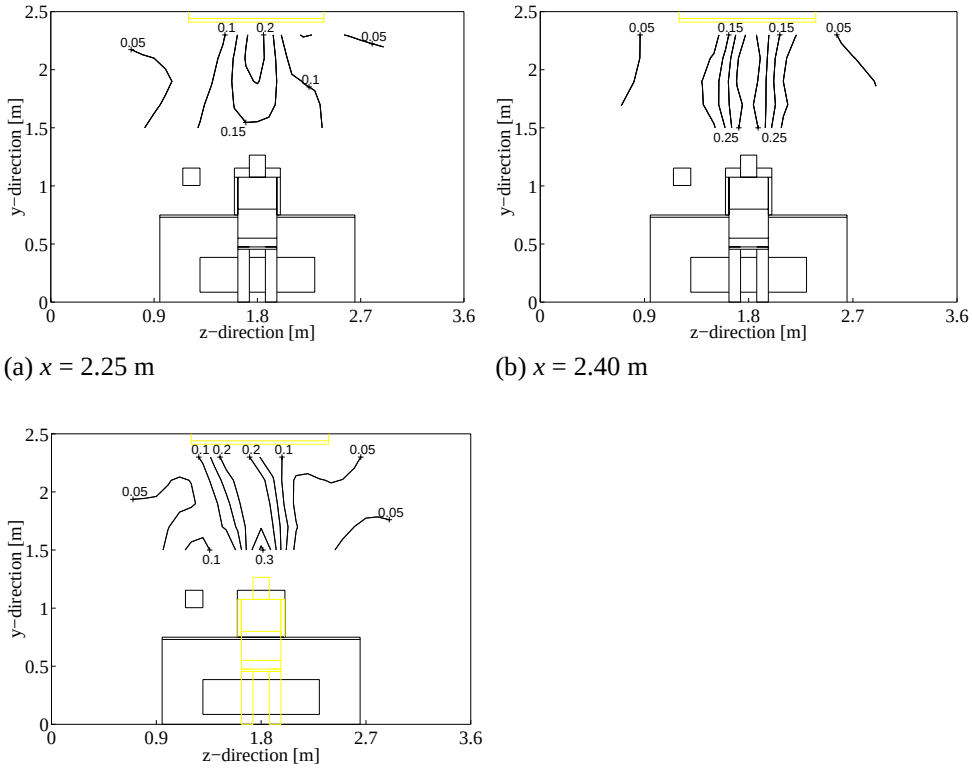

(a) x = 2.25 m (b) x = 2.40 m

(c) x = 3.00 m

Figure 6.9. Measured velocity distribution for case 8 [T+Q+V×] in three planes (x = 2.25 m: thermal mannequin, x = 3.0 m: PC-simulator) in [m/s].

6.4 DISCUSSION OF THE MEASUREMENT RESULTS

This section describes additional characteristics of the full-scale measurements. The heat balance, the vertical temperature gradient, the wall heat transfer characteristics and the plume characteristics are discussed. In order to determine the reliability of the measurements, the results have been compared to results described by Mundt (1996) and Krühne (1995). The discussion deals with whole room displacement ventilation flow patterns instead of the micro-climate only. The applicability of the DDV-concept will be discussed extensively in Chapter 8. This approach follows from the visualisation results, which indicate a normal whole room displacement ventilation flow pattern.

6.4.1 Heat balance

The surface temperature of the enclosure was controlled (see Chapter 5.4.3). In the experiments, therefore, part of the heat load is transferred to the walls. It has not been possible to determine the heat transfer through the walls with this climate chamber. As the heat transfer is low it was not ventured to measure the heat transfer at the surface. Therefore it is not possible to set-up the heat balance for the total configuration. The heat balance and the wall heat transfer will be discussed further in Chapter 7. In that chapter simulation results are described for the investigated configuration. The effect of heat transfer at the wall on the characteristics of the flow pattern will be discussed further in the section 6.4.2.

Instead of the heat balance, the heat loss through ventilation ($Q_{c\_v} = \rho c_p \dot{V} (T_{exhaust} - T_{supply})$) has been determined in relation to the total convective heat input (Q_{tot_c}). This relation is defined as the air cooling fraction (ξ),

$$\xi = Q_{c\_v} / Q_{tot\_c} \; . \qquad (6.2)$$

The air cooling fraction has been determined for each case and is given in Table F.3 (Appendix F). The air cooling fraction ranges from 0.16 for case 3 [T-Q+V-] to 1.89 for case 2 [T-Q-V+]. This means that for case 3 more than 80% of the heat input is transferred to the walls, neglecting possible heat input from (one of) the walls into the room. In contrast, for case 2 the total heat transfer rate indicates that the walls may be considered as an additional heat source. For all other investigated cases ξ is smaller than one.

In all cases the room air temperature at 2.3 m height is higher than the exhaust temperature. This is due to the convective heat transfer at the ceiling. As the ceiling temperature is lower than the air temperature, the ceiling operates as a cooled ceiling. The exhaust is situated just beneath the ceiling. The air that leaves the room through the exhaust therefore is cooled to some degree.

The temperature difference between any two walls on average is less than 0.5°C (Table F.1). As the wall temperatures are controlled there is no such influence of radiant heat transfer between the ceiling and the floor as described by Krühne (1995) and Müller and Renz (1996).

An example of a practical configuration in which the wall heat transfer cannot be neglected is found in a room with displacement ventilation and a radiant cooled ceiling. Normally, the load that can be cooled by displacement ventilation is limited for thermal comfort reasons (Fitzner 1996). For high thermal loads a radiant cooled ceiling may be incorporated to remove part of the heat load while maintaining the displacement ventilation flow pattern (Krühne 1996).

6.4.2 Vertical temperature gradient

The separate cases (see Table 6.1) can be compared in relation to the vertical temperature profile. The mean temperature, $\overline{T}_y$, at different heights (y) has been determined from the temperature measured at six positions in the room outside the buoyant plume (x = 1.50 / 2.00 / 4.50 m; z = 0.675 / 2.925 m). The dimensionless temperature (θ_y) then is calculated from

$$\theta_y = \frac{\overline{T}_y - T_{supply}}{T_{exhaust} - T_{supply}} = \frac{\sum_{n=1}^{6} \left(T_{y,n}/6\right) - T_{supply}}{T_{exhaust} - T_{supply}} . \qquad (6.3)$$

$\overline{T}_y$ has been determined for all cases and is summarised in Table F.4, Appendix F. The dimensionless temperature can be derived from Table F.3 and F.4.

Low heat load / High heat load - Figure 6.10 presents the comparison of the temperature profiles for the low (case 1 [T-Q-V-] and 2 [T-Q-V+]) and high (case 3 [T-Q+V-] and 5 [T-Q+V+]) heat load cases for a supply flow rate of 0.010 m^3/s (case 1 and 3) and 0.029 m^3/s (case 2 and 5). As the results between the two measurements for one case on average is smaller than 0.1°C, in the figure only one result per case is shown.

Clear differences are found in the temperature profiles. The averaged room air temperature is higher for the high heat load cases. As a result of the higher exhaust temperature, the dimensionless temperature at floor level is lower. Due to the additional heat sources and the higher position of these sources the temperature profile assumes a more linear path over the room height.

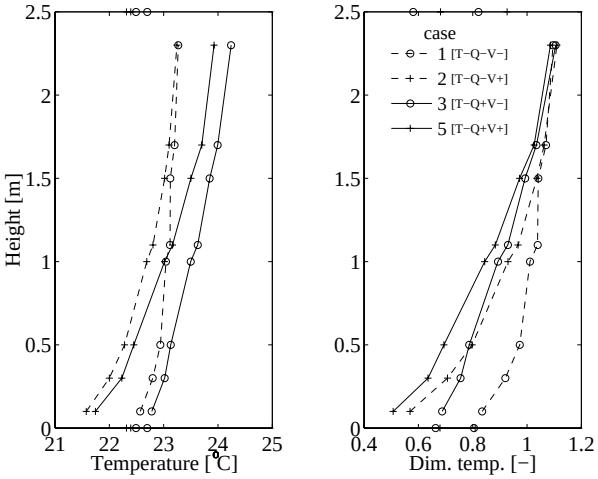

Figure 6.10. Mean temperature and dimensionless temperature profiles as a function of the height for case 1, 2, 3 and 5.

A characteristic of a displacement ventilation flow pattern in a room is the relatively sharply located interface between the supply air layer, indicated the lower layer, and the upper layer sketched in Figure 6.1. The interface height establishes itself where the total flow rate in the plume(s) equals the supply flow rate into the room. With Equation 6.1, this height can be estimated by calculating the plume flow rate from an empirical expression. The plume flow rate along a heated vertical wall can be determined from an empirical relation as given, for example, by Skistad (1994),

$$\dot{V}_{plume} = 3.06 \cdot 10^{-3} Q_{c\_h}^{2/7} y_h^{6/7} w_h , \qquad (6.4)$$

where $\dot{V}_{plume}$ is the plume flow rate, Q_{c_h} the convective heat load from the heat source (in [W/m]), w_h is the outline of the heat source and y_h the vertical distance to the lower edge of the heat source. This relation originates from a Nusselt (*Nu*) - Grashof (*Gr*) relation and has been obtained by fitting to measurement results. For laminar flows *Nu* scales with $Gr^{1/4}$, for turbulent flows with $Gr^{1/3}$ (Holman 1994). Equation 6.4 therefore has a limited applicability.

When the thermal mannequin is simplified to an equivalent cylinder (h = 1.2 m; d = 0.5 m) the interface height can be approximated. Given the configuration and the heat load the estimated interface heights are given in Table 6.2. Equation 6.4 is only valid for the flow along a heated surface. Therefore, an estimation of the interface height for case 2 [T-Q-V+] was derived using the plume flow rate model for a point source, derived by Mundt (1996). Equation 6.4 and the model of Mundt assume that no air will enter or leave the lower layer via an up- or downward flow along the walls. In view of the measured room air and wall temperatures, this assumption will certainly not be met for specific cases.

Table 6.2. Interface height (case 1, 3 and 5 calculated from Equation 6.4; case 2 determined from Mundt (1996)).

case	interface height
1	0.7 m
2	1.6 m
3	0.7 m
5	1.2 m

The interface height cannot be determined unambiguously from the measured temperature profiles (Figure 6.10). It can better be determined from local mean age of the air measurements as discussed in Roos (1998[a]) or from particle concentration measurements as discussed in Krühne (1995).

High heat load / Flow rate - Figure 6.11 presents the comparison of the temperature profiles for the high heat load cases (case 3 [T-Q+V-] to 7 [T×Q+V+]) in which the most important variable is the flow rate. The difference in the temperature gradients at the lower part of the room is small for cases 3 [T-Q+V-] to 6 [T-Q+V*]. From the dimensionless temperature gradient the sensitivity to the flow rate is more clear. Nevertheless, the sensitivity of the temperature gradient to the flow rate is significantly affected by the non-negligible influence of the heat transfer to the enclosure. With these prescribed boundary conditions, the wall heat transfer reduces the vertical temperature gradient. The close relation between the supply flow rate and the near floor temperature confirms the findings of Mundt (1996).

The variation in the flow rate affects the convective cooling load (Q_{c_v}) and thus the air cooling fraction (ξ; Equation 6.2). The value for the air cooling fraction ranges from ξ = 0.84 for case 6 to ξ = 0.16 for case 3. Following the results of Krühne (1995), for a room with displacement ventilation in combination with a cooled ceiling, a change in the near floor flow characteristics is expected when the air cooling fraction is reduced. At small values for ξ, the near floor air layer is entrained more significantly with air from the upper layer due to a downward flow along the walls. This effect was demonstrated by Krühne through the measurement of the degree of contamination in the near floor air layer as a function of the air cooling fraction.

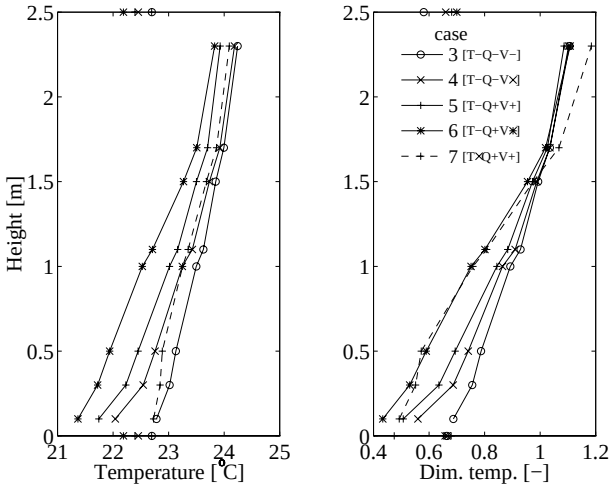

Figure 6.11. Mean temperature and dimensionless temperature profiles as a function of the height for case 3 to 7.

Assuming no heat loss over the enclosure, the air cooling fraction introduced by Krühne is defined as

$$\xi_{\text{Krühne}} = Q_{c\_v} / Q_{tot} = 1 - \left(Q_{tot\_cc} / Q_{tot}\right), \qquad (6.5)$$

where Q_{tot} comprises the convective and the radiant part of the internal heat load and Q_{tot_cc} the convective and radiant cooling load of the cooled ceiling.

The experiments as performed by Krühne (1995) differ at some points from the set-up used in this research.
In the research by Krühne:

1. Full-scale experiments were made in a climate chamber set-up with a displacement ventilation system in combination with a cooled ceiling. The heat loss over other walls was assumed negligible.
2. The value for the air cooling fraction was varied through the supply - exhaust air temperature difference at a constant supply flow rate. As a result, at a decreasing air cooling fraction, the supply temperature approaches the mean room temperature.

Whereas in this research:

1. The temperature variation between the walls is small and controlled. The influence of radiant heat transfer therefore is negligible, also at small values for ξ. The convective wall heat transfer cannot be neglected.
2. The change in the air cooling fraction results from the change in supply flow rate ($\dot{V}$) rather than the change in supply temperature.

The effect of a change in the air cooling fraction by changing the supply temperature is investigated in case 7 [T×Q+V+]. The air cooling fraction for case 7 is calculated at ξ = 0.27 which lies between the results for case 3 (ξ = 0.16) and case 4 (ξ = 0.37). The vertical temperature profile indicates the absence of a more pronounced gradient near the floor. Above a height of 1.0 m the temperature course coincides with the results of case 3 and 4. As the supply temperature is higher, the dimensionless temperature profile differs significantly.

From the above result it is concluded that there is no apparent difference in the vertical temperature distribution when either the flow rate or the supply temperature is changed. From the temperature profiles it is however not possible to determine a change in the flow pattern characteristics due to a reduction of the air cooling fraction. Visualisations show that a displacement type of flow pattern exists, also for case 3. The contribution of a downward air flow rate along the walls into the supply air flow layer however can be expected as, e.g., for case 3 over the full height the wall temperatures on average are lower than the air temperature.

A further indication of the influence of the reduced air cooling fraction on the characteristics of the lower layer is obtained from local mean age of the air ($\bar{\tau}$) measurements. These type of measurement results are described by Roos (1998[b]) for the same configuration and boundary conditions. Roos amongst others measured the local mean age of the air in the lower layer at y = 0.1 m. In Table 6.3 the experimentally obtained local mean age-of-air values are summarised. For this discussion the results for the low heat load cases are recapitulated. Despite an equal supply flow rate and estimated interface height for case 1 [T-Q-V-] and case 3 [T-Q+V-] (see Table 6.2), for case 3 a significant higher value for $\bar{\tau}$ is measured. The air cooling fraction for case 3 however is significantly lower than for case 1. Between case 2 [T-Q-V+] and case 5 [T-Q+V+] no significant difference is measured.

Table 6.3. Local mean age-of-air ($\bar{\tau}$) for x = 0.54 m / y = 0.1 m / z = 1.8 m (Roos 1998[b]).

case	$\dot{V}$ [m^3/s]	ξ [-]	$\bar{\tau}$ [min]
1*	0.010	0.52	8 ± 2
2	0.029	1.89	6 ± 2
3	0.010	0.16	14 ± 3
5	0.028	0.53	7 ± 2

* Q_{tot_m} = 150 W instead of 125 W as in Table 6.1

When ξ = 0.16 (case 3), the lower layer is 'contaminated' with 'older' air from the upper layer via a downward flow along the wall. When ξ > 0.5 this effect is less significant. For case 7 (T×Q+V+ ; ξ = 0.27) the local mean age was not measured. Nevertheless a similarly 'contaminated' lower layer is expected as the boundary conditions and the vertical air temperature profiles agree with those for case 3. Given the accuracy of these type of measurements (see Roos 1998[a]), the measurement results support the findings of Krühne (1995).

Displacement / Mixing ventilation - Figure 6.12 presents the comparison between a mixing ventilation (case 8 [T+Q+V×]) and a displacement ventilation (case 4 [T-Q+V×]) flow pattern. As a temperature gradient is evident in the lower part of the room, the mixing ventilation temperature profile indicates that the room air flow is not completely mixed. This results from the small value for the air change rate and from the low impulse with which the supply air is introduced. The gradient however is smaller than for the displacement ventilation case. The dimensionless temperature profile for mixing ventilation has an opposite course as now the near floor air temperature is lower than the supply and exhaust air temperature.

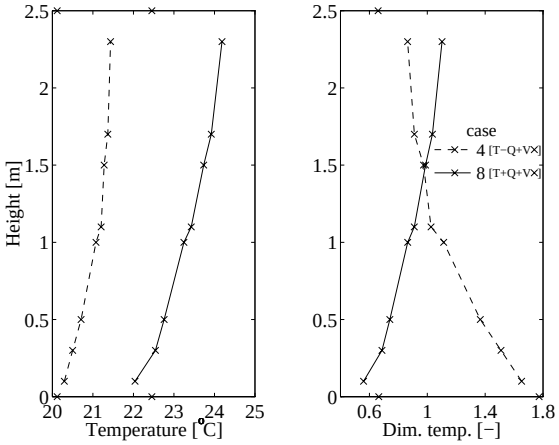

Figure 6.12. Mean temperature and dimensionless temperature profiles as a function of the height for case 4 and 8.

6.4.3 Wall heat transfer characteristics

The influence of the wall heat transfer on the heat balance and on the flow is evident from the previous discussion on the air cooling fraction. Therefore, knowledge of the wall heat transfer characteristics is required. Accurate measurement of the local wall heat transfer coefficient is difficult as the heat flux is small. These type of measurements have not been performed. Instead the measurement results have been compared with results found in literature. From these results the convective wall heat transfer coefficient has been estimated for the floor, ceiling and the walls.

Floor - Skistad (1994) summarises results which indicate that in a room with displacement ventilaton the near floor temperature at ~0.1 m height approximately lies midway (50%) between the supply and exhaust temperature. From Figure 6.10 and 6.11 this value is seen to lie between 46% and 85% for the investigated cases.

Mundt (1996) derived a simplified model to determine the dimensionless near-floor air temperature difference ($\theta_{0.1\ m}$) as a function of the air flow rate. The model takes the convective heat transfer from the floor to the supply flow and the radiant heat transfer from the ceiling to the floor into account, assuming that the exhaust air temperature equals the ceiling temperature. It ignores however the entrainment of room air into the near-floor air layer:

$$\theta_{0.1\,m} = \frac{T_{0.1\,m} - T_{supply}}{T_{exhaust} - T_{supply}} = \left(\frac{\dot{V}\rho c_p}{A_F} \left(\frac{1}{h_{rF}} + \frac{1}{h_{cF}} \right) + 1 \right)^{-1}, \qquad (6.6)$$

where h_{rF} is the radiant and h_{cF} the convective heat transfer coefficient at the floor and A_F is the floor area. The expression for the convective part in Equation 6.6 complies with the definition of the Stanton number ($St = Nu/(RePr) = h_{cF}/(u\rho c_p)$), which expresses the ratio of energy flux to momentum flux.

Krühne (1995) derived a more extended temperature model for a room with displacement ventilation with a cooled ceiling. When there is no heat loss over the enclosure good agreement was found with the model of Mundt (Equation 6.6). When heat is transferred over the walls into the room, $\theta_{0.1\ m}$ increases as heat is transferred into the room via the floor.

In Figure 6.13 Equation 6.6 is shown for h_{cF} = 2, 3, 5 and 10 W/m^2.K. Given the prevailing temperatures h_r is set at 5 W/m^2.K. Furthermore measurement results of Mundt (1996), Chen (1988) and of this research are shown. Most other measurement results described in literature have been obtained for higher flow rates. For the current measurements a discrimination is made in high and low heat load cases. The results are determined from Equation 6.6, in which the near floor air temperature, $\overline{T}^*_{0.1m}$, is the averaged value over all measured temperatures at 0.1 m height.

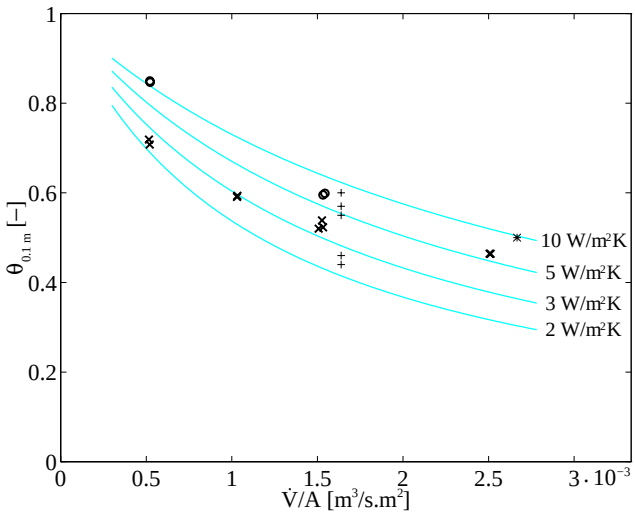

Figure 6.13. Dimensionless near floor temperature difference ($\theta_{0.1\ m}$) as a function of the supply flow rate per square meter floor area ([———] model results for four different indicated values of h_{cF}, [+] Mundt (1996), [∗] Chen (1988), current measurements: [x] high heat load, [o] low heat load).

For all measurement results a satisfactory agreement is found with the model results for h_{cF} = 2 to 10 W/m^2.K. Focussing on the high heat load results, h_{cF} increases from 2.5 to 5.5 W/m^2.K for $\dot{V}$ = 0.010 to 0.047 m^3/s, when the experimentally derived results in Figure 6.13 are compared to the model results.

As the near floor velocities are low, free convection heat transfer may dominate the heat transfer characteristics (Mundt 1996). In Recknagel et al. (1997) free convection heat transfer for an upward directed heat flux from a horizontal plate (floor heating) is calculated from

$$h_{cF} = 2 \cdot \left| T_{wall} - T_{\infty} \right|^{0.31} \equiv 2 \cdot \left| T_F - \overline{T}^{*}_{0.1m} \right|^{0.31}, \qquad (6.7)$$

where T_{∞} is defined as the temperature of the uninfluenced environment (T_{∞} = 0…20°C), which is taken here as the averaged temperature at 0.1 m above the floor. Inserting the measurement results, h_{cF} varies between 1.4 W/m^2.K and 1.9 W/m^2.K for case 4 to case 6. Remark that $\overline{T}^{*}_{0.1m}$ is slightly outside the validity range for T_{∞}. When the heat transfer coefficient is derived from Figure 6.6, based on the measurements and air flow rate, a value is rendered which is higher than obtained from Equation 6.7.

From the above comparison of measurement and model results, the assumption of pure free convection heat transfer appears not valid for the displacement ventilation configuration. In Table 6.4 the heat transfer characteristics therefore have been represented by the earlier introduced Stanton number (*St*). The required convective heat transfer coefficients, h_{cF}, have been estimated from Equation 6.6 and the measurement results (see Figure 6.13). The air velocity at 0.1 m height ($u_{0.1\ m}$) has been measured at x = 1.5 m and x = 2.0 m. In Figure 6.14 the averaged velocity over the width of the room is shown as function of the supply flow rate per square meter floor area. The velocity is seen to increase logarithmically at higher flow rates. The velocity magnitude however remains low. The averaged turbulence intensity, which also influences the heat transfer, is in all cases 25% ± 5%.

Table 6.4. Summary of floor heat transfer characteristics (values for x = 1.5 m).

case	h_{cF} [W/m^2.K]	$u_{0.1\ m}$ [m/s]	St = $h_{cF}/u_{0.1m}\rho c_p$ [-]
1 [T-Q-V-]	~10	(0.04)	0.20
2 [T-Q-V+]	6	0.08	0.061
3 [T-Q+V-]	2.5	(0.04)	0.051
4 [T-Q+V×]	3	0.06	0.041
5 [T-Q+V+]	3.5	0.08	0.036
6 [T-Q+V*]	5.7	0.09	0.051
7 [T×Q+V+]	4	0.06	0.054

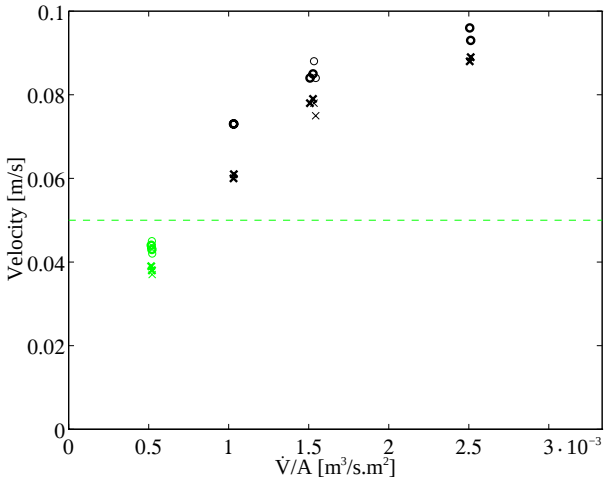

Figure 6.14. Averaged velocity over the width of the room at 0.1 m height as a function of the air flow rate ([o] *x = 2.0 m,* [x] *x = 1.5 m;* [bold] *high heat load,* [thin] *low heat load).*

The estimated heat transfer coefficients for the high heat load cases show good agreement with results as presented by Chen and Jiang (1992), in view of the spread of these results. Chen and Jiang present measured convective heat transfer coefficients at the floor as a function of the velocity for a displacement ventilated flow pattern. The large spread of these results do not allow a clear relation with the velocity. The Stanton number that can be calculated ranges from $St \approx 0.024$ at $u = 0.1$ m/s to $St \approx 0.008$ at $u = 0.6$ m/s and therefore is clearly lower than the results shown in Table 6.4.

In Table 6.4 the value of the Stanton number is of the same order of magnitude for the high heat load cases. For case 1 a large deviation is found. This deviation is explained from the large gradient in the convective heat transfer coefficient at low flow rates, the small temperature difference and the accuracy of the model and the measurements. As the variation in the free convection heat transfer for the different cases is small, the variation in h_{cF} is mainly explained from the change in the near floor air velocity. For the current configuration a constant Stanton number may be approximated at 0.05, h_{cF} then can be calculated from $St \cdot u_{0.1\ m} \cdot \rho c_p$. The heat transfer coefficient, h_{cF}, will be estimated lower when in the model of Mundt (Equation 6.6) the earlier described correction is applied for a situation in which wall heat transfer is present (Krühne 1995). As a result the Stanton number is lowered and approaches the results of Chen and Jiang.

From measurements Krühne (1995) concluded that the air cooling fraction has no significant influence on $\theta_{0.1\ m}$ and therefore the heat transfer coefficient. Comparing the results for the high heat load cases 5 [T-Q+V+] and 7 [T×Q+V+] the conclusion of Krühne

is confirmed. When the results for the low and high heat load cases are compared for the same flow rate (see Figure 6.13) then differences are larger. The difference is more pronounced at lower air flow rates and is partly explained from the difference in temperature of the in the lower layer induced room air.

Ceiling - For the heat transfer characteristics at the ceiling a similar derivation is more difficult. Impinging buoyant plumes, originating from the heat sources, result in a large variation of the local convective heat transfer at the ceiling. Chen and Jiang (1992) present convective heat transfer coefficients at the ceiling as a function of the velocity. The averaged value can be determined at 4 W/m^2.K. Again the sensitivity of h_{cC} to the velocity is not obvious.

Walls - The wall heat transfer will mainly result from free convection heat transfer, as only the PC-simulator near the West-wall will create a forced convection flow near the wall. Given the averaged wall temperature and the vertical temperature profiles shown in Figure 6.10 and 6.11 a downward convection flow is expected for the upper part of the room and an upward flow for the lower part. As a result the total heat transfer from the walls into the room will be significantly smaller than the heat flux from the floor or the ceiling. For indoor air flow normally a value is assumed of h_{c_wall} = 3 W/m^2.K (Tammes and Vos 1984).

6.4.4 Buoyant plumes

The heat sources in the room create buoyant plumes that transport the air from the lower part of the room into the higher part through entrainment. From the full-scale measurements information is available on the plumes above the thermal mannequin and the PC-simulator on the desk. These results can be compared with results described by Mundt (1996). Mundt performed extensive climate chamber measurements at buoyant plumes above different type of heat sources.

In Figure 6.16 the plume velocity as function of the temperature gradient is shown at two positions above the thermal mannequin and at one position above the PC-simulator. The positions and applied symbols are indicated in Figure 6.15. The temperature gradient (dT/dy) is calculated from the averaged temperature ($\overline{T}_y$) outside the plumes at 0.1 m and 2.3 m height and is indicated in Table F.3 (Appendix F). Only results for the displacement ventilation flow pattern are shown.

Figure 6.17 shows the plume temperature difference for one position above the thermal mannequin and one position above the PC-simulator. The temperature difference is calculated from the averaged temperature $\overline{T}_{2.0\,m}$ and the plume temperature. The plume

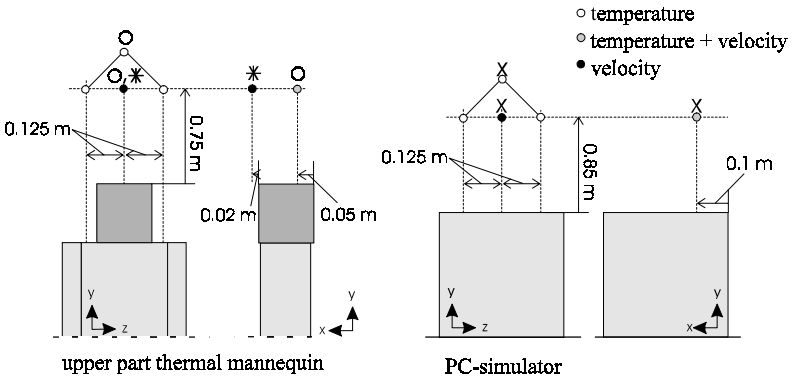

Figure 6.15. Measurement locations for plume velocity and temperature.

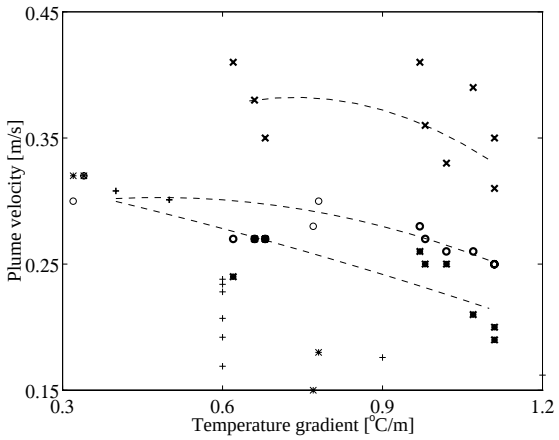

Figure 6.16. Plume velocity above the thermal mannequin and the PC-simulator at the central plane of the buoyant plume as a function of the vertical temperature gradient (measurement locations indicated in Figure 6.15, [thin] *low heat load ,* [bold] *high heat load, the dashed lines show the trend for the results at each location;* [+] *Mundt (1996)).*

temperature has not been measured at the central plane but has been averaged from the two measurement results at 0.125 m from the central plane (see Figure 6.15).

Thermal mannequin - With regard to the thermal mannequin, the measured velocities are higher than the velocities summarised by Mundt (1996; see Figure 6.16 [+]). The latter measurement results were obtained from different laboratories for the same heat source. Mundt used a person simulator consisting of a 1.0 m high duct with d = 0.4 m and Q_{tot} = 100 W. In one measurement the diameter of the heat source was d = 0.3 m. At dT/dy = 0.4 and 0.5 °C/m, higher velocities were registered (see Figure 6.16 [+]). Despite the variation between the different laboratories the sensitivity to the vertical temperature gradient was

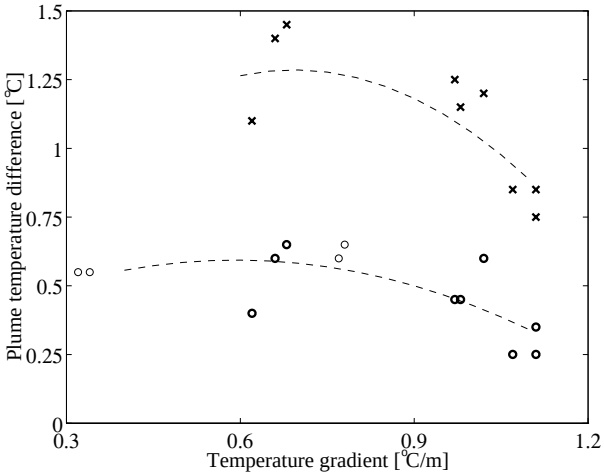

Figure 6.17. Averaged plume temperature difference above the thermal mannequin and the PC-simulator at the centre plane of the buoyant plume as a function of the vertical temperature gradient (measurement locations indicated in Figure 6.15, [thin] *low heat load,* [bold] *high heat load, the dashed lines show the tendency for the results at each location).*

confirmed in most measurements. The measured turbulence intensity in the plume was in the order of 15 - 20%, which agrees with the results of Mundt. The measured temperature difference and the sensitivity to the temperature gradient are in good agreement with the measurements of Mundt.

Mundt (1996) also refers to measurement results above a human being as reported by Mierzwinski (1981). Mierzwinski measured maximum velocities in the order of 0.17 - 0.23 m/s and a temperature difference of 0.5 - 0.8^{o}C at a vertical temperature gradient of 0.5 - 0.6^{o}C/m at 0.75 m above the human being. These results show good agreement with the measurement results of Mundt (1996). The spread in the results of Mierzwinski is explained from the differences between the persons that have been used in the experiments. Explanations for the deviation with the current measurement results are given by the difference in heat input (u scales with $Q^{1/3}$ (Kofoed and Nielsen 1988)), the shape of the heat source, the large gradients in the plume and the accuracy of the measurements. The above described results nevertheless confirm the applicability of the thermal mannequin to simulate a human being in the full-scale experiments.

PC-simulator - The plume velocity and temperature difference at the PC-simulator are significantly higher than at the thermal mannequin. The turbulence intensity is in the order of 15 - 20%. The sensitivity of the plume velocity to the temperature gradient is less well clear. In contrast, the sensitivity of the plume temperature difference is more profound.

Mundt (1996) presents results for a similar PC-simulator as measured in two different laboratories. A significant difference in the measured plume velocity is found between the two laboratories. The results of one laboratory show good agreement with the presented results here (u = 0.38 m/s at dT/dy = 0.6^{o}C/m). In both laboratories the sensitivity of the plume velocity to the temperature gradient was not apparent at 0.8 m height. No information is available on the plume temperature difference.

Mixing ventilation - For the mixing ventilation configuration (case 8 [T+Q+V×]; not indicated in Figure 6.16 and 6.17) small differences are found for the plume velocity in comparison to the corresponding displacement ventilation case (case 4 [T-Q+V×]). Higher plume velocities (~ +0.04 m/s) are measured at the thermal mannequin whereas significant lower velocities are measured above the PC-simulator (~ -0.15 m/s) at a significant higher turbulence intensity (~35%). The latter effect is explained from the rising air flow along the desk table side (Figure 6.7b). Entrainment of the air at this rising flow impedes the entrainment into the buoyant plume of the PC-simulator and therefore opposes the development of the plume. The plume temperature difference at both plumes is well in line with the results for the displacement ventilation cases.

6.5 SUMMARY

1. Full-scale climate chamber measurements are presented for a displacement ventilation and a mixing ventilation type of flow pattern. All measurement results are summarised in *x-y-z* coordinates as defined in Figure 5.2. The configuration and the boundary conditions are tabulated in Appendix D and F respectively.
2. The air flow pattern has been investigated on three variables: (a) the temperature difference between supply air and walls (ΔT = -3, -1, +3 ^{o}C), (b) the flow rate ($\dot{V}$ = 0.010…0.047 m^{3}/s) and (c) the internal heat load (Q = 125 and 500 W).
   (a) The temperature difference between wall and supply air is crucial for the ensuing air flow pattern. A negative value results in displacement ventilation, a positive value in mixing ventilation.
   (b) The flow rate was taken such that a relevant interface height, and therefore a displacement ventilation flow pattern, could establish when $\Delta T < 0^{o}$C. The flow rate has a clear effect on the near floor air temperature and also affected the heat transfer characteristics at the floor. The sensitivity of the temperature gradient to the flow rate is significantly influenced by the non-negligible heat transfer to the room enclosure.
   (c) A higher heat load increases the vertical temperature gradient and the average room air temperature. At low heat load the heat was introduced near floor level. The

introduction of additional heat sources at higher level resulted in a more linear profile for the vertical temperature gradient.

3. In the experimental configuration the walls are controlled at constant temperature. As a result the ceiling is found to operate as a cooled ceiling and heat is transferred from the floor into the room. In extreme situations (case 3 [T-Q+V-] and case 2 [T-Q-V+]) also the contribution of the walls in the total heat balance may not be neglected. For high heat loads and low flow rates the heat transfer over the room enclosure is the dominant heat transfer process.

   Krühne (1995) indicates that in case the air cooling fraction ($\xi = Q_{c\_v} / Q_{tot\_c}$) is reduced the near floor air layer characteristics are changed due to a downward flow along the walls. The experimental set-up and conditions applied in this work differ from the conditions used by Krühne. It was not possible to confirm the above mentioned findings of Krühne from the obtained temperature profiles. Using results of Roos (1998[a,b]) for the similar configuration, the findings of Krühne could be supported for the investigated boundary conditions.

   The importance of the wall heat transfer in the described experiments is of interest for numerical simulations given the known difficulties in simulating the wall heat transfer characteristics (see Chapter 4).

4. Though the convective heat transfer coefficients at the walls could not be determined directly, an estimation has been made using models by Mundt (1996) and Krühne (1995). The derived heat transfer coefficients agree quantitatively with results found in literature (Chen and Jiang 1992).

   The heat transfer at the floor will be underestimated when only free convection is taken into account. Using the model of Mundt, the Stanton number was approximated at 0.05. According to the model of Krühne, this number is lowered when there is a heat transfer over the walls into the room.

5. The buoyant plumes above the heat sources have similar characteristics as described by Mundt (1996). Measurements from literature confirm the applicability of the thermal mannequin for the (thermal) simulation of a human being.

6. From the discussion described in this chapter, the obtained measurement results are found to be realistic. They may be used for comparison with similar numerical simulations.

Chapter 7

NUMERICAL RESULTS

7.1 INTRODUCTION

Computational Fluid Dynamics (CFD) simulations have been performed for the full-scale experimental cases described in Chapter 6. The measurement results are used to validate the numerical model. The numerical model comprises the discretisation of the flow problem, the boundary conditions and the turbulence modelling. Validation here is defined as the experimental verification of the numerical model. In Chapter 4 the influence of mesh size, wall heat transfer, supply modelling and grid technique on the CFD-result was discussed. With the available experimental data, in this chapter limitations and additional requirements with regard to wall heat transfer and turbulence modelling are studied more in depth.

After a description of the numerical model, simulation results for one case are discussed with respect to heat transfer and turbulence modelling. These results are used to discuss the applicability of CFD for indoor air flow. Finally, simulation results are shown for all investigated cases.

7.2 MODEL DESCRIPTION

7.2.1 Geometry and boundary conditions

Geometry - The office room used in the experiments has been modelled according to the geometry description shown in Figure 5.2 and summarised in Appendix D. Note that this office room corresponds with the experimental set-up described in Chapter 5 and 6. It differs from the in Chapter 4.3 investigated office room that was described by Cox and Elkhuizen (1995). The dimensions of the thermal mannequin in the numerical model have been adopted to the Cartesian grid, such that the surface area of the modelled mannequin

closely agrees with the actual mannequin. This geometry of the thermal mannequin is also found in Appendix D.

Boundary conditions - The boundary conditions of the investigated cases (see Table 6.1) are listed in Appendix F.1. The walls of the office room are at constant temperature. A heat flux is defined as the thermal boundary condition for the heat sources. In the simulations radiant heat transfer has not been taken into account. The convective part of the total heat input can be derived from the data given in Appendix F.

The supply of the displacement ventilation unit has been modelled without a grille and the supply area is therefore too large (a 100% aperture instead of 15% in reality). In the simulations the actually measured velocity distribution at shortest distance to the supply was used (see Chapter 5.2.2). To obtain the required mass flow rate, in case of a 100% supply aperture, the velocity profile had to be compensated for measurement inaccuracies. In the adjustment the higher velocities were less reduced compared to the lower velocities in order to retain the momentum at the supply as much as possible. In Figure F.1 (Appendix F) a suggestion is given for the modelling of the supply velocity distribution at 100% aperture.

7.2.2 CFD-program, turbulence model and numerical methods

CFD-program - For the simulations unstructured versions of the CFD-code Fluent, Fluent/uns v.4 and v.5 (Fluent 1996[a], Fluent 1998), have been applied. This CFD-software does not allow the user to modify the source-code. Instead, it is possible to apply user-defined subroutines for special modifications of variables or boundary conditions. The user-defined subroutines are integrated in the simulation model via a C-pre-processor.

Turbulence model and numerical methods - The two turbulence models described in Chapter 4.2 have been used: the standard k-ε model and the RNG-k-ε model. For the RNG-k-ε model the low-Reynolds number interpolation formula (Equation 4.14) has been applied. The near-wall boundary layer in both models is calculated with the logarithmic wall function (Equation 4.8). The low-Reynolds number approach allows the flow to be calculated up to the wall. The grid requirements for a three dimensional problem then exceed however the available computer capacity. Therefore, currently this does not present a practical solution.

Following the discussion of the grid techniques in Chapter 4.5, the model office room has been discretised using a non-equidistant structured hexahedral grid. The structured grid has been set up with Fluent V.4.3 (Fluent 1995). From the results in Chapter 4.4 it was concluded that a grid independent solution is possible when the flow problem is discretised

with approximately 50,000 grid cells, in which case the wall heat transfer may possibly be modelled inaccurately. In total 123,000 grid cells have been used to model the room. This number of grid cells is regarded sufficient to obtain a grid independent solution of the flow field. Grid dependency has not been checked further due to computer capacity restrictions.

For all simulations the momentum and energy equation are solved applying a second order interpolation scheme. For most simulations also the remaining equations are solved with second order accuracy. In all described simulations a multigrid solver and the SIMPLE algorithm have been used. Pressure interpolation is performed by a staggered grid approach (Fluent 1996[a]).

Time has been used as an additional relaxation factor. The number of iterations per time step was restricted to three. In the simulation process the temperature and velocity were monitored at three positions close to the thermal mannequin. The end-value of the velocity and the temperature were found to fluctuate, in particular at the position in the convection plume. The simulation results for a time-dependent and a steady-state approach were compared with regard to this fluctuation in the calculated end-value. For the steady-state approach an approximately 50% higher standard deviation was calculated for all monitored points.

The problem is regarded to be converged if the mass balance is accurate within 1% and if the heat balance is accurate within 2% of the total sum of the heat fluxes in the room. Furthermore, the variation of flow variables (u, T) at specified positions in the flow field must approach a constant value or a constant sinusoidal variation with a restricted amplitude.

7.3 WALL HEAT TRANSFER & TURBULENCE MODELLING

7.3.1 Introduction

In Chapter 4.4 CFD-results are shown for a displacement ventilated office room as described by Cox and Elkhuizen (1995). The number of available measurement results was too limited to evaluate the applicability of the standard k-ε versus the RNG-k-ε model. Furthermore, the presented results indicated restrictions in the correct simulation of wall heat transfer. The measurement results described in Chapter 6, for the office room ventilated with the desk displacement ventilation concept, allow a more in depth evaluation of the applicability of the mentioned turbulence models and the simulation of the wall heat transfer. Both boundary conditions and measurement results are well-defined and in the

investigated configuration the wall heat transfer is an important part of the room heat transfer process. Therefore this flow problem is interesting to solve numerically.

For the investigation, different simulation variants have been used. In the description of the simulation results these variants are given an abbreviated notation as follows: the turbulence models are abbreviated to 'RNG' (RNG-*k*-ε model) and 'ke' (standard *k*-ε model); the wall heat transfer variants are abbreviated to 'wf' (wall functions) and 'htc' (heat transfer coefficient).

For the *htc*-variant the latest version of the available software was used (Fluent 1998). In this version it is possible to enter fixed heat transfer coefficients (h_{tc}) as part of the boundary condition definition through user-defined subroutines. The definition of h_{tc} differs from the definition for h_c given in Equation 4.18 and is defined as

$$h_{tc} = \dot{q}_c / (T_s - T_P), \tag{7.1}$$

where T_P is the temperature at the cell adjacent to the wall. In general the cell distance to the wall is smaller than 0.1 m, as defined in Equation 4.18.

In earlier results described in Loomans and Rutten (1997) and Loomans (1998) the wall heat transfer was adjusted by adaptation of the thermal conductivity and the dynamic viscosity at the first grid cell adjacent to the wall. Both fluid properties were increased. A higher conductivity increased the wall heat transfer indirectly. The dynamic viscosity was increased to maintain the value for the Prandtl-number (*Pr*). This approach indicated an improved agreement of simulation results with measurement results. However, acceptable results only could be obtained for the lowest flow rates (case 1 [T-Q-V-] and 3 [T-Q+V-]). Furthermore, modification of the dynamic viscosity changes the near wall flow properties unrealistically.

In next sections the configuration, boundary conditions and measurement results as determined for case 5a [T-Q+V+] (see Table 6.1) are used to investigate the wall heat transfer characteristics and the turbulence models. First, results are discussed with respect to the wall heat transfer, next the turbulence models are evaluated. After the discussion of these two topics the applicability of CFD for indoor air flow simulation is addressed.

7.3.2 Results and discussion on wall heat transfer

Results - In Figure 7.1 the simulated mean temperature profiles ($\overline{T}_y$) for the four indicated simulation variants are compared with measurement results. The mean temperature profile, $\overline{T}_y$, is averaged from six vertical temperature profiles outside the buoyant plume (x = 1.50 / 2.00 / 4.50 m; z = 0.675 / 2.925 m). Table 7.1 summarises the wall-averaged heat transfer

coefficient for the individual walls as determined from the simulation results. The heat transfer coefficient is derived similar to Equation 4.18:

$$h_c = \dot{q}_c \big/ \left(T_s - \overline{T}^*_{0.1m}\right), \tag{7.2}$$

where $\overline{T}^*_{0.1m}$ is the averaged air temperature over a plane parallel to the surface at 0.1 m distance. This value differs from the h_{tc}-value, defined in Equation 7.1, that has been prescribed in the boundary condition of the numerical model.

In Table 7.2 the normal-distance Reynolds number (y^+) is summarised. The presented value is averaged over the total wall. The y^+-value is closely related to the wall heat transfer as shown in Equation 4.10 and 4.11. Table 7.3 presents the plume flow rate at 0.75 m above the simulated thermal mannequin. For this result a plane was defined over the total plume width above the thermal mannequin. The flow rate through the defined plane then was determined. For each case the plane was newly defined.

Table 7.1. Wall-averaged heat transfer coefficient (h_c) determined according to Equation 7.2.

h_c [W/m^2.K]	h_{cN}	h_{cS}	h_{cW}	h_{cE}	h_{cF}	h_{cC}
RNG-wf	0.26	1.04	0.71	1.01	1.31	1.79
ke-wf	1.05	1.14	1.11	1.08	1.34	1.96
RNG-htc	2.61	1.88	2.20	1.76	6.61	5.41
ke-htc	2.96	1.96	2.14	1.82	4.96	4.92

Table 7.2. Wall-averaged normal distance Reynolds number (y^+) as used in Equation 4.8 and 4.9.

y^+ [-]	N	S	W	E	F	C
RNG-wf	9.7	10.0	13.1	7.8	11.8	12.1
ke-wf	12.7	14.2	22.3	9.3	15.1	14.0
RNG-htc	11.6	12.7	14.7	10.8	13.2	12.7
ke-htc	18.9	17.3	29.1	15.3	17.4	14.5

Table 7.3. Plume flow rate at 0.75 m above the thermal mannequin.

	$\dot{V}_{plume}$ [m^3/s]
RNG-wf	0.010
ke-wf	0.021
RNG-htc	0.029
ke-htc	0.029
Mierzwinski (1981)	0.028 - 0.056
Mundt (1996); 100 W; dT/dy = 0.6 - 1.5 ^{o}C/m	0.031 - 0.052

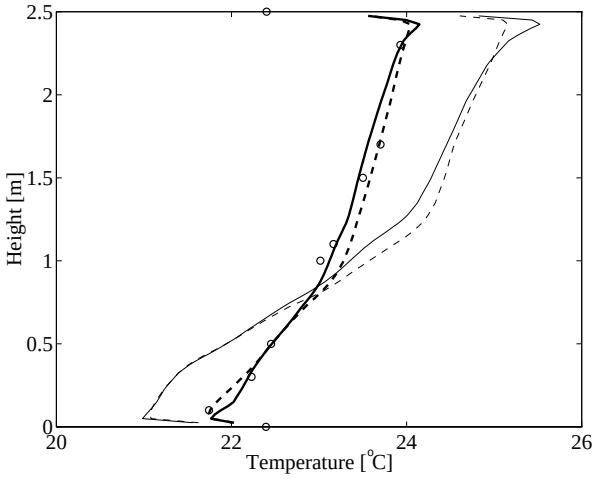

Figure 7.1. Measured and simulated temperature ($\overline{T}_y$) for case 5a [T-Q+V+]; ([——] *RNG-wf,* [– – –] *ke-wf,* [▏▏▏▏] *RNG-htc,* [▏ ▏ ▏] *ke-htc,* [o] *measurements).*

Discussion - From the results presented in Figure 7.1 it is apparent that the simulation of the investigated flow pattern applying wall functions will lead to significant deviations in the calculated temperature profile. The temperature gradient is overestimated significantly. The temperature difference between supply and exhaust is simulated 30% higher when wall functions are applied. As the plume velocity is related to the temperature profile (see Chapter 6.4.4), Table 7.3 shows that the increased temperature gradient results in an underestimation of the plume flow rate above the thermal mannequin, compared to values obtained from the *htc*-variants and from results found in literature (Mundt (1996) and Mierzwinski (1981)). The experimental results summarised by Mundt indicate that the deviation in the plume flow rate can be as high as 30% when *dT*/*dy* increases from 0.6 to 1.5 ^{o}C/m.

The convective heat transfer coefficients for the *wf*-variants, summarised in Table 7.1, indicate lower values than estimated in Chapter 6.4.3. At all boundaries the heat transfer coefficient merely assumes values that can be obtained for free convection conditions. The average y^+-value for both *wf* -variants (see Table 7.2) nevertheless is close to the values mentioned by Chen (1995) and Niu (1994). As shown in Niu (1994) the sensitivity of h_c to y^+ is high. For free convection flow, Niu determined a linear relation for h_c between y^+= 7 and y^+= 14, with $\partial h_c/\partial y^+$ = -0.34 W/m^2.K per viscous unit. To obtain a better agreement of the simulated heat transfer coefficient with the experimentally derived value, an unrealistically rigid control on the y^+-value would be required.

When a heat transfer coefficient is included in the definition of the boundary conditions for the enclosure, measurement and simulation values show better agreement. The value of the imposed coefficient (h_{tc}; Equation 7.1) was determined from the discussion described in Chapter 6.4.3. The values for the floor and ceiling boundary conditions then were fitted to the measured temperature profiles by adjusting the value for h_{tc}. Next, the convective heat transfer coefficient (h_c), as given in Table 7.1, was determined according to Equation 7.2.

The heat transfer at the walls did not result in a clear change of the room temperature gradient. Instead of the minimum and maximum room temperature, only the shape of the profile was changed. This effect is discussed further in Chapter 7.4. For case 5, the average heat flux over the walls, determined from the *RNG-htc* and *ke-htc* variant, was 16% of the total heat flux to the enclosure. Of the total heat transfer to the enclosure, relative most heat is transferred at the ceiling (62%) and the floor (23%).

The y^+-value slightly increases at the enclosure walls as a result of a higher friction velocity. At the vertical walls an increased free convection flow develops due to the larger heat transfer. At floor and ceiling the changes in the y^+-value are smaller. At the floor the increase might partly be explained from an increased buoyancy effect on the supplied air. The reduced vertical temperature gradient influences the plume development and therewith the flow near ceiling level.

The above results with the imposed heat transfer coefficient lead to the conclusion that the numerical model is fitted to the measurement results. The obvious improvement in the simulated temperature profile when the wall heat transfer characteristics of the simulation model are prescribed have a significant drawback as the heat transfer characteristics should be known in advance. As discussed in Chapter 6.4.3 and later on in Chapter 7.4, the heat transfer coefficient amongst others things is dependent on the configuration, flow pattern (Equation 4.10 and 4.11) and the supply flow rate. However, accurate information on wall heat transfer data for indoor air flow patterns often is lacking.

The development of new or improved wall functions for indoor air flow patterns will be difficult. The near wall flow field in a room is characterised by a combination of developing boundary layers, free and forced convection boundary layers, impinging jets and uneven wall finishes. As already discussed in Chapter 4.4.3, the option to abandon the wall functions by solving the near-wall flow characteristics via low-Reynolds number modified turbulence models is restricted in practice by fine grid requirements and the necessary computing power. The application of empirical relations currently presents a more realistic alternative when the relation and the position of the reference temperature are strictly

defined. Hatton and Awbi (1996) present some examples of such empirical relations for a free and a mixing convection configuration.

From the above results it is obvious that application of wall functions is not effective. Two additional examples are shown in Figure 7.2, for case 2 [T-Q-V×] and case 6 [T-Q+V*]. Fore case 5, the air cooling fraction (ξ [-]; Equation 6.2) was measured at 0.53. The (absolute) sum of the heat fluxes over the enclosure, $|Q_{tot\_k}|$, for the *htc*-variant, was calculated at 265 W. For case 2 these values were determined at ξ = 1.89 and $|Q_{tot\_k}|$ = 114 W and for case 6, ξ = 0.84 and $|Q_{tot\_k}|$ = 245 W. Given the smaller value for $|Q_{tot\_k}|$ in the *wf*-variant, the temperature gradient is larger and the air cooling fraction approaches unity. A lower heat flux over the enclosure (case 2) as well as an air cooling fraction that approaches unity (case 6) indicate a reduced effect of the wall heat transfer on the vertical temperature gradient. Focussing on the air cooling fraction, in order to determine the importance of the wall heat transfer on the simulated temperature gradient, however may be misleading when heat is both introduced and removed over the room enclosure. This applies for the investigated configuration. The importance of the wall heat transfer therefore is estimated better when also the (absolute) sum of the heat fluxes over the enclosure, $|Q_{tot\_k}|$, is taken into account.

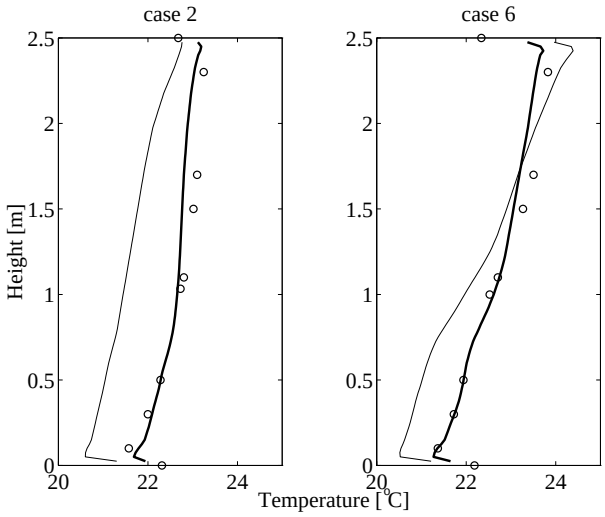

Figure 7.2. Measured and simulated temperature ($\overline{T}_y$) for case 2 [T-Q-V+] and case 6 [T-Q+V]; (* [——] *RNG-wf,* [| | | |] *RNG-htc,* [o] *measurement).*

The overestimation of the temperature gradient when using wall functions, as calculated for the above described cases, may have considerable implications in energy calculations and thermal comfort predictions. Furthermore, the effect on the plume development influences

the distribution of the local mean age of the air and consequently the simulated ventilation effectiveness as shown in Roos (1998[a, b]).

In order to achieve a quantitative reliability of the simulation results, correct simulation of wall heat transfer characteristics therefore is important. This is especially true when the sum of the heat fluxes over the enclosure forms a significant part of the total room heat balance, for example in a room with displacement ventilation and a cooled ceiling. The application of experimentally determined wall heat transfer data from similar flow field patterns then is necessary for a quantitative reliability. Measurement of the (local) wall heat transfer nevertheless is difficult given the low heat fluxes. In this respect the temperature profiles as presented in Chapter 6 allow a derivation of the coefficient through fitting with the temperature profile. Moreover, these results may be used to validate empirical heat transfer relations derived from similar flow patterns.

The obtained results query the applicability of CFD for a quantitative reliable simulation of indoor air flow. This will be the topic of concern in section 7.3.4. First, however, turbulence modelling will be discussed.

7.3.3 Results and discussion on turbulence modelling

Results - In the previous section it was concluded that the CFD-simulations in which the heat transfer is determined by the use of wall functions do not present a good agreement with the experimental results. Therefore in this section only results are discussed in which the wall heat transfer coefficients have been described: variant *RNG-htc* and *ke-htc*. From the results shown in Figure 7.1 the temperature differences between both variants are small. The important difference between both models is the derivation of the turbulent viscosity (μ_t). In Table 7.4 the definition for the calculation of μ_t is summarised for the two variants. Furthermore, a third variant is mentioned, *RNG-hR-htc*, where *hR* stands for high-Reynolds number. This variant uses the RNG-*k*-ε model described in Chapter 4.2.3. Instead of the low-Reynolds number interpolation formula (Equation 4.14), however, the high-Reynolds number expression (Equation 4.6) as used in the standard *k*-ε model is applied.

For the *RNG-htc* variant, μ_t is a function of the turbulence based Reynolds number ($Re_t = k^2\rho/\mu\varepsilon$), whereas the other two variants use the high-Reynolds number turbulence model to calculate μ_t. The latter model is valid for large values of Re_t. Besides the modelling of μ_t, the RNG-*k*-ε model incorporates additional modifications which account for low-Reynolds number effects. The *RNG-hR-htc* variant allows an assessment of the effect of these modifications on the simulation result.

Table 7.4. Calculation of the effective turbulent viscosity (μ_{eff}) for the CFD-simulation variants.

variant	μ_{eff} (= $\mu + \mu_t$)	*Equation*
RNG-htc	$\mu\left(1+\sqrt{\frac{c_\mu}{\mu}}\frac{k}{\sqrt{\varepsilon}}\right)^2$	(4.14)
ke-htc	$\mu + c_\mu \rho \frac{k^2}{\varepsilon}$	(4.6)
RNG-hR-htc	$\mu + c_\mu \rho \frac{k^2}{\varepsilon}$	(4.6)

The plume characteristics and the whole room turbulence intensity are being investigated. In Figure 7.3 and 7.4 the velocity magnitude and the turbulence intensity contour fields are shown for the three variants for a vertical plane in the centre of the room. The plume velocity is illustrated above the contour field for an intersection of the plume. As the applied turbulence models assume isotropic turbulence, following Equation 3.2, the simulated turbulence intensity has been determined from

$$TI = \frac{\sqrt{2k/3}}{\bar{u}}, \qquad (7.3)$$

where k is the turbulent kinetic energy per unit mass.

For the evaluation of the turbulence models, in Figure 7.5 to 7.7 contour lines for the measurement and simulation results are shown in planes of the convection plumes above the thermal mannequin and the PC-simulator on the desk. The indicated turbulence intensity for the simulations is determined according to Equation 7.3, whereas for the measurements Equation 3.3 is applied.

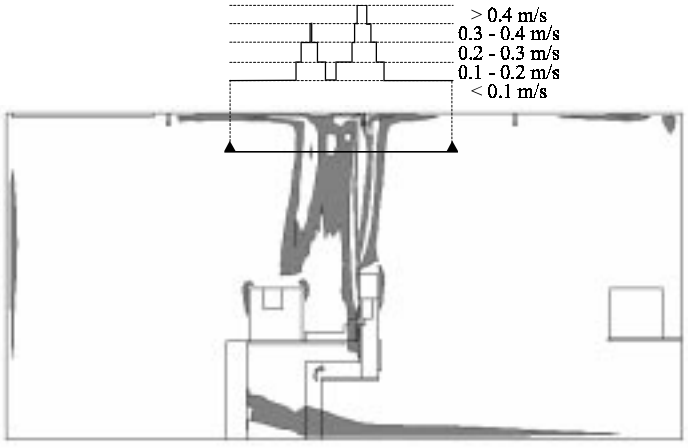

RNG-htc variant

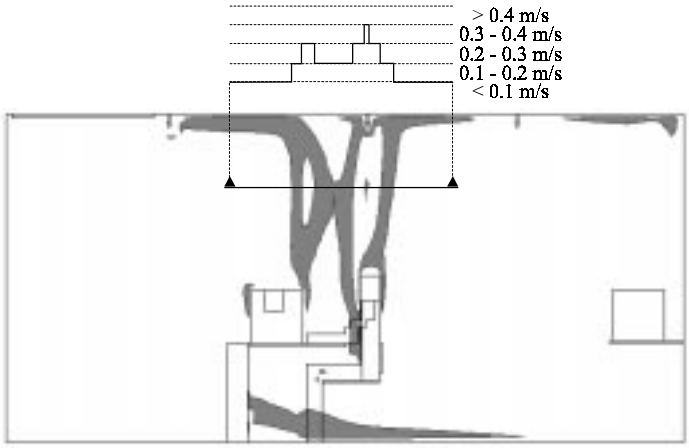

ke-htc variant

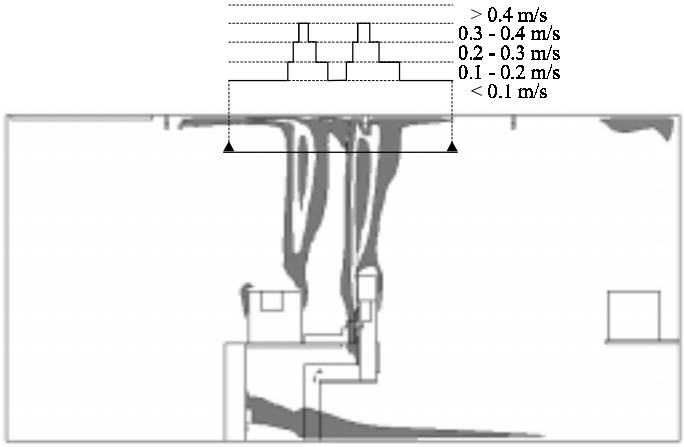

RNG-hR-htc variant

Figure 7.3. Velocity contour field for the three investigated turbulence model variants for a vertical plane in the centre of the room.

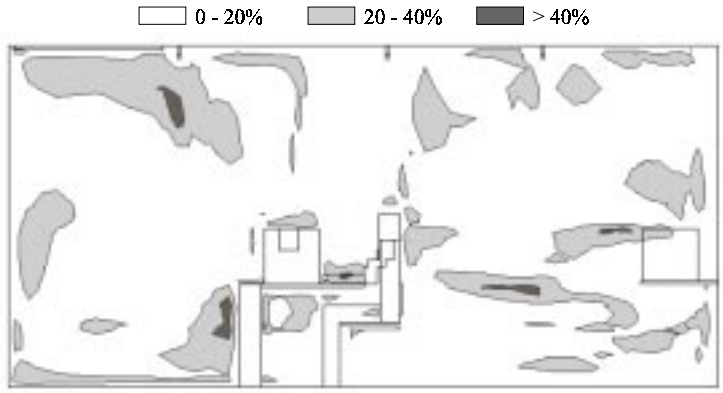

RNG-htc variant

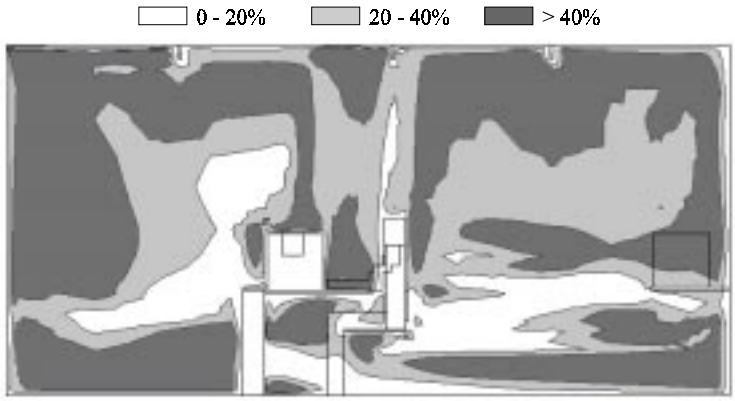

ke-htc variant

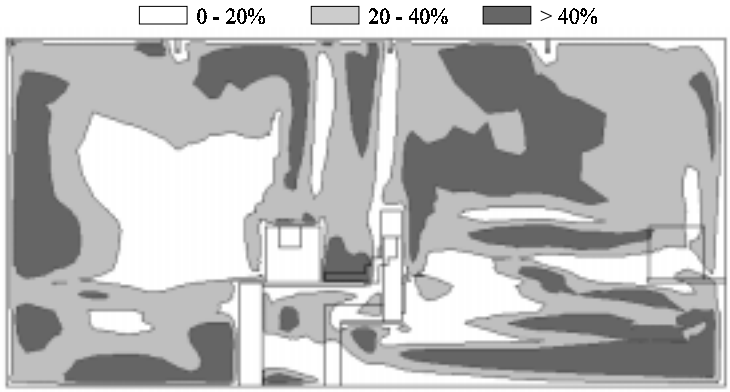

RNG-hR-htc variant

Figure 7.4. turbulence intensity contour field for the three investigated turbulence model variants for a vertical plane in the centre of the room.

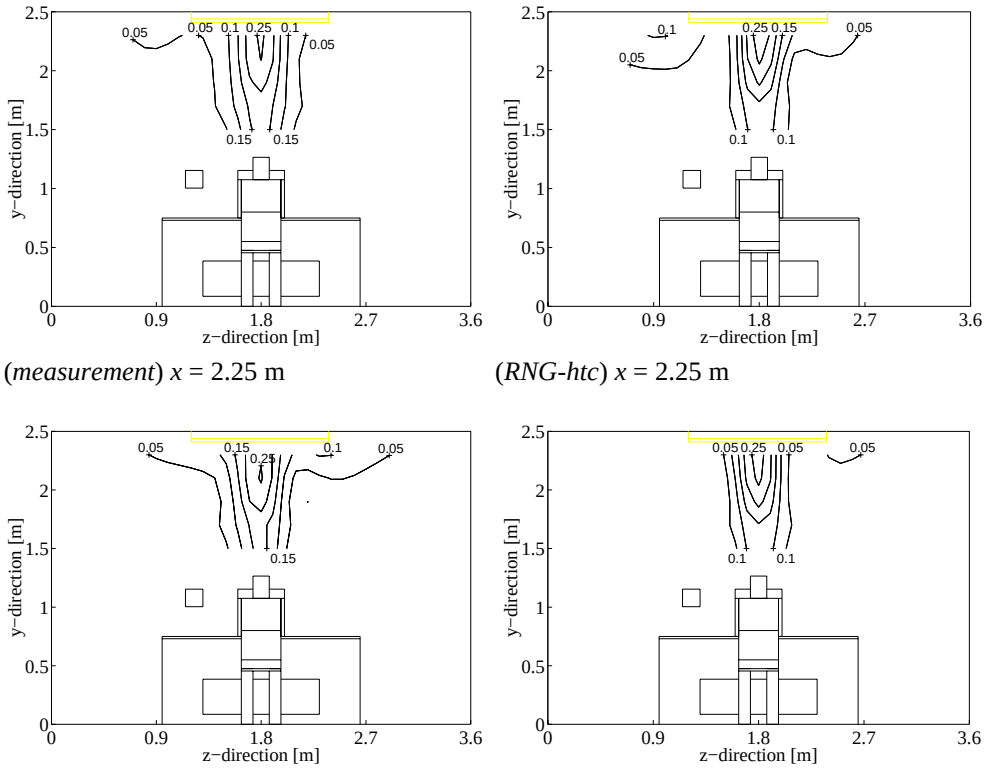

(*measurement*) x = 2.25 m (*RNG-htc*) x = 2.25 m

(*ke-htc*) x = 2.25 m (*RNG-hR-htc*) x = 2.25 m

Figure 7.5a. Measured and simulated velocity contour lines above the thermal mannequin, in [m/s], at x = 2.25 m (x = 2.36 m for simulation results).

Discussion - Comparison of the simulation results for the three variants, shown in Figure 7.3 and 7.4, reveal the following differences:

- Due to the smaller value that is calculated for the turbulent viscosity, the convection plume width above the thermal mannequin is smallest for the RNG-*k*-ε model with low-Reynolds number turbulence modelling. The plume velocity is higher than in the *ke-htc* variant. The *ke-htc* variant calculates a wider plume, due to the larger turbulent diffusion, at lower plume velocity. The simulated plume flow rates are similar (see Table 7.3). For the *RNG-hR-htc* variant the plume flow rate at 0.75 m above the thermal mannequin has been determined at 0.026 m^3/s. The effect of the RNG-modifications in the *RNG-hR-htc* variant compared to the *ke-htc* variant is visible in the higher plume velocities that are simulated. As the velocity gradients are relatively large, the source term R (Equation 4.16) may contribute to this effect.
- The turbulence intensity is considerably higher for the variants in which μ_t is calculated from Equation 4.6. The low-Reynolds number model significantly suppresses the turbulent viscosity in the low velocity areas outside the buoyant plumes. The

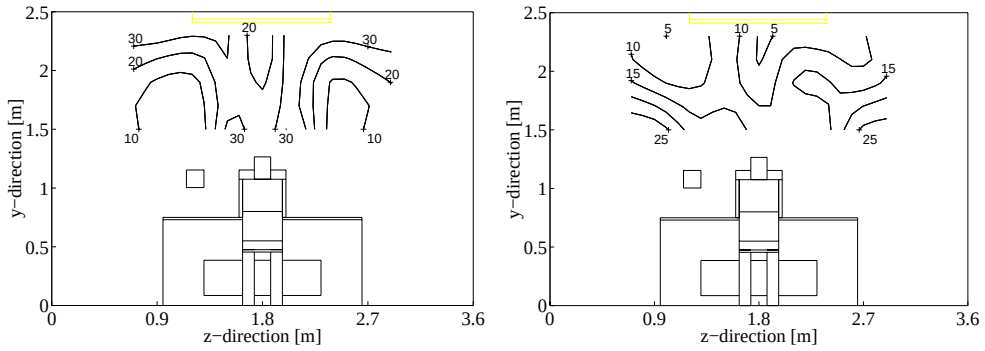

(*measurement*) x = 2.25 m (*RNG-htc*) x = 2.25 m

(*ke-htc*) x = 2.25 m (*RNG-hR-htc*) x = 2.25 m

Figure 7.5b. Measured and simulated turbulence intensity contour lines above the thermal mannequin , in [%], at x = 2.25 m (x = 2.36 m for simulation results).

modifications in the RNG-*k*-ε model (*RNG-hR-htc* variant) are able to reduce the turbulent diffusivity compared to the results obtained with the standard *k*-ε model. The most significant effect nevertheless results applying Equation 4.14.

The plume development and characteristics above the PC-simulator differ from the one above the thermal mannequin. For all variants the plume is shifted towards the thermal mannequin due to entrainment. The differences between the variants again are explained from the turbulence modelling. For the *RNG-htc* variant, because of the closeness of the two plumes and the higher velocities above the thermal mannequin, air cannot reach the entrainment area. This leads to a local negative pressure area which draws the plumes towards each other. For the *ke-htc* variant the larger width of the separate plumes results in an interference of the plumes. For the *RNG-hR-htc* variant, the plume velocity above the thermal mannequin remains lower than for the *RNG-htc* variant. Due to the suppression of the turbulent viscosity, two separate plumes have established above the two heat sources. As result higher velocities can develop above the PC-simulator.

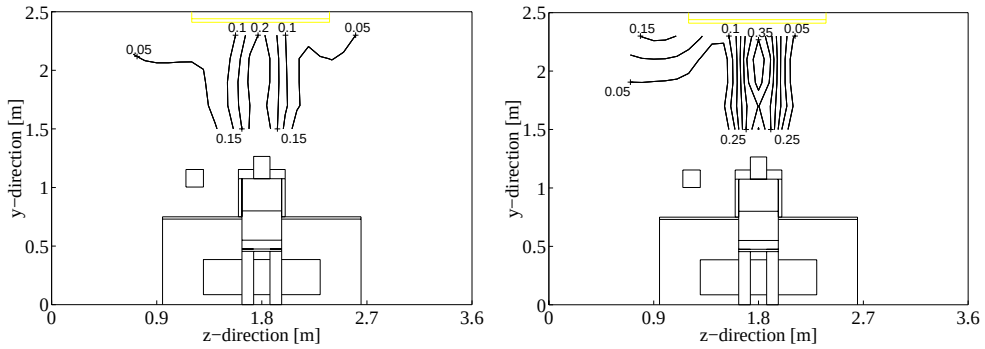

(*measurement*) x = 2.40 m (*RNG-htc*) x = 2.40 m

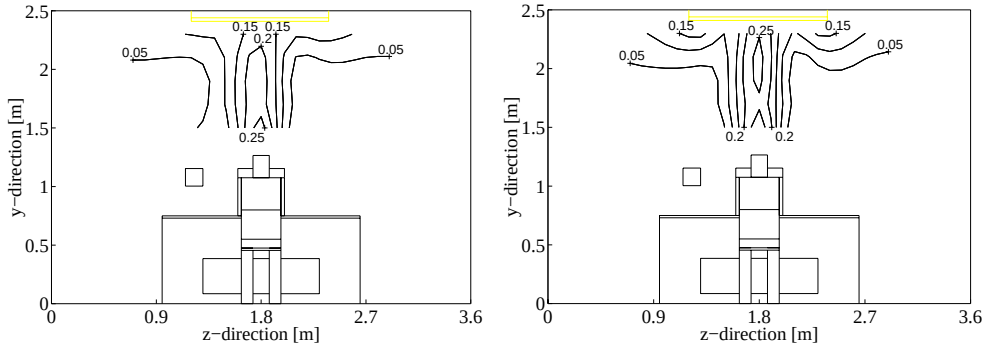

(*ke-htc*) x = 2.40 m (*RNG-hR-htc*) x = 2.40 m

Figure 7.6a. Measured and simulated velocity contour lines above the thermal mannequin, in [m/s], at x = 2.40 m (x = 2.48 m for simulation results).

The plume development at one side of the PC-simulator and the tilting of the plume towards the plume above the thermal mannequin is not apparent from the visualisation of the plumes discussed in Chapter 6 and shown in Figure 6.2 in which a separate plume is visible above the PC-simulator. As for the thermal mannequin, the simulated plume flow rate above the PC-simulator however is of the same order of magnitude for the different variants.

The deviation in plume development is explained from the simplification of the PC-simulator in the CFD-model by a closed boxed with uniform heat flux distribution. In reality a mass flow rate through the PC-simulator is present via the slot at the bottom and through the perforated opening at the top. Müller and Renz (1998[a]) discuss the more detailed modelling of a computer. The computer was modelled with a supply and exhaust and with heat flux boundaries. At the horizontal surfaces of the computer model a zero heat flux was prescribed. The reason for this was to suppress high turbulence production due to the buoyancy source term (G_b; see Table 4.1). The definition of a mass flow rate through the PC-simulator may result in an improved simulation of the plume characteristics. From the

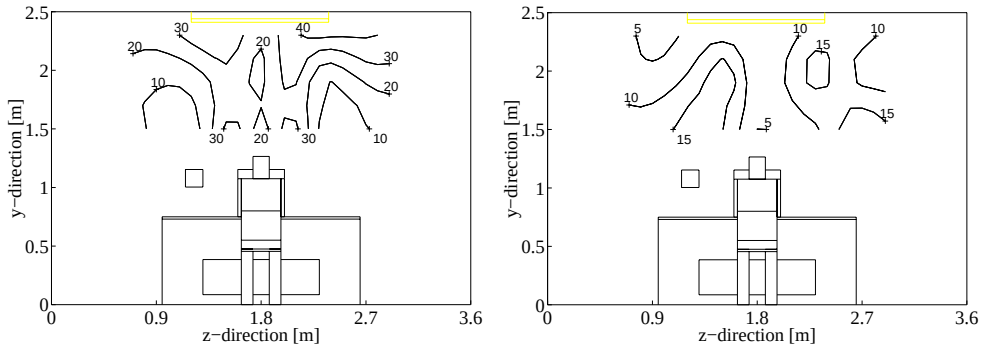

(*measurement*) x = 2.40 m (*RNG-htc*) x = 2.40 m

(*ke-htc*) x = 2.40 m (*RNG-hR-htc*) x = 2.40 m

Figure 7.6b. Measured and simulated turbulence intensity contour lines above the thermal mannequin, in [%], at x = 2.40 m.

simulation and measurement results it however is not clear whether the obtained turbulence intensity values are realistic or not: TI_{max} ~20-40% for the *RNG-htc* variant, TI_{max} ~50-60% for the *ke-htc* variant.

For the further evaluation of the turbulence models, comparison with measurement results is necessary. The applicability of the RNG-*k*-ε model, in comparison to the standard and modified *k*-ε models, for the simulation of indoor air flow is discussed by Chen (1995). Following the comparison of the models for typical two dimensional flow patterns in a room the RNG *k*-ε model (high-Reynolds variant) is preferred. Müller and Renz (1998[a]) compared the standard *k*-ε model with a low-Reynolds number *k*-ε model (Launder-Sharma). Based on the overall, though not convincing, agreement with measurement results, the latter model was preferred for the simulation of a room with displacement ventilation.

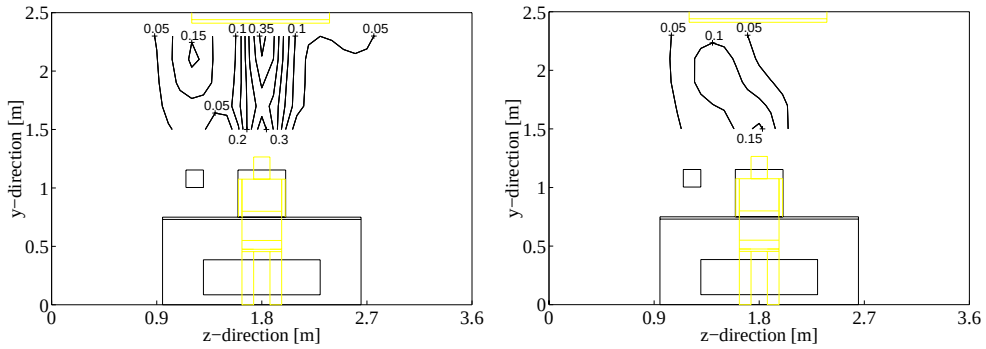

(*measurement*) x = 3.00 m (*RNG-htc*) x = 3.00 m

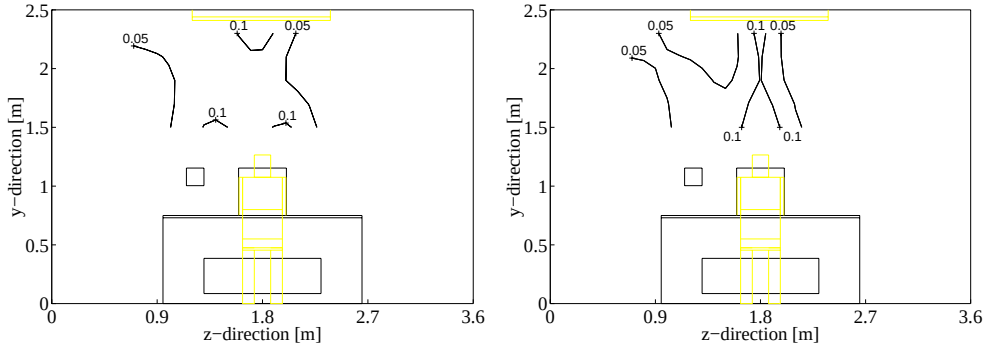

(*ke-htc*) x = 3.00 m (*RNG-hR-htc*) x = 3.00 m

Figure 7.7. Measured and simulated velocity contour lines above the PC-simulator, in [m/s], at x = 3.00m.

A numerical comparison of results from the two turbulence models with measurement results for a three dimensional indoor air flow is shown in Figure 7.5 to 7.7. From the comparison of the measured and simulated contour lines for the flow velocity and turbulence intensity and from additional results for the low velocity area outside the plume, the following conclusions are drawn:

- The plume velocities above the thermal mannequin simulated with the standard k-ε model show best agreement with the measurement results. The difference with the measured plume velocities at the measurement locations above the thermal mannequin on average is less than 0.02 m/s. For the *RNG-hR-htc* variant this is 0.04 m/s and for the *RNG-htc* variant 0.09 m/s. For x = 2.40 m the simulated velocities for the low-Reynolds number variant of the RNG-k-ε model are up to 80% higher compared to the measurement results presented in this work and compared to similar results available in literature. This difference is explained from the uneven boundaries at the thermal mannequin in the experimental set-up. Though modelled as a smooth wall, the actual surface of the mannequin will generate additional turbulence which is indirectly

represented better by the standard *k*-ε model. The additional turbulence improves mixing and opposes the development of large gradients and higher velocities.

- The turbulence intensity in the plume above the mannequin is overestimated with the standard *k*-ε model (on average +8%) and underestimated with the low-Reynolds number variant of the RNG-*k*-ε model (on average -11%). Best agreement is found with the *RNG-hR-htc* variant (on average +4%). In all results the turbulence intensity at the centre of the plume is lower than at the plume boundary due to the higher velocities in the centre and the interaction of the boundary with the air outside the plume. This is in agreement with the measurement results. Except for the *RNG-htc* variant, outside the plume the turbulence intensity in the shown planes reduces to smaller values. This deviation for the *RNG-htc* variant is explained from the lower velocities that are calculated outside the plume.
- In Chapter 3.6 the damping of the applied hot sphere anemometer was investigated and found to be significant. Given its damping, the turbulence characteristics of the plume are predicted best by the RNG-*k*-ε model which uses the high-Reynolds number relation (Equation 4.6).
- From velocity measurement results at 30 positions in the very low velocity area, outside the influence of the buoyant plumes or free convection flow along the wall (at x = 0.75 / 1.5 / 2.0 / 3.75 / 4.5 m, y = 1.5 / 1.7 m and z = 1.30 / 1.80 / 2.30 m), an average turbulence intensity $\overline{TI}$ was measured at 13% with a standard deviation of 6% (maximum TI = 26%, minimum TI = 5%).

  Due to the low velocities, this result may be partly influenced by self-heating of the sensor. Following the suggestion of Chen et al. (1998), the results of the measurements and simulations might be better compared in case the fluctuating velocity $\sqrt{\overline{u'^2}}$ is used, because of the inaccuracy at low velocities. For the indicated 30 positions, in Table 7.5 the measured and simulated averaged value and standard deviation are given for the turbulence intensity and the fluctuating velocity.

Table 7.5. Averaged turbulence intensity and fluctuating velocity over 30 positions in the room outside the buoyant plumes.

		measurement	*RNG-htc*	*ke-htc*	*RNG-htc-hR*
$\overline{TI}$	[%]	13	15	35	28
$\sigma\,(\overline{TI})$	[%]	6	7	19	16
$\overline{\sqrt{\overline{u'^2}}}$	[m/s]	0.0040	0.0025	0.0084	0.0054
$\sigma(\overline{\sqrt{\overline{u'^2}}})$	[m/s]	0.0020	0.0005	0.0040	0.0020

At low velocities, the influence of self-heating of the sensor on the fluctuating values is likely. Therefore, the results outside the buoyant plumes are best predicted with the low-Reynolds number RNG-*k*-ε model (*RNG-htc* variant).

- Comparison of results for the plume above the PC-simulator (x = 3.00 m) is restricted as the plume development in the simulations deviates from the actual plume as shown in Figure 6.2c and Figure 7.7 and as discussed above. The simulated velocities underestimate the measured values.

The obtained measurement results indicate the difference in flow characteristics over the room. The simulation results show that none of the applied models is able to predict all these characteristics well. The plume characteristics are best predicted with a high-Reynolds number approach (Equation 4.6). This agreement however cannot solely be explained from the turbulence modelling, as, for example, the standard *k*-ε model was fitted from results for decaying turbulence which opposes the turbulence development in a plume. Instead it is assumed that the modelling of the thermal mannequin has influenced the result. The effect of the surface roughness on the plume development has not been investigated further. Except for the plume flow rate, the accurate prediction of the plume characteristics normally is of less importance for indoor air flow simulation. The simulated plume flow rates for all investigated variants show good agreement.

Higher priority is given to the correct prediction of the turbulent characteristics outside the buoyant plumes. The importance is found in the accurate prediction of the local ventilation effectiveness (local mean age of the air) and the local contaminant distribution in the room (Roos 1998[a]). A higher turbulent viscosity results in an increased mixing, reducing the gradients in the flow pattern. For example, applying the procedure described by Roos (1998[b]), comparison of the local mean age of the air values for the *RNG-htc* and the *ke-htc* variant indicates that the deviation can be up to 20%. More specifically, the local mean age of the air close to the mannequin is simulated 20% higher with the *ke-htc* variant. Instead, at a position outside the plume, above the interface height, the local mean age of the air is up to 10% lower for the *ke-htc* variant. Therefore, the application of the RNG-*k*-ε model with low-Reynolds number turbulence modelling (Equation 4.14) is preferred. The validation of the results for the ventilation effectiveness is described further in Roos (1998[a]). An accurate validation of the local ventilation effectiveness, however, is very difficult to obtain.

7.3.4 Applicability of CFD for simulation of indoor air flow

From the above discussed results on wall heat transfer and turbulence modelling, the applicability of CFD for the simulation of indoor air flow is questioned. Depending on the required accuracy of the CFD-result, the requirements for the wall heat transfer and

Table 7.6. Matrix for the type of wall heat transfer and turbulence modelling given the requirements put to the CFD-result.

required	*heat transfer*			*turbulence*	
accuracy	*wf*	*htc (lit.)*	*htc (meas.)*	*high-Re*	*low-Re*
qualitative	+/-	+	++	+	+
quantitative (order)	--	+	++	+/-	+
quantitative (accurate)	--	+/-	++	-	+

turbulence modelling may be less strict. In Table 7.6 a summary is given with regard to the required accuracy and the type of wall heat transfer and turbulence modelling required. A differentiation is made with +'s and -'s, ranging from well suited (++) to fully unsuited (--). For the wall heat transfer a further differentiation is made for the source of the applied heat transfer coefficient (htc), whether obtained from literature (lit.) or measurement (meas.). The comparison is made for the total room air flow and not for the plume characteristics and is derived for the investigated desk displacement ventilation configuration.

For a qualitative result in which merely the velocity vector field is of interest to obtain information on the flow pattern in the room, the required accuracy of the wall heat transfer and turbulence modelling is relatively low. These characteristics have been predicted well for all investigated variants. Order of magnitude information on the velocity vector field and the temperature distribution, for example, to obtain an impression of the thermal comfort conditions in the room, at least require a more accurate prediction of the wall heat transfer than is calculated with the wall functions. The application of values for similar configurations, taken from literature, already will improve the reliability of the simulation results. As the velocities in the room are low, discomfort due to draught will not be important and either type of turbulence model may be applied. To derive (accurate) quantitative information on the ventilation effectiveness, the application of the high-Reynolds number turbulence model (Equation 4.6) should be avoided. The low-Reynolds number model however has not been rated 'well suited' (++) because an accurate validation of the calculated ventilation effectiveness has not been performed. In theory the model however should be well suited, given the very low velocities that appear in a room with displacement ventilation. Because the wall heat transfer is significant, a correct simulation using experimental validation data is required (see Roos 1998[a]). As the number of available heat transfer data for different type of configurations, as found in literature, is small, it often may be necessary to perform measurements.

The above discussion assumes a displacement ventilated room in which significant heat transfer to the enclosure is present and radiant heat transfer is less important. E.g., for case 5 [T-Q+V×] the air cooling fraction (ξ) was determined at 0.53 and the (absolute) sum of the heat fluxes over the enclosure ($|Q_{tot\_k}|$) was calculated at 265 W. In most practical indoor air flow configurations, the total heat transfer over the enclosure will be significantly smaller

and the effect on the temperature and flow characteristics therefore will be less. The air cooling fraction may not be the correct parameter to determine the importance of the heat transfer over the enclosure when heat is introduced as well as removed over the enclosure. Then also $|Q_{tot\_k}|$ should be used. When $|Q_{tot\_k}|$ is smaller and ξ approaches unity, the modelling requirements with regard to the wall heat transfer, as presented in Table 7.6, can be less stringent. This obviously is not true for natural convection flow problems. Furthermore, the influence of radiant heat transfer can become important when instead of the surface temperature, e.g., the total wall structure is modelled.

For mixing ventilation, the above remarks on the heat transfer are equally applicable. Chen (1995) discusses two-dimensional simulation results for mixed convection and an impinging jet. From the comparison Chen found best performance for the high-Reynolds number variant of the RNG-*k*-ε model. Simulation results for the Lam-Bremhorst low-Reynolds number *k*-ε model were similar to those for the standard *k*-ε model. From these results the high-Reynolds number RNG-*k*-ε model is preferred for mixing ventilation. A similar comparison for three dimensional mixing ventilation is not known.

The above discussion on the applicability of CFD requires an extension of the simulation results described in this work to other configurations. This extension is indicative. More conclusive results on, amongst others, wall heat transfer and turbulence modelling can only be obtained from similar full-scale investigations as described in this work.

7.4 RESULTS OTHER CASES

Based on the discussion in Chapter 7.3.4, the low-Reynolds number RNG-*k*-ε model has been applied in combination with fixed wall heat transfer coefficients (h_{tc}; Equation 7.1) to simulate the other cases presented in Chapter 6. In this section only the averaged room air temperature profile over the height ($\overline{T}_y$) and the wall heat transfer are discussed.

Results - In Figure 7.8 the measured and simulated temperature profiles for the investigated cases are shown as well as profiles which have been obtained when the heat transfer coefficient (h_{tc}) is only prescribed at floor and ceiling. Table 7.7 presents the heat transfer coefficients (h_c; Equation 7.2) and the heat flux distribution over the enclosure in relation to the total heat. In Table 7.7, h_{c_wall} is the averaged wall heat transfer coefficient over all vertical walls of the enclosure, $|Q_{tot\_k}|$ is the (absolute) sum of the heat which enters or leaves the room over all constant temperature boundaries, $|Q_{k\_walls}|$ is the (absolute) sum of the heat which enters or leaves the room over all vertical walls with a constant temperature and Q_{k_walls} is the sum of the effective heat flow.

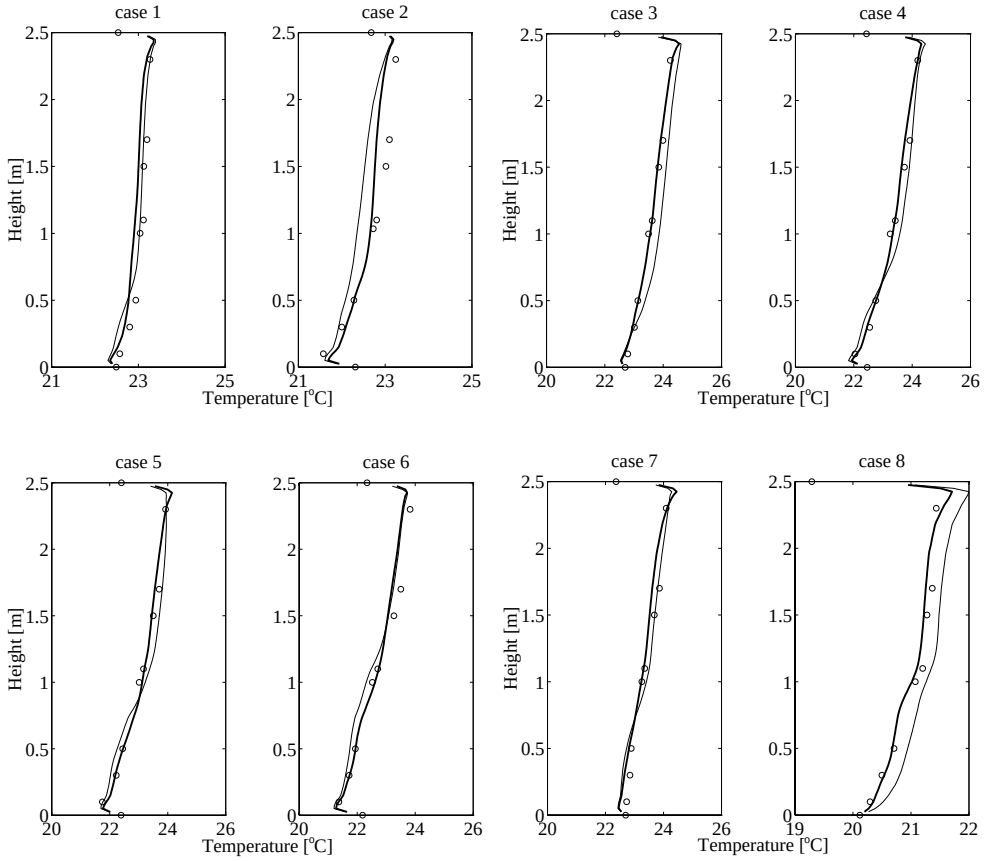

Figure 7.8. Comparison of simulated [| | | |] *and measured* [o] *temperature profiles for the investigated cases (*[——] *simulation result when heat transfer coefficients are prescribed at floor and ceiling only).*

Table 7.7. Numerical results of the heat transfer characteristics for the cases (convective heat transfer coefficients prescribed at all room boundaries).

case	h_{c_wall} [W/m^2.K]	h_{cC} [W/m^2.K]	h_{cF} [W/m^2.K]	$\lvert Q_{tot\_k}\rvert$ [W]	$\lvert Q_{k\_walls}\rvert$ [W]	Q_{k_walls} [W]
1 [T-Q-V-]	2.0	2.9	30.6	76.6	20.3	-3.9
2 [T-Q-V+]	2.2	3.6	6.4	113.9	24.8	+24.8
3 [T-Q+V-]	1.9	4.6	45.6	245.3	56.4	-51.6
4 [T-Q+V×]	2.2	5.1	7.9	256.5	47.3	-34.1
5 [T-Q+V+]	2.1	5.4	6.6	264.8	38.8	-18.0
6 [T-Q+V*]	2.4	5.6	5.6	244.7	20.2	+15.2
7 [T×Q+V+]	2.3	5.1	5.3	237.8	49.3	-31.3
8 [T+Q+V×]	2.0*	4.7	1.6	399.9	83.6	-78.4

* Result for North wall not included, value unrealistically high due to the definition of h_c (h_{cN} = 20.2 W/m^2.K).

Discussion - Figure 7.8 indicates that a good agreement in the mean room temperature profile can be obtained for all cases when the wall heat transfer is simulated realistically. For these simulations the results derived in Chapter 6.4.3 were taken as the point of departure. The fixed heat transfer coefficient (h_{tc}) was changed until the simulated temperature profiles agreed with the experimentally obtained profiles. The derived heat transfer coefficients, summarised in Table 7.7, based on Equation 7.2, differ from the in the simulations defined value as the heat transfer is calculated in the first near wall cell volume (Equation 7.1). The position of this cell is closer to the wall than the reference wall distance used in Equation 7.2. The heat transfer characteristics of the separate boundaries are discussed next.

In Table 7.7 the derived heat transfer coefficient at the vertical walls is in the order of 2 W/m^2.K. This value is in relative good agreement with the overall value given by Tammes and Vos (1984). As a result of the higher heat transfer at the wall, the simulated temperature profile is in better agreement with the measurement results. This effect is shown in Figure 7.8 for case 4 and 5. The actual influence on the temperature gradient nevertheless is small. Only for case 2, 3 and 8, when $Q_{k\_wall}/|Q_{tot\_k}| \geq \pm 0.2$, the temperature profile is influenced substantially. Increasing the heat transfer at the enclosure will result in a further reduction of the vertical temperature gradient for all cases. The sensitivity of the imposed wall heat transfer coefficient on the wall heat flux and flow pattern has not been investigated further.

The averaged heat transfer coefficient at the ceiling ($\overline{h_{cC}}$) for the two heat load variants is 4.2 W/m^2.K. This is in good agreement with the value given in Chapter 6.4.3 (h_{cC} = 4 W/m^2.K). For the high heat load cases [Q+] the heat transfer coefficient is increased by 1.5 - 2.0 W/m^2.K compared to the low heat load cases [Q-]. This increment is mainly caused by the extra impinging convection plumes from the PC-simulators and the lighting. A change in the coefficient mainly influences the vertical temperature profile in the upper part of the room.

For the heat transfer at the floor a decreasing value is found for h_{cF} at increasing flow rate. This result contradicts the results summarised in Table 6.4. The difference follows from the fact that the floor is temperature controlled at a higher temperature than the supply temperature. Therefore the temperature difference increases at higher flow rates. In the model of Mundt (1996) the floor temperature, besides the influence of radiant heat transfer from the ceiling, also depends on the supply temperature and flow rate.

The above results indicate the effect of heat transfer over the enclosure on the room averaged temperature profile over the height, for a room with displacement ventilation and a cooled ceiling. The temperature profile in the investigated configuration is mainly

influenced by the heat transfer over floor and ceiling. Given these results, the presented problem configuration is interesting for testing of newly developed wall functions or empirical heat transfer relations as a series of well documented results are available. Eventually it can also be used for comparison with results from a low-Reynolds number modified turbulence models in which the near wall flow field is solved more accurately. In this work no further attention has been given to the derivation of an improved wall function nor an empirical relation for the heat transfer.

7.5 SUMMARY

1. Comparison of experimental and numerical results for the full-scale experimental set-up described in Chapter 5 and 6 indicates that the wall heat transfer is not correctly modelled with wall functions. The wall heat transfer is underestimated significantly although the average y^+-value in the modelled room is close to values mentioned in literature. The sensitivity of the y^+-value to the heat transfer however is high (for free convection flow $\partial h_c/\partial y^+$ = -0.34 W/m^2.K per viscous unit for y^+ = 7 to 14; Niu 1994). The available wall functions are not valid for developing boundary layer flows, free convection flows and impinging plumes as appear indoors and will lead to grid dependent solutions.
2. The underestimation of the wall heat transfer results in a wrong prediction of the vertical temperature gradient in the room. Besides implications for the energy balance and thermal comfort prediction, the temperature gradient also affects the plume development and the flow pattern with regard to the ventilation effectiveness (Roos 1998[a]).
3. Application of a user-defined heat transfer coefficient as part of the boundary condition definition improves the agreement with measurement results considerably. The importance of a correctly predicted wall heat transfer increases when the (absolute) sum of the heat fluxes over the enclosure $|Q_{tot\_k}|$ is large. For $|Q_{tot\_k}|$ = 114 W the temperature gradient over the height was overestimated by 50% when using wall functions (Equation 4.8). The value for the air cooling fraction (ξ) may be misleading when the importance of the wall heat transfer is determined. Heat may be introduced as well as removed over the enclosure.
4. Comparison of the standard k-ε model and high- and low-Reynolds number variants of the RNG-k-ε model shows that the prediction of the plume characteristics above the applied thermal mannequin, obtained with the high-Reynolds number turbulence modelling (Equation 4.6), are in good agreement with the measurements. This agreement however appears, to a certain degree, to be the result of the modelling of the heat source. The low-Reynolds number variant of the RNG-k-ε model presents more realistic turbulent characteristics for the flow outside the buoyant plumes. As the latter is

regarded to be more important with respect to ventilation efficiency and contaminant distribution, the low-Reynolds model is preferred for the evaluation of a room with displacement ventilation.

5. The application of CFD for the simulation of the investigated configuration (with the desk displacement ventilation concept) is significantly hampered by the requirement to impose wall heat transfer coefficients. This is especially problematic when quantitative agreement is required. Table 7.6 presents an overview of the suitability of wall functions and turbulence modelling, based on the required accuracy of the simulation result. Besides user-defined heat transfer coefficients, the low-Reynolds number RNG-k-ε model is preferred.

   In most displacement ventilation configurations the total sum of the wall heat transfer is smaller than for the investigated case. In these cases the requirements for the wall heat transfer modelling may be less stringent. Two-dimensional results of Chen (1995) have been used to discuss turbulence modelling for non-isothermal mixing ventilation. Then the high-Reynolds number RNG-k-ε model is preferred. For three dimensional full-scale mixing ventilation flow problems, a comparison similar to the one described in this chapter is not known.
6. Comparison of the vertical temperature gradient ($\overline{T}_y$) for all measurements with similar simulation models shows good agreement if the heat transfer is modelled correctly. Given the close relation between temperature profile and wall heat transfer and the importance of the wall heat transfer, the experimental results may be used to validate specially derived wall functions or empirical relations for the wall heat transfer in a room with displacement ventilation with a cooled ceiling. The heat transfer coefficients derived in this work are well in line with results found in literature.

Chapter 8

APPLICABILITY OF THE DDV-CONCEPT

8.1 INTRODUCTION

In Chapter 2 the desk displacement ventilation (DDV-) concept was introduced. The DDV-concept intends to create a micro-climate by introducing the supply air below the desk, applying the rules set by the displacement ventilation principle (see Figure 2.6). After successful application in a dealers room, the combination of the positive features of displacement ventilation, e.g. the ventilation effectiveness, and of task conditioning, e.g. control on thermal comfort requirements, may be interesting for application in normal office configurations. As the performance of the DDV-concept for normal office configurations is not clear, in Chapter 2.3.3 several questions were posed with regard to the applicability of the DDV-concept.

In Chapter 6 and 7 experimental and numerical results for steady state conditions have been discussed. From these results the DDV-concept is evaluated below with regard to micro and macro-climate (see Figure 1.2) and thermal comfort. In order to discuss transient conditions, additional experimental and numerical results are presented. These results allow further insight in the applicability of the DDV-concept for standard office configurations and of the displacement ventilation principle for task conditioning purposes in general.

Finally, an example is presented of an improved version of the concept as investigated through the use of CFD. This example illustrates the use of the CFD-tool for improvement of the indoor environment.

8.2 STEADY STATE RESULTS

8.2.1 Flow pattern DDV-concept

Figure 8.1 presents an example of the flow pattern for an office configuration in which the DDV-concept is applied. The flow pattern represents case 3 [T-Q+V-] (see Table 6.1) and is obtained from the validated CFD-simulations described in Chapter 7.

From Figure 8.1a it is clear that the temperature gradient below the person is greater than at a position further away. A difference in the vertical temperature gradient is found on the opposite sides of the desk. These characteristics and the velocity contour field indicate the local influence of the system. Furthermore, the occupant is the only heat source which induces air from the fresh supply air layer near the floor. As the interface height is below head level, the air quality at the mouth of the occupant therefore will be significantly better than the air quality at other locations at similar height. This effect has been confirmed from

a)

b)

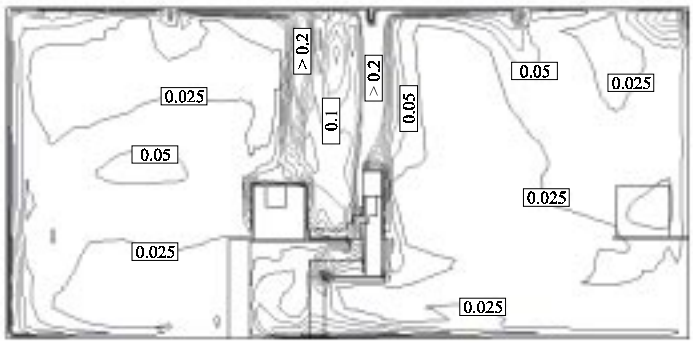

Figure 8.1. Typical example of numerically simulated temperature (a) and velocity (b) flow pattern at the central plane of the office configuration equipped with the DDV-concept (case 3 [T-Q+V-]; see Table 6.1 and Chapter 7).

local mean age of the air measurements as performed by Roos (1998[b]). Using the personal exposure model defined by Brohus (1997), the effectiveness of entrainment in the human boundary layer (η_e) however does not show an improvement compared to results for normal displacement ventilated rooms (Brohus 1997). For this comparison, the local mean age of the air was assumed proportional to the contaminant concentration.

The steady state results for the DDV-configuration presented in Chapter 6 and Chapter 7 have also been compared with measurement results from literature which focus on displacement ventilated rooms (Krühne (1995) and Mundt (1996)). The difference between the presented results and those for a displacement ventilated room were negligible. This is explained from the fact that the introduced colder supply air is spread over the total floor area first, before it returns to the heat source (the occupant) and enters the buoyant plume. This effect is confirmed from visualisations with smoke (Figure 6.1). The convection plume rate at the occupant near floor level is too small to take up all supplied air. Moreover, at higher level room air is induced into the plume due to entrainment.

8.2.2 Thermal comfort DDV-concept

As the supply temperature is below room temperature, relatively cold air is provided directly at a critical position of the body, i.e. the ankles. Though control is in the hands of the occupant, thermal comfort conditions can be derived for the in Chapter 6 investigated cases. Velocity and temperature measurements near the ankle have been used to determine the *PMV*, *PPD* and *PD*-value (Fanger 1970, Fanger et al. 1988). Fanger obtained the PMV relation for thermally uniform conditions (see Chapter 2.2.2), As the conditions at the ankle are most critical in the DDV-concept, these conditions are assumed to prevail for the whole micro-climate. The results are summarised in Table 8.1.

Table 8.1. PMV-, PPD- and PD-value near occupant when conditions at the ankle are applied for the whole micro-climate (M = 65 W/m^2; I_{clo} = 0.7 clo; φ = 50%).

Case	$\bar{u}$ [m/s]	σ_u [m/s]	T_{air} [^{o}C]	T_{mrt} [^{o}C]	*PMV* [-]	*PPD* [%]	*PD* [%]
1 [T-Q-V-]	0.12	0.01	21.3	22.7	-0.66	14	9
2 [T-Q-V+]	0.11	0.03	20.6	22.7	-0.75	17	10
3 [T-Q+V-]	0.12	0.02	21.6	22.9	-0.61	13	9
4 [T-Q+V×]	0.08	0.02	21.2	22.8	-0.60	13	6
5 [T-Q+V+]	0.11	0.03	20.9	22.7	-0.69	15	9
6 [T-Q+V*]	0.18	0.04	20.7	22.6	-0.98	25	18
7 [T×Q+V+]	0.11	0.03	22.6	22.8	-0.43	9	8
8 [T+Q+V×]	0.05	0.01	21.8	20.0	-0.83	20	0

From Table 8.1 it can be concluded that, according to the definition of the *PMV*-value, the thermal conditions are slightly cool and do not meet the requirements formulated in ASHRAE (1992): *PPD* < 10%, for all but case 7. Because the velocities remain very low, the percentage of dissatisfied due to draught on the other hand is in compliance with the formulated criteria (*PD* < 15%) for all flow rates except the highest supply air flow rate. To increase the *PMV*-value, the supply temperature should be increased.

The vertical air temperature difference between 0.1 m and 1.1 m height was less than 3^{o}C for all investigated cases and thus would meet the standards criterion (ASHRAE 1992). Skistad (1994) recommends that the vertical temperature gradient should be restricted to 2^{o}C/m, as higher than normal velocities are expected across the ankles. Assuming this point of departure, the criterion is not met for all displacement ventilated cases, except for case 1 and 3 which have a low air change rate and a slightly higher supply air temperature.

To determine the effect of the change in boundary conditions on the boundary layer velocity near the mannequin, the air velocity midway between chest and desk table was measured. From these results the boundary layer is found to be nearly independent of the supply flow rate.

Besides the full-scale measurements with the thermal mannequin, indicative subjective tests have been performed with test persons that were seated in the experimental set-up for 1.5 hour. In total five persons voted on the thermal comfort conditions at ACH = 1.5 h^{-1}, $T_{wall} \approx$ 23^{o}C, and a supply air temperature between 17^{o}C and 24^{o}C. The test person was the only heat source in the room and was not able to change the thermal conditions. The clothing insulation was estimated at 0.5 to 0.6 clo, the metabolic rate at 60 to 70 W/m^{2}. A questionnaire was designed following the description of Gan and Croome (1994). In the questionnaire thermal comfort votes were requested on a seven-point scale and subdivided to head, chest, leg and ankle level. Furthermore, an overall impression was asked for.

The overall thermal comfort votes for the given conditions ranged from slightly cool (*PMV* = -1) at temperatures between 17^{o}C and 22^{o}C to neutral (*PMV* = 0) at 24^{o}C. However, a large difference was found for the different levels. At ankle level the conditions ranged from cool (*PMV* = -2) at 17^{o}C to slightly cool at 24^{o}C, whereas at head level the thermal conditions were voted neutral for all investigated supply temperatures. At a supply temperature of 17^{o}C, the vertical temperature difference was larger than 3^{o}C.

8.2.3 Discussion steady state results

The experimental and numerical results indicate that the DDV-concept functions according to expectations: the system determines the direct surrounding of the occupant. As the system is located close to the occupant, the supply conditions are important. Assuming that within office environments cooling will be required predominantly, the prevailing thermal comfort conditions and the subjective tests indicate that the supply air temperatures should be relatively high (>20^{o}C) to obtain thermally comfortable conditions. The supply air flow rate cannot be increased significantly due to draught risk. The convective cooling load that can be obtained with the DDV-system therefore is low (in the order of 100 W). Under normal conditions the convective cooling load should be in the order of 200 W (~10 W/m^2) or higher, so additional cooling will be necessary, e.g., through a cooled ceiling.

From the visualised flow field it is concluded that the boundaries of the micro-climate are less defined than projected. This is supported by the local mean age of the air measurements of Roos (1998[b]) and the comparison with Brohus (1997). The results indicate a close agreement between the standard displacement ventilation principle (see Figure 1.1) and the DDV-concept (see Figure 6.1).

From the steady state results however an important specification of task conditioning systems cannot be investigated, the effective response to a change in supply conditions. As the supply is situated close to the occupant and individual control on thermal parameters is possible, the question remains whether the DDV-concept can operate as a task conditioning system. This will be the topic in the next section.

8.3 TRANSIENT BEHAVIOUR

8.3.1 Introduction

An important requirement of an individually controlled task conditioning system is a short *response time* between the moment of change of the control setting of a system parameter and when the user in fact notices a change. Little information is available on this combined physical, physiological and psychological subject. In order for the system to be regarded as an individually controlled system, the response time is postulated to have to be within the order of one minute. If the sensed response to the control action takes longer than one minute the system is not able to respond to the rapid physiological changes and therefore the thermal comfort requirements. From a psychological point of view, the occupant expects a nearly direct noticeable result after a change of the settings which would confirm the control.

The resulting effect near the occupant (e.g., $(T_{end} - T_{start})_i$) differs from the absolute change in the system parameter (e.g., $(T_{end} - T_{start})_{supply}$). This effect is indicated as the amplitude of the step response and will mentioned as the *step response*. The step response is defined as the ratio of the change at a point in the room to the change at the air supply at renewed steady state conditions. E.g., for a temperature change this would read,

$$step\ response = \frac{(T_{end} - T_{start})_i}{(T_{end} - T_{start})_{supply}}. \tag{8.1}$$

The step response preferably should approach unity. A small value of the step response indicates a large damping. The damping is defined as

$$damping = (1 - step\ response) \cdot 100\%. \tag{8.2}$$

For individually controlled systems (Bauman and Arens 1996) that force the air in the occupants direction at relatively high velocity, the response time in respect of velocity changes usually does not present a typical problem. This also accounts for the step response, as entrainment of room air will be limited if the distance between the supply and the occupant is small. For the DDV-concept these transient parameters are more critical. They have been investigated through experiments and by a parameter study using a relatively simple one-dimensional numerical model of the flow problem. These investigations are described in the next sections.

8.3.2 Experimental approach

Procedure - For the experimental approach, the experimental set-up described in Chapter 5 has been altered slightly. Additional temperature measurement locations were introduced close to the thermal mannequin at 'ankle', 'crotch', 'neck' and 'mouth' position. Temperatures above 'ankle' level were measured in the boundary layer flow at the mannequin, at 0.02 ± 0.005 m distance from the surface of the mannequin. The temperature measurements were undertaken with PTC's. Other measurement sensors (velocity anemometers and thermocouples) were positioned at different heights and distances from the supply as shown in Figure 8.2. The positions remained fixed for all measurements.

Measurements were taken for a period of 65 minutes with the thermal mannequin as the single heat source. Steady state conditions were maintained by the climate chamber control unit and temperatures typically were kept constant within ±0.15°C for more than one hour before the start of the measurements. These conditions were registered during a period of approximately 20 min, after which a step in the supply temperature was introduced. A temperature increase of +3°C was obtained at a maximum achievable rate of increase of temperature of 25°C/h. The end-point supply temperature was controlled by hand during the

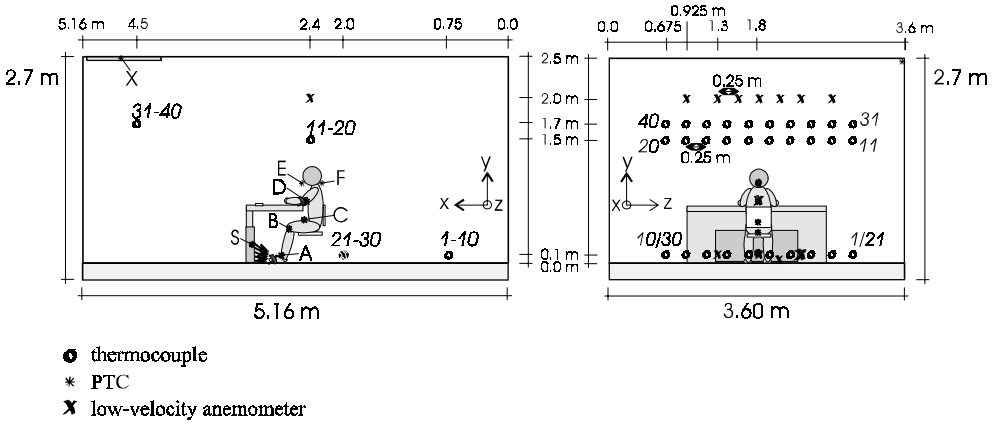

Figure 8.2. Configuration for the transient experiments.

remaining registration time. Wall temperatures were computer controlled. The average variation in the wall temperatures, during this part of the experiment, was less than 0.15°C (standard deviation 0.1°C). Only the floor temperature, that was controlled indirectly due to the raised floor construction, was found to vary up to 0.5°C. The average room temperature at the start of the measurements was set at 23°C. The flow rate for most measurements was set at $ACH \cong 1.5\ h^{-1}$.

All transient experiments were performed following the described procedure. Several parameters in the experimental set-up were varied in order to determine the influence on response time and step response. Table 8.2 summarises a selection of the measurement cases. In Table 8.2, T_{supply} refers to the set-point temperature at the supply before a step was introduced, ΔT_{supply} is the desired supply temperature difference between the end and start point of the measurement and T_{wall} is the wall temperature set-point, the air change rate is indicated by *ACH*.

Table 8.2. Selection of the investigated transient measurement cases.

case	T_{supply} [°C]	ΔT_{supply} [°C]	T_{wall} [°C]	*ACH* [h^{-1}]	$\dot{V}$ [m^3/s]	*	** [m]	*** [m]
a	17	+3	23	1.5	0.019	-	-	-
b	20	+4.5	23	1.5	0.019	-	-	-
c	17	+3	23	1.5	0.019	×	0.5	×
d	17	+3	23	1.5	0.019	×	0.5	2.4
e	17	+3	23	2.3	0.029	-	-	-

* obstruction at 1.0 m from table behind the thermal mannequin [no = -; yes = ×]
** height obstruction
*** obstruction over full width of the room [no = - ; yes = ×]; #: centred [m]

The supply temperature and the temperature step were chosen to allow a displacement type of flow pattern to remain after the change (T_{supply} = 17°C; ΔT_{supply} = +3°C) or to allow the flow pattern to change due to buoyancy (T_{supply} = 20°C; ΔT_{supply} = +4.5°C).

An obstruction was introduced behind the occupant to reduce the room volume at the lower part of the room (case *c* and *d* in Table 8.2; not shown in Figure 8.2). The height and width of the obstruction were also taken as a parameter. In other cases the sides of the desk and 0.5 m on both sides of the occupants side of the desk were screened, so that the flow was restricted to a small area in which the occupant was seated. Finally, measurements have been performed at a higher flow rate (case *e* in Table 8.2).

Results and discussion - Velocities were smaller than 0.15 m/s, with the exception of the average plume centre velocity, and do not present a typical problem with regard to thermal comfort (Fanger et al. 1988). Velocity variations in the transient regime are a result of temperature changes, because only the temperature was varied in the experiments. The discussion on the results therefore is limited to temperature registrations.

Figure 8.3 and Figure 8.4 show typical results for the temperature course at different positions near the thermal mannequin for case *a* (1) and *b* respectively. The characters and numbers in both figures refer to the measurement positions as presented in Figure 8.2. Results for the step response are shown in Table 8.3. They are determined from $(T_{end} - T_{start})_i/(T_{end} - T_{start})_{supply}$, in which *i* represents the measured air temperature at the specific PTC or thermocouples. Also results of a second run for case *a* are given, allowing an examination of the reproducibility of the experiments. Given the measurement accuracy the step response is accurate up to ±0.05 for a step response smaller than 0.3.

Step response (Damping) - Figure 8.3 indicates a temperature increase at the supply from 17°C to 20°C. As the supply temperature will remain below the average room temperature, a displacement type of flow pattern is maintained. The results show a nearly immediate response at the 'ankles' of the thermal mannequin seated at the desk (position *A*). This point is located at only 0.3 m from the supply, but the damping due to entrainment is already 22%. At other positions the damping increases rapidly to 80% and higher. Comparing these results with the damping at the exhaust (position *X*) or at the thermocouple positions in the room (see Table 8.3), it can be concluded that the increase in temperature near the thermal mannequin corresponds with the temperature increase of the room as a whole. *There is therefore no particular advantage in sitting close to the unit.*

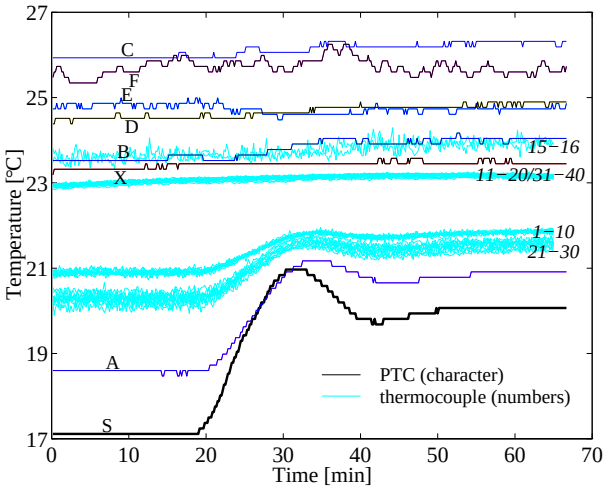

Figure 8.3. Temperature as function of the time for measurement case a (1) (see Figure 8.2).

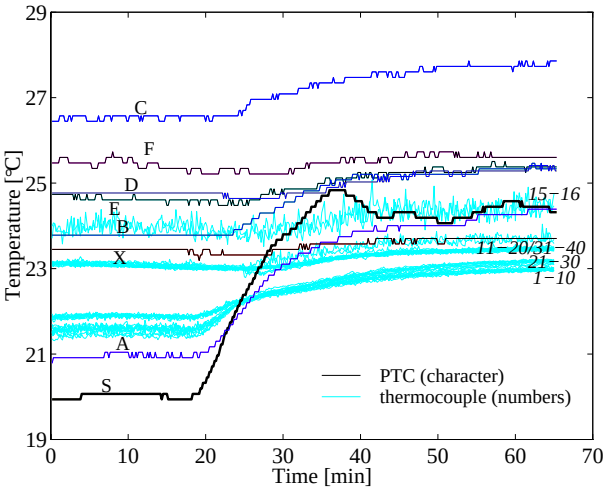

Figure 8.4. Temperature as function of the time for measurement case b (see Figure 8.2).

Table 8.3. Measurement results step response, $\frac{(T_{end} - T_{start})_{PTC\,/\,thermocouple}}{(T_{end} - T_{start})_{supply}}$.

	case				
	a (1)	*a* (2)	*b*	*b*$^{\#}$	*e*
$(T_{end}\text{-}T_{start})_{supply}$	2.96°C	2.95°C	4.38°C	2.14°C	3.01°C
PTC					
A	0.78	0.78	0.76		0.88
B	0.18	0.15	0.35		0.26
C	0.13	0.11	0.29		0.08
D	0.12	0.09	0.13		0.11
E	-0.02	-0.02	0.16		0.09
F	0.04	0.04	0.03		0.17
X	0.04	0.02	0.06		0.09
thermocouples					
1-10	0.31	0.29	0.26	0.38	0.40
11-20	0.05	0.03	0.10	0.19	0.08
15-16	0.11	0.10	0.12	0.25	0.18
21-30	0.42	0.44	0.37	0.46	0.57
31-40	0.05	0.03	0.10	0.19	0.08

\# damping determined from $T_{supply} = T_{thermocouples,\ 21\text{-}30}$

If the supply temperature increases to above the mean room temperature (case *b*), the flow pattern is changed. The flow reversal occurs just before T_{supply} equals the temperature measured at thermocouple positions 21-30 ($T_{thermocouple,\ 21\text{-}30}$). The system then is not operated as a displacement ventilation system: the incoming flow will rise because of buoyancy. This effect is most clearly visualised by the temperature measured at positions *B* ('knees') and *C* ('crotch') as shown in Figure 8.4. The temperature increase at position *C* is not continued at position *D* ('chest'), which is situated above *C*, just above desk level. Visualisation of the flow field (see Chapter 6.3.2) indicates that the desk table obstructs the flow above the legs. The flow deflects and spreads in different directions. Therefore more mixing will occur. As a result, the damping at position *D* is of the same order of magnitude as for the displacement ventilation flow pattern. In contrast, at 'mouth' height (position *E*) a greater step response is measured when the displacement type of flow pattern is disturbed. This effect is explained from entrainment of air originating from the unit which has not ascended through the buoyant plume. The temperature at the 'neck' of the thermal mannequin (position *F*) is hardly affected by the change in the supply temperature for both flow field types.

The thermocouple measurements indicate the effect of the change in the room flow pattern (see Figure 8.4). The vertical temperature gradient is gradually reduced as a result of increased mixing with the incoming flow. The effect is less clear from the step response results (see Table 8.3). However, if T_{start} at the supply is set to $T_{supply} = T_{thermocouple,21\text{-}30}$, the step response for the upward directed flow pattern is found ($b^{\#}$, Table 8.3).

Response time - The step response can be determined according to objective criteria, i.e. mean start- and end-point temperature. For the response time this is not possible given the supply temperature step-up and the present overshoot. An order of magnitude value may only be estimated graphically. From the figures it is apparent that the response time is longer than the postulated maximum response time, for a large part of the body.

Variants - Improvement of the step response and response time has been investigated further via the described cases (see Table 8.2). For those cases where the displacement ventilation flow pattern remains intact after the temperature step, differences with the described results for case *a* are small and restricted to the lower part of the room. Near the thermal mannequin, above the legs, no significant improvement in the step response was measured.

For the cases where the desk sides were covered, a significant reduction in the step response was measured. When a mixing type of flow pattern established itself, an improvement is determined when the desk sides are covered. At higher flow rate (case *e*) the step response near the mannequin on average is increased by about 30% compared to case *a*. In case of mixing ventilation the average step response near the mannequin is improved by about 10% compared to case *b*.

8.3.3 Numerical approach

Introduction - Using the experimental results, the research focus is directed towards the transient effect of a displacement ventilated room as a whole after a change in the supply conditions. This indicates a worst case scenario for the DDV-concept and it would allow a comparison with the results found close to the occupant. If differences in the transient parameters are significant, the DDV-concept can result in an improvement of the efficiency of the displacement ventilated system compared to a set-up where the unit is situated against a wall. Furthermore, in the experimental results the response time aspect has been neglected almost completely as it could not be determined from the measurement results.

In order to obtain a pragmatic understanding of the influence of different parameters on the step response and response time, for a normal displacement ventilation system, a relatively

simple numerical model has been developed. The modelling and validation of this numerical model is presented first after which results of a parameter study are discussed.

Theory and modelling - The model is based on the temperature stratification which is characteristic for displacement ventilation. The room is represented by a number of stacked zones (see Figure 8.5). Heat is transported through convection (Q_c) and transferred at the walls (Q_k). Furthermore, in each zone a heat source ($Q_{h,i}$) can be introduced. The heat balance is solved for each zone according to

$$\rho c_p V_i \frac{dT_i}{dt} = Q_{h,i} - Q_{k,i} - Q_{c,i}\,, \tag{8.3}$$

where V_i is the volume of zone i, T_i the air temperature at zone i, t the time and Q the heat. The transient temperature per zone, following a temperature change or flow rate change at the supply, is calculated from

$$\frac{dT_i}{dt} = \left(Q_{h,i} - h_{c,i}A_i\left(T_i - T_{wall,i}\right) - \rho c_p \dot{V}\left(T_i - T_{i-1}\right)\right)/\rho c V_i\,, \tag{8.4}$$

where $T_{wall,i}$ is the wall temperature at zone i, $h_{c,i}$ the convective heat transfer coefficient at zone i, A_i the surface at zone i and $\dot{V}$ the flow rate.

As the model is one-dimensional and complete mixing is assumed for each zone, a factor (q_i), the heat source effect factor, is introduced to account for the fact that part of the heat $Q_{h,i}$, introduced into zone i, is transported directly into the above lying zones by the convective plume. A specific zone is heated by a fraction of the heat source present. This treatment is consistent with that of the contamination distribution described in (Krühne, 1995) and with the degree of flushing described in (Bach et al., 1993). The convected heat, $(1\text{-}q_i)\cdot Q_{h,i}$, must be distributed over the other zones. An extra factor (qq_i), the heat distribution factor, is introduced to account for the distribution of the extra heat input over the zones ($\Sigma qq_i = 1$). Introduction of these two factors allows a correct representation of the

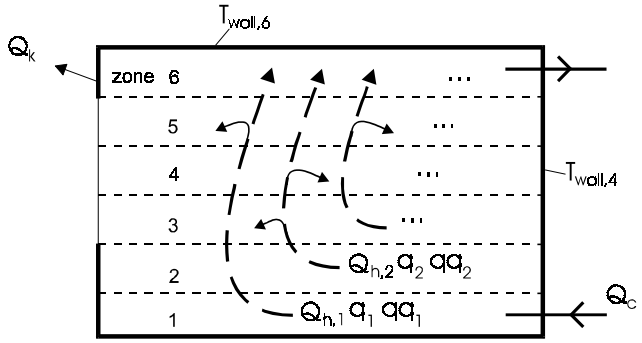

Figure 8.5. Zonal model (see Equation 8.5).

temperature gradient in the room and a more accurate calculation of the heat transfer rate at the wall. The final equation therefore is written as

$$\frac{dT_i}{dt} = \frac{\left(q_i \cdot Q_{h,i} + qq_i \left(\sum_{i=1}^{n} (1 - q_i) \cdot Q_{h,i} \right) - h_{c,i} A_i (T_i - T_{s,i}) - \rho c_p \dot{V} (T_i - T_{i-1}) \right)}{\rho c_p V_i}, \qquad (8.5)$$

where, q_i is the heat source effect factor, qq_i the heat distribution factor and n the number of zones.

Visualisation of the flow field indicates that the upper zone returns air to the lower zones along the walls (see Figure 6.1). As the model is one-dimensional, the zonal conditions can only be influenced by upstream conditions. This is partly resolved by the introduction of qq_i. The delay caused by the heat transfer from the heat source from one zone to another has been neglected. This has no influence on the simulated response time, as unsteady state conditions are only prescribed for the supply. The walls have not been modelled and the boundaries of the zones therefore act as heat sinks. For the climate chamber set-up from which the measurement results have been obtained this represents a realistic situation. For high density and high specific heat of the room walls a heat sink representation is valid. In the model radiant heat exchange has not been taken into account.

Validation - The model is constructed of six zones of equal volume and height. Krühne (1995) developed a steady state model for a room with displacement ventilation with cooled ceiling. For this model, Krühne determined that a discretisation into six zones is sufficiently accurate for rooms of 3 to 4 m height. In Hensen et al. (1996) a comparison is presented for a 3 and 6 zonal displacement ventilation model. The maximum difference in results between the two models is in the order of 0.2^{o}C.

Dimensions and boundary conditions were taken from measurement case *a* (1) (see Table 8.2). The supply is situated in zone 1, the exhaust in zone 6. The convective part of the heat source was taken from Appendices D and F and divided over zone 1 (20 W) and 2 (45 W). In the other zones no heat sources were prescribed. The heat transfer coefficients were taken from literature (Chen and Jiang 1992) and from the measurement and simulation results (floor: h_{cF} = 4.5 W/m^2.K; ceiling: h_{cC} = 4.0 W/m^2.K; walls: h_{c_wall} = 2.5 W/m^2.K). The model parameters, q_i and qq_i, have been tuned to the experiments until a qualitative good agreement was found for q_i = [0.6; 0.3; 1; 1; 1; 1] and qq_i = [0; 0; 0.025; 0.15; 0.15; 0.675] (see Figure 8.6). The thermocouple results indicate the room temperature distribution and its transient course.

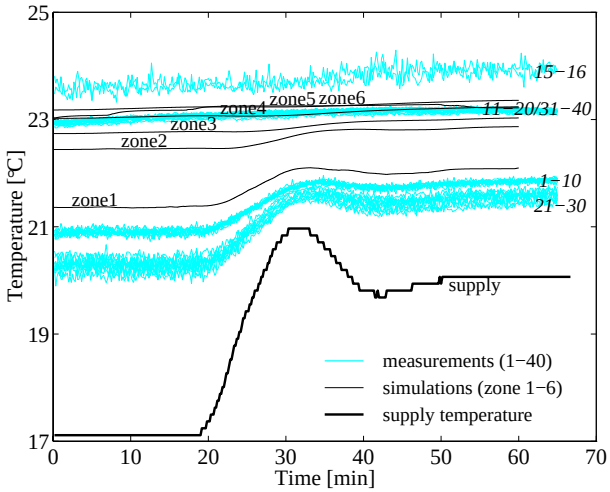

Figure 8.6. Comparison of simulation results and thermocouple data for case a (see Figure 8.2 and 8.5).

The measured exhaust temperature was consistently 0.2°C higher than the calculated temperature at the highest zone. The simulated heat balance, therefore, is not completely in agreement with the measurements. The difference results from the discretisation in the height and the applied overall heat transfer coefficients. The sensitivity of the settings for h_c, q_i and qq_i was determined using the cases mentioned in Table 8.2. Considering the simplicity of the model, a satisfying agreement was found. The applied constants are useful for transient application at $\dot{V}$ = 0.010 to 0.039 m^3/s.

Parameter study - For a true step in the temperature and/or the flow rate the response time (τ_i) is determined according to the 1-e^{-1} method. The step response ($\Delta T_{zone,i}$ /ΔT_{supply}) is defined as the zonal temperature difference between end and start condition relative to the temperature step at the supply. Both parameters were investigated for a temperature step, a flow rate step and a combined temperature-flow rate step. Furthermore, the sensitivity of the response time and step response to the heat transfer coefficient and the room volume was determined. From the parameter study general remarks regarding the response time and the step response are summarised. They are only valid for a room with (nearly) constant temperature boundary conditions, which is ventilated with the displacement ventilation principle.

Given the reference settings presented in Table 8.4 the step response is small (see Figure 8.7 and Table 8.5). After a temperature step of -3°C at the supply the temperature change in zone 1 is -0.68°C and is reduced further to -0.03°C in zone 6. The step response for zone 1 is 0.13 - 0.31 for $ACH \cong 1$ to 3 h^{-1}. The convective heat loss via the floor has a large

influence on the total introduced cooling energy. For zone 2 the step response decreases to 0.06 - 0.23. The response time for zone 1 is of the order of 1 minute for $ACH \cong 1$ to 3 h^{-1}, increasing to 10 minutes at zone 6 for $ACH \cong 3$ h^{-1} and to 20 minutes for $ACH \cong 1$ h^{-1}.

Table 8.4. Settings for the reference case.

supply temperature (T_{supply})	=	20	^{o}C
flow rate ($\dot{V}$)	=	0.028	m^3/s ($ACH \cong 2$ h^{-1})
temperature step (ΔT_{supply})	=	-3	^{o}C
flow rate step ($\Delta\dot{V}$)	=	0	m^3/s

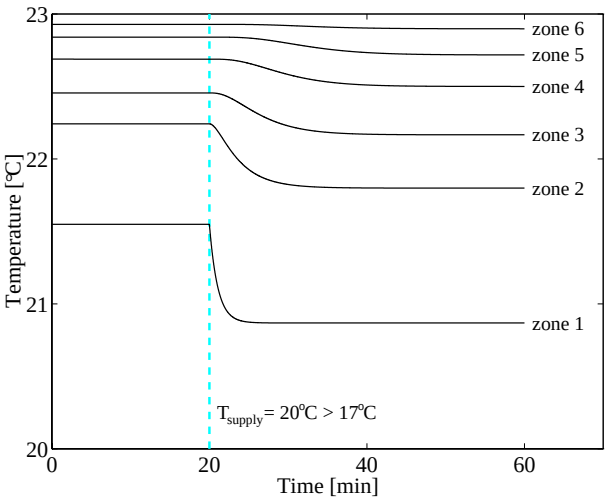

Figure 8.7. Numerical results for the reference case.

Table 8.5. Numerical results for the reference case.

	zone	1	2	3	4	5	6
τ_i	[s]	63	255	458	658	855	927
$\lvert\Delta T_{zone,i}\rvert$	[^{o}C]	0.68	0.44	0.29	0.19	0.112	0.03
$\Delta T_{zone,i}/\Delta T_{supply}$	[-]	0.23	0.15	0.10	0.06	0.04	0.01
$\tau_i/\lvert\Delta T_{zone,i}\rvert$	[s/^{o}C]	$9.21 \cdot 10^1$	$5.78 \cdot 10^2$	$1.58 \cdot 10^3$	$3.46 \cdot 10^3$	$7.12 \cdot 10^3$	$3.09 \cdot 10^4$

If the rate of change of the temperature is determined from $\tau_i / \Delta T_{zone,i}$ [s/^{o}C], differences in the transient behaviour of the temperature in the room are more obvious (see Table 8.5). This ratio also allows a better comparison between the results found in the parameter study. Differences in the rate of temperature change between zone 1 and zone 6, for the reference temperature step at the supply, are in the order of 100 to 2000 for $ACH \cong 1$ to 3 h^{-1}.

A step in the flow rate ($\Delta\dot{V}$; from $ACH \cong 1 \rightarrow 2$ h^{-1}, $2 \rightarrow 3$ h^{-1} or $1 \rightarrow 3$ h^{-1}) results in smaller differences in the transient behaviour between the separate zones. For zone 6, the relative difference of τ_i /$\Delta T_{zone,i}$ with zone 1 is of the order of 20 to 50, almost independent of the flow rate and the step size. An increase in the flow rate results in a higher rate of change of temperature for the upper zones compared to the values applied in the reference case. For zone 1 a smaller influence is found as the decrease in the zonal temperature is the resultant of the convective heat transfer at the wall and the increased cooling energy from the supply. The cooling energy results from the increased flow rate at the same temperature and not from a temperature decrease.

The rate of change of temperature remains the same when the heat transfer coefficient for the floor and ceiling is lowered to 2.5 W/m^2.K. The step response ($\Delta T_{zone,i}$ / ΔT_{supply}) however is increased by a factor ~1.5.

The response should be highest in the lower zones as the postulated requirements refer to the values at these zones. Reducing the volume of the lower zone by 30% results in a decrease of the rate of change of temperature for all zones by 26% on average. If the volumes of zone 1 and 2 are reduced by 30%, the average decrease is 35%.

8.3.4 Discussion transient behaviour

The transient measurements and simulations have confirmed the earlier conclusion that the DDV-concept is not able to create a well-defined micro-climate. When the supply conditions are changed realistically, the step response close to the occupant is in the order of 0.1, whereas a value >0.6 should be aimed at. The response time is beyond the postulated value of one minute. Only less realistic large changes at the supply are able to adjust the thermal conditions in a room fast enough to adjust to occupant desired changes within a relative short period, most probably jeopardising thermal comfort.

Applying the boundary conditions of the measurement run for case *a* (Table 8.2), the response time is calculated at ~0.5 min. and ~3 min. for zone 1 and 2 respectively. The step response is calculated at 0.17 and 0.10 respectively. The transient aspects of the DDV-system applied in the experiments equal those of a normal displacement ventilation system (compare with results in Table 8.3). For a room with complete mixing (one zone model), where the same stepwise change is applied as in case *a*, the step response is 0.08 and the response time ~1.5 min. The rate of change of the temperature is situated between zone 1 and 2 for case *a*, the step response nearly equals that of zone 2.

8.4 APPLICABILITY OF THE DDV-CONCEPT

Combining the results from Chapter 8.2 and 8.3, the final conclusion is that the desk displacement ventilation (DDV-) concept cannot be used solely as an individually controlled (task) conditioning system for standard office environments. The thermal conditions that arise at floor level cannot be obtained at head level, because of entrainment and mixing of room air at the interface of the convection plume and the surrounding air. The short distance of the supply unit to the occupant makes no difference. The system operates as a normal displacement ventilation system.

The conditions set forward earlier, a fast response and little damping, in order to obtain an individually controlled system, cannot be accomplished by a displacement ventilation flow pattern only. This applies to standard displacement ventilation units as well as to floor based grilles, which under cooling load conditions introduce the air at low velocity (0.1...0.5 m/s). A fast change of the environmental conditions should be effected by a parallel system as e.g. a high air velocity system close to the occupant.

The fact that the DDV-system has been introduced successfully at a dealers room in Sydney, Australia [mentioned in Chapter 2.3.3] was the result of correct positioning of the system. Long rows of DDV-systems at both sides of a small corridor restricted the spread of the displacement flow and forced the flow in upward direction, along the occupant. Therefore, the time response is short as the lower zone volume is small and the damping is restricted as the surface heat transfer is relatively small compared to the experimental set-up as described above. A recent application of the DDV-concept, described in HLH (1997), again applied for a dealers room, benefited from the same design conditions as for the dealers room in Sydney.

However, also other intentions for application of displacement ventilation in combination with a micro-climate are being reported (Diel and Schiller 1997). The above results clearly show that the expected benefits from bringing displacement ventilation close to the occupant will not outweigh the limitations with regard to thermal comfort. Also, the cooling load that can be achieved is limited to approximately 50 to 100 W. This normally is below the present convective cooling load in offices (in the order of 200 W [~10 W/m^2] or higher).

8.5 IMPROVED VERSION OF THE DDV-CONCEPT

8.5.1 Introduction

In Chapter 8.4 the use of a parallel system was indicated necessary to improve the transient characteristics of the DDV-concept. The CFD-model validated in Chapter 7 has been applied to investigate the response improvement of an additional system that is incorporated in the concept. Figure 8.8 presents the combination of the desk displacement ventilation unit and a variant of the so-called 'Climadesk' (Wyon 1995); a small slot in the desk top though which air is supplied close to the occupant at desired velocity and temperature. The displacement ventilation system is used to allow a base ventilation and the flow rate through the desk slot is small (< 15% of the base flow). This combination is indicated as the improved DDV-concept (DDV+).

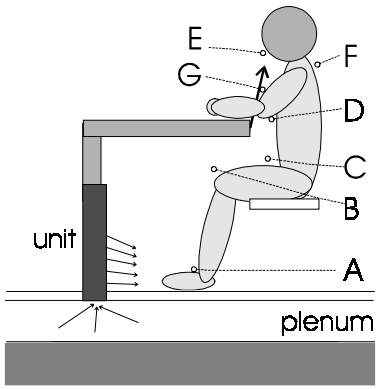

Figure 8.8. Improved DDV-concept + measurement locations.

8.5.2 Validation

First, the transient CFD-simulation of the original concept has been compared with measurement results as obtained for case *a* (Table 8.2). In the simulations the time step was set to 60 sec. For each time step 1000 iterations were solved if there was a temperature variation over the time step. If not, 250 iterations were solved. Steady state simulations indicated that the number of iterations for each time step was ample to reach a stable solution.

Figure 8.9 presents the temperature course as a result of a temperature variation at the supply for the experiment and the simulation. The characters in Figure 8.9 correspond to the positions indicated in Figure 8.8. Differences in the absolute value mainly result from the discretisation of the flow problem close to the heat source and the large gradients that

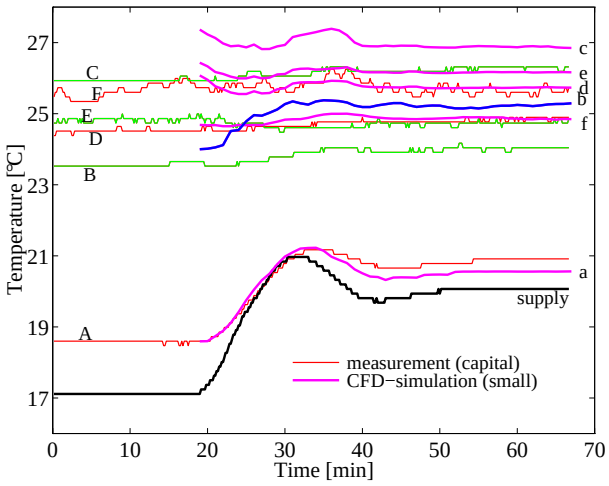

Figure 8.9. Comparison of simulation and measurement results for case a (see Figure 8.8).

appear. The transient course of the temperature is predicted relatively well. As for the measurements also in the simulations the limited variation in the air temperature is evident despite the almost 3°C temperature step at the supply.

The calculations require an extended simulation time duration. From the comparison it is however concluded that the application of CFD for the qualitative investigation of a time dependent flow problem is feasible.

8.5.3 Results improved concept (DDV+)

Figure 8.10 presents the temperature as function of the time for three positions near the occupant. These positions are indicated in Figure 8.8. For the *DDV* case only the temperature at the displacement ventilation unit is lowered step-wise by 3°C. For the *DDV+* case, besides the displacement ventilation unit, the desk slot is operated. The temperature conditions at the desk slot are the same as for the unit. The flow rate is 0.0025 m^3/s (A = $3.3 \cdot 10^{-3}$ m^2). In the simulations the time step was set to 10 sec for the first three minutes of the simulation process. After that a time step of 60 sec was applied up to a total simulation time of 50 min. In Table 8.6 the damping as defined in Equation 8.2 is given for the two cases. The steady state end-point value is determined by averaging over the last 10 minutes of the simulation process (average standard deviation 3 %).

The positive effect of the desk slot is shown by the nearly instant change of the temperature at mouth height (position *E*). The step response is a factor two higher compared to the original situation. Compared to the results for zone 1 in the reference case, as described in

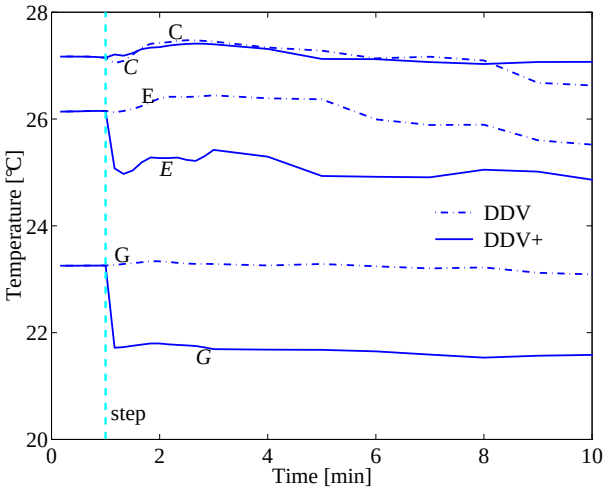

Figure 8.10. Temperature course as function of the time for the original (DDV) and the improved (DDV+) concept (see Figure 8.8).

Table 8.6. Damping of the original and the improved concept [%] (Equation 8.2).

position	*A*	*B*	*C*	*D*	*E*	*F*	*G*
DDV	33	104	81	82	80	86	93
DDV+	35	97	93	97	58	81	44

Chapter 8.3.3, the step response is almost a factor two higher, despite the higher flow rate for that case. At the other positions near the mannequin the damping is not improved. This is in agreement with the intention for the use of the desk slot. The velocity at position *G* due to the flow at the desk slot is 0.30 m/s, whereas at position *E* the velocity increased from 0.26 m/s to 0.33 m/s.

8.5.4 Discussion

The addition of a so called desk slot (suggested in Wyon (1995)) considerably improves the response time and step response (damping) of the thermal parameters close to the head. From Table 8.6 it is obvious that a large step response (> 0.6; Equation 8.1) is difficult to obtain with the applied supply flow rate at the desk slot (0.0025 m^3/s).

In the example the desk slot is operated at a constant (desired) velocity and supply air temperature. Another option would be to maintain the required supply conditions at the desk slot for a restricted period of time. After this time (e.g. 5 minutes) the air supply through the desk slot would gradually reduce to zero. This type of adjustment would mitigate the short-

term response of the desk displacement ventilation system. Furthermore, it would provide an answer to the fact that often changes in the thermal requirements are short-term based.

8.6 SUMMARY

1. The steady state and transient measurements and simulations indicate that the DDV-concept cannot be used on its own as task conditioning system for a standard office environment. The concept does not fulfil the postulated requirements, especially with regard to the response time and the step response.
2. The convective cooling load that can be obtained is low (in the order of 50 - 100 W). As in normal office configurations the cooling load is higher (in the order of 200 W [~10 W/m^2] or higher) additional cooling is required, also for conditioning the macro-climate.
3. The combination of the displacement ventilation principle and the task conditioning principle in general is not practical, unless special attention is given to the room configuration.
4. The DDV-concept may be improved by incorporating a desk-slot. The task conditioning is provided by the desk-slot, whereas the base ventilation is provided by the DDV-system. Additional cooling can be provided with a cooled ceiling.
5. The in point 4 indicated improvement was investigated with CFD. The application of CFD for this type of comparative study of ventilation concepts is feasible. It is this type of investigation in which the application of CFD is intended, in the design phase. The options to investigate other variants within CFD are numerous, but the computer requirements are heavy. Furthermore, the discussion on the applicability of CFD for simulation of indoor air flow, described in Chapter 7.3.4, should be taken into account.

- Chapter 8 -

Chapter 9

GENERAL OVERVIEW AND CONCLUSIONS

9.1 INTRODUCTION

This chapter presents the conclusions of this research. As the range of topics that have been addressed is wide also a general overview is given. This chapter is arranged to the approach described in Chapter 1: the tools to predict the indoor climate (measurement and simulation) and the technical context. After each overview of a topic the most important conclusions are pointed out. Finally, possible developments with respect to the measurement and simulation of indoor air flow are indicated.

9.2 MEASUREMENTS

9.2.1 Overview

Technique - As the available temperature measurement techniques are well developed, this work has focussed on velocity measurement. Accurate measurement of the indoor air velocity is difficult, as the mean velocity is low (0…1 m/s) and the turbulence intensity high (>10%). The specifications of most available velocity sensors restrict their usage for indoor air flow. From a careful evaluation, the omni-directional hot sphere anemometer and the Particle Tracking Velocimetry (PTV-) technique are chosen at present as the most practical and the most promising technique for the measurement of indoor air flow.

The accuracy of the described hot sphere anemometer (see Chapter 3.6) is highly dependent on the similarity between measurement situation and calibration conditions. If similarity between application and calibration is not taken into account, a measurement error up to

0.05 m/s or higher can be expected for the 0…0.5 m/s velocity range. Within this work a relative simple calibration set-up was designed for the calibration of the hot sphere anemometer.

The amplitude damping of the hot sphere anemometer in the measurement of a fluctuating velocity is significant. Results from a numerical model of the hot sphere anemometer indicate that the amplitude is being damped up to 20% in the lower frequency range (0.1…1 Hz) (see Figure 3.12). The turbulent fluctuations of the flow therefore cannot be measured reliably. Draught discomfort is strongly dependent on the turbulence intensity (see Figure 2.3; Fanger et al. 1988). An amplitude damping of 20% at a mean velocity of 0.2 m/s (*TI* = 40%) results in an underestimation of the percentage of dissatisfied due to draught (*PD*) by 10%. As the *PD*-relation was derived using similar hot sphere anemometers, the draught sensation will be overestimated when an anemometer with less damping is used. The same applies to the use of numerical results.

The applied PTV-system was able to determine the time-averaged two-dimensional velocity vector field in a plane of the flow. The use of a (nearly) neutrally buoyant helium filled soap bubble ($d_p \approx 0.003$ m) as tracer particle in indoor air flow was supported by theoretical analysis. The practical application of the PTV-technique however was restricted significantly due to the requirement of a constant and sufficient production of (nearly) neutrally buoyant particles at constant density. Therefore, the helium filled soap bubble must be replaced by a better verifiable, more easy to generate and less staining tracer particle to improve the practical application. Furthermore, the camera resolution should be increased to allow a larger interrogation area to be monitored. The applied video camera (512×512 pixels) restricted the area to 0.5×0.5 m^2.

Data - From a literature review, only a very restricted number of full-scale indoor air flow experiments, suitable for validation purposes, was found. Therefore, extensive full-scale climate chamber measurements have been performed. The flow has been investigated in a configuration in which the task conditioning and the displacement ventilation principle were combined. In this configuration a displacement as well as a mixing ventilation flow field could be established. For the displacement ventilation flow pattern the supply temperature difference, the heat input and the supply flow rate have been varied. In Chapter 6 the results are discussed and the obtained data were found to be realistic and applicable for comparison with numerical simulations. All measurement results are summarised in *x*-*y*-*z* format and available via the internet (http://www.tue.nl/bwk/bfa/research/aio_research.html).

In the experimental configuration the walls are not assumed to be adiabatic, but are controlled at a constant temperature. As a result the ceiling is found to operate as a cooled

ceiling. For cases with a high heat load and low air change rate the heat transfer to the enclosure even is the dominant heat transfer process. Though the convective heat transfer coefficients at the enclosure could not be determined directly, an estimation was made using model and experimental results from literature. The derived heat transfer coefficients for the floor agree quantitatively with those found in literature.

The buoyant plume above the designed thermal mannequin has similar characteristics as plumes above person simulators and persons described in literature. The mannequin was designed to emulate the human body, geometrically and thermally. This thermal mannequin cannot be applied for the prediction of thermal comfort.

9.2.2 Conclusions

- The hot sphere anemometer currently remains the most practical technique for velocity measurements at indoor air flows. A series of possible measurement errors however restrict the accuracy considerably. Examples of errors are: velocity and/or temperature difference between the measuring and reference sensor, directional sensitivity and damping. A relative simple low-velocity calibration set-up has been described to calibrate the anemometer.
- Particle Tracking Velocimetry (PTV) is the most promising technique for measurement at indoor air flow patterns. The main restriction is found in the generation of tracer particles. The applicability of PTV will remain restricted unless the helium-filled soap bubble can be replaced by a (nearly) neutrally buoyant, easy to generate, non-staining tracer particle.
- Extensive full-scale measurement data have been presented for the air flow in a climate-chamber set-up of an office room in which task conditioning and displacement ventilation are combined. Data have been obtained for a series of boundary conditions and are applicable for validation purposes.

9.3 SIMULATIONS

9.3.1 Overview

Technique - The developments in mathematical and numerical modelling of turbulent flows in theory allow an improved simulation of the indoor air flow problem with Computational Fluid Dynamics (CFD). Validation of these models however remains an issue of concern given the indoor air flow characteristics and the limited number of validation studies for

realistic indoor air flow patterns to evaluate the improved models. Nonetheless, CFD has taken a prominent position in the indoor climate research.

Validity - The CFD-simulation of a displacement ventilated room, using a configuration description mentioned in literature, has shown an important problem; the correct calculation of the convective heat transfer at the walls. The application of wall functions yields grid dependent solutions for the temperature distribution. A possibly improved treatment of the near wall flow field with low-Reynolds number turbulence models requires considerable near-wall grid refinement. This approach is currently of limited use due to computer capacity restrictions. Given the grid distribution, the convective heat transfer normally will be underestimated when the near-wall grid distribution is not rigidly controlled. This also has implications for modelling the radiant heat transfer when for example a heat flux is defined at the boundary of the heat source.

In the full-scale experimental results obtained within this research, the wall heat transfer is important. Given the difficulty to correctly simulate the wall heat transfer, these results are interesting for evaluating similar CFD-simulations. Comparison of experimental and numerical results confirm the fact that the wall heat transfer for a room with displacement ventilation and a cooled ceiling is underestimated significantly in the numerical model. Grid conditions nevertheless conform close to values mentioned in literature. The main explanation for this deviation lies in the fact that the available wall functions are not valid for developing boundary flows, free convection boundary layers and impinging plumes as they appear indoors.

Underestimation of the wall heat transfer affects the vertical temperature gradient and therewith the energy balance and the thermal comfort prediction. Also the plume development above heat sources and therefore the flow pattern is affected. This in turn impacts on the derived ventilation effectiveness.

Applying a prescribed heat transfer coefficient as part of the boundary condition definition improves the agreement with measurement results considerably. The major disadvantage of entering the heat transfer coefficient as part of the boundary condition however lies in the limited availability of heat transfer coefficients for the variety of indoor air flow configurations. In this respect, a sharp definition of the conditions under which a heat transfer coefficient has been determined is important. Moreover, temperature profiles over the height may serve as an alternative to resolve the coefficient. The obtained full-scale experimental results are well suited to validate newly derived wall functions or empirical relations for the wall heat transfer in a displacement ventilated room with a cooled ceiling.

Comparison of the standard *k*-ε and the high- and low-Reynolds number variants of the RNG-*k*-ε turbulence model indicates that the low-Reynolds variant of the RNG-*k*-ε model is preferred for the simulation of displacement ventilation. This variant presents most realistic turbulent characteristics for the flow outside the buoyant plumes.

The apparently improved grid use in pseudo-unstructured and unstructured grids has drawbacks in terms of time spent to build the grid and in the reliability of the final solution, for the investigated flow problem and the applied segregated solver (see Chapter 4.5). A structured grid set-up presents the most reliable results and therefore currently may remain the point of departure for the simulation of indoor air flow.

Results from a grid dependency check or grid improvement by grid adaption were not considered to be realistic for the presented problem with the applied solver. Grid doubling for the simulation of a room with displacement ventilation indicated a grid independent solution for the flow pattern at ~50,000 cells. This requires grid refinement at boundaries and minimisation of numerical diffusion and does not take into account the above discussion on wall heat transfer.

9.3.2 Conclusions

- The wall heat transfer characteristics are not correctly predicted with logarithmic wall functions unless rigid control on the y^+-value is executed (in the order of ±1) and therewith on the near-wall grid distribution. The law-of-the-wall is not valid for the type of boundary layer flows that appear indoors.
- Correcting the wall heat transfer characteristics by imposing convection heat transfer data improves the agreement between measured and simulated temperature distribution and flow pattern. The use of low-Reynolds number turbulence models to solve the boundary layer flow up to the wall currently does not represent an alternative, given the high computer capacity requirements to model an indoor air flow configuration. The in this work derived measurement data can be used to validate new wall functions or empirical relations.
- The low-Reynolds number variant (Equation 4.14) of the RNG-*k*-ε model is preferred for the simulation of indoor air flow. The predicted turbulence characteristics in the room with displacement ventilation are in good agreement with the measurement results.
- A non-equidistant Cartesian grid is capable of predicting a reliable flow pattern for the normally rectangular indoor space. For a typical room with displacement ventilation, a grid with 50,000 grid cells can be sufficient to calculate grid independent results.
- The applicability of CFD for the simulation of the investigated displacement ventilation configuration is confirmed. The accuracy depends mainly on the accuracy with which

wall heat transfer and turbulence are modelled. The applicability for other indoor air flow configurations is discussed in Chapter 7.3.4.

9.4 TECHNICAL CONTEXT

9.4.1 Overview

The indoor climate is determined by the indoor air quality and by the thermal comfort of the occupant. Thermal comfort was investigated with a literature research. Following the conclusions from this research attention was focussed on individually controlled task conditioning systems. The results on thermal comfort and task conditioning are summarised below.

Thermal comfort - The current opinions on thermal comfort agree that thermal comfort is a condition of the mind that is strictly personal. When the same indoor conditions are provided to a group of occupants individual adaptation will take place. Furthermore, the definitions of ‘average thermal comfort’ and ‘thermal comfort at dot-level’ are meaningless.

Task conditioning ventilation (DDV-concept) - Contrary to whole room climatising principles as displacement and mixing ventilation, the task conditioning principle may support the individual adaptation through control of the required thermal conditions in a small space around the occupant. If the task conditioning includes the supply of fresh air, also considerable improvement in the air quality at micro-climate level is possible. Task conditioning therefore has found renewed interest in the conditioning of the indoor climate. The development of task conditioning systems mainly relies on design principles which already were developed in the 1970s.

The desk displacement ventilation (DDV-) concept was introduced as a combination of the task conditioning and the displacement ventilation principle. After successful introduction of the concept in a dealers room configuration, the applicability for standard office configurations was investigated in full-scale. From extensive steady state and transient measurement and simulation results it is concluded that the DDV-concept cannot be used on its own as task conditioning system for a standard office environment. The step response and the response time to a set-point shift do not fulfil the postulated requirements for a task conditioning system. Furthermore, as a result of thermal comfort requirements near the occupant, the convective cooling load that can be obtained is maximum about 100 W. Therefore, normally an additional cooling system is required, also for conditioning the macro-climate. The results furthermore show that the combination of the displacement

ventilation principle and the task conditioning principle in general is not applicable, unless special attention is given to the room configuration.

An example of an improvement of the task conditioning capability of the DDV-concept is presented by incorporating a desk-slot close to the occupant. Task conditioning is provided by the desk-slot, whereas the base ventilation is provided by the DDV-system. The improvement was investigated with the validated CFD-model. The positive effect from the desk-slot was confirmed and the application of CFD proved useful.

9.4.2 Conclusions

- Literature presents ample results which indicate that thermal comfort, contrary to the standards requirements, should be focussed at the occupant level and not at the group level. In this respect task conditioning systems are attractive as individual control of important indoor air parameters such as temperature and air velocity is possible.
- The application of displacement ventilation for the purpose of task conditioning is not feasible because it does not meet the postulated requirements for the step response and the response time to a change in the control settings. There is no further particular advantage in bringing the displacement ventilation unit close to the occupant. The transient characteristics of the system are not changed significantly unless the room configuration is part of the task conditioning strategy.

9.5 POSSIBLE DEVELOPMENTS

The measurement and simulation of indoor air flow will remain important in the designing and evaluation of the indoor climate. More stringent requirements and also the application of new ventilation strategies will restrict the use of simplified models and empirical results.

Measurements
Accurate measurement of the flow velocity and the turbulent fluctuations is necessary for validation purposes. In this respect whole room measurement techniques such as PTV are most promising. They allow accurate measurement of low air velocities and an ‘overview-like’ information on the flow pattern. For wide-spread practical application of PTV in practise however the helium-filled soap bubble, the currently applied tracer particle, should be replaced with a non-staining, easy to generate and reproducible equivalent.

The hot sphere anemometer probably will remain the dominant anemometer for in-situ measurements for some time to come, mainly because of its ease of use. Given the required accuracy it may well serve its purpose in most situations.

For validation purposes the number of carefully documented full-scale measurement results should be increased. In this respect the work of Chen et al. (1998), which also presents well documented full-scale indoor air flow data, supports to this goal.

Simulations

The use of CFD will take an increasingly important position in the prediction of the indoor air flow characteristics. Nevertheless, the reliability will only be improved by validating realistic indoor air flow configurations so that newly derived turbulence models and numerical techniques can be tested. The latter also assumes a careful description of the modelling characteristics. Improvement of the CFD-model for indoor air flow should certainly address the convective heat transfer mechanism.

Calculation of the ventilation effectiveness from the simulated flow pattern is relatively straightforward (Roos 1998[a]). A reliable validation of the simulation results by measurement data however is currently not possible. The obvious differences in the simulated turbulence characteristics between the investigated turbulence models and the resulting preference for the low-Reynolds number variant of the RNG-k-ε model should be confirmed more convincingly by more extended measurements of the ventilation effectiveness.

Simulation of natural ventilation presents a challenge to the current CFD-models. Given the increasing interest put in natural ventilation, attention should be directed towards the numerical simulation of natural ventilation and especially to the definition of the boundary conditions.

Ventilation techniques

The recently introduced hybrid ventilation adheres to the above indicated attention to natural ventilation. Hybrid ventilation most probably will be able to bring mechanical and natural ventilation together to optimise and combine the advantages of both techniques. When individual control and the micro-/macro-climate principle are included in the hybrid ventilation strategy, probably an optimum indoor climatising system can be obtained, with regard to thermal comfort, air quality, energy use and psychology.

References

ASHRAE. 1992. *ANSI/ASHRAE Standard 55-1992, Thermal Environmental Conditions for Human Occupancy*, Atlanta: American Society of Heating, Refrigerating, and Airconditioning Engineers, Inc., USA.

ASTM. 1981. *Manual on the Use of Thermocouples in Temperature Measurements*, ASTM special Technical Publications 470 B, Baltimore, USA.

Auton, T.R., Hunt, J.C.R. and Prud'homme, M. 1988. The force exerted on a body in inviscid unsteady non-uniform rotational flow. *Journal of Fluid Mechanics*, vol.197, pp.241-257.

Awbi, H.B. 1991. *Ventilation of Buildings*, 1st edition, Chapman & Hall, London, United Kingdom.

Bach, H.; K. Becher; B. Biegert; R.Detzer; W. Diebschlag; et al. 1993. *Gezielte Belüftung der Arbeitsbereiche in Produktionshallen zum Abbau der Schadstoffbelastung*, BM FTFB report 01 HK 216 (HLK-1-92), Stuttgart (Germany): Verein der Förderer der Forschung im Bereich Heizung-Lüftung-Klimatechnik (in German).

Baker, A.J. and Kelso, R.M. 1990. On the validation of Computational Fluid Dynamics procedures for room air motion prediction, *ASHRAE Transactions*, vol.96 part 1, pp.760-774.

Baker, A.J., Williams, P.T. and Kelso, R.M. 1994. Numerical calculation of room air motion - part 1: Math, Physics and CFD Modeling, *ASHRAE Transactions*, vol.100 part 1, pp.514-530.

Baker, A.J., Kelso, R.M., Gordon, E.B., Roy S. and Schaub E. G. 1997. Computational Fluid Dynamics: A two-edged sword, *ASHRAE Journal*, august, pp.51-58.

Bauman, F., Arens, E., Fountain, M., Huizenga, C., et al. 1994. *Localized thermal distribution for office buildings*, final report - phase III, Center for Environmental Design Research, University of California, Berkeley, USA.

Bauman, F.S. and Arens, E.A. 1996. *Task/Ambient conditioning systems: Engineering and application guidelines*, CEDR-13-96, University of California, Berkeley, USA.

Bennetsen, J.C., Sørensen, J.N., Søgaard, H.T. and Christiansen, P.L. 1996, Numerical simulation of turbulent airflow in a livestock building, *Proc. Roomvent'96*, vol.2, pp.169-176, Yokohama, Japan.

Benzinger, T.H. 1979. The Physiological basis for thermal comfort, *Indoor Climate*, ed. P.O.Fanger and O.ValbjØrn, pp.441-476, Danish Building Research Institute, Copenhagen, Denmark.

Berglund L.G. and Gonzalez, R.R. 1978[a]. Application of acceptable temperature drifts to built environments as a mode of energy conservation, *ASHRAE Transactions*, vol.84 part 1, pp.110-121.

Berglund L.G. and Gonzalez, R.R. 1978[b]. Occupant acceptability of eight-hour long temperature ramps in the summer at low and high humidities, *ASHRAE Transactions*, vol.84 part 2, pp.278-284.

Besse, L., Gottschalk, G., Moser, A. and Suter, R. 1992. Measurement of the spatial, stationary and time variable velocity distribution of airflow using tracer particles and still video technique, *Flow Visualization VI Proc. 6th Int. Symp. On Flow Visualization*, Yokohama, pp.223-227.

Bluyssen, P.M., De Oliveira, F.E., Fanger, P.O., Groes, L., Clausen G., Roulet, C.A., Bernhard, C.A. and Valbjorn, O. 1995. *European audit project to optimize indoor air quality and energy consumption in office buildings*, final report, CEC.

Boussinesq, J. 1877. Théorie de l'écoulement tourbillant, *Mem.Pre.par.div.Sav.*, 23, Paris, France.

Brager, G.S., Fountain, M.E., Benton, C.C., Arens, E.A. and Bauman, F.S. 1994. A comparison of methods for assessing thermal sensation and acceptability in the field, *Proc. Thermal comfort: past, present and future* (ed: Oseland N.A. and Humphreys, M.A.), pp.17-37, Garston, United Kingdom.

Brager G.S. and de Dear, R.J. 1998. Thermal adaptation in the built environment: a literature review, *Energy and Buildings*, 27, pp.83-96.

Brightman, H.S., Womble, S.E., Girman, J.R., Sieber, J.F., McCarthy, J.F., et al. 1997. Preliminary comparison of questionnaire data from two IAQ studies: occupant and workspace characteristics of randomly selected buildings and 'complaint' buildings, *Proc. Healthy Buildings/IAQ'97*, vol. 2, pp.453-458, Washington D.C., USA.

Brohus, H. 1997. *Personal Exposure to Contaminant Sources in Ventilated Rooms*, thesis, Aalborg University, Aalborg, Denmark.

Bruun, H.H. 1995. *Hot-wire Anemometry*, Oxford University Press Inc., New York, USA.

Byrne, C.E.I. and Holdo, A.E. 1994. The effect of choice of inlet boundary conditions for the *k*-ε turbulence model, *Comp.Fluid.Dyn.*, vol.3, pp.321-327.

Cabanac, M. 1981. Physiological signals for thermal comfort, In: *Bioengineering, Thermal physiology and Comfort* (ed: Cena, K. and Clark, J.A.), pp.181-192, Elsevier Amsterdam.

Cabanac, M. 1996. Pleasure and joy, and their role in human life, *Proc. Indoor Air '96*, vol.3 , pp.3-14, Nagoya, Japan.

Carrier Air Conditioning Company. 1965. *Handbook of Air Conditioning System Design*, 4th edition, McGraw-Hill, New York, USA.

Cheesewright, R., King, K.J. and Ziai, S. 1986. Experimental data for the validation of computercodes for the prediction of two-dimensional buoyant cavity flows, *Proc. ASME Meeting HTD*, vol. 60 (heat transfer), pp.75-81.

Cheesewright, R. and Ziai, S. 1986. Distributions of temperature and local heat-transfer rate in turbulent natural convection in a large rectangular cavity, *Proc. 8th Int. Heat Transfer Conf.*, pp.1465-1470.

Chen, Q. 1988. *Indoor Airflow, Air Quality and Energy Consumption of Buildings*, thesis, Delft University of Technology, Delft, The Netherlands.

Chen, Q. 1995. Comparison of different k-ε models for indoor air flow computations, *Num. Heat Transfer*, vol.28 part B, pp.353-369.

Chen, Q. 1997. Computational Fluid Dynamics for HVAC: Successes and Failures, *ASHRAE Transactions*, vol.103 part 1, pp.178-187.

Chen, Q. 1998. (personal communications).

Chen, Q. and Jiang, Z. 1992. Significant questions in predicting room air motion, *ASHRAE Transactions*, vol.98 part 1, pp.929-939.

Chen, Q., Peng, X. and Paassen, A.H.C. van. 1995. Prediction of room thermal response by CFD technique with conjugate heat transfer and radiant models, *ASHRAE Transactions*, vol.101, part II, pp.50-60.

Chen, Q., Yuan, X., Hu, Y., Glicksman, L.R. and Yang, X. 1998. Detailed experimental data of room airflow with displacement ventilation, *Proc. Roomvent'98*, vol.1, pp.133-140, Stockholm, Stockholm.

Clarke, J.A. 1985. *Energy Simulation in Building Design*, Adam Hilger Ltd., Bristol, United Kingdom.

Clift, R., Grace, J.R. and Weber, M.E. 1978. *Bubbles, Drops and Particles*, Academic Press, New York, USA.

Cox, C.J.W. and Elkhuizen, P.A. 1995. Verdringingsventilatiesysteem in een kantoor, *TVVL Magazine*, 9, pp.48-55 (in Dutch: Displacement ventilation system in an office).

Crommelin, R.D. 1992. *Het ijken van luchtsnelheidsmeters voor lage luchtsnelheden*, TNO-report B-92-0905, TNO-Bouw, Delft, The Netherlands (In Dutch: The calibration of air velocity anemometers for low velocities).

Crommelin, R.D. and Dubbeld, M. 1976. Modified anemometers for indoor climate research, *Journal of Physics E: Scientific Instruments*, vol.9, pp.1005-1009.

Dalziel, S. 1995. *DigImage - Image Processing for Fluid Dynamics*, version 1.5, Cambridge Environmental Research Cons. Ltd., Cambridge, Great Britain.

Dantec. 1985. *54N50 Low Velocity Flow Analyzer mark II*, Dantec Electronik, Denmark.

Davidson, L. and Nielsen, P.V. 1996. Large eddy simulations of the flow in a three-dimensional ventilated room, *Proc. Roomvent'96*, vol..2, pp.161-168, Yokohama, Japan.

Diehl, J.; and Schiller, H. 1997. Entwicklungsstand, neue Systeme, Trends in der Raumtechnik. *Heizung, Lüftung, Haustechnik (HLH)*, Vol.48 no.11, pp.30-37 (In German).

DIN 1946, part 2. 1994. *Raumlufttechnik - Gesundheitstechnische Anforderungen*, DIN Deutsches Institut für Normung e.V., Berlin, Germany (in German).

Donaldson, B. and Nagengast, B. 1994. *Heat & Cold - Mastering the Great Indoors*, Atlanta: American Society of Heating, Refrigerating, and Airconditioning Engineers, Inc., USA.

Eggels, J.M.G. 1994. *Direct and Large Eddy Simulation of Turbulent Flow in a Cylindrical Pipe Geometry*, thesis, Delft University of Technology, Delft, The Netherlands.

Emvin, P. and Davidson, L. 1996. A numerical comparison of three inlet approximations of the diffuser in case E1 Annex 20, *Proc. Roomvent'96*, vol.1, pp.219-226, Yokohama, Japan.

Fanger, P.O. 1970. *Thermal Comfort*, thesis, Technical University of Denmark, Lyngby, Denmark.

Fanger, P.O. 1988. Introduction of the olf and the decipol units to quantify air pollution perceived by humans indoors and outdoors, *Energy and Buildings*, 12, pp.1-6.

Fanger, P.O. 1994. How to apply models predicting thermal sensation and discomfort in practice, *Proc. Thermal comfort: past, present and future* (ed: Oseland N.A. and Humphreys, M.A.), pp.11-16, Garston, United Kingdom.

Fanger, P.O. 1997. Global issues related to offices and public assembly halls from a building perspective, *Proc. Healthy Buildings/IAQ'97*, vol. 2, pp.19-24, Washington D.C., USA.

Fanger, P.O., Melikov, A.K., Hanzawa, H. and Ring, R. 1988. Air turbulence and sensation of draught, *Energy and Buildings*, 12, pp.21-39.

Ferziger J.H. and Peric, M. 1996. *Computational Methods for Fluid Dynamics*, Springer Verlag, Berlin, Germany.

Fingerson, L.M. and Freymuth, P. 1983. Thermal anemometers, In: *Fluid Mechanics Measurements* (ed: R.J. Goldstein), Chapter 4, Hemisphere Publishing Corporation, Washington, USA.

Fitzner, K. 1998, Perceived air quality: should we use a linear or a non-linear scale for the relation between odour intensity and concentration ?, *Proc. Roomvent'98*, vol.1, pp.149-153, Stockholm, Sweden.

Fluent, Inc. 1993. *Introduction to the Renormalization Group Method and turbulence modeling*, Technical Memorandum TM-107, Fluent Inc., Lebanon, USA.

Fluent, Inc. 1995. *Fluent User's Guide*, version 4.3, Lebanon, USA.

Fluent, Inc. 1996[a]. *User's Guide for Fluent/UNS & Rampant*, release 4.0, Lebanon, USA.

Fluent, Inc. 1996[b]. *Tgrid User's Guide*, release 2.4, Lebanon, USA.

Fluent, Inc. 1996[c]. *GeoMesh User's Guide*, release 3.0, Lebanon, USA.

Fluent, Inc. 1998. *Fluent/UNS*, release 5.0, Lebanon, USA.

Fountain, M., Arens, E., de Dear, R., Bauman, F. and Miura, K. 1994. Locally controlled air movement preferred in warm isothermal environments, *ASHRAE Transactions*, vol.100 part 2, pp.937-950.

Fransen, B. 1997. *Bureau-geïntegreerde verdringingsventilatie*, internal report 97.19.K, Eindhoven University of Technology, Eindhoven, The Netherlands (in Dutch: Desk Displacement Ventilation).

Fuchs, N.A. 1964. *The Mechanics of Aerosols*, Pergamon Press, London, Great Britain.

Gagge, A.P., Fobelets, A.P. and Berglund, P.E. 1986. A standard predictive index of human response to the thermal environment, *ASHRAE Transactions*, vol. 92 part 2B, pp.709-729.

Gan, G. and Croome, D.J. 1994. Thermal comfort models based on field measurements, *ASHRAE Transactions*, vol.100 part 2, pp.782-794.

George, W.K., Beuther, P.D. and Lumley, J.L. 1978. Processing of random signals, *Proc. Dynamic Flow Conference*, pp.757-799, Marseille, France.

Gosman, A.D., Nielsen, P.V., Restivo, A. and Whitelaw, J.H. 1980. The flow properties of rooms with small ventilation openings, *Journal of Fluids Engineering, Transactions of ASME*, vol.102, pp.316-323.

Grimitlin, M. 1970. Zuluftverteilung in Räumen, *Luft- und Kältetechnik*, 5, pp.247-256 (in German).

Hale, R.W., Tan, P., Stowell, R.C. and Ordway, D.E. 1971. *Development of an integrated system for flow visualization in air using neutrally-buoyant bubbles*, SAI-RR 7107, SAGE ACTION, Inc., New York, USA.

Hanzawa, H., Melikov, A.K. and Fanger, P.O. 1987. Airflow characteristics in the occupied zone of ventilated spaces, *ASHRAE Transactions*, vol.93 part 1, pp.524-539.

Hatton, A. and Awbi, H.B., Heat transfer from room surfaces, *Proc. Roomvent'96*, vol.2, pp.395-402, Yokohama, Japan.

Hawkes, D. 1996. *The Environmental Tradition*, E&FN Spon, London, Great Britain.

Hawkins, A.N., Hosni, M.H. and Jones, B.W. 1995. A comparison of room air motion in a full size test room using different diffusers and operating conditions, *ASHRAE Transactions*, vol.101 part 2, pp.81-100.

Heikkinen, J. 1991. Modelling of a supply air terminal for room air flow simulation, *Proc. 12th AIVC Conf.*, Ottawa, Canada.

Henkes, R.A.W.M. 1990. *Natural Convection Boundary Layers*, thesis , Delft University of Technology, Delft, The Netherlands.

Henkes, R.A.W.M. and Hoogendoorn, C.J. 1992. *Turbulent natural convection in enclosures - A computational and experimental benchmark study*, Proceedings Eurotherm Seminar 22, Delft, The Netherlands.

Hensel, H. 1979. Thermoreception and human comfort, In: *Indoor Climate* (ed: P.O. Fanger and O. Valbjørn), pp.425-440, Danish Building Research Institute, Copenhagen, Denmark.

Hensel, H. 1981. *Thermoreception and Temperature Regulation*, Monogr. of the Phys. Soc. No.38, Academic Press, London, United Kingdom.

Hensen, J.L.M. 1991. *On the Thermal Interaction of Building Structure and Heating and Ventilation System*, thesis, Eindhoven University of Technology, Eindhhoven, The Netherlands.

Hensen, J.L.M., Hamelinck, M.J.H. and Loomans, M.G.L.C. 1996. Modelling approaches for displacement ventilation in offices, *Proc. Roomvent'96*, vol.2, pp.467-474, Yokohama, Japan.

Hinze, J.O. 1975. *Turbulence*, 2nd edition, McGraw-Hill, New York, USA.

HLH. 1997. Individuelle RLT-Lösungen aus dem Labor, *Heizung, Lüftung, Haustechnik (HLH)*, Vol.48 no.3, pp.120 (In German).

Holman, J.P. 1997. *Heat Transfer*, 8th edition, McGraw-Hill, New York, USA.

Hu, S.C., Wu, Y.Y. and Liu, C.J. 1996. Measurements of air flow characteristics in a full-scale clean room, *Building and Environment*, vol.31 no.2, pp.119-128

Humphreys, M.A. 1976. Field studies of thermal comfort compared and applied, *Building Services Engineering*, 44, pp.5-27.

Humphreys, M.A. 1978. Outdoor temperatures and comfort indoors, *Building Research and Practice (Bâtiment international)*, March/April, pp. 91-105.

Humphreys, M.A. 1994. Field studies and climate chamber experiments in thermal comfort research, *Proc. Thermal comfort: past, present and future* (ed: Oseland N.A. and Humphreys, M.A.), pp.52-72, Garston, United Kingdom.

Hutchinson, B.R. and Raithby, G.D. 1986. A multigrid method based on the additive correction strategy, *Numerical Heat Transfer*, vol.9, pp. 511-537.

ISO. 1984. *ISO 7730 Moderate Thermal Environments - Determination of the PMV and PPD indices and specification of the conditions for thermal comfort*, International Standards Organisation, Geneva, Switzerland.

Jaakkola, J.J.K. 1994. Sick building syndrome in relation to indoor air temperature, relative humidity and air change, *Proc. Thermal comfort: past, present and future* (ed: Oseland N.A. and Humphreys, M.A.), pp.168-181, Garston, United Kingdom.

Jaakkola, J.J.K., Heinonen, O.P. and Seppänen O. 1989. Sick building syndrome, sensation of dryness and thermal comfort in relation to room temperature in an office building: need for individual control of air temperature, *Environment International*, vol.15, pp.163-168.

Joubert, P., Sandu, A., Béghein, C. and Allard, F. 1996. Numerical study of the influence of inlet boundary conditions on the air movement in a ventilated enclosure, *Proc. Roomvent'96*, vol.1, pp.235-242, Yokohama, Japan.

Jouini, D.B., Saïd, M.N. and Plett, E.G. 1994. Measurements of room air distribution in a ventilated office environment, *Building and Environment*, vol.29, no.4, pp.511-521.

Kaga, A., Yamaguchi, K., Inoue, Y., Kondo, A., Kamoi, S. and Yamaguchi, T. 1996. PIV system for airflow measurement using smoke particles, *Proc. Roomvent'96*, vol.2, pp.421-426, Yokohama, Japan.

Katz, Ph. 1989. Luftströmung im Raum, *Handbuch der Klimatechnik*, vol. 1, chapter 6, Verlag C.F. Müller GmbH, Karlsruhe, Germany (in German).

Kehro, M.F. 1989. *A study of the accuracy of neutrally buoyant bubbles used as flow tracers in air*, master thesis, University of Southern California, Illinois, USA.

King, L.V. 1914. On the convection of heat from small cylinders in a stream of fluid: Determination of the convection constants of small platinum wires with applications to hot-wire anemometry, *Philosophical Transaction Roy. Soc.*, vol. A 214, pp.373-432.

Kofoed, P. and Nielsen, P.V. 1988. Thermal plumes in ventilated rooms - an experimental research work, *3rd Seminar on Application of Fluid Mechanics in Environmental Protection*, Silesian Technical University, Gliwice, Poland.

Krantz. 1984. *Air distribution systems*, report No. 3554 E, Krantz Products, Colchester, United Kindom.

Krühne, H. 1995. *Experimentelle und Theoretische Untersuchungen zur Quelluftströmung*, thesis, Technical University Berlin, Berlin, Germany (in German).

Launder, B.E. 1991. Current capabilities for modelling turbulence in industrial flows, *J. of Applied Scientific Research*, vol.48, pp.247-269.

Launder, B.E. and Spalding, D.B. 1974. The numerical computation of turbulent flows, *Comp. Meth. Appl. Mech. Energy*, vol.3, pp.269-289.

Lee, T. and Budwig, R. 1991. Two improved methods for low-speed hot-wire calibration, *Meas. Sci. Technol.*, 2, 643-646.

Lemaire, A.D. 1992. *Room Air and Contaminant Flow - Evaluation of computational methods*, Subtask-1 Summary report, IEA Annex 20 'Air Flow Patterns within Buildings', Delft, The Netherlands.

Lemaire, A.D., Ham, P.J. and Luscuere, P.G. 1995. Evaluation of computer flow modelling in operating theatres, *Proc.13th Int. Symp. on Contaminant Control*, The Hague, The Netherlands.

Liddament, M.W. 1996. *A Guide to Energy Efficient Ventilation*, IEA Annex V, Air Infiltration and Ventilation Centre, Coventry, Great Britain.

Linden, E., Todde, V. and Sandberg, M. 1998. Indoor low speed air jet flow: 3-dimensional particle streak velocimetry, *Proc. Roomvent'98*, vol.2, pp.569-576, Stockholm, Sweden.

Loomans, M.G.L.C. 1997. *Design of and discussion on a thermal mannequin*, FAGO-report 97.16.K, Eindhoven University of Technology, Eindhoven, The Netherlands.

Loomans, M.G.L.C., and Mook, F.J.R. van. 1995. *Survey on measuring indoor airflows*, FAGO-report 95.25.W, Eindhoven University of Technology, Eindhoven, The Netherlands.

Loomans, M.G.L.C., Mook, F.J.R. and Rutten, P.G.S. 1996. The introduction of the desk displacement ventilation concept - Measurement of indoor airflows applying the PTV-technique, *Proc. Roomvent'96*, vol.1, pp.99-106, Yokohama, Japan.

Loomans, M.G.L.C. and Rutten, P.G.S. 1997. Task conditioning + Displacement ventilation, 1 + 1 > 2 ?, *Proc. Healthy Builings/IAQ'97*, vol. 2, pp.305-311, Washington DC.

Loomans, M.G.L.C. 1998. Measurements at and simulations of the (improved) desk displacement ventilation concept, *Proc. Roomvent'98*, vol.1, pp.241-248, Stockholm, Sweden.

Loomans, M.G.L.C. and Schijndel, A.W.M. van. 1998. *Simulation and measurement of the stationary and transient characteristics of the hot sphere anemometer*, FAGO-report 98.08.K, Eindhoven University of Technology, Eindhoven, The Netherlands.

Lotens. W.A. 1993. *Heat Transfer from Humans wearing Clothing*, thesis, Delft University of Technology, The Netherlands.

Majumdar, S. 1988. Role of underrelaxation in momentum interpolation for calculation of flow with nonstaggered grids, *Numerical Heat Transfer*, vol.13, pp.125-132.

McIntyre, D.A. 1981. Design requirements for a comfortable environment, In: *Bioengineering, Thermal physiology and Comfort* (ed: Cena, K. and Clark, J.A.), pp.157-168, Elsevier Amsterdam.

Melikov, A.K., Hanzawa, H. and Fanger, P.O. 1988. Airflow characteristics in the occupied zone of heated spaces without mechanical ventilation, *ASHRAE Transactions*, vol. 94 part 1, pp.52-70.

Melikov, A.K., Langkilde, G. and Derbiszewski, B. 1990. Airflow characteristics in the occupied zone of rooms with displacement ventilation, *ASHRAE Transactions*, vol. 96 part 1, 555-563.

Melikov, A.K., Krüger, U., Zhou, G., Madsen, T.L. and Langkilde, G. 1997. Air temperature fluctuations in rooms, *Building and Environment*, vol.32 no.2, pp.101-114.

Mierzwinski, S. 1981. *Air motion and temperature distribution above a human body in result of natural convection*, A4-serien no.58, Inst. för Uppv.- o Vent. Teknik, KTH, Stockholm, Sweden.

Mook, van, F. 1995. *Lage luchtsnelheden - visualiseren en meten*, internal report 95.69.W, Eindhoven University of Technology, Eindhoven, The Netherlands (in Dutch: Low air velocities - visualising and measuring).

Morton, B.R., Taylor, G.F.R.S. and Turner, J.S. 1956. Turbulent gravitational convection from maintained and instantaneous sources, *Proc. Roy. Soc. London*, vol.234 A, pp.1-23.

Müller, D. 1998. (personal communications).

Müller, D. and Renz, U. 1998[a]. Measurement and predictions of room airflow patterns using different turbulence models, *Proc. Roomvent'98*, vol.1, pp.109-116, Stockholm, Sweden.

Müller, D. and Renz, U. 1998[b]. A low cost particle streak tracking system (PST) and a new approach to three dimensional airflow velocity measurements, *Proc. Roomvent'98*, vol.2, pp.593-600, Stockholm, Sweden.

Mundt, E. 1996. *The Performance of Displacement Ventilation Systems*, thesis, Royal Institute of Technology Building Services Engineering, Stockholm, Sweden.

Murakami, S. and Kato, S. 1989. Numerical and experimental study on room airflow - 3-D predictions using the k-ε model, *Building and Environment*, vol.24 no.1, pp.85-97.

Nansteel, M.W. and Greif, R. 1981. Natural convection in undivided and partially divided rectangular enclosures, *Journ. of Heat Transfer*, vol.103, pp. 623-629.

Negrão, C.O.R. 1995. *Conflational of Computational Fluid Dynamics and Building Thermal Simulation*, thesis, University of Strathclyde, Glasgow, Scotland.

Negrão, C.O.R. 1998. Integration of computational fluid dynamics with building thermal and mass flow simulation, *Energy and Buildings*, vol.27, pp.155-165.

NEN 1087. 1997. *Ventilatie van Gebouwen - Bepalingsmethode voor nieuwbouw*, NNI - Nederlands Normalisatie-Instituut, Delft, The Netherlands (in Dutch: Ventilation of Buildings - Regulation method for new buildings).

Nevins, R.G. and Feyerherm, A.M. 1967. The effects of floor surface temperatures on comfort, Part IV, cold floors, *ASHRAE Transactions*, vol. 73, part 2.

Nielsen, P.V. 1974. *Flow in Air Conditioned Rooms*, thesis, Nordborg DK.

Nielsen, P.V., Restivo, A. and Whitelaw, J.H. 1978. The velocity characteristics of ventilated rooms, *Journal of Fluid Engineering*, vol.100, pp.291-298.

Nielsen, P.V., Restivo, A. and Whitelaw, J.H. 1979. Buoyancy-affected flows in ventilated rooms, *Numerical Heat Transfer*, vol.2, pp.115-127.

Nieuwstadt, F.T.M. 1992. *Turbulentie*, Utrecht: Epsilon Uitgaven, The Netherlands.

Niu, J. 1994. *Modelling of Cooled-Ceiling Air Conditioning Systems*, thesis, Delft University of Technology, Delft, The Netherlands.

Olesen, B.W., Schøler, M. and Fanger, P.O. 1979. Discomfort caused by vertical air temperature differences, In: *Indoor Climate* (ed: P.O. Fanger and O. Valbjørn), pp.561-579, Danish Building Research Institute, Copenhagen, Denmark.

Ong, B.L. 1995. Designing for the individual: A radical reading of ISO 7730, In: *Standards for thermal comfort* (ed: Nicol, F., Humphreys, M., Sykes, O. and Roaf, S.), pp.70-77, E & FN Spon, London, United Kingdom.

Parsons, K.C. 1994. Thermal comfort standards: past, present and future, *Proc. Thermal comfort: past, present and future* (ed: Oseland N.A. and Humphreys, M.A.), pp.184-196, Garston, United Kingdom.

Patankar, S.V. 1980. *Numerical Heat Transfer and Fluid Flow*, Hemisphere Publishing Corporation, USA.

Patankar, S.V. 1981. A calculation procedure for two-dimensional elliptic situations, *Numerical Heat Transfer*, vol.4, pp.409-425.

Peng. X. 1996. *Modeling of Indoor Thermal Conditions for Comfort Control in Buildings*, thesis, Delft University of Technology, Delft, The Netherlands.

Piomelli, U., Cabot, W.H., Moin, P. and Lee, S. 1991. Subgrid-scale backscatter in turbulent and transitional flows, *Phys. Fluids A*, vol.3(7), pp.1766-1771.

Popiolek, Z., Melikov, A.K. and Jorgensen, F.E. 1996. Dynamic response of thermal anemometers for low velocity measurements indoors, *Proc. Roomvent'96*, vol.1, pp.477-484, Yokohama, Japan.

Prasad, K.K. 1994. *Introduction to turbulent flows*, lecture notes, Eindhoven University of Technology, Eindhoven, The Netherlands.

Preller, L., Zweers, T., Brunekreef, B. and Bolej, J.S.M. 1990. Sick leave due to work-related health complaints among office workers in the Netherlands, *Proc. Indoor Air '90*, vol.1, pp.227-230, Ottowa, Canada.

Ranz, W. and Marshall, W. 1952. Evaporation from drops - Part I, *Chemical Engineering Progress*, vol.48 no.3, pp.141-146.

Raw, G.J., Roys, M.S. and Leaman A. 1990. Further findings from the office environment survey: productivity, *Proc. Indoor Air '90*, vol.1, pp.230-236, Ottowa, Cananda.

Recknagel, H., Sprenger, E. and Schramek, E.-R. 1997. *Taschenbuch für Heizung und Klimatechnik*, R. Oldenbourg Verlag, München, Germany.

Regenscheit, B. 1959. Die Luftbewegung in klimatisierten Räumen, *Kältetechnik*, vol. 11 - 1, pp.3-11 (in German).

Rhie, C.M. and Chow, W.L. 1983. Numerical study of the turbulent flow past an airfoil with trailing edge separation, *AIAA Journal*, vol.21 no.11, pp.1525-1532.

Rohles, F.H., Hashinaga, M. and Yamada, T. 1993. Measuring the comfort-producing effectiveness of space-heaters during transient warming, *ASHRAE Transactions*, vol.99 part 2B, pp. 747-760.

Roomvent. 1992. *Roomvent '92 Air Distribution in Rooms*, Proceedings 3rd conference, 3 volumes, Aalborg, Denmark.

Roomvent. 1994. *Roomvent '94 Air Distribution in Rooms*, Proceedings 4rd conference, 2 volumes, Kraków, Poland.

Roomvent. 1996. *Roomvent '96 Air Distribution in Rooms*, Proceedings 5rd conference, 3 volumes, Yokohama, Japan.

Roomvent. 1998. *Roomvent '98 Air Distribution in Rooms*, Proceedings 6rd conference, 3 volumes, Stockholm, Sweden.

Roos, A. 1998[a]. *On the effectiveness of ventilation*, thesis, Eindhoven University of Technology, Eindhoven, The Netherlands (to be published).

Roos, A. 1998[b]. The air exchange efficiency of the desk displacement ventilation concept - Theory, measurements and simulations, *Proc. Roomvent'98*, vol.1, pp.249-256, Stockholm, Sweden.

Rutten, P.G.S. 1996. The twin duct variable air volume system, *Proc. Indoor Air '96*, vol.1, pp.307-312, Nagoya, Japan.

Saffman, P.G. 1965. The lift on a small sphere in a slow shear flow, *J. Fluid Mechanics*, vol.22 part 2, pp.385-400.

Sandberg, M. and Sjöberg, M. 1983. The use of moments for assessing air quality in ventilated rooms, *Building and Environment*, vol. 18, pp.181-197.

Scholzen, F. 1997. *Bestimmung des Dreidimensionalen Geschwindigkeitsfeldes in Räumen durch Quantitative Strömungsvisualisierung*, thesis, ETH Zürich, Switzerland.

Schubauer, G.B. 1935. *Effect of humidity in hot-wire anemometry*, Journal of Research of the Nat. Bureau Standards, 15, pp.575-578.

Skistad, H. 1994. *Displacement Ventilation*, Research Studies Press Ltd., Somerset, Great Britain.

Sprague, C.H. and McNall, P.E.,jr. 1970. The effects of fluctuating temperature and relative humidity on the thermal sensation (thermal comfort) of sedentary subjects, *ASHRAE Transactions*, vol. 76 part 1, pp.146-156.

Stengele, F.R. 1993. *Einfluß der Freien Konvektion auf den Wärmeübergang bei Thermischen Anemometern*, thesis, Universität Bremen, Germany.

Stolwijk, J.A.J. 1971. *A mathematical model of the physiological temperature regulation in man*, NASA-report CR-1855, Washington D.C., USA.

Strawberry Tree. 1995. *Data Acquisition Systems User Manual*, Strawberry Tree Inc., Sunnyvale, California, USA.

Tammes, E. and Vos, B.H. 1984. *Warmte en vochttransport in Bouwconstructies*, Kluwer, Deventer, the Netherlands.

Tanis, F.J., Sampson, R.E. and Wagner, T.W. 1976. *Thermal imagery for evaluation of construction and insulation conditions of small buildings*, Report 116600-12-F, Environmental Research Institute of Michigan, Michigan, USA.

Tavoularis, S. 1986. Techniques for turbulence measurement, In: *Encyclopedia of Fluid Mechanics, volume 1: Flow Phenomena and Measurement* (ed: N.P. Cheremisinoff), Chapter 36, Gulf Publishing Company, Houston, USA.

Tennekes, H. and Lumley, J.L. 1972. *A First Course in Turbulence*, MIT Press, Cambridge, Massachusetts, USA.

The Mathworks, Inc. 1993. *Matlab User Guide*, reprint, Natick, Massachusetts, USA.

Thorsauge, J. 1982. Air-velocity fluctuations in the occupied zone of ventilated spaces, *ASHRAE Transactions*, vol. 88 part 2, 753-764.

Ward-Smith, A.F. 1980. *Internal Fluid Flow - The fluid dynamics of flow in pipes and ducts*, Claredon Press, Oxford.

Westerweel, J. 1993. *Digital Particle Image Velocimetry*, thesis, Delft University of Technology, The Netherlands.

Whittle, G.E. 1991. Evaluation of measured and computed test case results from annex 20, subtask 1, *Proc. 12th AIVC Conference*, Ottawa, Canada.

Williams, P.T., Baker, A.J. and Kelso, R.M. 1994. Numerical calculation of room air motion - part 2: The continuity constraint finite element method for three-dimensional incompressible thermal flows, *ASHRAE Transactions*, vol.100 part 1, pp.531-548.

World Health Organization. 1983. *Indoor Air Pollutants: Exposure and health effects* (Report of a WHO meeting, EURO Reports and studies no. 78), WHO Regional Office for Europe.

Wyon, D.P. 1993. Healthy Buildings and their impact on productivity, *Proc. Indoor Air'93*, vol. 6, pp.3-13, Helsinki, Finland.

Wyon, D.P. 1994. Assessment of human thermal requirements in the thermal comfort region, *Proc. Thermal comfort: past, present and future* (ed: Oseland N.A. and Humphreys, M.A.), pp.144-155, Garston, United Kingdom.

Wyon, D.P. 1995. Thermal manikin experiments on Climadesk. *Proc. from the workshop on Task/Ambient Conditioning Systems in Commercial Buildings*, ed. F.Bauman, CEDR, University of California, Berkeley, USA.

Yakhot, V. and Orszag, S.A. 1986. Renormalization group analysis of turbulence. I. Basic theory, *Journal of Scientific Computing*, vol. 1 no.1, pp.3-51.

Yuan, X., Chen Q. and Glicksman, L.R. 1997. *Experimental validation of a Computational Fluid Dynamics model for modeling displacement ventilation flows*, Phase 2 report ASHRAE TC 5.3 'Room Air Distribution on Performance Evaluation and Development of Design Guidelines for Displacement Ventilation (RP-949)', MIT, Cambridge, USA (draft version).

Zandt, M. in 't. 1995. *Simulatie en calibratie van hete film anemometers*, internal report, Eindhoven University of Technology, Eindhoven, The Netherlands (in Dutch: Simulation and calibration of hot film anemometers).

Zeidler, O. and Fitzner, K. 1998. Investigation of the impact of natural ventilation through windows on thermal comfort, *Proc. Roomvent'98*, vol.2, pp.323-326, Stockholm, Sweden.

- References -

Nomenclature

A	area	[m^2]
ACH	air change rate	[h^{-1}]
c_w	particle drag coefficient	[-]
c_p	constant pressure specific heat	[J/kg.K]
c_μ,$c_{\varepsilon 1}$, $c_{\varepsilon 2}$, $c_{\varepsilon 3}$	coefficients in turbulence model	[-]
C	concentration	[m^3/m^3_{air}]
C	heat capacity	[J/K]
d	diameter	[m]
E	function of wall roughness	[-]
f	frequency	[Hz]
F_e	external force	[N]
g_i	gravity vector	[m/s^2]
G_b	generation of turbulent energy due to buoyancy	[W/m^3]
h	height	[m]
h_c	convective heat transfer coefficient (Equation 4.18)	[$W/m^2.K$]
h_{rad}	radiant heat transfer coefficient	[$W/m^2.K$]
h_{tc}	convective heat transfer coefficient (Equation 7.1)	[$W/m^2.K$]
H	specific enthalpy	[J/kg]
I_{clo}	thermal resistance from skin to outer surface of clothed body (1 clo = 0.155 m^2.K/W)	[clo]
k	thermal conductivity	[W/m.K]
k	turbulent kinetic energy per unit mass	[J/kg]
l	length	[m]
L_s	length scale	[m]
M	rate of metabolic heat production	[W/m]
N	total number of realisations	[-]
Nu	Nusselt number	[-]
p	pressure	[Pa]
P_k	production of turbulent energy due to turbulent stress	[W/m^3]
Pr	Prandtl number	[-]
PD	percentage of dissatisfied due to draught	[%]
PMV	predicted mean vote	[-]
PPD	predicted percentage of dissatisfied	[%]
PS	percentage of satisfied	[%]

$\dot{q}$	heat flux	[W/m^2]
$\dot{q}_c$	convective heat flux	[W/m^2]
Q	heat load	[W]
r	radius	[m]
r	damping	[-]
R	additional source term introduced in RNG k-ε model	[W/m^3.s]
Re	Reynolds number	[-]
S_ϕ	source term of general fluid property	
S_{ij}	magnitude of rate-of-strain	[s^{-1}]
Sc	Schmidt number	[-]
St	Stanton number	[-]
t	time	[s]
T	temperature	[K] or [^{o}C]
$\overline{T}_y$	average air temperature (over six positions outside buoyant plume)	
	at height y	[K] or [^{o}C]
T_{avg}	averaging time	[s]
T_s^{tot}	total sampling time	[s]
$\overline{T}_{0.1\,m}^{*}$	average air temperature (over all measurement/simulation positions)	
	at 0.1 m distance from the surface	[K] or [^{o}C]
ΔT	temperature difference (T_{supply} - T_{wall})	[K] or [^{o}C]
TI	turbulence intensity	[-]
u	flow velocity	[m/s]
u_i, u_j	index notation of velocity components	[m/s]
u_τ	friction velocity	[m/s]
v	velocity component	[m/s]
$\dot{V}$	air flow rate	[m^3/s]
w	width	[m]
w	velocity component	[m/s]
x, y, z	cartesian coordinates in three directions	[m]
x_i, x_j	index notation of cartesian coordinates	[m]
X	sample	
Y	constant	[-]
Z	constant	[-]

Greek symbols

β	volumetric thermal expansion coefficient	[K^{-1}]
Γ	diffusion coefficient	[kg/m.s]
δ_{ij}	Kronecker delta function	[-]
ε	rate of dissipation of turbulent kinetic energy per unit mass	[J/kg.s]
ε	emmisivity factor	[-]
ζ	inverse Prandtl-number	[-]
η_0, η	parameters in RNG-*k*-ε model	[-]
θ_h	dimensionless temperature at height *h*	[-]
θ_H	relative specific enthalpy	[J/kg]
κ	von Karman's constant (0.42)	[-]
μ	dynamic viscosity	[kg/m.s]
ξ	air cooling fraction	[-]
ρ	density	[kg/m^3]
σ_ϕ	standard deviation	
$\sigma_{k,\varepsilon,H,C}$	turbulent Prandtl (*k*,ε,*H*) or Schmidt (*C*) number	[-]
τ_{ij}	Reynolds stress	[N/m^2]
τ_w	wall shear stress	[N/m^2]
τ	time constant, response time	[s]
$\bar{\tau}$	local mean age of the air	[min]
φ	relative humidity	[%]
ϕ	general fluid property	

Subscripts

avg	average
c	convective
cc	cooled ceiling
cs	'cold' sensor
C	ceiling
d	diameter
eff	effective
E	east
f	fluid
F	floor
h	heat source, height
hs	heated sensor
i, j	coordinate
k	conductive

ke	kernel
m	thermal mannequin
mrt	mean radiant temperature
n	neutral
N	north
op	operative
p	particle, pipe
P	first cell adjacent to wall
r	radiant
s	surface
S	south
t	turbulent
tot	total
v	ventilation
w	wall
W	west
ϕ	general fluid property

Superscripts

int	integral scale
L	averaging length
n	realisation
N	total number of realisations
tot	total
T_s	averaging time
+	dimensionless variable
-	average component of turbulent parameter
′	fluctuating component of turbulent parameter
ˆ	measured value

Other symbols

0	reference, base
$\rightarrow$	flow direction
$\mid$ or —	alignment hot-sphere anemometer

Appendix A

STATISTICAL UNCERTAINTY IN A MEASUREMENT

Assuming a Gaussian distributed probability density function (pdf), the pdf $p(X^{(n)})$ of a number of statistically independent samples $X^{(n)}$ from a random (ergodic) process will be centred around the true ensemble average, $\overline{X}$, with a standard deviation $\sigma_{\overline{X}}$. Given the standardised variable $z = (X - \overline{X})/\sigma_{\overline{X}}$, the standardised Gaussian pdf, $p(z)$, can be expressed as

$$p(z) = \frac{1}{\sqrt{2\pi}} e^{-z^2/2}, \tag{A.1}$$

and the corresponding cumulative probability distribution function takes the form

$$P(z) = \int_{-\infty}^{z} p(\xi) d\xi . \tag{A.2}$$

If $X^{(n)}$ is taken as an estimate for the ensemble average $\overline{X}$, the uncertainty can be expressed as

$$-z_{\alpha/2} < \left(X^{(n)} - \overline{X}\right)/\sigma_{\overline{X}} < z_{\alpha/2}, \tag{A.3}$$

where $z_{\alpha/2}$ is the value of z for which $P(z_{\alpha/2}) = 1 - \alpha/2$. Statistically $X^{(n)}$ will fall within the interval $\overline{X} - z_{\alpha/2}\,\sigma_{\overline{X}} < X^{(n)} < \overline{X} + z_{\alpha/2}\,\sigma_{\overline{X}}$, with a probability of $(1-\alpha)\cdot 100\%$.

Denoting the measured value by $\hat{X}$ and the true value by $\overline{X}$, the measured mean value, $\overline{\hat{X}}$, will statistically fall within

$$\overline{X} - z_{\alpha/2}\sigma[\overline{\hat{X}}] < \overline{\hat{X}} < \overline{X} + z_{\alpha/2}\sigma[\overline{\hat{X}}], \tag{A.4}$$

with a probability of $(1-\alpha)\cdot 100\%$. The uncertainty in the estimated statistical quantity can be specified when the variance of that quantity is determined. The variance of $\overline{\hat{X}}$ is

$$\mathrm{var}[\overline{\hat{X}}] = \sigma^2[\overline{\hat{X}}]. \tag{A.5}$$

Given the ensemble mean X^N (Equation 3.4) and assuming identically distributed and statistically independent samples, then

$$\mathrm{var}[X^N] = \frac{1}{N}\mathrm{var}[X] = \frac{\sigma_x^2}{N}, \tag{A.6}$$

for N independent realisations, where σ_x^2 is the variance of the sample record (George et al. 1978). Given an ergodic process, the statistical quantity can be evaluated by time-mean averaging: var[X^N] = var[$\hat{X}$]. The variance then can be expressed by

$$\mathrm{var}[\overline{\hat{X}}] = \sigma^2[\overline{\hat{X}}] = \frac{\sigma_x^2}{N} \approx \frac{2T_s^{int}\sigma_x^2}{T_s^{tot}}, \qquad \text{(A.7)}$$

where T_s^{tot} is the total sampling time and consequently $N \approx T_s^{tot}/2T_s^{int}$ (Tennekes and Lumley, 1972). Time-history record samples separated by two integral time scales contribute to the evaluated quantities as statistically independent samples. In Equation A.7, T_s^{int} is determined from the autocorrelation function and presents the interval for which X is correlated with respect to time. The time interval scales with the large eddy flow characteristics (dimension and velocity). The optimum sample interval, Δt, equals $2T_s^{int}$. Sampling more slowly would extend the measuring time without a significant increase in accuracy, sampling at a faster rate will increase the uncertainty as the samples will not be statistically independent.

Introducing the normalised root mean square error

$$\varepsilon[\overline{\hat{X}}] = \frac{\sigma[\overline{\hat{X}}]}{\overline{X}} = \frac{1}{\sqrt{N}}\frac{\sigma_x}{\overline{X}} \approx \left(\frac{2T_s^{int}}{T_s^{tot}}\right)^{1/2}\frac{\sigma_x}{\overline{X}}, \qquad \text{(A.8)}$$

the uncertainty in the measured mean value can be expressed by

$$1 - z_{\alpha/2}\varepsilon[\overline{\hat{X}}] < \frac{\overline{\hat{X}}}{\overline{X}} < 1 + z_{\alpha/2}\varepsilon[\overline{\hat{X}}], \qquad \text{(A.9)}$$

with a probability of (1-α)·100%.
Given $X(t) = \overline{X} + x(t)$, for the turbulent quantities a similar derivation can be described:

$$\varepsilon[\overline{\hat{x}^2}] = \frac{\sigma[\overline{\hat{x}^2}]}{\sigma_x^2} \approx \left(\frac{2T_s^{int}}{T_s^{tot}}\right)^{1/2}. \qquad \text{(A.10)}$$

Given the same sample criteria the uncertainty in the turbulent quantities is larger than the uncertainty in the mean value.

Appendix B

NUMERICAL MODEL HOT SPHERE ANEMOMETER

The anemometer has been described numerically by modelling the electrical circuit and the heat transfer characteristics of both sensors (in ‘t Zandt 1995; in Loomans and van Schijndel 1998). By coupling both models a relation can be calculated between the bridge voltage and the air velocity.

In Figure B.1 the electrical circuit is shown. From this circuit the following combined resistors can be derived,

$$R_k = R_1 + R_8,\ R_i = R_2 + (\frac{1}{R_6} + \frac{1}{R_7 + R_{cs}})^{-1},$$

$$R_j = R_3 + (\frac{1}{R_{hs}} + \frac{1}{R_4 + R_5})^{-1},\ R_{br} = (\frac{1}{R_k} + \frac{1}{R_i} + \frac{1}{R_j})^{-1}. \qquad \text{(B.1)}$$

In Equation B.1, R is the electrical resistance. The electrical resistance of the nickel film is given by $R_{hs} = R_{0\_hs}(1+\beta \cdot T_{s\_hs})$ and $R_{cs} = R_{0\_cs}(1+\beta \cdot T_{s\_cs})$, with T_{s_hs} and T_{s_cs}, the temperature of the nickel film of the heated and ‘cold’ sensor respectively and β the temperature coefficient of resistivity [K^{-1}].

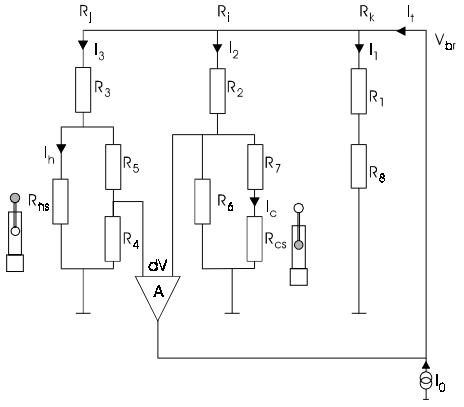

Figure B.1. Electrical circuit of the hot sphere anemometer.

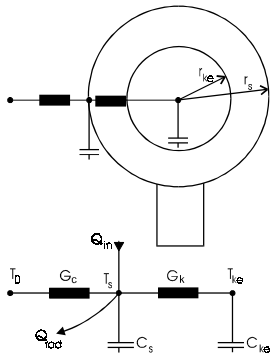

Figure B.2. Heat transfer model of a single sensor.

The current through the heated and 'cold' sensor, needed for calculating the heating of the sensors, is calculated by

$$I_{hs} = \frac{V_{br}}{R_j} \cdot \frac{R_4 + R_5}{R_{hs} + R_4 + R_5} \quad \text{and} \quad I_{cs} = \frac{V_{br}}{R_i} \cdot \frac{R_6}{R_6 + R_7 + R_{cs}}, \tag{B.2}$$

where I is the electrical current. Finally, the bridge voltage V_{br} can be determined by

$$V_{br} = (I_0 + a \cdot dV) \cdot R_{br}, \tag{B.3}$$

where a is the amplification and I_0 the base electrical current.
In Figure B.2 the heat transfer model of one sensor is given. The model is similar for both sensors. The sensor is divided in two sub shells representing the surface temperature (T_s) and the kernel temperature (T_{ke}). The heat balances for both nodes are given by:

$$\frac{dT_s}{dt} \cdot C_s = Q_{in} - Q_k - Q_c - Q_{rad} \quad \text{and} \quad \frac{dT_{ke}}{dt} \cdot C_{ke} = Q_k, \tag{B.4}$$

heating: $$Q_{in} = I^2 \cdot R, \tag{B.5}$$

conduction: $$Q_k = G_k(T_s - T_{ke}) = 4\pi \cdot k \cdot \frac{r_s \cdot r_{ke}}{r_s - r_{ke}}(T_s - T_{ke}), \tag{B.6}$$

convection: $$Q_c = G_c(T_s - T_0) = \frac{A_s \cdot Nu_d \cdot k_{air}}{2 r_s} \cdot (T_s - T_0), \tag{B.7}$$

radiation: $$Q_{rad} = \sigma \cdot \varepsilon \cdot A_s \cdot (T_s^4 - T_{mrt}^4), \tag{B.8}$$

where Nu_d is the Nusselt number based on the diameter of the sensor, $Nu_d = 2 + 0.60 \cdot Pr^{1/3} Re_d^{1/2}$ (Ranz and Marshall 1952), and C is the heat capacity, $C_s = \rho c_p \, 4\pi(r_s^3 - r_{ke}^3)/3$.

Appendix C

DESCRIPTION PROBLEM SET-UP (Chapter 4)

This appendix presents the full description of the problem set-up for the simulation of the office configuration as described in Chapter 4.4.

Table C.1 Geometry displacement ventilated office room.

geometry	dimensions		place
room	$l \times w \times h$	$4.5 \times 3.6 \times 2.7$ m^3	
window	$w \times h$	2.3×1.3 m^2	middle of West wall at height 0.7 m
window-sill	depth	0.25 m	
table	$l \times w \times h$	$2.0 \times 1.5 \times 0.03$ m^3	middle of room at height 0.7 m; table legs neglected
chair	$l \times w$	0.45×0.45 m^2	aside table at height 0.35 m; chair legs neglected
lamp	$l \times w \times h$	$0.3 \times 0.15 \times 0.05$ m^3	aside table at height 2.0 m
unit	$w \times h$	0.48×0.68 m^2	corner South-West wall at height 0.27 m
exhaust	$l \times w$	0.15×0.15 m^2	aside table at ceiling
person	$l \times w \times h$	$0.2 \times 0.15 \times 0.35$ m^3	volume 0.01 m^3; at chair
computer	$l \times w \times h$	$0.15 \times 0.09 \times 0.15$ m^3	volume 0.002 m^3; 2 samples at middle of the table, separation 0.36 m.

Table C.2 Boundary conditions displacement ventilated office room.

walls	T [^{o}C]	
window	24.5	
parapet	23.0	
East wall	23.0	
South wall	24.5	
North wall	23.5	
ceiling	24.5	
floor	24.0	
heat sources	Q [W]	convective fraction
person	100	52 %
computer	60	63 %
lamp	70	25 %
supply		
temperature	18.0 ^{o}C	
volume flow rate	0.058 m^3/s	
turbulence intensity	35 %	

- Appendix C -

Appendix D

GEOMETRY AND FEATURES OF THE EXPERIMENTS

Table D.1. Location and convection heat load of objects in model office room (thermal mannequin not included).

objects	x_1 [m]	x_2 [m]	y_1 [m]	y_2 [m]	z_1 [m]	z_2 [m]	Q_{tot_c}/Q_{tot} [-]
supply unit	3.32	3.48	0.0	0.725	0.95	2.65	-
supply grille	3.32	3.32	0.085	0.385	1.30	2.30	-
exhaust	4.14	5.12	2.47	2.50	3.60	3.60	-
large table	2.58	3.48	0.725	0.75	0.95	2.65	-
small table	0.0	0.565	0.75	0.77	2.05	2.85	-
PC-simulator 1	2.90	3.30	0.75	1.15	1.60	2.00	0.625
PC-simulator 2	0.15	0.55	0.77	1.17	2.25	2.65	0.625
light simulator	3.05	3.20	1.00	1.15	1.15	1.30	0.39
fluorescent lamp 1	1.26	1.29	2.41	2.50	1.20	2.38	0.39
fluorescent lamp 2	2.39	2.42	2.41	2.50	1.20	2.38	0.39
fluorescent lamp 3	3.91	3.94	2.41	2.50	1.20	2.38	0.39
chair	2.30	2.755	0.455	0.75	1.63	1.97	-

Table D.2. Location and convective heat input of thermal mannequin in model office room.

sections	x_1 [m]	x_2 [m]	y_1 [m]	y_2 [m]	z_1 [m]	z_2 [m]	$Q_{section}$ / Q_{tot} [-]	$Q_{section\_c}$ / $Q_{section}$ [-]
head	2.32	2.465	1.075	1.265	1.73	1.87	0.17	0.59
chest	2.32	2.455	0.475	1.075	1.63	1.97	0.30	0.43
left arm	2.36	2.87	0.75	1.075	1.60	1.66	0.08	0.38
right arm	2.36	2.87	0.75	1.075	1.94	2.00	0.08	0.38
left leg	2.455	2.87	0.0	0.59	1.63	1.73	0.19	0.53
right leg	2.455	2.87	0.0	0.59	1.87	1.97	0.19	0.53

- Appendix D -

Appendix E

DESIGN AND DIMENSIONS THERMAL MANNEQUIN

The geometry of the mannequin is designed to emulate the proportions of a human being, although stylistically (see Figure E.1). The surface areas of the different sections of the mannequin approximate the surface areas as are given by different authors (Stolwijk 1971 and Lotens 1993; see Table E.1). The surface areas of the sections of the mannequin are corrected for the fact that they are connected to other sections. However, the surface area of the chest and legs are not corrected for the fact that they, to some part, will be isolated by the chair. The surface area of the leg-section of the mannequin is relatively large compared to the chest-section area, as compared with the proportions as presented by Stolwijk and Lotens.

The mannequin is constructed from aluminium tubes with a synthetic coating and aluminium sheets for the chest-section. For the flexible joints, aluminium flexible tubes are used. The top of the tubes are closed with aluminium caps, also synthetically coated. The mannequin is painted black in order to approximate an overall radiant emission coefficient of ~0.9. This coefficient has not been measured explicitly.

Table E.1. Surface area of the human body in [m^2] and [%].

section	thermal mannequin [in m^2 (% of total)]	Stolwijk (1971) man 30-35 years [in m^2 (% of total)]	Lotens (1993) [% of total]
head	0.13 [7%]	0.133 [7%]	7%
chest	0.59 [30%]	0.680 [36%]	35%
arms + hands	0.37 [19%]	0.348 [18%]	17%
legs + feet	0.85 [44%]	0.727 [39%]	40%
total body	1.94 [100%]	1.888 [100%]	99%

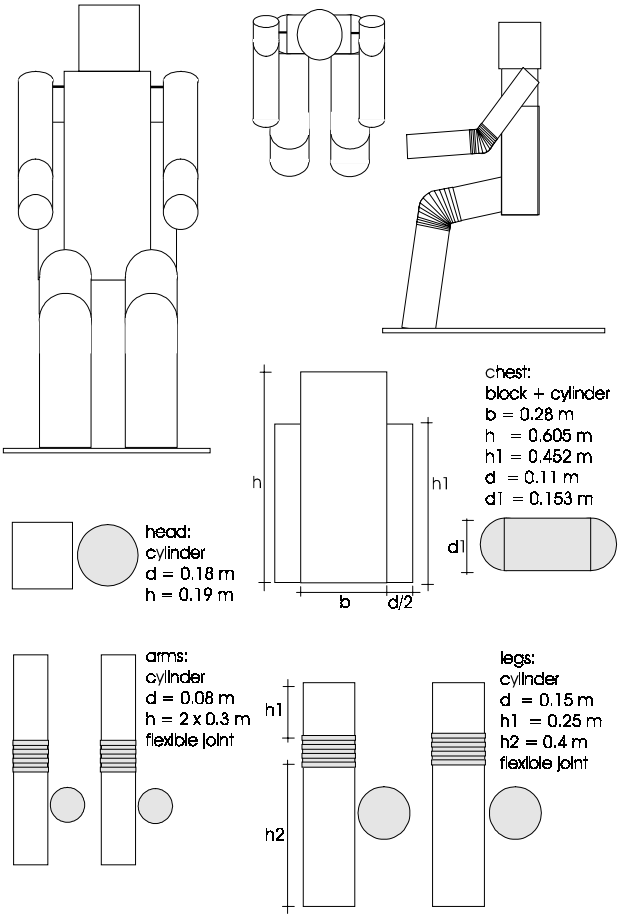

Figure E.1. Design and dimensions of the thermal mannequin.

Appendix F

FULL-SCALE EXPERIMENTS

This appendix summarises the boundary conditions and the characteristics of the measurement results for the full-scale experiments as described in Chapter 6. All the measurement results that are presented for a case are mean values. One case comprises 13 separate measurements (see Chapter 5).

Boundary conditions

Table F.1. Boundary conditions for the full-scale experiments.

Case	T_N [^{o}C]	T_S [^{o}C]	T_W [^{o}C]	T_E [^{o}C]	T_F [^{o}C]	T_C [^{o}C]	T_{supply} [^{o}C]	$\dot{V}$ [m^3/s]	Q_{tot_m} [W]	Q_{tot_h} [W]
1a	23.2	22.8	22.6	22.8	22.5	22.5	20.3	0.010	125	0
1b	23.2	22.8	22.7	22.8	22.5	22.5	22.4	0.010	123	0
2a	23.2	22.7	22.6	22.8	22.3	22.7	19.8	0.029	117	0
2b	23.1	22.8	22.6	22.8	22.3	22.7	19.8	0.029	120	0
3a	23.7	23.1	22.5	22.8	22.7	22.4	20.4	0.010	122	363
3b	23.6	23.1	22.5	22.8	22.7	22.4	20.4	0.010	122	363
4a	23.6	23.0	22.5	22.8	22.5	22.4	19.8	0.019	122	364
4b	23.6	23.0	22.5	22.8	22.5	22.4	19.8	0.019	122	364
5a	23.5	23.0	22.4	22.8	22.4	22.4	19.8	0.029	120	368
5b	23.2	22.7	22.6	22.8	22.2	22.3	19.8	0.029	118	360
6a	23.2	22.8	22.6	22.7	22.2	22.3	19.8	0.047	122	362
6b	23.1	22.8	22.6	22.7	22.2	22.3	19.8	0.047	122	361
7	23.6	23.0	22.4	22.7	22.7	22.4	21.8	0.029	122	366
8a	21.0	20.3	19.3	19.7	20.1	19.3	22.7	0.020	122	361
8b	21.1	20.3	19.4	19.7	20.2	19.3	22.7	0.020	122	360

Table F.2. Fraction of total heat input (Q_{tot_m} and Q_{tot_h}) to determine convective heat load (Q_c).

sections	*head*	*chest*	*right-arm*	*left-arm*	*right-leg*	*left-leg*
fraction of Q_{tot_m} [-]	0.1	0.13	0.03	0.03	0.10	0.10
heat sources	*desk lamp*	*PC-1*	*PC-2*	*Fl. lamp 1*	*Fl. lamp 2*	*Fl. lamp 3*
fraction of Q_{tot_h} [-]	0.03	0.17	0.17	0.05	0.05	0.05

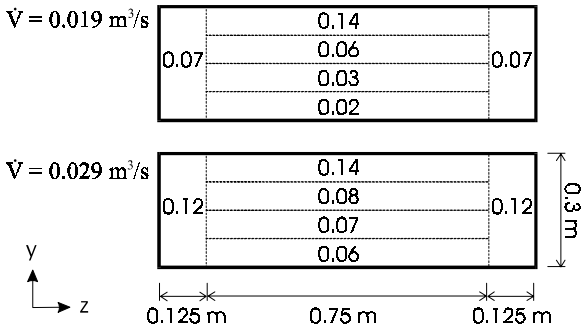

Figure F.1. Velocity distribution at the supply unit for $\dot{V}$ = 0.019 m³/s and $\dot{V}$ = 0.029 m³/s in [m/s].

Table F.1 summarises the boundary conditions for the full-scale measurements. The convective heat load of the separate sections of the thermal mannequin and the different heat sources in the room can be determined from a fraction of the indicated total heat load (Q_{tot_m} and Q_{tot_h}). These fractions are summarised in Table F.2.

From the velocity measurements at the supply unit, described in Chapter 5.2.2, information is available on the velocity distribution at the unit. Figure F.1 shows the experimentally obtained velocity distribution for $\dot{V}$ = 0.019 m³/s and $\dot{V}$ = 0.029 m³/s. The supply unit has been divided in six segments. For each segment the mean velocity is determined from the measurement results. This value furthermore has been corrected to allow a 100% aperture for the modelling of the supply in a CFD-model (see Chapter 4.4.2).The difference in distribution between the supply air flow rates is explained from the air distribution within the supply unit. Furthermore, for $\dot{V}$ = 0.029 m³/s measurements were performed at 0.08 m from the supply grill whereas for $\dot{V}$ = 0.019 m³/s measurements were made at 0.015 m.

For lower flow rates an evenly distributed velocity may be assumed. For $\dot{V}$ = 0.010 m³/s this results in an averaged velocity of 0.033 m/s. For higher velocities accurate measurements on the velocity distribution at the supply have not been performed. Given the limited sensitivity of the supply conditions to the whole room flow pattern (see Chapter 4.4.4) an extrapolation of the velocity distribution as obtained for $\dot{V}$ = 0.029 m³/s is estimated to be sufficiently accurate.

The measured turbulence intensity at the supply is in the order of 15% for all cases. Due to damping of the anemometer, described in Chapter 3.6.3, the actual turbulence intensity will be higher (estimated in the order of 25%).

Characteristics of the measurement results

Table F.3. Measured flow characteristics.

Case	T_{supply} [°C]	$T_{exhaust}$ [°C]	Q_{c_v} [W]	ξ [-]	$\overline{T}^{*}_{0.1m}$ [°C]	dT/dy [°C/m]	$\overline{u}_{max(1)}$ [m/s]	$\overline{u}_{max(2)}$ [m/s]
1a	20.3	23.0	32	0.52	22.6	0.32	0.30	0.32
1b	20.4	23.0	32	0.53	22.6	0.32	0.32	0.32
2a	19.8	22.9	108	1.89	21.7	0.73	0.30	0.18
2b	19.8	22.9	109	1.83	21.7	0.77	0.28	0.15
3a	20.4	23.9	41	0.16	22.9	0.64	0.27	0.27
3b	20.4	23.8	41	0.16	22.9	0.68	0.27	0.27
4a	19.8	23.8	93	0.37	22.2	1.00	0.27	0.25
4b	19.8	23.8	93	0.37	22.2	0.95	0.28	0.26
5a	19.8	23.6	132	0.53	21.9	1.00	0.26	0.25
5b	19.8	23.5	128	0.52	21.7	1.14	0.26	0.21
6a	19.8	23.4	208	0.84	21.5	1.09	0.25	0.20
6b	19.8	23.4	208	0.84	21.5	1.09	0.25	0.19
7	21.8	23.7	67	0.27	22.8	0.64	0.27	0.24
8a	22.7	21.2	-36	-	20.4	0.50	0.23	0.31
8b	22.7	21.3	-35	-	20.4	0.50	0.23	0.31

Q_{c_v} : Heat load removed from the room by ventilation.

ξ : Air cooling fraction (= Q_{c_v} / Q_{tot_c}).

$\overline{T}^{*}_{0.1m}$: Temperature at 0.1 m height averaged over all measured temperatures at 0.1m height.

dT/dy : Vertical temperature gradient (0.1 m - 2.3 m height) [averaged value over six positions].

$\overline{u}_{max(1)}$: Velocity in plume thermal mannequin at 2.0 m height (x = 2.25 m).

$\overline{u}_{max(2)}$: Velocity in plume thermal mannequin at 2.0 m height (x = 2.40 m).

Table F.4. Averaged temperature ($\overline{T}_y$ [^{o}C]) at different heights outside the buoyant plumes.

Case	0.0 m	0.1 m	0.3 m	0.5 m	1.0 m	1.1 m	1.5 m	1.7 m	2.3 m	2.5 m
1a	22.5	22.6	22.8	22.9	23.0	23.1	23.1	23.2	23.3	22.5
1b	22.5	22.6	22.8	22.9	23.1	23.1	23.2	23.2	23.3	22.5
2a	22.3	21.6	22.0	22.3	22.7	22.8	23.0	23.1	23.2	22.3
2b	22.3	21.6	22.0	22.3	22.7	22.8	23.0	23.1	23.3	22.3
3a	22.7	22.8	23.0	23.1	23.5	23.6	23.8	24.0	24.2	22.7
3b	22.7	22.8	23.0	23.1	23.5	23.6	23.9	24.0	24.3	22.7
4a	22.5	22.0	22.5	22.8	23.2	23.4	23.7	23.9	24.2	22.5
4b	22.5	22.1	22.5	22.8	23.3	23.4	23.7	23.9	24.2	22.5
5a	22.4	21.7	22.2	22.5	23.0	23.2	23.5	23.7	23.9	22.4
5b	22.2	21.5	22.0	22.3	22.9	23.0	23.4	23.7	24.0	22.2
6a	22.2	21.4	21.7	21.9	22.5	22.7	23.3	23.5	23.8	22.2
6b	22.2	21.4	21.7	21.9	22.5	22.7	23.3	23.5	23.8	22.2
7	22.7	22.7	22.8	22.9	23.3	23.4	23.7	23.9	24.1	22.7
8a	20.1	20.3	20.5	20.7	21.1	21.2	21.3	21.4	21.4	20.1
8b	20.2	20.3	20.6	20.7	21.1	21.2	21.3	21.4	21.4	20.2

$\overline{T}_y$: Temperature at height *y*, averaged over six positions in the room outside the buoyant plume (*x* = 1.50 / 2.00 / 4.50 m; *z* = 0.675 / 2.925 m).

Dankwoord

Na tien jaar is het tijd geworden om afscheid te nemen van de TUE en in het bijzonder van FAGO. Na een succesvol afgeronde studie, vier jaar blijven hangen op vloer 10. Het uitzicht is en blijft wonderschoon maar het moment is gekomen om af te dalen.

Voor ik dat doe ben ik velen dank verschuldigd die mij in de afgelopen vier jaar hebben geholpen om dit werk te kunnen voltooien:

Mijn eerste promotor Paul Rutten, voor het vertrouwen en de grote vrijheid die hij mij heeft gelaten in het opzetten en uitvoeren van het onderzoek. Het was deze vrijheid die het mij mogelijk maakte om veel facetten van *het binnenklimaat* te belichten en om interessante reizen te ondernemen en vele interessante mensen te ontmoeten. Jacob Wisse ben ik dankbaar voor zijn grote inzet in de laatste fase van mijn werk, het schrijven van het proefschrift. In dit verband wil ik ook dank zeggen aan prof. van Steenhoven en dr. Chen voor hun instemming om mijn lijvige werk onder grote tijdsdruk te lezen en te becommentariëren.

Terugkerend bij FAGO ben ik op de eerste plaats dank verschuldigd aan Henk Schellen voor zijn tomeloze optimisme en hulpbereidheid in de afgelopen vier jaar. Opnieuw heeft hij gelijk gehad ! Jos van Schijndel, Rien Bergmans, Wim van de Ven en Jan Vermeulen waren onmisbaar bij het realiseren van de experimentele opstellingen. Ik hoop dat ze er nog even plezier van kunnen hebben. Jos, hartelijk dank voor je hulp bij alle hete bol activiteiten. Jan Diepens verdient een pluim voor zijn inzet om gedurende vier jaar het netwerk open te houden, broodnodig voor de vele langdurige berekeningen. Dank aan alle afstudeerders en T8-/T9-studenten, verzameld in 'Stroco' (het stromingscollectief), die mij de mogelijkheid hebben gegeven om met vele ogen te kijken naar luchtstroming op alle niveau's binnen de bouwfysica. Ten slotte ben ik al diegenen erkentelijk die mij in de afgelopen vier jaar van informatie en adviezen hebben voorzien en/of een steuntje in de rug hebben gegeven, op welk vlak en op welke manier dan ook, en op die manier hun steentje hebben bijgedragen aan dit werk.

Het hart van het plezierige verblijf in de afgelopen vier jaar bij FAGO werd echter met name gevormd door de collega-AiO's. Gedeelde last is halve last ! Ik zal de lunches met zijn bijna onvermijdelijke discussies missen. Dat geldt ook voor mijn vertrouwde overbuurman en voorbeeld in werkdiscipline Harold. Nagenoeg tien jaar hebben we elkaar

nageäapt en ook hierna zullen we weer collega's zijn. Dat is geen toeval meer. Een meer dan collegiale genegenheid heb ik in dit laatste jaar ontwikkeld voor Ellie. Net op tijd en wederzijds ! Ik hoop van harte dat er vanaf nu meer ruimte over blijft om daar nog meer van te genieten.

Tenslotte, home sweet home: pa, ma, het zusje en Schabol; Een goede basis wordt thuis gelegd. Bedankt daarvoor en voor alle steun en toeverlaat.

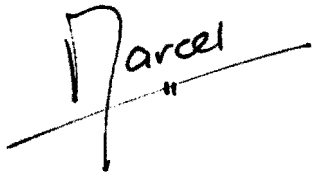

Curriculum vitae

Marcel Loomans werd geboren op 6 april 1970 in het Brabantse plaatsje Dongen. Hij heeft daar zijn jeugd doorgebracht en in 1988 behaalde hij het Atheneum diploma aan het Dr. Schaepmancollege te Dongen. Nog in datzelfde jaar werd een aanvang genomen met de studie Bouwkunde aan de Technische Universiteit Eindhoven (TUE). Binnen deze studie specialiseerde hij zich in de bouwfysica bij de toenmalige vakgroep FAGO en behaalde in 1994 het ingenieursdiploma (met lof). Als een vervolg op het afstudeeronderwerp 'Thermisch gedreven stroming' bleef hij gedurende 4 jaar verbonden aan de TUE, dit keer als Assistent-in-Opleiding. In deze periode werd onder leiding van prof.ir. P.G.S. Rutten het in dit proefschrift beschreven onderzoek verricht. De auteur is momenteel werkzaam bij TNO-Bouw te Delft als wetenschappelijk medewerker.

Propositions

- The Measurement and Simulation of Indoor Air Flow -

Marcel Loomans

1. The reliability in measuring in-situ indoor air velocities should not be overestimated given the current state of the art in low air velocity measurement techniques (see Chapter 3 of this thesis).
2. The importance of the heat transfer coefficient on the thermal aspects and flow characteristics of the indoor air flow is inversely proportional to the possibility to determine this coefficient (see Chapter 6 and 7 of this thesis).
3. There is no particular advantage in sitting close to a displacement ventilation unit (see Chapter 8 of this thesis).
4. The definition of thermal comfort given in the standards (ASHRAE 1992[1]) "the condition of mind that expresses satisfaction with the thermal environment" implies that thermal comfort is strictly personal. The model of Fanger (1970[2]), which is prescribed in the standards, however does not predict personal thermal comfort.
5. Measuring is knowing, if you know what you are measuring; this accounts especially to the measurement of indoor air velocities.
6. Despite its restrictions Computational Fluid Dynamics (CFD) is able to extend knowledge on flow problems at every level encountered in building physics (building / room / detail).
7. Architects personalise their creations (buildings) and in that phase may forget about the future occupant.
8. A lot of energy is put into energy saving.
9. Though non-smoking is regarded to as the normal social behaviour for almost two decades already (4th World Conference, Stockholm 1979[3]) and despite the very negative effect of smoking on the indoor air quality, sociability is still associated with smoking.
10. Wherever you live, you come to love it (Japanese saying).
11. Whether biking is a healthy activity should be taken into doubt more and more considering the increased motorised traffic on the road and especially on the bicycle lane.

---

[1] ASHRAE. 1992. *ANSI/ASHRAE Standard 55-1992, Thermal Environmental Conditions for Human Occupancy*, American Society of Heating, Refrigerating, and Airconditioning Engineers, Inc., Atlanta, USA.

[2] Fanger, P.O. 1970. *Thermal Comfort*, thesis, Technical University of Denmark, Lyngby, Denmark.

[3] World Health Organisation. 1979. *Controlling the smoking epidemic. Report of the WHO expert committee on smoking control*, World Health Orginisation Technical Report Series 636, Genove, Switzerland (adopted as recommendations by the participants at the *Fourth World Conference on Smoking and Health*, Stockholm, June 18-21, 1979).

Stellingen

- The Measurement and Simulation of Indoor Air Flow -

Marcel Loomans

1. De betrouwbaarheid van in-situ metingen van luchtsnelheden in de binnenruimte moet niet worden overschat gegeven de huidige stand van zaken in de techniek van het meten van lage luchtsnelheden (zie Hoofdstuk 3 van dit proefschrift).
2. Het belang van de warmteoverdrachtscoëfficient op de thermische en stromingstechnische aspecten van een luchtstroming in de binnenruimte is omgekeerd evenredig met de mogelijkheid om deze coëfficient te bepalen (zie Hoofdstuk 6 en 7 van dit proefschrift).
3. Er is geen duidelijk voordeel te behalen door dichter bij een verdringingsventilatie unit te zitten (zie Hoofdstuk 8 van dit proefschrift).
4. De definitie van thermisch comfort zoals gegeven in de normen (ASHRAE 1992[1]) "the condition of mind that expresses satisfaction with the thermal environment" impliceert dat thermisch comfort strikt persoonlijk is. Het in de normen voorgeschreven model van Fanger (1970[2]) voorspelt echter niet het persoonlijke thermisch comfort.
5. Meten is weten, als je weet wat je meet; dit geldt in het bijzonder voor het meten van luchtsnelheden in de binnenruimte.
6. Ondanks de beperkingen is CFD in staat om de kennis ten aanzien van stromingsproblemen op elke niveau binnen de bouwfysica (gebouw / ruimte / detail) te vergroten.
7. Architecten personifiëren hun creaties (gebouwen) en in die fase kunnen ze soms de toekomstige gebruiker uit het oog verliezen.
8. Er wordt veel energie besteed aan energie besparing.
9. Hoewel niet-roken al bijna twee decennia wordt beschouwd als het normale sociale gedrag (4th World Conference, Stockholm 1979[3]) en ondanks het feit dat roken een zeer negatief effect heeft op de luchtkwaliteit, wordt gezelligheid (sociaal gedrag) nog steeds geässocieerd met roken.
10. Waar je ook woont, je gaat er van houden (Japans gezegde).
11. Aan het gezonde karakter van fietsen moet steeds meer getwijfeld worden gezien de verdere toename van het gemotoriseerde verkeer op de weg en met name op het fietspad.

---

[1] ASHRAE. 1992. *ANSI/ASHRAE Standard 55-1992, Thermal Environmental Conditions for Human Occupancy*, American Society of Heating, Refrigerating, and Airconditioning Engineers, Inc., Atlanta, Verenigde Staten.

[2] Fanger, P.O. 1970. *Thermal Comfort*, proefschrift, Technical University of Denmark, Lyngby, Denemarken.

[3] World Health Organisation. 1979. *Controlling the smoking epidemic. Report of the WHO expert committee on smoking control*, World Health Orginisation Technical Report Series 636, Genove, Switzerland (aangenomen als aanbevelingen door de deelnemers aan de *Fourth World Conference on Smoking and Health*, Stockholm, 18-21 juni, 1979).